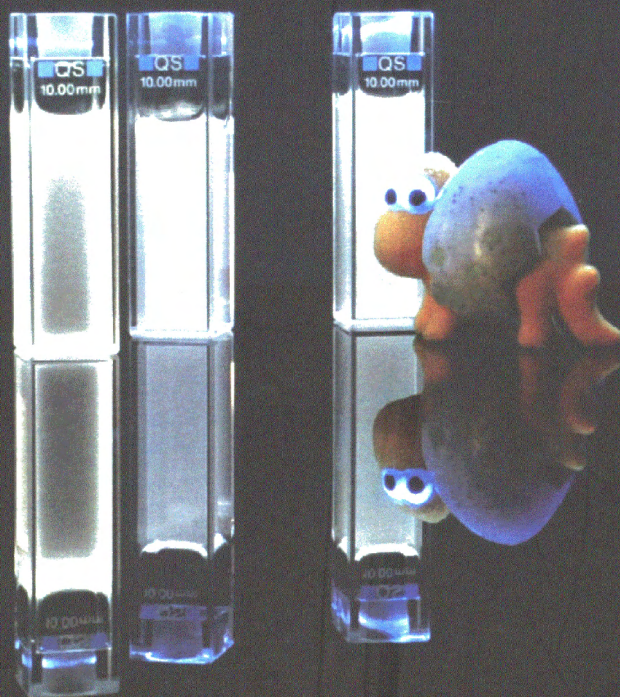


Ewelina Karolak-Solarska

**Photoinduced electron transfer
in triarylmethane lactones.
Photophysics-structure relationship**



**Photoinduced electron transfer
in triarylmethane lactones.
Photophysics-structure relationship**

A-21-15
K-c-123

Ewelina Karolak-Solarska

**Photoinduced electron transfer
in triarylmethane lactones.
Photophysics-structure relationship**



Biblioteka Instytutu Chemii Fizycznej PAN

F-B.448/13



PhD dissertation written under the supervision of
Jerzy Karpiuk, DSc

This dissertation has been completed in the framework of the International PhD Studies
at the Institute of Physical Chemistry of the Polish Academy of Sciences,
Kasprzaka 44/52, 01-224 Warsaw

Warsaw, February 2013

<http://rcin.org.pl>



B. 440/13

*Ich werde die Tests bestehn,
die mir das Leben stellt
weitergehn, suchend nach dem,
was mich am Leben hält.
Bin damit nicht allein
und werd es nie mehr sein,
weil mich zum ersten Mal seit langer Zeit
Verbundenheit befreit,
bin ich soweit...*

*Komm hierher, komm hierher,
herzlich willkommen zuhaus.*

Thomas Dürr

*Moim najbliższym,
„Millionen Legionen hinter mir“*

Abstract

This thesis presents results of a study on the structure–property relationships in a class of donor acceptor (D–A) molecules, triarylmethane lactones (LTAM). By introducing systematic structural and orientational modifications the effect on the photoinduced electron transfer processes was investigated. For this purpose, a series of triarylmethane lactones was designed, synthesized and characterized by spectroscopic methods.

In LTAM molecules, separation of the electron donating moiety from the electron accepting one by an sp^3 carbon atom allows in the ground state for preservation of individual photophysical properties of the structural subunits. On the excited state level, the tetrahedral carbon link in combination with a C–heteroatom bond serves as an effective channel for intramolecular electronic communication and enables strong electronic coupling resulting in an ultrafast and efficient ET with formation of an intramolecular exciplex of a radical ion pair structure. Based on the study of LTAM with two (D–D–A triad) or with one (D–A dyad) D moieties it was found that not only the primary ET process occurs in close analogy in both molecules, but also the deactivation paths of the CT states are virtually the same in triads and dyads. Hence, in symmetric D–D–A triads only one D group is actively involved in the charge separation (CS) process. Both, dyads and triads form CT triplet states in excited state deactivation. The work explored the effect of structural modifications resulting in changing the reduction potential of the acceptor subunit in LTAM of the D–D–(DA) type. The rate and yield of the ET process in these molecules are strongly solvent dependent, since the solvation dynamics generally controls the energy and availability of the excited states. Special attention was paid to the effect of mutual orientation of the D and A subunits on the excited state processes in spiro–derivatives of LTAM. The presence of spiroconjugation between D and A was demonstrated and its effect on the photophysics described. Almost equal energies of the D and A subunits result in inversion of nearly degenerated excited states and fluorescence switching as a function of solvent polarity and temperature. Moreover, the rigid spiro–structure affects not only the energetics, but it opens new deactivation pathways for the initially excited molecule. It was shown that a vibronically hot molecule can undergo a lactone ring–opening reaction with formation of a short–lived (on the ps time scale) zwitterionic species. It was also found that minor modifications of the structural subunits of LTAM result in significant changes in energies of the lowest excited states, and consequently in the involvement of the primary ET in a sequence of processes, enabling manipulation of the CS reaction, and even molecular engineering, especially because these simple D–A systems display dual fluorescence. The question of exploiting dual fluorescence in white light generation in derivatives of crystal violet lactone (CVL) was addressed. Using two CVL analogues, it was shown that dual emission is a general property of the D–D–(DA) structures built on an sp^3 carbon atom.

Streszczenie

W ramach niniejszej pracy zbadano relacje między strukturą a właściwościami w laktonach triarylometanowych (LTAM), stanowiących klasę cząsteczek donorowo-akceptorowych (D–A). Wpływ struktury na fotoindukowane przeniesienie elektronu (ET) określono na podstawie badań systematycznie wprowadzanych modyfikacji strukturalnych oraz wpływu zmiany przestrzennego ułożenia podjednostek. W tym celu zaprojektowano i zsyntetyzowano serię cząsteczek laktonów triarylometanowych oraz zbadano ich fotofizykę.

W cząsteczkach LTAM, oddzielenie podjednostki elektronodonorowej od podjednostki elektroakceptorowej przez atom węgla o hybrydyzacji sp^3 pozwala na zachowanie indywidualnych właściwości fotofizycznych poszczególnych chromoforów. Na poziomie stanu wzbudzonego, tetraedryczny zwornik D i A w połączeniu z wiązaniem C–heteroatom działa jako efektywny kanał wewnątrzcząsteczkowej komunikacji elektronowej i umożliwia silne sprzężenie elektronowe prowadzące do ultraszybkiego i wydajnego procesu ET z wytworzeniem wewnątrzcząsteczkowego ekscypleksu o strukturze pary jonorodników. Na podstawie badań cząsteczek laktonów triarylometanowych z dwoma (triada D–D–A) lub jedną (diada D–A) podjednostką D wykazano, że pierwotny proces ET przebiega analogicznie w triadzie i w diadzie, a ponadto, że ścieżki dezaktywacji stanu CT są praktycznie identyczne dla obu układów. Na tej podstawie stwierdzono, że w symetrycznych układach D–D–A tylko jedna grupa D jest zaangażowana w proces ET. Zarówno w diadach, jak i w triadach, w procesie dezaktywacji stanów wzbudzonych obsadzone są stany trypletowe z separacją ładunku. W ramach niniejszej pracy określono wpływ modyfikacji strukturalnych polegających na zmianie potencjału redukcji podjednostki DA w cząsteczkach typu D–D–(DA) na fotofizykę LTAM. Stwierdzono, że szybkość oraz wydajność procesu ET są silnie zależne od polarności rozpuszczalnika, a energia stanów wzbudzonych, a tym samym ich dostępność, jest kontrolowana przez solwatację. Wiele uwagi poświęcono zagadnieniu wpływu wzajemnej orientacji D i A na procesy zachodzące w stanie wzbudzonym w spirocyklicznych pochodnych LTAM. Potwierdzono obecność oddziaływania spirokonjugacyjnego oraz określono jego wpływ na fotofizykę cząsteczek. Zbliżone energie podjednostek D i A prowadzą do inwersji praktycznie zdegenerowanych stanów wzbudzonych, a tym samym do przełączania fluorescencji cząsteczki w funkcji polarności rozpuszczalnika oraz temperatury. Ponadto, sztywna spirocykliczna struktura cząsteczki nie tylko wpływa na energetykę, ale również otwiera nowe ścieżki dezaktywacji pierwotnie wzbudzonego stanu elektronowego. Pokazano, że oscylacyjnie „gorąca” cząsteczka może ulegać reakcji otwarcia pierścienia laktonowego z wytworzeniem krótkożyjącego (na skali ps) jonu obojnego. Wykazano, że niewielkie modyfikacje podjednostek LTAM prowadzą do znaczących zmian w energetyce niższych stanów wzbudzonych, a w konsekwencji do włączenia reakcji ET w całą sekwencję procesów, umożliwiając tym samym sterowanie procesem separacji ładunku, a nawet prostą inżynierię molekularną (głównie ze względu na podwójną fluorescencję prostych układów LTAM). W ramach niniejszej pracy podjęto zagadnienie wykorzystania podwójnej fluorescencji pochodnych laktonu fioleto krystalicznego (CVL) w generacji światła białego. Na podstawie badań pochodnych CVL wykazano, że podwójna fluorescencja jest cechą układów typu D–D–(DA) zbudowanych na atomie węgla o hybrydyzacji sp^3 .

Table of Contents

Chapter 1	1
Introduction	
1.1 Introduction.....	1
1.1 Objectives of the thesis	4
Chapter 2	6
Leuco-derivatives of triarylmethane dyes as a platform for multichromophoric D-A systems	
2.1 Intramolecular ET – a theoretical background.....	6
2.2 Rotation in excited state deactivation of triarylmethane dyes.....	10
2.3 Photodissociation in triarylmethane leuconitriles	12
2.4 Lactonic forms of triarylmethane dyes	16
2.4.1 Colour forming reaction.....	16
2.4.2 LTAM as multichromophoric D-A systems.....	17
2.4.3 Ultrafast electron transfer in MGL and PP.....	18
2.4.4 Coexistence of two emitting CT excited states in CVL	22
2.4.5 Charge separation dynamics in CVL	24
2.4.6 CVL as a probe of solvation dynamics in ionic liquids.....	28
2.5 Structure-properties relationship in triarylmethane derivatives—a summary	30
2.6 Dual fluorescence and intramolecular electron transfer.....	32
2.7 Dual fluorescence in white light generation.....	36
2.8 Perception of colour and colour representation.....	38
Chapter 3	40
Experimental methods and instrumentation	
3.1 Materials used in the investigations	40
3.1.1 Triarylmethane lactones studied in this work.....	40
3.1.2 Structural subunits.....	44
3.1.3 Solvents.....	47
3.2 Absorption and emission spectra	47
3.3 Transient absorption measurements.....	48
3.4 X-ray structures	49
3.5 Calculations	50

Chapter 4 51

Triad vs. dyad donor–acceptor structure: Malachite Green Lactone and its analogue (MGLA)

4.1 Ground state structure of MGLA and MGL	52
4.2 Absorption transitions in aprotic solvents	55
4.3 Fluorescence at room temperature	58
4.4 Excited state dipole moment	62
4.5 Absorption and fluorescence in alcohols	64
4.6 Nature of the triplet states populated at room temperature	65
4.7 Fluorescence thermochromism and luminescence in glasses	68
4.7.1 Fluorescence thermochromism of MGL and MGLA	68
4.7.2 Charge transfer and local triplet states – luminescence in glasses	72
4.8 Discussion	75

Chapter 5 81

Relaxation to the CT state as a general deactivation route for D–A–D and D–A structures

5.1 Absorption in aprotic solvents	82
5.2 Fluorescence at room temperature	85
5.3 Summary	90

Chapter 6 91

Dual fluorescence from two polar excited states in an amino analogue of Crystal Violet Lactone (CVLH2)

6.1 Ground state structure	91
6.2 Absorption in aprotic solvents	92
6.3 Fluorescence at room temperature	95
6.4 Excited state dipole moment	100
6.5 Nature of the triplet states populated at room temperature	103
6.6 Luminescence in glasses	107
6.7 Discussion	108

Chapter 7 113

Ultrafast radiationless deactivation in spiro-bridged Crystal Violet Lactone structure (CVLB)

7.1 Spectroscopic characteristic of structural subunits of CVLB	113
7.1.1 6–dimethylaminophthalide (6–DMAPd)	113
7.1.1.1 Ground state structure	114
7.1.1.2 Electronic structure	115
7.1.1.3 Emission as a function of solvent polarity and temperature	117
7.1.2 3,6–bis(dimethylamino)fluorene (DMAF)	118

7.1.2.1 Ground state structure	119
7.1.2.2 Electronic structure	122
7.1.2.3 Emission as a function of solvent polarity and temperature.....	124
7.2 Ground state structure of CVLB	128
7.3 Electronic absorption in aprotic solvents	133
7.4 Molecular orbitals	137
7.5 Fluorescence at room temperature	141
7.6 Excited state dipole moment	146
7.7 Temperature dependent fluorescence switching	148
7.8 Electron transfer and ring opening reaction – a transient absorption study	152
7.9 Luminescence in glasses	158
7.10 Summary and discussion.....	159
Chapter 8.....	163
White fluorescence – main goal or byproduct?	
8.1 DA structure effect on the equilibrium between the emitting states	164
8.2 Effect of spirocyclic structure on the parameters of white fluorescence.....	168
8.3 Summary.....	170
Chapter 9.....	171
Summary and outlook	
Acknowledgements	175
Publications	177
Conferences	177
Appendix	179
References.....	185

Chapter 1

Introduction

1.1 Introduction

Photoinduced electron transfer (PET) reactions are considered to be the most fundamental physicochemical processes with rates covering different time domains, from femtoseconds^{1,2} to seconds.³ PET underlies a huge number of processes occurring in animate and inanimate nature. Photoinduced charge separation (CS) is the basic process in photosynthesis, where after energy transfer from the light harvesting system, the initial charge separation and consecutive charge transport take place, leading to building up a proton gradient that powers ATP production and stores energy in the reduced coenzyme NADPH.^{4,5} PET plays a key role in conversion of solar energy to electricity in photovoltaic devices based on organic as well as semiconductor materials.⁶

Ultrafast ET is a fundamental requirement for D–A systems employed for effective conversion of photon energy into useful redox potential. The ET process in heterogeneous systems reached a very low femtosecond limit, charge separation during 6 fs was reported for alizarin complexed on a surface of a TiO₂ semiconductor colloid.⁷ Schnadt *et al.*⁸ observed a sub–3 fs ET time for the bi–isonicotinic acid/TiO₂ system. Such a fast ET processes are possible due to ultrafast electron injection from the photoexcited dye to the conduction band of TiO₂, resulting from a very strong electronic coupling between the sensitizer and the semiconductor. On the other hand, the studies on ultrafast intramolecular ET on the time scale of single vibrations (tens of fs) are just at the outset. Jortner *et al.*⁹ have theoretically predicted and discussed charge separation process with k_{ET} up to 10^{14} s^{-1} , but reports on ultrafast ET in organic systems are scarce, due to difficulties in finding molecules with a barrierless ET processes that do not need any solvent assistance. In Nile blue connected to a 3–ferrocenophane moiety electron is transferred within 90 fs,¹⁰ Barbara *et al.*¹¹ reported on a ruthenium complex in water to undergo ET on the same timescale. Until now, the fastest intramolecular charge separation process was reported by Kovalenko *et al.*¹² for cyanobianthryl to take place within 10 fs along a high

frequency coordinate. The search of new donor–acceptor systems with high ET rates is very important both for applications and for gaining a deeper insight into the nature of this process. Although the research into structure–property relationship has since long been accompanying PET studies, it is still hindered by the scarcity of knowledge regarding the optimum geometries for fast electron transfer. In this context, malachite green lactone (MGL) and phenolphthalein, members of the triarylmethane lactone (LTAM) family, with photoinduced ET on a sub–100 fs time scale are very promising molecules.¹³ Simple structure and well–defined geometry together with identified reaction coordinate (C–O bond in the lactone ring), make triarylmethane lactones excellent objects for studies on ultrafast ET and the effects and interplay of inertial solvation and intramolecular modes promoting charge separation. Crystal violet lactone, a derivative of MGL (having an additional electron–donating group), also undergoes ET, its rate, however, is controlled by the solvent dynamics. In this thesis the emphasis is put on the influence the molecule structure exerts on the excited state energetics and the ultrafast ET process, both forward and backward, in triarylmethane lactones. It turns out that minor modifications in structure of the donor or the acceptor subunit and thus in energy of the lowest excited states, lead to involvement of the primary ET reaction in a sequence of processes taking place in the excited state and enable the manipulation and control over the ET reaction. The insights into structure–property relationships obtained in this thesis significantly contribute to the knowledge about systems with ultrafast ET and the factors affecting it. LTAM are convenient systems, since the mutual distance and orientation between the donor and the acceptor are strictly controlled and easily changeable.

In systems designed for artificial photosynthesis, in molecular photonic and photovoltaic devices it is of paramount importance that the charge separation is asymmetric, i.e., the primary electron transfer step is ultrafast but the recombination of charges is slower by orders of magnitude. Strategies implemented so far to slow down the charge recombination include shifting the energetics of the ET reaction to the Marcus inverted region,¹⁴ orbital symmetry control in simple D–A dyads,^{15,16} multistep long range ET in complex multichromophoric systems,^{17,18} and electron spin control in simple donor–bridge–acceptor systems.^{19,20} MGL is known to undergo ultrafast ET reaction and relatively slow (on the ns time scale) recombination. The presence of the triplet charge transfer state and its degeneracy with the lowest singlet charge transfer state in malachite green lactone and its structural analogues make these molecules unique candidates for studies on the spin control over the lifetime of intramolecular radical ion

pairs. Furthermore, these molecules can be used in studies on the CT singlet–triplet coupling and interaction, as well as for exploring (so far poorly investigated) the area of CT phosphorescence in structurally simple and well–defined D–A systems. Systems with clearly identified CT triplet states are scarce, and this work provides knowledge about a new class of molecules, where the population of CT triplet states is experimentally confirmed.

The use of dual fluorescence in white light generation is an important topic in the search for new chromophores for use in organic light emitting diodes (Section 8). Crystal violet lactone and its derivatives were found to emit spectrally continuous dual fluorescence appearing as white light. In this thesis, structures of LTAM were defined, for which broad dual fluorescence is a general property.

The goal of this thesis was to investigate the structure–property relationship in a class of D–A molecules, LTAM. By introducing systematic structural and orientational changes the impact on the ET processes was investigated. As the outcome, new knowledge on the influence of the molecular structure on photophysics and on the ET process itself was gained.

This thesis is organised as follows: Chapter 1 introduces the problems, issues and questions addressed in the thesis. The scope of the thesis is presented and the compounds studied herein are described. Chapter 2 provides the basic theoretical and literature background. Furthermore, the photophysics of different triarylmethane derivatives is described with special emphasis put on the leuco derivatives. A short introduction to dual fluorescence as a prospective source of white light is given as well. Chapter 3 contains the description of synthetic procedures, materials and instrumentation used in this work. Chapter 4 analyses the effect of simplification of the LTAM molecules from a D–A–D triad (natural for these systems) to a D–A dyad structure in a malachite green lactone analogue. Chapter 5 gives an overview on the photophysics of different derivatives of malachite green lactone (having various donor substructures and sulphur atom incorporated in the lactone ring). Chapter 6 focuses on the effect of the local excited state energy of the acceptor moiety on the ET process in LTAM by analysing the photophysics of a crystal violet lactone derivative. Chapter 7 describes consequences of bridging the LTAM structure and resulting spiroconjugation as exemplified by the photophysics of a rigid spirocyclic analogue of crystal violet lactone. Chapter 8 addresses the spectrally broad dual fluorescence of crystal violet lactone and its analogues in terms of white light generation by molecular systems. The last

Chapter provides a summary and reviews open questions, problems and issues emerging from this work.

1.1 Objectives of the thesis

Studies on lactonic forms on triarylmethane dyes (LTAM) have been rather scarce and incomplete until a series of papers started in 2003 by J. Karpiuk. These publications formed the basis for the present thesis.

An overriding goal of this work was to investigate the structure – photophysics relationship in triarylmethane lactones. Special emphasis was put on the effect the molecular structure has on the kinetics and energetics of the ET process (recombination). Particular regard was devoted to the effect of structure simplification on the ET reaction. Analogues of malachite green lactone (MGL) and phenolphthaleine (PP) with only one electron donating subunit were investigated. Furthermore, the influence of new electron donating subunits on the energetics and rate of the ET process was explored. Special attention was paid to the relation between the structure of the electron accepting unit and the energetics of the excited states. Structural analogues of CVL (different D and A substructures) were studied for the impact of structure on the energetics of the excited states and the availability of different deactivation pathways. Conditions for equilibrium between the excited states were carefully analysed. Particular attention attracted a rigid spirocyclic CVL derivative that was initially included in this study to explore the LTAM photophysics in well-defined perpendicular orientation of D and A. It turned out, however, that such structural modification has far reaching consequences due to a variety of excited state processes in this derivative (CVLB) including photodissociation of the C–O bond. The photophysical study was rounded up with an attempt to use dual fluorescence of CVL derivatives for white light generation by organic fluorophores. Conditions for the spectrally broad dual fluorescence were elaborated and directions for the development of useful white light emitters formulated.

It should be noted that some of the molecules studied were for the first time synthesized for the purpose of this thesis (tetrahydroquinoline and julolidine derivatives, bridged MGL and CVL, CVLH2, derivatives of MGL with sulphur in the lactone ring; Fig. 1.1).

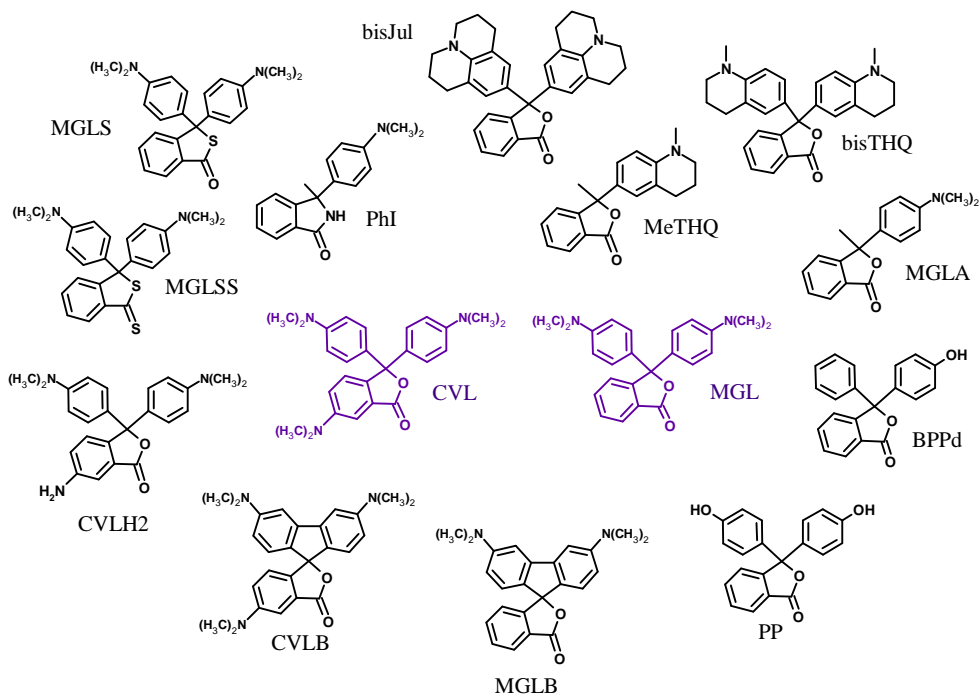


Fig. 1.1 Compounds studied in this work.

The molecule pairs MGL–MGLA, PP–BPPd, bisTHQ–MeTHQ were used for investigations on the effect of structure simplification on the ET process in the excited state. Moreover, based on research done on these molecules, together with bisJul and molecules where the oxygen atom is substituted by sulphur or nitrogen (MGLS, MGLSS and PhI) allowed drawing general conclusions on the photophysical properties of triarylmethane lactones. The effect of oxidation potential on the excited state energetics was elucidated based on CVLH2 and CVL as model compound. Further, spirocyclic CVLB and MGLB were selected as objects for investigations on the impact of a rigid and well–defined structure on the processes in the excited state with special emphasis put on the ET reaction.

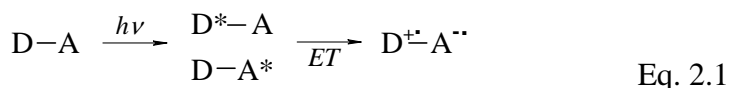
Chapter 2

Leuco–derivatives of triarylmethane dyes as a platform for multichromophoric D–A systems

This Chapter starts with a short introduction to the ET theory, focusing on intramolecular photoinduced charge separation, and its thermodynamical and kinetic aspects. Then, the photophysics of coloured cationic triarylmethane (TAM⁺) dyes and their colourless leuco forms of are reviewed with special attention put to what has been known on the lactonic forms of TAM dyes, i.e., CVL, MGL and PP. Final sections provide an introduction to dual fluorescence and its implementation in white light generation, and a brief review of our perception of colour and colour representation.

2.1 Intramolecular ET – a theoretical background

Intramolecular photoinduced ET is a process that takes place after photon absorption and consists in transferring an electron from an electron donating (D) to an electron accepting moiety (A) (Eq. 2.1).



This simple sequence of events allows for converting light into useful chemical potential. The product of a charge separation (CS) process is a charge transfer (CT) state with a structure of an intramolecular exciplex or an ion pair, comprising the radical cation of the donor (D⁺) and the radical anion of the acceptor (A⁻). Due to its radical ion pair structure, the CT state has a highly polar nature and can undergo further reactions, i.e., bond cleavage or new bond formation, but in most cases it undergoes recombination (radiative or radiationless) leading finally to the initial state. The fluorescence from the CT state is strongly dependent on the polarity of the environment due to the high dipole moment of the emitting state.

The Gibbs free energy “stored” in a CT state formed from a neutral D–A species can be estimated based on the oxidation potential of D

$[E^0(D^+/D)]$ and the reduction potential of A $[E^0(A/A^-)]$ molecules using the following expression derived by Weller (Eq. 2.2):^{21,22}

$$\Delta G^0_{D+A^-} = e[E^0(D^+/D) - E^0(A/A^-)] - \frac{e^2}{4\pi\epsilon_0\epsilon_s R_C} - \frac{e^2}{8\pi\epsilon_0} (1/r_{D^+} + 1/r_{A^-})(1/\epsilon_{ss} - 1/\epsilon_s) \quad \text{Eq. 2.2}$$

where e denotes the elementary charge; ϵ_0 – vacuum permittivity; ϵ_s is the dielectric constant of the solvent; ϵ_{ss} is the dielectric constant of the solvent in which the redox potentials were measured; r_{D^+} and r_{A^-} are effective ionic radii of the D and A, respectively; R_C stands for the center-to-center distance between the D and A. The first term of the Weller equation describes the driving force, the second introduces coulombic interactions between the ions and the last term is responsible for solvation (if the electrochemical data was obtained from measurements in the same solvent as the Gibbs energy is calculated, then $\epsilon_{ss} = \epsilon_s$ and this term is zero). In order to calculate the Gibbs free energy of charge separation (the “driving force”) in the excited state, the energy difference between the S_0 and S_1 states has to be accounted for:

$$\Delta G^0_{ET} = \Delta G^0_{D+A^-} - E_{00} \quad \text{Eq. 2.3}$$

where E_{00} is the energy of the excited state of the absorbing species. Based on the Weller equation (Eq. 2.2) it is possible to judge if ET can take place (as long as $\Delta G^0_{D+A^-} < E_{00}$ the reaction occurs).

The rate of ET reactions is usually considered in terms of Marcus theory, linking the thermodynamics of the process to its kinetics.^{23,24,25} It was originally formulated for the outer sphere ET reactions, where the reactants do not share a common atom or group of atoms and hence the interaction between the electronic orbitals of D and A is weak.

The electron transfer between D and A is described by invoking the Franck–Condon principle: the ET takes place, when nuclear configurations of both moieties are identical and the total potential energy of the reactants and the surrounding medium is equal to that of the products and the surrounding medium. The potential energy surfaces are multidimensional, since they are functions of many variables including nuclear coordinates of the reactants and of surrounding solvent molecules. These potential energy surfaces can be reduced to one-dimensional profiles by introducing a reaction coordinate (from the transition state theory). The Marcus theory assumes that the initial and the final states of the ET process can be described by parabolic potential energy curves (Gibbs free energy) with similar shapes and widths. The criteria for the ET are met at the intersection

of the parabolas describing the reactants and the products. Thermal fluctuations are a prerequisite for the system to reach the intersection region.

Three different ways of intersection of the potential energy curves of the reactants and the products as functions of the reaction coordinate can be distinguished based on the relationship between the activation energy (ΔG^\ddagger) and the reorganization energy (λ) in the ET reaction (Fig. 2.1). The relationship between the two energies can be derived by analysing the geometry of the intersecting parabolas:

$$\Delta G^\ddagger = (\Delta G_{\text{ET}}^0 + \lambda)^2 / 4 \lambda \quad \text{Eq. 2.4}$$

The reorganization energy λ is a sum of the reorganization energy of the solvent (changes of solvent orientation coordinates, referred to as external reorganization energy) and the internal reorganization energy related to the change in bond angles and distances in reactants. The rate constant of ET reactions (k_{ET}) can be expressed in terms of the Arrhenius formalism, where the reaction rate depends on the activation energy (E_a) of the reaction, the temperature (T), and the pre-exponential (frequency) factor (A):

$$k_{\text{ET}} = A \exp(-\Delta G^\ddagger / k_B T) \quad \text{Eq. 2.5}$$

where k_B is the Boltzmann constant.

The Marcus theory predicts the existence of three regions in the dependence of k_{ET} on the ΔG_{ET}^0 . In the first region, where $\lambda = -\Delta G_{\text{ET}}^0$ and the ET process is barrierless, the ET rate is the highest under given conditions. The normal region is described by $\lambda > -\Delta G_{\text{ET}}^0$, and the ET rate increases with increasing “driving force” of the reaction, ΔG_{ET}^0 . In the inverted region, when $\lambda < -\Delta G_{\text{ET}}^0$, k_{ET} decreases in spite of increasing ΔG_{ET}^0 . The reorganization energy λ is defined as the energy needed to distort the product (final) state and its surroundings to reach the equilibrium configuration of the reactants (initial) state (while staying on the potential energy curve of the product) (Fig. 2.1).

The predicted existence of the Marcus inverted region was considered controversial, due to its counter-intuitive decrease of the ET rate on increasing reaction exoergonicity, but eventually found empirical evidence.^{26,27,28} However, the observed k_{ET} in this region are higher than resulting from the classical Marcus theory due to the fact that electron tunnelling plays an important role in the inverted region.

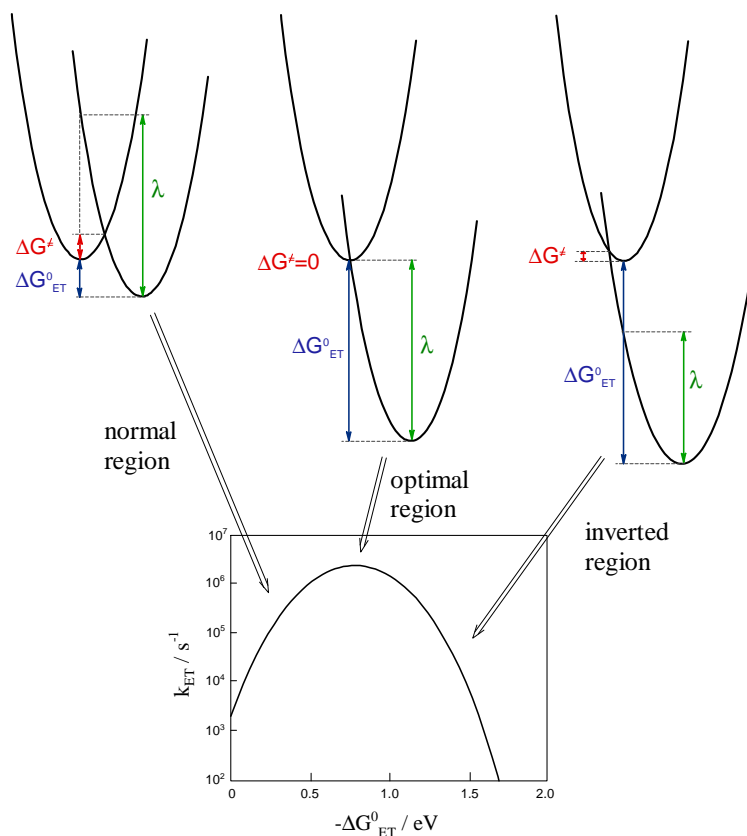


Fig. 2.1 Representation of the free energy regimes after Marcus: normal region, optimal region, where k_{ET} reaches its maximal value and inverted region, where the increase of activation energy results in decreasing k_{ET} . On the bottom, the bell shaped Marcus curve is presented (using the classical Marcus equation, Eq. 2.5).

Numerous modifications and extensions of the classical Marcus theory were introduced based on experimental evidence as well as theoretical considerations. Development of a quantum chemical approach allowed for satisfying description of temperature and ΔG_{ET}^0 dependence^{29,30} due to inclusion of quantum modes, i.e., tunnelling.^{31,32} Accounting for dynamic properties of the solvent³³ enabled to explain the temperature and solvent dependencies of k_{ET} in intramolecular ET reactions. In order to explain the ET reactions faster than orientational solvation, new reaction coordinates were introduced. The Sumi–Marcus model³⁴ takes into account both, the vibrational (low frequency mode) and polarization coordinates and explains nonexponential kinetics of some ET reactions. Barbara *et al.*^{35,36} proposed a hybrid model combining the Sumi–Marcus model and ideas of Jortner and

Bixon (the role of high frequency vibrational modes)³⁷ hence introducing three reaction coordinates. This extension allows for explanation of the enhancement of the rate of barrier crossing in ET reactions.³⁸

Some aspects and predictions of the modified Marcus theory are still awaiting experimental confirmation, especially issues connected with ultrafast ET processes with predicted rates of 10^{14} s^{-1} . Processes occurring on this timescale are possible only in the presence of strong electronic coupling between D and A, and the existence of a quasi-continuum of Franck-Condon states of the product. It seems that LTAM molecules could be used as testing objects for the applicability of the extended theories, since the ultrafast ET process in LTAM occurs under barrierless conditions and its dynamics is determined by intramolecular vibrational modes (C–O vibration) and not by orientational solvation.¹³

2.2 Rotation in excited state deactivation of triarylmethane dyes

Triarylmethane dyes (TAM^+) were among the first synthetic dyes to be developed³⁹ and still are suitable for a variety of technological applications. They have been widely used in textile, food, cosmetic and photographic industry as colorants because of their brilliant colours, high tinctorial strength and low light fastness.⁴⁰ TAM^+ are employed in laser spectroscopy as saturable mode absorbers for mode locking due to their poor fluorescence quantum yield and fast nonradiative decay.⁴¹ Their photophysical properties make them good candidates for modelling barrierless chemical reactions in solution triggered by photoexcitation.⁴² Triarylmethane dyes are extensively used for analytic spectrometric analysis,⁴³ are important components in dye-sensitized solar cells⁴⁴ and as sensitizers for photoconductivity. In addition, TAM^+ are utilized in medical and biological sciences due to their antibacterial and antifungal properties.^{45,40}

Colourless derivatives of triarylmethane dyes (leucocyanides, leucohydroxides, leucohalides, leucoethers) also found many applications and their spectroscopic properties were broadly exploited.⁴⁶

Triarylmethane dyes have attracted much attention also because of their interesting spectroscopic properties. Cationic forms of triarylmethane derivatives exhibit intense bright colours covering the whole range of hues,

depending on the nature and position of the auxochromic substituents in the benzene rings. The photophysics and photochemistry of the arylcarbonium ion have been since long widely studied: ground state isomerisation processes,⁴⁷ femtosecond excited state isomerisation,⁴⁸ dependence of the fluorescence quantum yield on viscosity and temperature of the surrounding medium,^{49,50} and related enhanced nonradiative deactivation via rotational motions of the aryl rings.⁵¹ The area of primary interest in TAM⁺ in relation to this work is the intrinsically barrierless excited state relaxation involving rotation of aryl substituents.

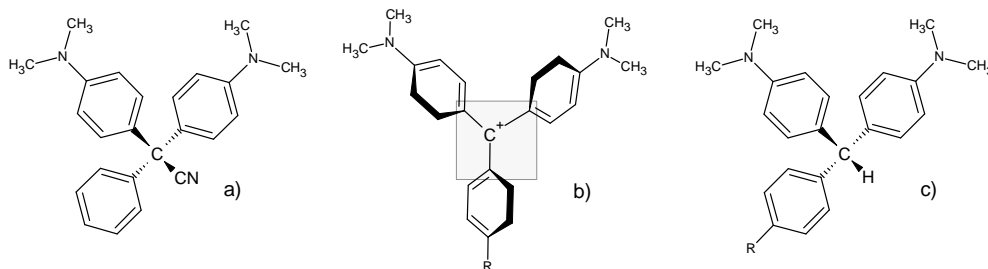


Fig. 2.2 Molecular structure of a) malachite green leuconitrile (MGCN), b) R=H: malachite green cation, MG⁺, R=N(CH₃)₂: crystal violet cation, CV⁺; c) R=H: leuco malachite green (MGH), R=N(CH₃)₂: leuco crystal violet. The molecular plane is marked by grey square.

Malachite green (MG⁺) and crystal violet (CV⁺) are typical examples of cationic triarylmethane dyes. The arylcarbonium ion in these species is nearly planar, with the positive charge delocalized over aryl substituents (Fig. 2.2). The structure of TAM⁺ resembles a three blade propeller in which steric restrictions force the blades to move out of the molecular plane containing the central carbon atom and three C atoms of the aryl rings attached to it. With three identical (dimethylaniline) substituents, CV⁺ belongs to the D₃ point group. Its electronic absorption spectrum displays a characteristic band with a maximum at 590 nm (16950 cm⁻¹) characterized by a high molar absorption coefficient⁵² of ca. 110000 M⁻¹cm⁻¹ in ethanol (responsible for the blue colour) and bands in the UV, due to transitions within dimethylaniline subunits. MG⁺ has a lower symmetry (C₂) since one of the dimethylaniline subunits is replaced by benzene ring. Being asymmetrical, MG⁺ has two axes of polarizability, which lie at right angles to each other (x, y directions). Hence, the absorption spectrum in the visible consists of two bands due to splitting of the degenerate states: the primary band at 614 nm (16300 cm⁻¹, ε = 106000 M⁻¹cm⁻¹ in ethanol⁵²) corresponding to the 590 nm peak in CV⁺ and an additional band at 425 nm

(23530 cm^{-1} , $\epsilon = 21000\text{ M}^{-1}\text{cm}^{-1}$ in ethanol⁵³).

The emissive properties of TAM⁺ dyes are strongly dependent on solvent viscosity, but not polarity. In low viscous solvents picosecond lifetimes ($2 \pm 1\text{ ps}$ for MG⁺ in water⁵⁴) and low fluorescence quantum yields ($\sim 10^{-5}$)⁵⁵ have been reported. In more viscous media, upon lowering the temperature or binding of TAM⁺ to a surface or protein, the fluorescence quantum yield increases⁵⁶ and the lifetime elongates considerably (at low temperatures the lifetime is limited by the radiative decay time and the fluorescence quantum yield can approach unity⁵⁷). The ultrafast deactivation of the excited singlet state is due to diffusive rotational motion of the three phenyl rings of the TAM⁺ around their axes.⁴⁸ The relaxation of the excited state occurs via a very efficient transition to a twisted intermediate state of the TAM⁺ molecule.⁵⁰ The potential energy surface for the rotational motion of the phenyl rings of these molecules was shown to be barrierless and relatively flat (Fig. 2.3).^{42,58,59}

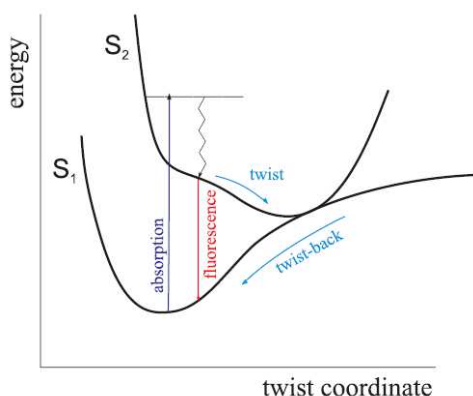


Fig. 2.3 Ground and excited state potentials of MG⁺.

2.3 Photodissociation in triarylmethane leuconitriles

Leuco-derivatives of triarylmethane dyes are photochromic systems: these colourless molecules undergo photoinduced dissociation of the central carbon – substituent bond (e.g., C–CN bond) with formation of a coloured dye cation.⁶⁰

Triarylmethane leuco-derivatives (e.g., leucodyes, leucocyanides, leucoethers, leucocarbinols) are tetrahedral structures built around the central (methane-like) carbon atom. Their conformations differ from those of the corresponding carbonium ions that have planar central carbon atom with aromatic subunits moved out of plane in a three blade propeller

conformation⁶¹ (Fig. 2.2). In TAM leuco-derivatives, the central C atom serves as a link between the structural subunits, providing for their effective electronic decoupling in the ground state.

Leuco-derivatives of triarylmethane dyes having the simplest structure and photophysics similar to those of TAM⁺ forms are leuco malachite green or leuco crystal violet.

A widely examined example of a TAM leuco-derivative is malachite green leucocyanide (MGCN). The absorption spectrum of colourless MGCN in low energy region is essentially a sum of absorption transitions localized on MGCN subunits and resembles the absorption spectrum of dimethylaniline (DMA).⁵² The fluorescence spectra in low polar solvents are characteristic of the $S_1(\pi\pi^*)$ of DMA, phosphorescence is also displayed from the local $T_1(\pi\pi^*)$ DMA state.⁶² Quantum yield for T_1 formation and intersystem crossing rate constant were determined to be 0.7–0.9 and $2.9 \times 10^8 \text{ s}^{-1}$, respectively, in nonpolar solvents at room temperature.⁶² The photophysics of MGCN change on going from low polar to polar solvents (for $\epsilon \geq 4.7$), where the fluorescence from the primary excited chromophore is effectively quenched due to ionic dissociation resulting from photoinduced dissociative electron transfer (also referred to as photoionisation) with a very high quantum yield of 0.9–1.0.⁴⁶ Herz,⁵² and later Brown and Cosa,⁶³ found that the process leading to fluorescence quenching occurs from the S_1 state, with the electronic excitation energy being transferred from the DMA chromophore to vibrational modes of the C–CN bond. The photoionisation is rapid due to almost barrierless ET process and therefore hinders the deactivation of the S_1 state by competitive routes such as intersystem crossing and fluorescence ($k_{\text{rad}} = 3.6 \times 10^8 \text{ s}^{-1}$).⁵²

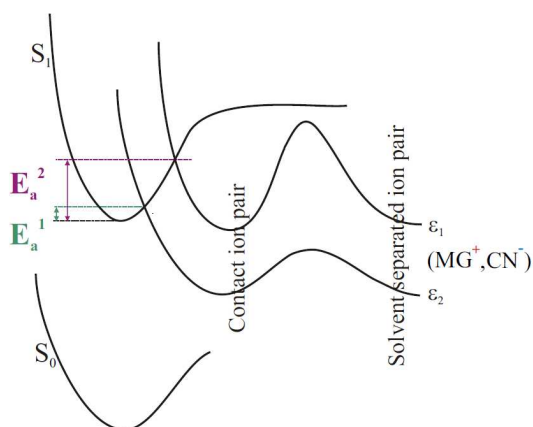


Fig. 2.4 One dimensional schematic presentation of the free energy of electron transfer in MGCN in two solvents with different polarities, $\epsilon_2 > \epsilon_1$. S_0 and S_1 are the ground and the excited states of MGCN; the two curves ϵ_2 and ϵ_1 correspond to the ionic products of electron transfer, MG^+ and CN^- ; E_a^1 and E_a^2 are activation energies in respective solvents.

Spears and co-workers⁶⁴ conducted a series of experiments to determine the rates of photoionisation as a function of solvent properties (polarity and proticity) and temperature. The calculated ET rates vary from $k_{\text{ET}} = k_{\text{ion}} = 10^7 \text{ s}^{-1}$ to 10^{10} s^{-1} , depending on solvent polarity. The determined activation energy in a simplified one reaction coordinate scheme was constant in polar solvents averaging at $\sim 1 \text{ kcal/mol}$ (ϵ_1 , E_a^1); on going to nonpolar solvents ($\epsilon_2 < 6$, E_a^2) it increased enough to inhibit the electron transfer reaction (Fig. 2.4). After the ET step, a contact ion pair is created, which can either undergo back ET or solvent reorganization to form solvent-separated ions.

Spears *et al.*⁶⁵ elucidated the role of the solvent in formation of the carbonium ion. Based on temperature measurements in solvents in a wide polarity range the authors deduced that the barrier for the ET process consists of two components: an intrinsic barrier and a viscosity-related barrier that is solvent dependent. The activation energy is dominated by the solvent frictional component, the intrinsic ET barrier being on the order of $k_{\text{B}}T$ (0.5 kcal/mol or 175 cm^{-1} ; for 298 K $k_{\text{B}}T$ is 207 cm^{-1}) solvent independent. The existence of those two barrier components implies that a conformational change in the excited molecule plays an important role in the ionization process. Furthermore, it is possible to untangle the reaction coordinate into two components: a solvent configuration coordinate connected to the entropy term and an ET coordinate. The following mechanism for photoionisation was proposed. First, after excitation a favourable solvent configuration has to be achieved to enable a large amplitude motion, in other words, the solvent has to reorganize into a precursor state (Fig. 2.5, transition 2 \rightarrow 3). Such changes in the solvent configurational entropy are prerequisite for stabilisation of an ionic transition state (Fig. 2.5, product 4). The solvent entropy control of the ET reaction is called solvent gating and is the rate-limiting step for a successful ET. Once a suitable solvent configuration is achieved, a vibrational motion of the carbon framework leads to distortion of the structure that proceeds without an intrinsic barrier but with a barrier connected to solvent friction effects. The structural distortion (large amplitude motion) is a change in the bond angle at the central carbon atom from 109 to 120° (Fig. 2.5, process 3 \rightarrow 4). The rotational motion coupled with major charge displacement – formation of a cationic site on dimethylaniline and an anionic site located on the cyanide group – enables the ET reaction (Fig. 2.5, process 4 \rightarrow 5). The intrinsic charge transfer step is described by the authors as nonadiabatic and barrierless occurring along a one-dimensional coordinate for a large amplitude motion. The nonadiabaticity of the ET process is postulated since

the C–CN bond breaking leads to formation of an ion pair, and thus to charge displacement outside this bond. Furthermore, the overlap between the C–CN bond and the CN^- orbital is small until a considerable delocalization of the positive charge on the dimethylaniline subunits occurs. The nonadiabatic ET process is efficient and fast due to reasonable coupling between states involved in the reaction. The next step is the ionic dissociation of the ET products in their electronic ground states leading to creation of a contact ion pair MG^+CN^- . Solvent stabilization and reorganization follows and solvent separated ion pair is formed as the final product. The formation of ion pairs can be summed up in the reaction Fig. 2.5.

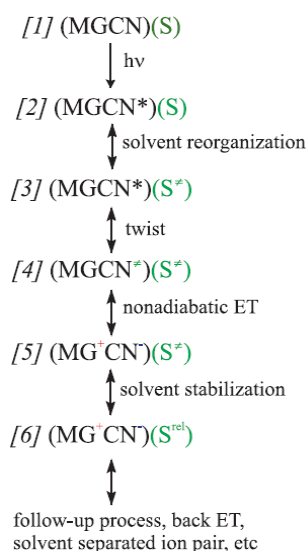


Fig. 2.5 Mechanism of photoionisation of MGCN. S stands for solvent molecules, * denotes the excited state, \ddagger the transition state, rel stands for relaxed solvent molecules.

The dissociative intramolecular electron transfer process is common for all TAM leucoderivatives, its rate depending, inter alia, on the electron affinity of the leaving group.⁶⁶ Light-induced dissociation of leucocarbinols made them a useful tool in studying the effect of sudden (on the nanosecond time scale) alkaline pH jump on biological process such as folding/unfolding of proteins.^{67, 68}

2.4 Lactonic forms of triarylmethane dyes

2.4.1 Colour forming reaction

Another class of leucoderivatives of triarylmethane dyes are triarylmethane lactones (LTAM). Compared with extensive body of research on photophysics and photochemistry of TAM⁺ and TAM leuconitriles it is surprising that the spectroscopy of lactonic forms of TAM have been until recently scarcely reported in the literature despite multiple applications of these molecular systems as colour formers or dye precursors. When in contact with a proton donor, colourless lactones undergo a ring-opening reaction with formation of a coloured cation with extended π -conjugated system (Fig. 2.6). This reaction is widely employed in carbonless copy papers, where LTAM serving as dye precursor is microencapsulated and then coated onto the rear of the original copy page.⁶⁹ Applying pressure destroys the capsules and the content is spilled onto the top of the copy page, which is coated with an acidic colour developer.^{70,71} In direct thermal imaging the lactonic dye precursor and developer are evenly distributed in a polymeric matrix. Upon heat application the two reactants fuse and display colour.⁷²

Crystal Violet Lactone (CVL, a lactonic derivative of CV) was the first molecule to be used as a colour precursor and is still attractive for colour forming industry.⁷⁰ A more exotic application of CVL is the use as thermochromic substance in chameleon-type building coatings. The underlying idea is to develop a building coating with a colour that can be changed reversibly between cool tones (summer) and warm (winter) tones by ambient temperature in the different seasons.⁷³

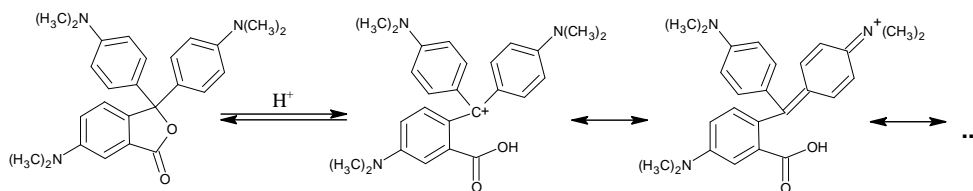


Fig. 2.6 Colour forming reaction of lactonic TAM exemplified by CVL; colourless lactone, dark blue cation of CVL.

The first reports on photophysics of CVL were focused on the coloured form of CVL (Fig. 2.6).^{74,75} Kaneko and Neckers⁷⁵ explored the mechanism of the colour forming reaction of CVL in the absence and in the presence of an iodonium salt which served as colour developer. Allen *et al.*⁷⁴

investigated the light-induced fading process of the open-ring form of CVL (cationic form, Fig. 2.6) and found it to be an oxidative process involving peroxides.

A more detailed picture of the spectroscopy of CVL has been gained in the recent decade, after Karpiuk has published a series of papers on photophysics of the three representative LTAM molecules: malachite green lactone (MGL),⁷⁶ crystal violet lactone (CVL)⁸² and phenolphthalein (PP).¹³ The outcome of these studies provided an inspiration to study further the interesting spectroscopy of triarylmethane lactones and to gain more insight into the complex photophysical behaviour displayed by these molecules.

2.4.2 LTAM as multichromophoric D–A systems

Triarylmethane lactones (LTAM) are multichromophoric donor–acceptor systems (D–A), where the two moieties are linked via a tetrahedral (sp^3) carbon atom. In CVL and other lactonic derivatives the two DMA donor moieties make dihedral angles of 119° and 93° with flat 6–DMAPd and 69° with each other.⁸² Crystal structure studies point out that all C–C bonds of the central carbon atom are of the same length (1.514–1.518 Å). These observations hold for other triarylmethane lactones⁷⁷ and indicate that there is no delocalization of π –electrons of the aromatic donor substituents on the central carbon atom and by implication on phthalide, proving that tetrahedral arrangement of structural subunits effectively weakens their interactions in the ground state. Accordingly, absorption transitions are localized on structural subunits and the absorption spectrum can be considered as a superposition of two D and one A moieties. No additional CT absorption transitions could be identified in all LTAM studied. In other leuco derivatives, like leuconitriles or carbinols, where three aromatic subunits and the nitrile or hydroxyl group are linked via sp^3 carbon atom, the electronic structure can also be regarded as a sum of four almost non-interacting moieties and therefore the absorption spectrum is virtually a superposition of transitions localized on these subunits.

The tetrahedral arrangement of subunits reduces ground state interactions between the moieties, but on the other hand enables strong electronic coupling in the excited state. In MGL and PP, an ultrafast electron transfer follows photoexcitation with formation of a CT state with intramolecular radical ion pair structure.



2.4.3 Ultrafast electron transfer in MGL and PP

MGL and PP (Fig. 2.7) are triad structures, each with two identical donors and phthalide as an electron acceptor (D–A–D type structure). CVL differs from MGL by addition of an electron donating group (dimethylamino group) in the acceptor moiety (D–D–DA).

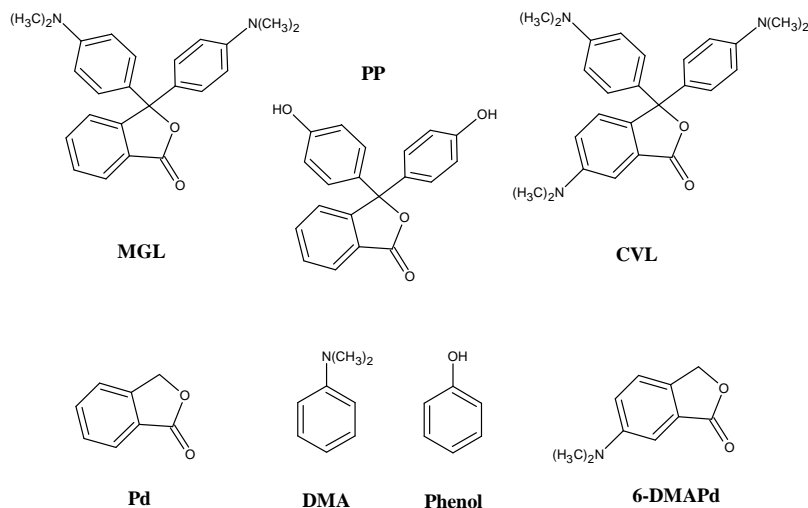


Fig. 2.7 Malachite green lactone (MGL), phenolphthalein (PP), crystal violet lactone (CVL) and their structural subunits: phthalide (Pd), 6-dimethylaminophthalide (6-DMAPd), dimethylaniline (DMA) and phenol.

As mentioned above, the absorption spectrum of MGL can be regarded as a superposition of transitions localized on two DMA subunits and Pd subunits (in the low energy region, 30000 – 36000 cm^{-1}). A detailed examination of absorption in the low energy region reveals a tail⁷⁸ with molar absorption coefficient estimated to be less than 50 $\text{M}^{-1}\text{cm}^{-1}$ at 27800 cm^{-1} .¹³ Bizjak *et al.*¹³ ascribed this “shoulder” to impurity traces since it has not been reproduced in the fluorescence excitation spectra.

The first and the second absorption bands in MGL with maxima at ca. 32200 cm^{-1} and 36900 cm^{-1} (in ACN) are similar to the first two absorption bands of DMA and additionally to the first two transitions observed in MGCN and MGH (Fig. 2.2), and were ascribed to local transitions within DMA subunits. Absorption of Pd starts at 35000 cm^{-1} and is quite weak (absorption coefficient at 35700 cm^{-1} equals 1700 $\text{M}^{-1}\text{cm}^{-1}$) thus its contribution to the second absorption band is not significant. The lowest excited singlet state S_1 (n,π^*) of Pd deactivates via efficient, ultrafast

intersystem crossing, yielding Pd non-fluorescent both at room temperature and at 77 K, thus only phosphorescence was observed.⁷⁹

The lowest singlet state of MGL populated upon excitation is the $S_1(\pi,\pi^*)$ state of DMA (in analogy to MGCN). Despite electronic decoupling of structural subunits in MGL, no local fluorescence from DMA was detected. The excited molecule emits broad fluorescence that is characterised by a large Stokes shift and a very strong solvatochromic effect, from a highly polar CT state ($\mu_e = 25.0$ D). Structurally related MGCN and other leuco dyes also exhibit additivity of absorption transitions, proving that the tetrahedral carbon atom allows for efficient decoupling of chromophores, however, only local fluorescence from the primary excited DMA is observed. The absence of DMA emission in MGL suggests a rapid and efficient deactivation channel of the primarily excited S_1 state, which was identified as electron transfer process from DMA to the phthalide moiety (Fig. 2.8). This assignment was based on solvatochromic plots and steady state spectroscopy experiments combined with comparison with structurally related compounds (MGCN and DMA). The electron transfer rate was identified with the rate of deactivation of the primary excited state located on DMA subunit estimated in the manner described below. The upper limit for quantum yield of a possible local fluorescence (DMA) in MGL in acetonitrile was calculated as follows: the spectrum (in fact a background signal due to dark current in the photomultiplier) was integrated in the region where fluorescence of DMA was expected, and compared with the integral intensity of the CT emission (in 430 – 800 nm region). Since the ratio of integrals is 2×10^3 , and the quantum yield of the CT fluorescence equals 0.0018, the yield of a possible local MGL fluorescence was determined to be not greater than 3.6×10^{-6} . Taking into account the quantum yield of insulated DMA molecules ($\Phi_{DMA} = 0.11$ in acetonitrile), the reduction factor is greater than 3×10^4 , which indicates a very efficient ultrafast relaxation process of the initially excited DMA chromophore in MGL resulting in population of the emitting state. The rate constant of this deactivation, k_q , was estimated assuming that the deactivation process follows first order kinetics and neglecting vibrational relaxation. Thus k_q was evaluated by comparison of the fluorescence quantum yield of the insulated DMA (Φ_{DMA}) with the quantum yield of fluorescence from the primary excited DMA subunit in MGL (Φ_{loc}) via the following formula:

$$k_q = (\Phi_{DMA} / \Phi_{loc})(1 / \tau_{DMA}) \quad \text{Eq. 2.6}$$

where τ_{DMA} equals 3.8 ns and is the fluorescence lifetime of the insulated

DMA chromophore in acetonitrile. Subsequently, the rate constant of electronic deactivation process in MGL equals $7.8 \times 10^{12} \text{ s}^{-1}$ and points to an ultrafast process that was identified as intramolecular ET taking place within 130 fs.

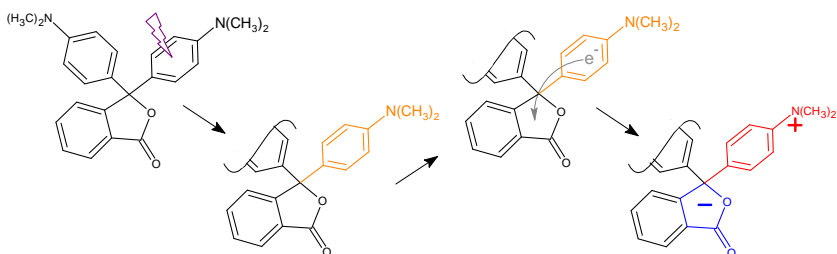


Fig. 2.8 A scheme of excited state processes taking place in MGL. After excitation of the DMA subunit, an electron is transferred from the DMA moiety to phthalide with formation of an intramolecular radical ion pair: radical cation of DMA and radical anion of Pd.

Nanosecond transient absorption (TA) spectra additionally support the radical ion pair structure of the excited state formed after the ultrafast ET in MGL due to direct observation of the radical cation of dimethylaniline (a TA band with a maximum at 470 nm). The room temperature triplet–triplet transient absorption spectra also reveal the presence of radical cation of DMA, strongly suggesting that the charge separation attained in the singlet state is still maintained in the triplet state.

Furthermore, measurements performed at low temperatures also suggest CT character of the lowest triplet state in MGL. The fluorescence consists of one structureless band with a maximum at 21750 cm^{-1} , emitted from the CT state, and contributions from local chromophores were ruled out due to the fact that phthalide is non-fluorescent and fluorescence of DMA is located at higher energies (maximum at 30200 cm^{-1} in methyltetrahydrofuran at 77 K). The phosphorescence of MGL is slightly red-shifted relative to the fluorescence (maximum at 21250 cm^{-1}) and consists of one broad band. Spectral position and shape of the band exclude assignments of the observed phosphorescence to the triplet states localized on either structural subunit (DMA: 23700 cm^{-1} , Pd: 26000 cm^{-1} , both structured bands) and point to charge transfer character of the emitting triplet in butyronitrile. Upon cooling MGL in liquid BTN a gradual decrease of intensity is accompanied by significant red shift of the fluorescence band (from 17300 cm^{-1} at 295 K to 16400 cm^{-1} at 193 K). The red shift is due to increasing polarity of BTN with decreasing temperature. Upon further

cooling the fluorescence spectrum exhibits a very large blue thermochromic shift from 16400 cm^{-1} at 163 K to 21800 cm^{-1} at 93 K . For this effect the elongation of the solvent relaxation time in respect to the ns excited state lifetime of MGL is responsible. The emission no longer originates from a fully relaxed CT state.

Phenolphthalein (PP), a triarylmethane lactone with the same triad structure as MGL (D–D–A) has two phenol subunits as donor moieties and phthalide as an electron acceptor. Due to orthogonality of these moieties the additivity of absorption transitions in the low energy region is maintained, no CT band is identified. In PP, the lowest excited state populated upon excitation is localized on the A subunit. No traces of local emission were detected, which points to ultrafast and efficient conversion of the primary excited Franck–Condon state to the CT state, in full analogy to MGL. Electron transfer takes place within 50 fs and the CT state with excited state dipole moment of 21 D is formed. The emission is ascribed to come from the highly polar state based on its characteristic features: large Stokes shift, significant solvatochromic effect (4500 cm^{-1} between ACN and dibutyl ether) and large halfwidth of the fluorescence band (6400 cm^{-1} in ACN).⁸⁰

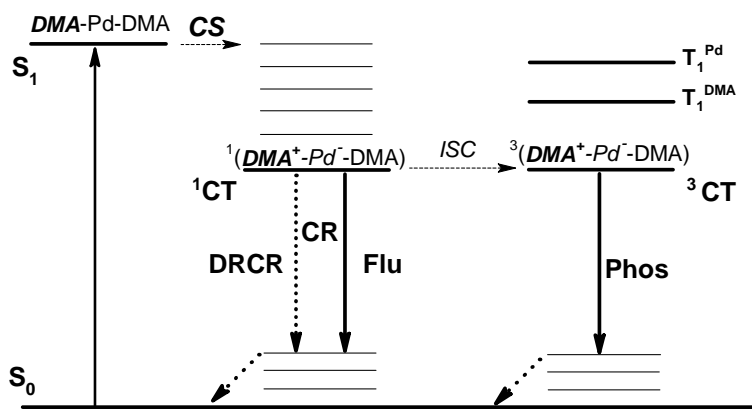


Fig. 2.9 Diagram of energy levels for MGL. Abbreviations: CS, charge separation; CR, charge recombination; DRCCR, direct radiationless charge recombination; ISC, intersystem crossing; Flu, fluorescence; Phos, phosphorescence.

Photoinduced electron transfer in PP and MGL (Fig. 2.9) was confirmed by observation of radical cations of the electron donor moiety (phenol and dimethylaniline, respectively) in femtosecond transient absorption measurements. Even in a nonpolar solvent such as hexane the signature of the charge separated state was detected. The kinetics of the ET

process were studied directly by recording the absorption built-up curves in the radical cation band of MGL and PP.

In PP in acetonitrile, the ET products appear within 50 fs, which is faster than inertial/diffusive solvation dynamics.⁸¹ For MGL, the radical cation of the D part is formed within 150 fs, but in this case the molecule was excited into the S_2 state, so the intrinsic ET step might be faster. The charge separation process is strongly exothermic and occurs in the nearly barrierless regime, as indicated by the free energy ΔG_{ET}^0 (PP/ACN: $\Delta G_{ET}^0 = -0.84$ eV, MGL/ACN: $\Delta G_{ET}^0 = -1.19$ eV). Detection of the DMA radical cation in MGL in nonpolar hexane (together with CT fluorescence) and phenol radical cation in PP demonstrates that polar solvation is not a prerequisite for efficient CS. Thus, the ultrafast ET process in MGL and PP is solvent independent and is promoted by vibronic coupling with the C–O bond in the lactone ring as a reaction coordinate.¹³ 50 fs–ET in PP is not only faster than inertial solvation component but occurs on the time scale of a single low frequency vibration corresponding to 670 cm^{-1} .

2.4.4 Coexistence of two emitting CT excited states in CVL

Crystal violet lactone (CVL) differs from MGL by the presence of an additional dimethylamino group at position 6 of the phthalide moiety (Fig. 2.7).⁸² This minor structural change results in huge differences in the photophysics. CVL displays solvent polarity dependent dual fluorescence ascribed to come from two polar excited states: (i) an optically populated, moderately polar state denoted as CT_A ($\mu_e = 10.7$ D), and (ii) a highly polar excited state CT_B ($\mu_e = 25.2$ D) populated upon electron transfer (ET) from one of the dimethylaniline (DMA) groups to the dimethylaminophthalide (6–DMAPd) moiety, respectively.

The additivity of absorption transitions holds also for CVL. The first absorption band is almost identical with that of 6–DMAPd with regard to spectral shape and position, considerable solvatochromic shift and molecular absorption coefficient. The first absorption transition is a (π, π^*) transition involving significant charge displacement resulting in formation of a polar excited state (CT_A) directly in the absorption transition. The second and third absorption bands involve mainly transitions localized on the DMA subunits.

In nonpolar solvents CVL emits one short-wave fluorescence band (A), which is almost identical with the fluorescence from isolated 6–DMAPd. Above a specific solvent polarity threshold (ϵ between 7.6 and

8.9) a second, long-wave fluorescence band (B) appears. A comparison of its spectral features with those of MGL led Karpiuk⁸² to the conclusion that these two bands come from excited states with very similar electronic structures: a charge transfer state with electron transferred from DMA to 6-DMAPd. The radical ion pair structure of the CT_B state manifests itself in transient absorption where the signature of the radical cation of DMA is observed (TA band with a maximum at 475 nm). Since the fluorescence spectra of MGL and CVL in polar solvents are virtually identical the conclusion can be drawn that the presence of the dimethylamino group in the 6 position in phthalide does not contribute to the electronic structure of the CT_B state. In solvents of low polarity, the CT_B state lies above the primary excited state CT_A and is not accessible from the latter. Polar solvents solvate the excited state and lower its energy, first leading to a gradual approach and subsequently to inversion of the CT_A and CT_B states. The time, in which the equilibrium between the two excited states is established, is solvent dependent and corresponds to solvation times, indicating solvent's dynamics control over the ET reaction (Fig. 2.10).

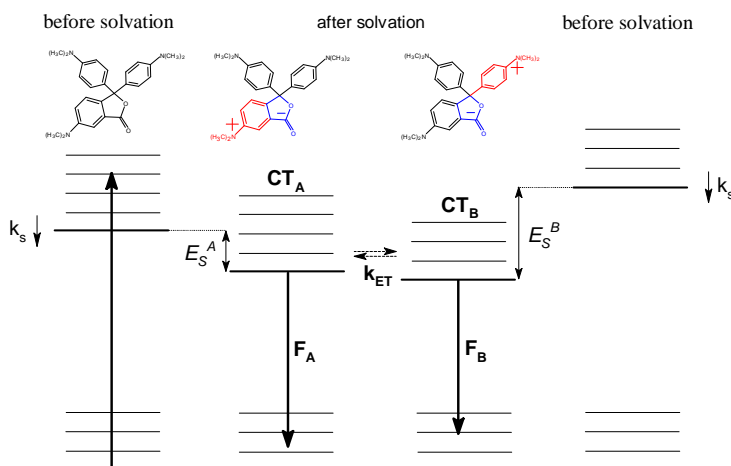


Fig. 2.10 Energy level diagram for CVL before and after solvation. Abbreviations: k_s , solvation rate constant; E_S^A and E_S^B , solvation energies of CT_A and CT_B , respectively; F_A and F_B , fluorescence from CT_A and CT_B ; k_{ET} , rate constant of intramolecular electron transfer.

The triplet state populated in CVL in polar solvents is also of CT nature. Triplet–triplet transient absorption spectra match those of singlet–singlet, strongly suggesting identical electronic structure of the CT_B singlet state and the triplet state populated in ACN. In CVL in low polar solvents,

however, triplet state localized on 6-DMAPd is populated (${}^3T_{6\text{-DMAPd}}$), similarly as in the case of singlet states (CT_A).

Unlike at room temperature, at 77 K the CT states are not populated. The lowest lying singlet and triplet states are those localised on the electron acceptor. At 77 K, fluorescence of CVL in BTN resembles closely in shape and position that of 6-DMAPd, with the maximum at 24000 cm^{-1} . The long lived (phosphorescence) emission of CVL is again almost identical with that of 6-DMAPd (19100 cm^{-1}).

2.4.5 Charge separation dynamics in CVL

Kinetics of population of the two excited states in CVL was resolved by means of femtosecond transient absorption (TA) measurements.⁸³ In nonpolar solvents with $\epsilon < 7.6$ the recorded TA spectra do agree with the spectra of 6-DMAPd, confirming that the CT_B is not accessible and only the local CT_A is populated. Measurements performed in polar solvents show the interplay between the two excited states: the spectrum changes from a double peaked one to a single peaked one with the formation of an isosbestic point, characteristic of a two-state process. The recorded multiexponential kinetics with fitted time constants do not closely match with measured solvation times, but correlate with the dielectric response, solvation energy and viscosity of the solvent.

The scenario is as follows: after excitation to the CT_A state, the solvent molecules start to rearrange themselves around the emerging dipole (as long as the molecule is in the ground state, the CT_B state lies above the local CT_A state, even in highly polar solvents). Since the CT_A and CT_B states share the similar location of the negative charge, during solvation of CT_A the more polar CT_B is even more stabilized. When the two states are equal in energy, adiabatic electron transfer becomes possible due to thermal fluctuations of the surrounding solvent molecules. At this moment the rates of the forward and backward reaction are equivalent. As a result of further solvation the dynamic equilibrium is more and more shifted in favour of the CT_B state. On the nanosecond timescale the two states are in thermodynamic equilibrium (Fig. 2.10). The femtosecond kinetic study on CVL excited state dynamics⁸³ concluded that the rate of electron transfer is time dependent in the sense that the barrier for the ET process changes its height in the course of solvation. The authors constructed a model of the ET during solvation; its foundations are outlined below.⁸³

The Onsager solution for the dipolar reaction field⁸⁴ neglecting the

solute polarizability was applied to obtain the value of solvation energies E_S^x for each excited state. The difference of solvation energies of CT_A and CT_B ($\Delta E_S = E_S^B - E_S^A$) minus the initial energy gap between them (ΔE_0) corresponds to the energy gap after solvation (ΔE_{B-A}) and at the same time stands for the Gibbs free energy change ΔG_{ET}^0 from the Marcus theory of ET processes (Fig. 2.11). ΔE_{B-A} in vacuum was estimated to amount $\Delta E_0 = 1660 \text{ cm}^{-1}$ (Eq. 2.8).

$$\Delta E_S = E_S^B - E_S^A \quad \text{Eq. 2.7}$$

$$\Delta E_S - \Delta E_0 = \Delta E_{B-A} \quad \text{Eq. 2.8}$$

For DMSO, for example, where the difference of solvation energies of CT_A and CT_B is equal to 1960 cm^{-1} , the driving force of the ET transfer reaction is equal to 300 cm^{-1} . The excited state equilibrium of CVL in DMSO is shifted strongly in favour of the CT_B state, so that the ET reaction takes place in 80% of all CVL molecules.

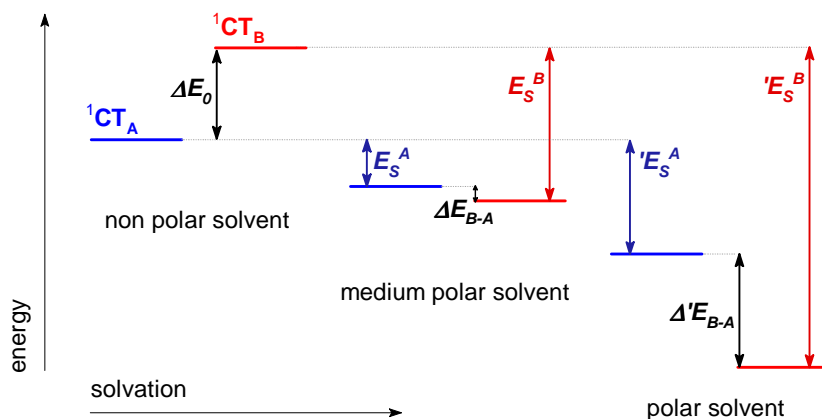


Fig. 2.11 Simplified scheme of solvation of CT_A and CT_B in CVL in solvents of different polarities. Symbols used are explained in the text below; prime (') denotes magnitudes connected with polar solvents.

While the solvation dynamics and associated reorientation of solvent molecules occurs in low ps time domain, the electronic polarization is essentially completed during optical transition. Thus, the energy gap ($\Delta G_{ET}^0(t=0)$) between the CT_B and CT_A states for the time zero is the energy difference in vacuum minus the electronic polarization contribution to solvation energy ($\Delta E_{S,el}$):

$$\Delta G_{ET}^0(t=0) = \Delta E_0 - \Delta E_{S,el} \quad \text{Eq. 2.9}$$

Accounting for the reorientational solvation in the expression for $\Delta G_{ET}^0(t=0)$ (Eq. 2.9) leads to time dependence of the Gibbs free energy change for the ET:

$$\Delta G_{ET}^0(t) = \Delta G_{ET}^0(t=0) - \Delta E_{S,or} [1 - \sum_i a_i \exp(-t/\tau_i)] \quad \text{Eq. 2.10}$$

where a_i and τ_i are the amplitudes and solvation time scales, respectively, taken from the literature.⁸⁵ This model demonstrates that the ratio of the initial energy gap ($\Delta E_{B-A} = \Delta G_{ET}^0$) and the solvation energy (ΔE_S) together with the time needed for solvation are crucial parameters for determining the population of the CT_B state.

Using the formula (Eq. 2.10), the authors⁸³ conducted simulations on the time dependence of the energy gap in CVL in polar solvents with different dielectric relaxation properties. In acetonitrile, where the solvation process is fast, the resonance between CT_A and CT_B and the consecutive ET process take place already after a few hundred femtoseconds, for DMSO and propylene carbonate the resonance occurs at a somewhat later time, at about 1.5 ps. The relation between stabilization capability ($\Delta E_{S,or}$) and the initial energy gap $\Delta G_{ET}^0(t=0)$ is the reason why the solvent-controlled ET does not show the same time constants as the pure solvation. The main body of the ET reaction is accomplished “on flight” during solvation, in the phase where the two states approach one another in terms of energy. This is consistent with the assumption that the intrinsic ET process in CVL is as fast as in MGL and PP, ergo faster than diffusive and inertial solvation. For ultrafast processes, high-frequency intramolecular vibrational degrees of freedom acting as ET promoting modes become dominant. In lactonic forms of triarylmethane dyes a source of vibronic coupling is provided by the C–O bond in the lactone ring.

The time dependence of the ET barrier translates into a time dependent ET rate. The reaction rate can be expressed in terms of Marcus theory using the value of $\Delta G_{ET}^0(t)$ derived from the expression (Eq. 2.11):

$$k_{ET}(t) = k_{ET}^{\max} \exp\left(\frac{-(\lambda \pm \Delta G_{ET}^0(t))^2}{4\lambda k_B T}\right) \quad \text{Eq. 2.11}$$

where λ is the reorganization energy, T – temperature, k_{ET}^{\max} is the preexponential factor defined by the electronic coupling, its value is determined when there is no barrier. Having the ET rate, the time dependence of the population of CT_A and CT_B can be determined by

$\Delta_{\text{ET}}H^{\ddagger} = 11 \pm 2$ kJ/mol). Moreover, the free energy changes, $\Delta_{\text{ET}}G$, associated with the excited state electron transfer reaction were determined and correlated with dielectric properties of the solvent yielding -10 kJ/mol in hexane and $+14$ kJ/mol in propylene carbonate and were equal to zero for solvents with dielectric constant between 5 and 6. The ET rates were found to be dependent on solvent friction and solvation times, however, the electronic structure calculations ruled out the contribution from large amplitude motions to this effect due to steric hindrance. Thus, Maroncelli and coworkers describe the $\text{CT}_A \rightarrow \text{CT}_B$ reaction as an adiabatic ET along a 1-D reaction coordinate involving primarily solvent polarization modes and having a modest barrier to reaction in contrast to Karpiuk and coworkers, who used a 2-D reaction coordinate including solvent degrees of freedom as well as vibronic coupling (Sumi–Marcus model).

2.4.6 CVL as a probe of solvation dynamics in ionic liquids

The Maroncelli group used also the intramolecular electron transfer reaction in CVL as a tool for studying solvation dynamics in ionic liquids,⁸⁷ the work being focused on possible dynamic heterogeneity of ionic liquids (ILs). The characteristic features of ILs are high densities and viscosities, but most important, long dielectric relaxation timescales extending from 100 ps to 100 ns.⁸⁸ Solutes dissolved in ILs display dispersive kinetics as a result of dynamic heterogeneity, i.e., subensembles of molecules are trapped in quasi-static local solvent cages, and experience structurally different microscopic surroundings. Long trapping time compared to the lifetime of the excited state and the incapability of the ions to adiabatically relax leads to site-specific spectroscopic responses. Multiple solvation environments are responsible for the “red-edge effect”, i.e., the dependence of emission wavelength on the excitation energy.⁸⁹

Maroncelli and coworkers⁸⁷ reported that in CVL in polar solvents the emission dynamics follows the reversible two-state ($\text{CT}_A \leftrightarrow \text{CT}_B$) interconversion model established by Karpiuk.⁸² The reaction times are on the order of 10–30 ps and the equilibrium constants are between 50 and 100 ps. The ET kinetics in CVL in ILs slows down significantly and becomes nonexponential, with reaction times following the viscosity of ILs. More importantly, a dramatic variation of the intensities of CT_A and CT_B fluorescences with excitation frequency was reported (ratio of integrals up to 2.5). This variation was interpreted as an example of dynamic heterogeneity in IL.

Annapureddy and Margulis⁹⁰ provided theoretical support for Maroncelli's⁸⁷ conclusions concerning the dynamic heterogeneity of ILs. Calculations performed on CVL in ILs reproduced the excitation wavelength dependence of fluorescence emitted from both excited states (CT_A and CT_B). By changing the energy of the incident radiation, subensembles of CVL molecules, which experience different polarities, are selectively excited. An increase in energy of absorbed light results in increasing solvent contribution to the energy barrier for electron transfer. The authors conclude, that both kinetics as well as thermodynamics of the ET process in CVL are dependent on local solvent–environment.

This picture changed, however, in 2010, when Maroncelli and co-workers published a notice,⁹¹ where they commented on the experimental material published earlier. It turned out that the steady–state spectra with large variation of the intensity ratio of the two CVL fluorescence bands with changing excitation wavelength were spurious, and most probably were due to contributions from impurities. As a result, no experimental evidence to support the conclusion on the dynamic heterogeneity was available from CVL studies in ILs and the conclusion was withdrawn.

The influence of polarity, viscosity and proticity of ILs on the fluorescence of CVL was further studied by Santhosh and Samanta.⁹² They observed that the higher the viscosity of the IL, the slower the interconversion process $CT_A \rightarrow CT_B$. In highly viscous ILs the interconversion is retarded or even hindered due to slow solvent reorganization dynamics. Based on the rise time of the CT_B band (1 ns) that is comparable with the solvation time of IL (1-butyl–2,3 dimethylimidazolium bis(trifluoromethanesulfonyl)imide; 690 ps), Santosh and Samantha suggested that the ET reaction in IL is controlled by solvation dynamics, as is the case in dipolar solvents. When dissolved in an IL with hydrogen bond donating ability, CVL emits a single fluorescence band coming from the CT_A state with a red tail (arising from the CT_B state), as in conventional protic solvents (alcohols). Karpiuk⁸² proposed that CVL in alcohols deactivates via two channels. The first path originates from the CT_A state from which the molecule can relax adiabatically by forming a hydrogen bond with the solvent (leading to a fluorescent state). The second deactivation channel is diabatic consisting of ultrafast C–O bond dissociation in the CT_B state, which in polar alcohols becomes sufficiently stabilized to be populated (Fig. 2.13). Subsequently, the lactone ring closes within tens of ns. In ILs, the first channel via hydrogen bond formation seems to be more efficient due to slow solvent dielectric relaxation times.

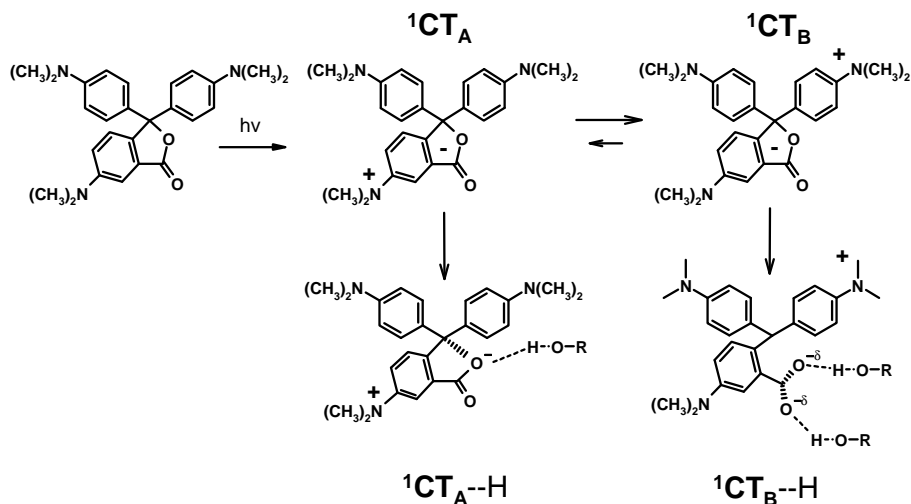


Fig. 2.13 Photophysics of CVL in protic solvents: formation and structure of proposed intermediates.⁸²

The relationship between the ET reaction and solvation times in IL was studied by the Maroncelli group,⁹³ who used CVL as probe for solvation dynamics. An approximate equality between the reaction ($CT_A \rightarrow CT_B$) time and the solvation time was observed, in accordance with the results obtained by Santosh and Samanta,⁹² leading to conclusion on solvent-controlled ET in CVL both in fast relaxing polar aprotic solvents and slowly relaxing ILs.

2.5 Structure – properties relationship in triarylmethane derivatives – a summary

All substances described in this introductory Chapter share common molecular skeleton consisting of three aromatic subunits connected to a methane-like central carbon atom: two dimethylanilines and benzene ring for malachite green derivatives and three dimethylaniline subunits in the case of crystal violet derivatives. Minor structural modifications at the central carbon strongly affect the excited state processes in respective subclasses of triarylmethane derivatives.

In TAM⁺ dyes, the positive charge is delocalized over the entire molecule leading to planarization of its structure around the central sp² carbon atom with the aryl rings arranged in a propeller-like fashion. In

colourless derivatives, leuconitriles and lactones, typical tetrahedral structure around the central carbon atom is preserved (with angles between the central sp^3 C atom and the C atoms attached to it around 109°) (Fig. 2.14).

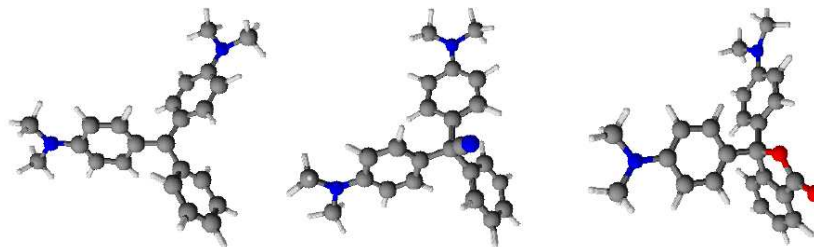


Fig. 2.14 3-D optimized structures of MG^+ , MGCN and MGL (from left to right).

In TAM^+ dyes the central carbon atom does allow for extensive conjugation of subunits, in leuconitriles, however, it serves as a separator for the moieties. In lactonic forms of TAM the tetrahedral carbon plays two roles, it functions as a link/spacer, but also provides an effective channel for electronic communication. In colourless derivatives, due to lack of electronic coupling in the ground state, the absorption spectra are virtually a superposition of absorption transitions localized on subunits.

The dominating excited state process in TAM^+ dyes is enhanced nonradiative deactivation due to simultaneous rotation of aryl substituents. In colourless derivatives, composed of electron donor and electron acceptor subunits, the electron transfer reaction controls the kinetics of excited state processes. In leuconitriles, the excited state reached in absorption deactivates nonradiatively via dissociative electron transfer. Almost barrierless ET from DMA to vibrational modes of the C–CN bond leads to formation of a carbonium ion (TAM^+) and CN^- anion. A large amplitude motion is a prerequisite for the ET reaction to take place. The charge separation is enhanced in polar solvents due to solvation of ionic products of the reaction. However, in lactonic forms of TAM, no evidence has been found for photodissociation of the central carbon–oxygen bond in aprotic solvents. In MGL and PP the initially excited local state of DMA undergoes ultrafast and effective charge separation. The dynamics of the adiabatic primary ET process are determined mainly by high-frequency intramolecular vibrational motions and not by solvation, although the emitting CS state is strongly stabilized by interaction with polar environment. CVL differs from MGL by addition of an electron donating group in the phthalide subunit making CVL a molecule of a (D–D–DA) structure. The state populated in absorption is localized on the DA subunit and has CT character. In low polar solvents

fluorescence is also displayed from this state. Above certain polarity threshold a second fluorescence band appears and is emitted from a highly polar CT state having the same radical ion pair structure as MGL. The excited state energetics, the availability of the states and their population kinetics depend not only on solvation dynamics but also on the extent of stabilization that is achieved on a certain time scale. In ILs the equilibrium between the two emitting states of CVL is established on a longer timescale due to slow solvent reorganization dynamics. The C–O bond present in all lactonic forms of TAM acts as a source of strong vibronic coupling. Basically, the intrinsic ET processes in MGL, PP and CVL have the same reaction coordinate identified as the C–O vibrational mode. The difference between CVL and MGL is that in the latter molecule polar solvation is not a precondition to reach the CT state.

Although all subclasses of TAM derivatives have common structure, minor structural modifications have strong effect on excited state processes (ET, rotation, dissociation) and energetics, and determine their dependence on several solvent properties, including polarity (MGCN), viscosity (TAM⁺), solvation dynamics (CVL), or the extent of population transfer between available excited states (MGL).

2.6 Dual fluorescence and intramolecular electron transfer

Dual fluorescence emitted from organic molecules in solution has been an area of vivid interest and extensive research, since Weller's⁹⁴ discovery of the first case of intramolecular excited state proton transfer and dual emission from two tautomers of methyl salicylate over a half a century ago. In the meantime, the phenomenon found many applications, especially because of the dependence of band shapes and their relative intensities on solvent parameters (e.g., polarity, proticity, viscosity, relaxation times), the presence of various chemical individuals in solution (e.g., ions) or conformational changes in molecular species (e.g., proteins) attached to a fluorescence probe, etc. Although dual fluorescence was first observed more than a half a century ago,⁹⁵ it still attracts much attention. The long-lasting efforts to understand the nature of dual fluorescence in various systems have provided a lot of information and, simultaneously, have demonstrated the complexity of mechanisms at its origin.

Dual fluorescence results from absorption of light and subsequent intra- and intermolecular processes. The mechanisms underlying this

phenomenon can be divided into the following groups:⁹⁶ (i) excited state proton transfer or protonation/deprotonation – tautomerization processes, (ii) excited state isomerisation, (iii) intra- and intermolecular electron transfer, (iv) excited state conformational changes,⁹⁷ (v) excited state bond dissociation, (vi) emission from lowest and higher excited states,^{98,99,100} (vii) intramolecular/intermolecular excimer/exciple formation,^{101,102,103} (viii) independent excitation of different ground state conformers,^{104,105} (ix) energy transfer processes,¹⁰⁶ (x) other mechanisms.

From the view point of this thesis, the most interesting source of dual fluorescence is an electron transfer reaction in the excited state. In contrast to most mechanisms mentioned above, the ET process can lead to formation of different excited states of the same chemical species and is the basic process behind many mechanisms of dual fluorescence. The excited state reached upon absorption, denoted as the locally excited (LE) state, undergoes electron transfer leading to population of a polar charge transfer state (CT) according to precursor–successor scheme. Before, during and after the electron transfer, conformational changes may take place, leading to further transformation of the molecule, i.e., twisting, planarization, bond dissociation. The literature describes a few classes of molecular D–A systems displaying dual fluorescence due to different intramolecular processes.

The most famous (and studied) molecule that displays dual luminescence from two excited states (LE and CT) is *p*-dimethylaminobenzonitrile (DMABN),¹⁰⁷ where the intramolecular ET reaction is accompanied by excited state structural relaxation. Grabowski *et al.*¹⁰⁸ interpreted this dual fluorescence within the TICT (Twisted Intramolecular Charge Transfer) model and ascribed the long-wave charge transfer emission to come from a state with twisted dimethylamino group in respect to the planar benzonitrile moiety, the rotation facilitated by the dielectric polarization of the solvent (Fig. 2.15). A different interpretation was proposed by Zachariasse^{109,110} with the concept of the PICT (Planar Intramolecular Charge Transfer) model, according to which the CT state is populated as a result of planarization of the dimethylamino group (Fig. 2.15). The distortion of the molecule in the locally excited state lowers its symmetry and permits the electronic coupling between the local (S_1) and the closely-lying CT state (S_2) (pseudo-Jahn–Teller effect).¹¹¹ Until now, the two models are still under debate, and the mechanism of dual fluorescence in DMABN and its derivatives is not fully explained.

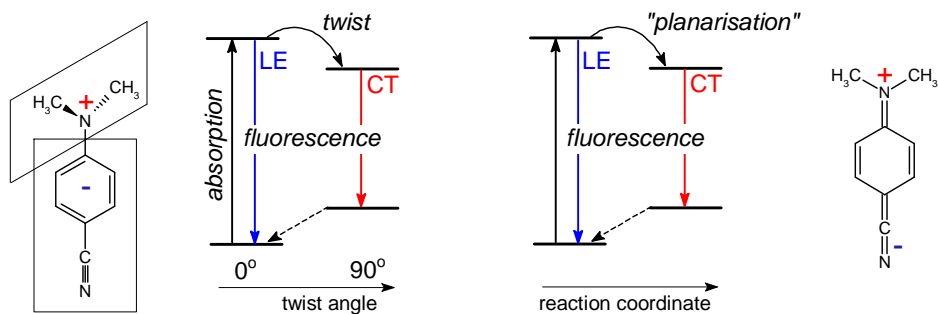


Fig. 2.15 Schematic presentation of the Twisted Intramolecular CT (TICT) model and Planar Intramolecular CT (PICT) model on the example of DMABN.

Another group of well studied compounds are biaryls, especially derivatives of 9,9'-bianthryl (BA).¹¹² The interest in these molecules is mainly due to the fact that BA undergoes symmetry breaking upon excitation. As a result, the molecule displays single "local" fluorescence in nonpolar solvents, whereas in polar solvents, CT fluorescence can be observed. The ET process in the excited state takes place on the timescale of 20–50 ps depending on the viscosity of the medium, pointing to the role of large amplitude motions in formation of the CT state.¹¹³

An exciplex (according to IUPAC Gold Book), is an excited state complex of definite stoichiometry, which is non-bonding in the ground state, and can be formed for example by ET reaction.¹¹⁴ The formation of an exciplex results in fluorescence quenching of the primary excited chromophore and in the appearance of structureless emission of lower energy. In contrast to intermolecular exciplexes,^{115,116} intramolecular exciplexes, where the D and A moieties are linked,^{117,118,119,120} were less frequently investigated. After excitation of a subchromophore, ET takes place and the intramolecular exciplex is formed independent of solvent polarity. Hence, dual fluorescence is observed originating from a local chromophore and the formed exciplex. The emission of the latter due to its CT character is broad and structureless with fluorescence maxima strongly shifted towards longer wavelengths. The relative intensities of both fluorescence bands depend strongly on solvent polarity, with increasing dielectric constant of the medium the share of the exciplex emission grows.

In spirocyclic D–A systems represented by lactonic forms of rhodamines, analogues of triarylmethane lactones with oxygen bridge between the donor subunits, the electron transfer process from xanthene to

phthalide moiety induces bond dissociation in the lactone ring.^{121,122,123} After excitation, an electron is transferred, and the CT state of rhodamine lactone can be formed and simultaneously adiabatic photodissociation of the C–O bond in the lactone ring can take place with formation of an excited zwitterion (Fig. 2.16).

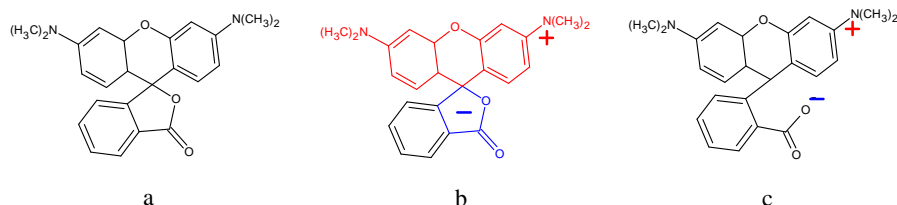


Fig. 2.16 Rhodamine B lactone (a), structure of the CT state (b) and zwitterion formed upon ring opening in the excited state.

The zwitterionic form is the source of long-wave emission, while the CT state emits short-wave fluorescence. In the case of rhodamine lactones, the two different species formed in the excited state process, deactivate radiatively.

In CVL (see Section 2.4.4), dual luminescence originates from the LE state of the 6–dimethylaminophthalide moiety (blue emission) and the CT state extends over the entire molecule (red emission). The uniqueness of this system lies in the nature of the LE state, which is populated in an optical electron transfer process. The LE state of 6–DMAPd (CT_A), corresponds essentially to a HOMO→LUMO transition involving a displacement of charge from the amino nitrogen lone pair to the benzene ring.^{124,125} Depending on solvent polarity, the second, highly polar CT state (CT_B) can be sufficiently stabilized and becomes accessible in solvents of dielectric constant higher than 7.6. The CT_B state populated upon electron transfer from one of the DMA groups to the lactone ring of the 6–DMAPd subunit has the structure of an intramolecular ion pair. Any meaningful changes in the conformation of the molecule when populating the CT_B state can be ruled out based on viscosity independence of the electron transfer process. CVL provides the first example of an equilibrium between two excited states, both with charge transfer properties. Due to the nature of both emissions, the displayed fluorescence bands are broad and characterized by large solvatochromic shifts, when considered separately, the full width at half maximum (FWHM) of the CT_A fluorescence ranges from 3000 – 4500 cm⁻¹, for the more polar CT_B state FWHM varies from 4100 – 5550 cm⁻¹. When combined, the FWHM of dual fluorescence can be larger than 7500 cm⁻¹ in

solvents of medium and high polarity, with the spectrum extending over 300 nm, from 390 to 690 nm. The contributions of the two fluorescences are also governed by the dielectric constant of the solvent: with increasing solvent polarity the CT_B contribution grows at the expense of the CT_A intensity. Such a broad fluorescence in the visible spectral range results in white or almost white perception of the combined emissions of CVL, with the blue band from a local chromophore and an orange CT band from the intramolecular exciplex formed adiabatically at appropriate medium polarity. White light emission from a single molecule is a highly regarded and rarely found phenomenon. Studies on CVL in this context match well current research trends concerning new white light sources (Organic Light Emitting Diodes).

2.7 Dual fluorescence in white light generation

For the last two decades many efforts and research have been devoted to the development of new energy-saving light sources. The (still) ubiquitous incandescent light bulb converts only less than 5% of the total input electrical energy into light, the fluorescent tube performs much better, but suffers from several drawbacks, e.g., poor colour-rendering index, unaesthetic shape, environmental problems with mercury disposal. Inorganic light emitting diodes (LED) are already an established part of the lighting market, and the first marketed lighting LED produced 15 years ago was based on gallium nitride crystals.¹²⁶ Popular white LEDs (used in flashlights, festive decoration), are made by embedding a blue gallium nitride emitter chip in a matrix containing yellow phosphor, based on a rare earth doped yttrium aluminium garnet.¹²⁷ The major disadvantage of the LEDs is their narrow (25–50°) beam-like emission, which makes them suitable for point-source illumination rather than surface-source illumination.

An alternative for inorganic LEDs may be OLEDs (Organic Light Emitting Diodes), where organic solid state material is used as emitter. Due to their structure and preparation methods, the OLEDs can display following features: any desired shape, big dimensions, flexibility and transparency. Such attributes make organic light emitting devices perfect candidates for applications as backlights for large-area flat-panel displays and solid state lighting. To date, white OLEDs have been produced using a combination of primary colour emitters by depositing multiple layers on top of each other, by mixing them into one a single emitting layer or by combining them into

polymeric matrixes. Another approach is to generate white light emission from a single organic emitting component. OLEDs based on a single component emitter are much cheaper in preparation due to lower consumption of materials and simplified processing methods. Various organic,¹²⁸ inorganic¹²⁹ and hybrid^{130,131} materials and coordination networks^{132,133} were found to be suitable white light emitters. The advancement achieved in this area, has not been paralleled by the development of white chromophores, i.e., small molecules capable of displaying broad fluorescence covering the whole visible range 430–700 nm.

The strategies implemented so far to obtain white emission from organic fluorophores have been to combine three (blue, green and red) or two complementary colours using: (i) different molecules emitting in different spectral regions,^{134,135,136} (ii) macromolecules consisting of multiple emissive chromophores,^{137,138,139,140} (iii) different ground state forms of one molecule coexisting in a ground state equilibrium and co-excited to their excited states to display different emissions,^{141,142,143} (iv) monomers and excited bimolecular species involving aggregates, excimers, exciplexes or electric field induced electroplexes or electromers.^{144,145,146,147} Another approach (v), yet much less successful to date, is to make use of spectrally broad dual fluorescence from two different emitting states of one molecule, e.g., one locally excited and one formed in an intramolecular adiabatic process. There have been, however, only a few such molecules reported to date. Almost white emission (Commission International d'Eclairage, CIE 1931 chromaticity coordinates: $x = 0.28$; $y = 0.30$) of a trinuclear iridium–europium–iridium supramolecular assembly reported by DeCola *et al.*¹⁰⁶ results from mixing of continuous blue phosphorescence from Ir^{3+} complex with discrete red emission of Eu^{3+} ion, sensitized by energy transfer from one of the Ir^{3+} moieties. Based on the same principle, Ward and co-workers¹⁴⁸ obtained white light from an $\text{Ir}^{3+}/\text{Eu}^{3+}$ dyad with CIE coordinates $x = 0.34$, $y = 0.32$. Frustrated energy transfer has been recently utilized by Park *et al.*¹⁴⁹ in a conceptually interesting white light emitting dyad (CIE coordinates: $x = 0.33$; $y = 0.37$) consisting of two noninteracting chromophores displaying fluorescence from tautomers populated in two separate excited state proton transfer processes. The colour and hue of the resulting emission is sensitive to excitation wavelength. He *et al.*¹⁵⁰ designed a fluorophore that exhibits tunable emission of the three primary colours and white light. Depending on the excitation wavelength, the molecule is able to emit either red light from an Eu^{3+} moiety, blue fluorescence from a coumarin chromophore acting as a ligand, or green emission from rhodamine 6G dye attached to the coumarine subunit, as well as white light (excitation 388 nm,

$x = 0.33$; $y = 0.33$). A different approach to white light generation was used by Bolink *et al.*,¹⁵¹ where degenerate emitting states of mixed character in an Ir^{3+} complex are at the origin of a spectrally broad phosphorescence perceived as white light (CIE coordinates: $x = 0.28$; $y = 0.36$). In this context, CVL seems to be a promising object for white light generation from small molecules. CVL provides the first example of spectrally continuous white fluorescence displayed in solution, comprising complementary emissions from two CT excited states (see Chapter 8).

2.8 Perception of colour and colour representation

The retina of the human eye contains three types of cone cells, corresponding roughly to red (maximum sensibility at 575 nm), green (535 nm), and blue (445 nm) sensitive detectors. Thus, any colour sensation can be described in terms of mixing the three primary colours:

$$C = bB + gG + rR \quad \text{Eq. 2.11}$$

where C is an arbitrary colour, B , G , R are unit values for blue, green and red, and b , g , r denote the relative intensities of the respective primary colours, and are called the tristimulus values. The tristimulus values are most often given in the Commission Internationale de l'Eclairage (CIE) 1931 colour space, in which they are denoted as X , Y , and Z . In the CIE colour space, the X , Y , Z primaries are not real colours, but convenient mathematical constructs related to the sensitivity of the human eye by use of colour matching functions (called $\bar{x}(\lambda)$, $\bar{y}(\lambda)$, $\bar{z}(\lambda)$),¹⁵² which match to the CIE 1931 standard observer (Fig. 2.17).¹⁵³ The tristimulus values for a colour with a spectral power distribution $I(\lambda)$, understood as the power of light at each wavelength, are given in terms of the standard observer by:

$$X = \int_0^\infty I(\lambda)\bar{x}(\lambda)d\lambda, \quad Y = \int_0^\infty I(\lambda)\bar{y}(\lambda)d\lambda, \quad Z = \int_0^\infty I(\lambda)\bar{z}(\lambda)d\lambda \quad \text{Eq. 2.12}$$

From the tristimulus values the chromaticity coordinates can be derived:

$$x = \frac{X}{X + Y + Z}, \quad y = \frac{Y}{X + Y + Z}, \quad z = \frac{Z}{X + Y + Z} \quad \text{Eq. 2.13}$$

where $x + y + z = 1$. Thus, the CIE 1931 system characterizes colours by two chromaticity coordinates x and y which specify the point in the chromaticity diagram (Fig. 2.17).

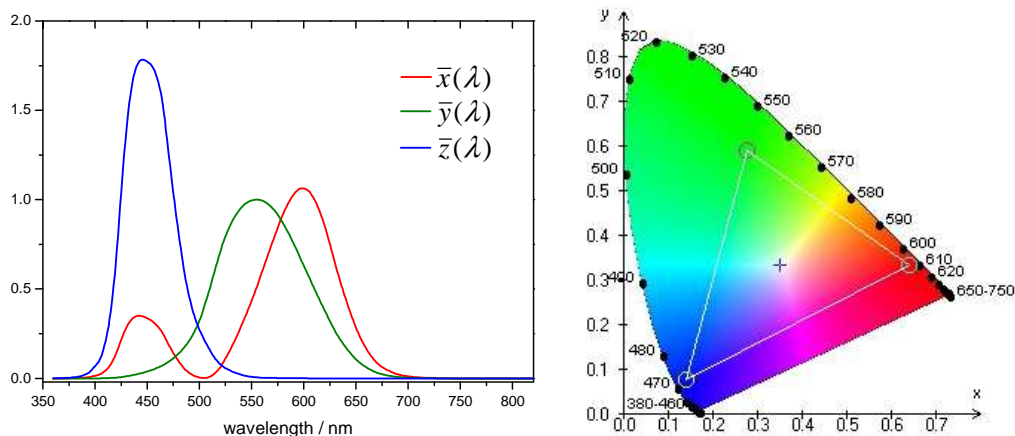


Fig. 2.17 Left: the CIE standard observer colour matching functions, taken from <http://www.cie.co.at>. Right: The CIE 1931 colour space chromaticity diagram.

The horseshoe-like or tongue-like CIE 1931 colour space represents all of the chromaticities visible to an average person, called the gamut of human vision.¹⁵⁴ The fully saturated spectral colours (composed of a single wavelength) are distributed on the boundary of the colour space, called the spectral locus. The "line of purples" at the bottom represents colours that cannot be produced by any single wavelength of light, but still are saturated. The point characterized by x and y values equal 0.33 represents the white chromaticity and corresponds to pure white. All complementary colours lie on two ends of a line passing through the equal energy point (e.g., green–purple, blue–yellow). For mixing of any two chromaticities, the resulting hues can be found on a straight line connecting the two initial points. For a combination of three colours, the resulting hues are found inside a triangle spanned on the initial points. The CIE 1931 chromaticity diagram is widely used for colour representation, it separates colour from colour appearance and offers an independent colour scale.

Chapter 3

Experimental methods and instrumentation

3.1 Materials used in the investigations

3.1.1 Triarylmethane lactones studied in this work

MGL was synthesized according to the classical procedure described by Fischer,¹⁵⁵ and subsequently repeatedly recrystallized from *l*-propanol. Commercially available PP (POCh) was purified according to standard methods.¹⁵⁶ CVL (Aldrich) was crystallized twice from acetone. CVLH2 and CVLB were synthesized according to the literature methods,^{157,158} as well as BPPd.¹⁵⁹ MGLS was synthesised and kindly provided by Ms. Oksana Pietraszkiewicz (Institute of Physical Chemistry, PAS). CVLH2 was repeatedly crystallized from *l*-propanol with active carbon and CVLB was recrystallized from ethyl acetate/hexane mixture. MGLA, BPPd and PhI were synthesised by the author of this thesis, while all remaining synthetic procedures described below were carried out by Dr. Jacek Nowacki from the Faculty of Chemistry, Warsaw University.

3-methyl-3-(4-dimethylaminophenyl)phthalide (MGLA)

To a solution of methyl magnesium iodide prepared from 2.31 g (0.095 mole) magnesium, 13.46 g (0.095 mole) methyl iodide and 50 ml ether, 10.20 g (0.038 mole) of finely powdered *o*-(4-dimethylaminobenzoyl)benzoic acid was added in small portions while the reaction mixture was stirred for one hour. The resulting mixture was subsequently heated under reflux for another hour, then cooled down and decomposed with 40 ml of cold 3 N hydrochloric acid. The aqueous layer was extracted with two 40 ml portions of ether. The combined ethereal solution was subsequently washed with 40 ml of 5% sodium bicarbonate solution, 40 ml of 1 N sodium thiosulfate solution, then with water, and finally dried over anhydrous magnesium sulfate. Evaporation of the solvent left 7.3 g of a brick-red oil. Flash chromatography of the latter on silica gel with dichloromethane as the eluent gave pink crystalline product which after repeated crystallization from *l*-propanol with decolorizing charcoal melted at 143.5–145°C. Yield 6.8 g (67%).

¹H NMR δ (ppm): 2.01 (s, 3H), 2.92 (s, 6H), 6.65 (d, 2H, J = 8.79 Hz), 7.24 (d, 2H, J = 8.79 Hz), 7.41 (d, 1H, J = 7.57 Hz), 7.48 (dd, 1H, J = 7.32 and 7.33 Hz), 7.64 (dd, 1H, J = 7.33 and 7.57 Hz), 7.88 (d, 1H, J = 7.32 Hz);

^{13}C NMR δ (ppm): 27.15 q, 40.54 q, 88.33 s, 112.25 (2C) d, 122.34 d, 125.59 s, 125.86 d, 126.61 (2C) d, 127.69 s, 129.03 d, 134.33 d, 150.55 s, 154.94 s, 170.42 s.

3-(4-dimethyloaminophenyl)phthalimidine (PhI)

5 g (0.0186 mol) *o*-(4-dimethylaminobenzoyl)benzoic acid were heated for 2 h at 200 °C with 3.3 g (0.037 mol) 2-amino-2-methylpropan-1-ol. After cooling down, the solidified reaction mixture was dissolved in methylene chloride. A small amount of white precipitate was removed, the remaining solution was concentrated and separated on a silica gel column using a gradient mixture of 1–3% methanol in methylene chloride. Four products were isolated, among them 3-(4-dimethyloaminophenyl)phthalimidine, 1.1 g (23.5%) yellowish crystals with melting point 234–236°C (lit. 235–236°C).¹⁶⁰

^1H NMR δ (ppm): 2.93 (6H, s); 5.53 (1H, s); 6.59 (1H, bs); 6.67 (2H, dm, $J=8.79$ Hz); 7.91 (2H, dm, $J=8.79$ Hz); 7.24 (1H, m); 7.38–7.54 (2H, m); 7.86 (1H, m).

^{13}C NMR δ (ppm): 40.46 q; 60.47 d; 110.69 s; 2×112.61 d; 123.34 d; 123.61 d; 125.28 s; 2×127.81 d; 128.07 d; 130.98 s; 132.13 d; 148.66 s; 150.64; 170.81 s.

Spiro-3-[3,6-bis(dimethylamino)fluorene]phthalide (MGLB)

Aluminium chloride (10 g, 0.072 mol), urea (1.5 g, 0.024 mol) and aluminium chloride hexahydrate (0.15 g, 0.62 mmol) were stirred and heated to 125° C. MGL (0.9 g, 2.42 mmol) was added and the mixture stirred at 135 – 140° C for 4 h. Heating was continued for another 18 hours by which time the reaction mixture had become a solid mass. The reaction was quenched by gradual addition of water (80 ml) to give a green suspension, which then was treated with hydrogen peroxide (30%, 0.25 ml) and stirred for 1.5 h. The suspension was extracted several times with dichloromethane; the combined extracts were washed and dried over magnesium sulfate. Removal of the drying agent and solvent furnished a dull green solid (0.34 g, 38.0% crude yield). Three recrystallizations (methylene chloride/hexane) under nitrogen atmosphere (drybox) gave MGLB as colourless crystals (0.085 g, m.p. 289° C; 312 – 313° C).

^1H NMR, δ (ppm): 3.04 (12H, s); 6.50 (2H, dd, $J_1=8.54$ Hz, $J_2=2.44$ Hz); 6.82 (2H, d, 2.54 Hz); 6.74 (1H, m); 7.00 (2H, d, $J=2.44$ Hz); 7.50 (2H, m); 7.97(1H, m).

^{13}C NMR, δ (ppm): 40.77; 92.75; 103.55; 111.80; 122.37; 124.78; 125.14; 128.93; 129.39; 130.80; 134.31; 142.44; 151.74; 152.21; 171.14.

Tetrahydroquinoline and julolidine derivatives were synthesized from respective benzoic acids. The synthesis of these acids is reported below, followed by the description of the reaction path leading to the final products.

2-(1-Methyl-1,2,3,4-tetrahydroquinoline-6-oyl)benzoic acid

To a stirred solution of 7.4 g (0.05 mol) 1-methyl-1,2,3,4-tetrahydroquinoline¹⁶¹ in 30 g carbon disulfide, 6.5 g of finely powdered aluminium chloride was added in small portions for approx. 45 minutes. Then, 3.2 g (0.02 mol) of finely powdered phthalic anhydride was added in portions to the reaction mixture. Addition of every portion of the anhydride induced boiling of the solvent. After 15 minutes a deep green resinous mass deposited on the bottom of the flask. The supernatant colourless solution was decanted. The residue was washed with a portion of carbon disulfide (30 g) and decomposed with cold, diluted sulfuric acid (6 g conc. H₂SO₄ – 25 ml H₂O). After 30 minutes the green, tarry mass turned into a fine beige suspension. The latter was diluted with 600 ml water and left for one week at ambient temperature. Greenish crystals deposited over that time were filtered and recrystallized from ethanol to give 5.1 g (81 %) of almost colourless product. (m. p. 201.5 – 203.5°).

¹H NMR, δ (ppm): 1.92 (2H, m); 1.99 (3H, s); 2.69 (2H, m); 2.85 (3H, s); 3.19 (2H, m); 6.50 (1H, d, J=8.54 Hz); 6.93 (1H, d, J=2.44 Hz); 7.06 (1H, dd, J₁=8.54 Hz, J₂=2.44 Hz); 7.42 (1H, m); 7.48 (1H, m); 7.62 (1H, m); 7.87 (1H, m).

¹³C NMR, δ (ppm): 22.25; 27.08; 27.99; 39.00; 51.13; 88.38; 110.43; 122.29; 122.74; 124.39; 125.47; 125.71; 126.12; 127.14; 128.89; 134.23; 146.75; 154.91; 170.40.

2-(julolidin-9-oyl)benzoic acid.

The above procedure applied to julolidine instead of tetrahydroquinoline derivative and phthalic anhydride resulted in 2-(julolidin-9-oyl)benzoic acid with 43% yield.

¹H NMR, δ (ppm): 1.92 (4H, m); 2.66 (4H, m); 3.25 (4H, m); 7.19 (2H,s); 7.33 (1H, m); 7.50 (1H, m); 7.57 (1H, m); 8.06 (1H, m).

¹³C NMR, δ (ppm): 21.49; 27.87; 50.20; 120.03; 123.52; 128.30; 128.61; 128.96; 129.96; 131.21; 132.54; 143.36; 147.50; 170.09; 195.58.

3,3-bis(1-methyl-1,2,3,4-tetrahydroquinolin-6-yl)phthalide (bisTHQ)

A mixture of 2.95 g (0.01 mol) 2-(1-methyl-1,2,3,4-tetrahydroquinoline-6-oyl)benzoic acid, 1.50 g (0.01 mol) 1-methyl-1,2,3,4-tetrahydroquinoline and 40 g of freshly distilled acetic anhydride were refluxed for 15 minutes. 46 ml of diluted hydrochloric acid (15 ml conc. HCl

aq – 31 ml H₂O) was added and the reaction mixture was kept at boiling for next 15 minutes. After cooling in an ice–water bath, the reaction mixture was made strongly basic by adding approx. 20 ml conc. ammonia. The precipitated slightly greenish solid was crystallized from ethanol to give 3.0 g (70.7%) of the product.

¹H NMR, δ (ppm): 1.92 (4H, m); 2.67 (4H, m); 2.85 (6H, s); 3.20 (4H, m); 6.47 (2H, d, J=8.54 Hz); 6.92 (2H, d, J=2.20 Hz); 6.98 (2H, dd, J₁=8.54 Hz, J₂=2.20 Hz); 7.50 (2H, m); 7.62 (1H, m); 7.88 (1H, m).

¹³C NMR, δ (ppm): 22.40; 28.04; 39.12; 93.18; 110.12; 122.56; 124.23; 125.79; 125.92; 126.45; 127.97; 128.35; 128.79; 133.94; 146.68; 153.70; 170.55.

3,3–bis(julolidin–9–yl)phthalide (bisJul)

Following the method described above with 2–(julolidin–9–oyl)benzoic acid and julolidine, 3,3–bis(julolidin–9–yl)phthalide was obtained with 29% yield.

¹H NMR, δ (ppm): 1.92 (8H, m); 2.65 (8H, m); 3.11 (8H, m); 6.72 (4H, s); 7.48 (2H, m); 7.60 (1H, m); 7.86 (1H, m).

¹³C NMR, δ (ppm): 21.89; 27.71; 49.87; 93.19; 120.85; 124.07; 125.55; 125.75; 125.95; 127.62; 128.48; 133.72; 142.72; 153.61; 170.70.

3-methyl-3-(1-methyl-1,2,3,4-tetrahydroquinolin-6-yl)phthalide (MeTHQ)

To a solution of methyl magnesium iodide prepared from 2.31 g (0.095 mol) magnesium, 13.46 g (0.095 mol) methyl iodide and 50 ml ether, 11.2 g (0.038 mol) of finely powdered 2–(1–methyl–1,2,3,4–tetrahydroquinoline–6–oyl)benzoic acid was being added in small portions while stirring for one hour. The reaction mixture was then refluxed for one hour, cooled down and decomposed with 40 ml of cold 3N hydrochloric acid. The aqueous layer was extracted with two 40 ml portions of ether and the combined organic solutions were washed successively with 40 ml of 5% sodium bicarbonate solution, 40 ml of 1 N sodium thiosulfate solution, water and dried over anhydrous magnesium sulfate. A red–orange oil left after evaporation of the solvent was purified by chromatography (silica gel, dichloromethane) to yield 6.1 g (55.5%) of off–white crystals.

¹H NMR, δ (ppm): 1.92 (2H, m); 1.99 (3H, s); 2.69 (2H, m); 2.85 (3H, s); 3.19 (2H, m); 6.50 (1H, d, J=8.54 Hz); 6.93 (1H, d, J=2.44 Hz); 7.06 (1H, dd, J₁=8.54 Hz, J₂=2.44 Hz); 7.42 (1H, m); 7.48 (1H, m); 7.62 (1H, m); 7.87 (1H, m).

¹³C NMR, δ (ppm): 22.25; 27.08; 27.99; 39.00; 51.13; 88.38; 110.43; 122.29; 122.74; 124.39; 125.47; 125.71; 126.12; 127.14; 128.89; 124.23; 146.75; 154.91; 170.40.

3,3-bis(4-dimethylaminophenyl)dithiophthalide (MGLSS)

Malachite green lactone (2.65 g, 5.83 mmol) and Lawesson's reagent (2.65 g, 6.56 mmol) were heated to reflux in toluene (37 ml) for four hours. Next, the solvent was removed and the greasy residue dissolved in hot ethanol and filtered. The reddish-brown crude product left after evaporation of alcohol was purified by chromatography (silica gel, dichloromethane) to yield 2.02 g (86.1 %) of a deep-red crystalline solid with m. p. 146.0 – 147.5° after crystallization from hexane-methylene chloride.

¹H NMR, δ (ppm): 2.93 (12H, s); 6.62 (4H, d, $J=9.03$ Hz); 7.16 (4H, d, $J=9.03$ Hz); 7.24 (1H, m); 7.43 (1H, m); 7.53 (1H, m); 8.04 (1H, m).

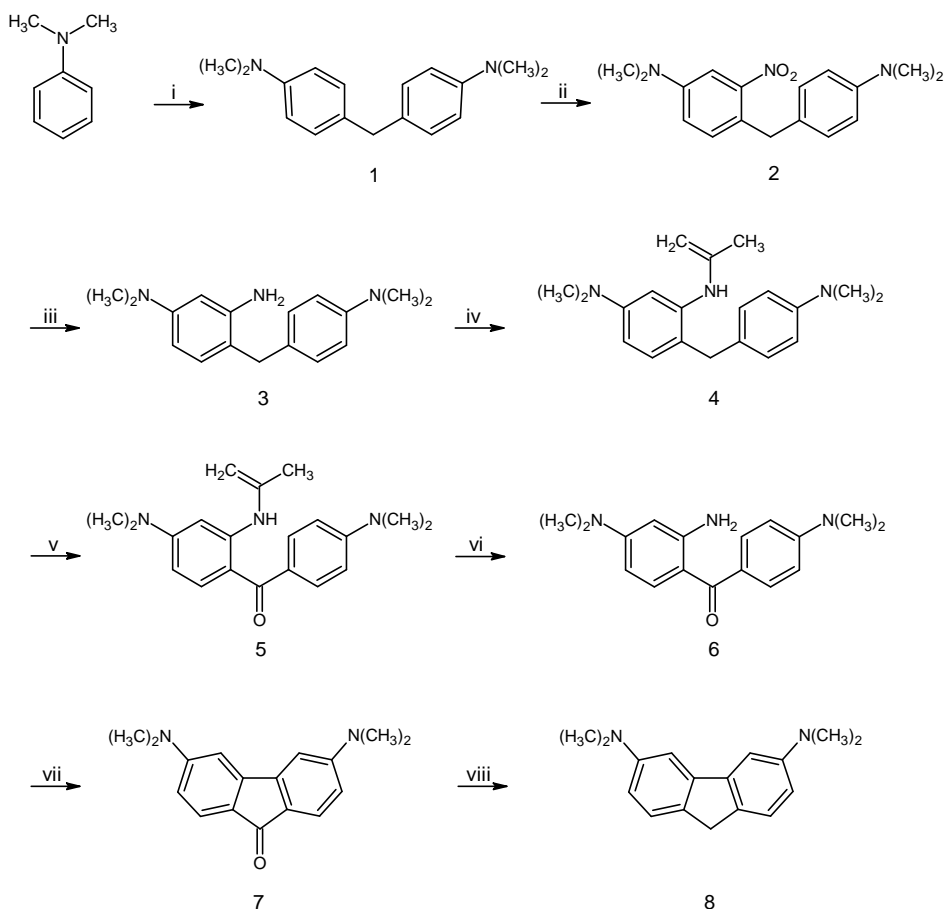
¹³C NMR, δ (ppm): 40.55; 112.12; 125.01; 127.39; 128.38; 129.25; 129.45; 132.70; 142.44; 149.95; 154.44.

3.1.2 Structural subunits

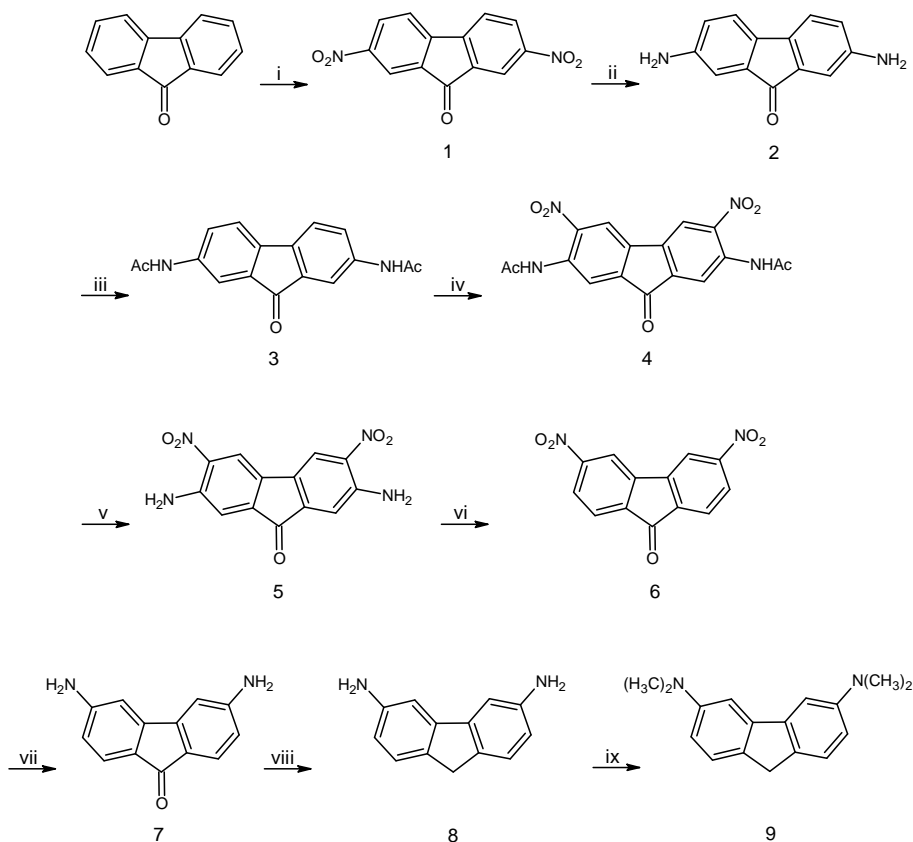
DMA and tBuDMA, bisphenol A and *t*-Bu-phenol (all from Aldrich) were used as received. MGH (Aldrich) was recrystallized from *l*-propanol with active charcoal prior to use and MGCN (Aldrich) was used as received. Phthalide (Aldrich) was recrystallized from water. 6-APd and 6-DMAPd were kindly provided by Dr. Jacek Nowacki and Dr. Jerzy Karpiuk.

3,6-bisdimethylaminofluorene (DMAF)

A new approach to the synthesis of 3,6-bisdimethylaminofluorene was worked out based on the procedures described in the literature^{162,163,164,165} (Scheme 3.1). Compared with the synthesis reported by Barker and Barker^{166,167} (Scheme 3.2) the new method is shorter and the product is obtained with twice as high yield (11%, Barker and Barker 5%). Moreover, a much better solubility of intermediates resulting from introduction of the dimethylamino substituents in the initial steps of the synthesis makes the new method less environmentally hazardous, as solvents such as pyridine, nitrobenzene and aniline can be avoided. The last step, the Wolff-Kishner reduction of fluorenone **7** to the final fluorene **8** (Scheme 3.1) was accomplished according to the procedure reported by Barker and Barker¹⁶⁶ for conversion of 3,6-diaminofluorenone **7** to 3,6-diaminofluorene **8** (described below).



Scheme 3.1. Synthetic path for DMAF worked out in this thesis. i: HCHO, AcOH; ii: 65% HNO₃/H₂SO₄; iii: SnCl₂/HCl_{aq}; iv: Ac₂O, NaOH; v: chloranil, EtOH; vi: 10% HCl, NH_{3aq}; vii: H₂SO₄/NaNO₂, CuSn, Na₂SO₄, NaOH; viii: trimethylene glycol, 100% N₂H₄*H₂O, NaOH.



Scheme 3.2. Synthetic path for DMAF reported by Barker and Barker¹⁶⁶ i: $\text{HNO}_3/\text{H}_2\text{SO}_4$; ii. $\text{SnCl}_2/\text{HCl}_{\text{aq}}$; iii. $\text{Ac}_2\text{O}/\text{HOAc}$; iv. $\text{HNO}_3/\text{Ac}_2\text{O}$; v. $\text{H}_2\text{SO}_4/\text{H}_2\text{O}$; vi. $\text{H}_2\text{SO}_4/\text{NaNO}_2$, H_3PO_2 ; vii. $\text{SnCl}_2/\text{HCl}_{\text{aq}}$; viii. trimethylene glycol, 100% $\text{N}_2\text{H}_4 \cdot \text{H}_2\text{O}$, NaOH ; ix. Me_3PO_4 , $\text{NaOH}/\text{H}_2\text{O}$.

A stirred suspension of 2.7 g (10 mmole) 3,6-dimethylaminofluorenone **7** in solution of 1 g (25 mmole) sodium hydroxide and 1 ml of 100% hydrazine hydrate in 15 ml propylene glycol was heated to 165° for 10 min. Then the temperature was raised gradually during 5 hours to 215° . The deep red solution was cooled down and diluted with 50 ml water. The precipitated brown solid was purified on a column with neutral alumina (III grade activity) using 1% methanol in methylene chloride as eluent to give, after twofold crystallization from ethanol, 2.15 g (85%) of slightly yellowish, colourless plates, m.p. $148\text{--}149^\circ$, (lit.: 149°)¹⁶⁷.

^1H NMR (200 MHz) δ (ppm): 3.02 (12H, s), 3.71 (2H, s), 6.74 (2H, dd, $J_1=8.30$ Hz, $J_2=2.44$ Hz), 7.14 (2H, d, $J=2.44$ Hz), 7.36 (2H, d, $J=8.30$ Hz).

Elemental analysis: found: C, 81.1; H, 7.8; N, 11.0. C₁₇H₂₀N₂ requires: C, 80.9; H, 8.0; N, 11.1%.

3.1.3 Solvents

The solvents: *n*-hexane (HEX), cyclohexane (CHEX), methylcyclohexane (MCHEX), ethyl ether (EE, inhibitor free), butyl acetate (BA), ethyl acetate (EA), tetrahydrofuran (THF), 2-methyltetrahydrofuran (MTHF), 1,2-dichloroethane (DCE), dichloromethane (DCM), acetonitrile (ACN), dimethylformamide (DMF), dimethylsulfoxide (DMSO), methanol (MeOH), *l*-propanol (PrOH), *l*-butanol (BuOH) were of spectroscopic quality. Butyl ether (anhydrous, Aldrich) was distilled over CaH₂. Diisopropyl ether (iPE) was of analytical grade (Aldrich). MTHF was additionally distilled over LiAlH₄ prior to use. MCHEX was passed through a column containing activated silica gel and aluminium oxide prior to use. Butyronitrile (Merck) was triply distilled over KMnO₄ + K₂CO₃, P₂O₅ and CaH₂, respectively.

3.2 Absorption and emission spectra

All luminescence measurements were carried out using solutions deoxygenated by saturation with purified and dried argon (typically for 30 minutes prior to measurement). Electronic absorption spectra were recorded with a Shimadzu UV 3100 spectrophotometer, and the measurements of emission spectra were carried out using an Edinburgh Analytical Instruments FS900 and a Spex Fluorolog 3 spectrofluorimeter. Luminescence spectra were subsequently corrected by subtraction of the background due to the solvent (e.g., Raman lines, excitation line passed as the second order of monochromator grating), and for spectral response of the detection system using correction factor files provided by manufacturers of respective spectrofluorimeters. Fluorescence spectra were recorded as a function of wavelength and subsequently multiplied by a factor of λ^2 to convert counts per wavelength interval into counts per wavenumber interval. The samples were excited in the first absorption band, usually near the band maximum. Fluorescence quantum yields were determined using quinine sulfate in 0.1 N H₂SO₄ as a standard ($\Phi_f=0.51$)¹⁶⁸ and corrected for the refractive index of a solvent.¹⁶⁹ The following formula was used:¹⁷⁰

$$\Phi_{fl} = \Phi_{fl}^{ref} \frac{n^2 A^{ref} \int I_{fl}(\lambda_{fl}) d\lambda_{fl}}{n_{ref}^2 A \int I_{fl}^{ref}(\lambda_{fl}) d\lambda_{fl}} \quad \text{Eq. 3.1}$$

where Φ_{fl} – fluorescence quantum yield, n – refractive index, A – absorption, I_{fl} – intensity of fluorescence, λ_{fl} – wavelength of fluorescence. The index “ref” is related to the reference (standard) sample (here quinine sulfate), whereas the symbols without the index relate to the system studied. For quantum yield determinations, optical density of both the sample and the standard were identical at the wavelength of excitation, and were of the order 0.1 – 0.15.

Fluorescence lifetimes were obtained with an Edinburgh Analytical Instruments FL900 time resolved spectrofluorimeter. The χ^2 test and the distribution of residuals were the main criteria in evaluation of the quality of the fit.

All temperature–dependent luminescence measurements down to 93 K have been carried out with a Jasny spectrofluorimeter and phosphorimeter,¹⁷¹ and low temperature fluorescence and phosphorescence measurements (at 77 K) – with a FL–1040 phosphorimeter option of the Spex Fluorolog 3 spectrofluorimeter. Some of measurements at 77 K were also performed with the Jasny phosphorimeter, where phosphorescence was separated from the total emission by means of a mechanical chopper system coupled with the apparatus (modulation frequency of about 4 kHz).

3.3 Transient absorption measurements

Nanosecond transient absorption measurements were carried out with a transient absorption spectrophotometer constructed by Jasny that allows for spectral measurements from 380 to 790 nm at delays ranging from –2 to 100 ns in relation to the excitation pulse (PTI PL 2300 nitrogen laser, FWHM = 0.6 ns, pulse energy about 1.3 mJ), with a temporal resolution better than 1 ns.¹⁷²

Femtosecond transient absorption study in this work involved measurements of spectra and decays of CVLB in various solvents in a pump–probe experimental setup built around a 1 kHz–repetition–rate regenerative Ti:Sapphire femtosecond amplifier (BMI alpha–1000). The pump beam was generated by frequency doubling the output of a noncollinear optical parametric amplifier (NOPA Topas–White from LightConversion). Pump pulses were centered around 365 nm

(measurements in acetonitrile and diethyl ether) or 370 nm (measurements in DMSO) and had the energy of approx. 2 μJ at the sample. A white light supercontinuum generated from fundamental pulses in a CaF_2 plate was used as the probe beam. The measurements were carried out at the magic angle (54.7°) between polarization directions of pump and probe beams. The recorded data were corrected for the chirp of the probe pulses. The sample solution was pumped through a flow-through cell with 0.14 mm-thick windows and a 1.2 mm-thick spacer. The results were analysed with global analysis. The femtosecond transient absorption measurements and global analysis on CVLB were completed in collaboration with Dr. Piotr Fita from the Faculty of Physics, Warsaw University.

Microsecond and sub-microsecond transient absorption was measured after excitation with a laser pulse from a pulsed Nd:YAG laser (Continuum Surelite II-10). MGL and MGLA were excited at 266 nm, and CVL and CVLA – at 355 nm. The light from a pulsed Xe-lamp passed through the sample perpendicularly to the exciting laser beam and was used as a probe. The probe light was then dispersed by a monochromator and recorded by a CCD camera. All samples used in transient absorption measurements with this setup were degassed by five freeze-pump-thaw cycles prior to measurement. The sample concentrations were as follows: CVL: $4\text{--}7 \cdot 10^{-5}$ M; CVLA: $\sim 4 \cdot 10^{-5}$ M; MGL: $\sim 1.5 \cdot 10^{-5}$ M; MGLA: $\sim 2 \cdot 10^{-5}$ M. In these measurements, transient absorption spectra were usually recorded at a 60 ns delay, and the laser excitation intensity for solutions in ACN and BTN was about 0.4 mJ. For EA solutions, the excitation intensity was increased about ten times to obtain a measurable signal. The duration of the exciting laser pulse was ~ 7 ns. The transient absorption data were recorded in collaboration with Dr. Joanna Wiberg and Prof. Bo Albinsson from the Chalmers University of Technology, Gothenburg, Sweden.

3.4 X-ray structures

The data were collected using a BRUKER KAPPA APEXII ULTRA diffractometer controlled by APEXII software¹⁷³, equipped with a MoK α rotating anode X-ray source ($\lambda = 0.71073$ Å, 50.0 kV, 22.0 mA) monochromatized by multi-layer optics and an APEX-II CCD detector. The experiments were carried out at 100 K using the Oxford Cryostream cooling device. The crystal was mounted on a Mounted CryoLoop with a droplet of Pantone-N oil and immediately cooled. Indexing, integration and initial scaling were performed with *SAINTE*¹⁷⁴ and *SADABS*¹⁷⁵ software (Bruker,

2008). The data collection and processing statistics are reported in tables for according structures. The crystal was positioned at 50 mm from the CCD camera. 2300 frames were measured at 0.5° intervals with a counting time of 20 sec.

The structures were solved by direct methods approach using the SHELXS-97¹⁷⁶ program and refined with the SHELXL-97.¹⁷⁷ Multi-scan absorption correction was applied in the scaling procedure. The refinement was based on F^2 for all reflections except those with negative intensities. Weighted R factors, wR, and all goodness-of-fit S values were based on F^2 , whereas conventional R factors were based on the amplitudes, with F set to zero for negative F^2 . The $F_0^2 > 2\sigma(F_0^2)$ criterion was applied only for R factors calculation and was not relevant to the choice of reflections for the refinement. The R factors based on F^2 are for all structures about twice as large as those based on F . The hydrogen atoms were located in idealized geometrical positions, except for hydrogens in the solvent molecule(s). Scattering factors were taken from Tables 4.2.6.8 and 6.1.1.4 from the International Crystallographic Tables Vol. C.¹⁷⁸ All X-ray structures were determined in collaboration with the group of Prof. Krzysztof Woźniak from the Faculty of Chemistry, Warsaw University.

3.5 Calculations

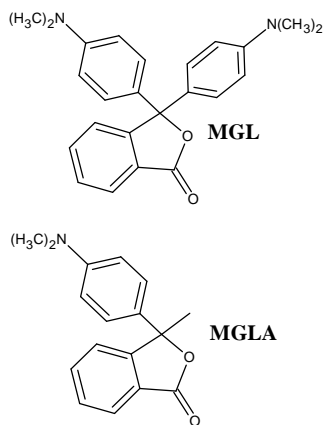
Density functional theory (DFT) was chosen as the quantum chemical modelling method, due to its relatively balanced accuracy-to-cost ratio for medium sized organic molecules. Within this theory the properties of molecules are determined by using functionals of the spatially dependent electron density.

In our case, the versatile B3LYP hybrid functional^{179,180} of well established performance was applied. The split-valence double-zeta type basis set with addition of polarisation functions (one set of d-functions for all non-hydrogen atoms and one set of p-functions for hydrogen atoms) supplemented by diffuse functions on non-hydrogen atoms, referred to as 6-31+G(d,p) basis set, was used (for MGLA and MGL a simpler 6-31G(d) basis set was used). For all the stationary points vibrational frequencies have been calculated to check if the geometry corresponds to the energy minimum. The electronic transition energies were obtained with time-dependent DFT (TDDFT).¹⁸¹ All computations were done with Gaussian 09 suite of programs by mgr Michał Kijak (Institute of Physical Chemistry, PAS).

Chapter 4

Triad vs. dyad donor–acceptor structure: Malachite green lactone and its analogue (MGLA)

Malachite green lactone (MGL) is an interesting example of multichromophoric molecular structure comprising two identical electron-donating (DMA) and one electron-accepting (Pd) subunits. For the purposes of this thesis such a structure is referred to as a triad donor–acceptor system, or simply D–A–D triad. A natural question arises as to whether one or two D groups take actively part in the photoinduced electron transfer process in such a triad. This Chapter addresses the question by presenting and analysing the results of spectral, photophysical and theoretical studies on 3-methyl-3-(4-dimethylaminophenyl)phthalide (MGLA), a D–A dyad counterpart of MGL, together with structurally related malachite green leuco derivatives



MGH, MGCN, and the MGL (also MGLA) structural subunits, DMA and Pd. The main goal here is to investigate how the simplification of the D–A–D triad of LTAM molecules (MGL) to the dyad structure (MGLA) affects the excited state electron transfer reaction and its kinetics.¹⁸² The problem was studied by examining solvent polarity, solvent proticity and temperature effects on MGLA photophysics and comparing them with MGL. The electronic structure was determined with TDDFT calculations and the excited state processes were quantitatively characterised by determining fluorescence quantum yields, lifetimes, radiative and radiationless parameters, excited state dipole moment, transition dipole moments and by estimating the ET rate. Moreover, the nature of the triplet states of MGLA and MGL is elucidated. The photoinduced electron transfer processes in MGLA show close analogy with MGL and prove that (i) the tetrahedral carbon atom coupled with C–O bond in quasi-spiro configuration is a very efficient link in ultrafast intramolecular electronic communication, and that (ii) the photoinduced charge separation and recombination processes in triarylmethane lactone molecules involve essentially only one electron-donating group.

LTAM molecules, such as MGL or PP, are systems with two identical electron donor subunits linked via tetrahedral carbon atom to phthalide acting as an electron acceptor. Spatial arrangement of the subunits in such triad structures of the D–A–D type is that the donor groups form a certain angle with the acceptor group and with each other. MGLA has a dyad structure of the D–A type, where one DMA unit is replaced by a methyl group attached to the central carbon atom. Due to a simplified structure MGLA can serve as a model compound for studying ET processes in D–A systems with tetrahedral connector between the D and A. The presence of only one donor excludes possible involvement of excitonic coupling in the excited state processes.

4.1 Ground state structure of MGLA and MGL

This Section presents the structure of MGLA in the solid state and in the gas phase, as studied by experimental (crystallography, X–ray analysis) and theoretical methods (DFT), respectively. The structure of MGLA is compared with the structure of its subunits (or their derivatives) and confronted with a structurally related MGL.

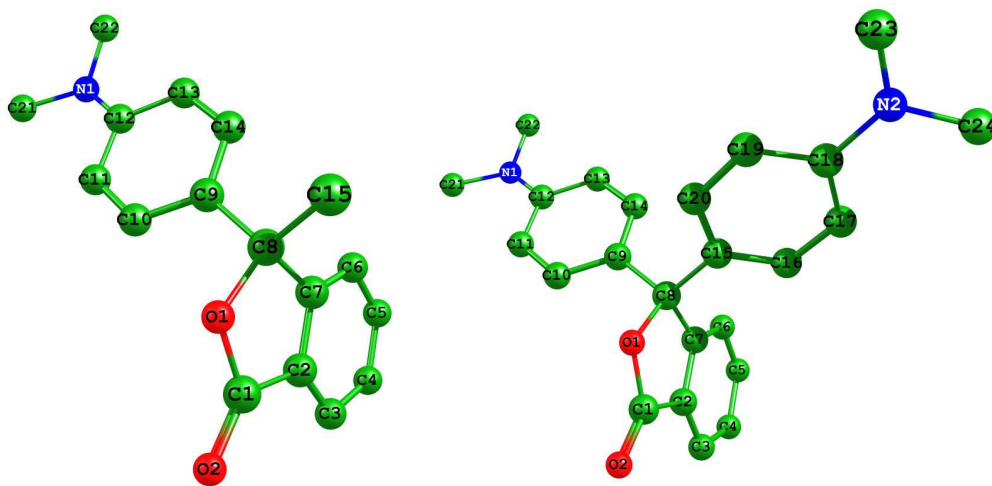


Fig. 4.1. Molecular structure of MGLA and MGL ground states obtained with DFT calculations (B3LYP/6–31G(d)). The atomic numbering scheme for atoms in MGLA and MGL is also used throughout the thesis as a base for structurally related molecules with similar carbon framework.

Tab. 4.1 Structural data on MGLA compared with MGL, Pd and DMA.

Bond length [Å]	MGLA		DMA	Pd		MGL	MGL	
	DFT	X-ray		DFT	DFT	X-ray	DFT	X-ray
		MGLA1	MGLA2					
C8–O1	1.477	1.482	1.466		1.442	1.455(4)	1.479	1.478
C8–C7	1.522	1.509	1.510		1.506	1.491(4)	1.526	1.521
C8–C9	1.525	1.518	1.517				1.531	1.524
C8–C15	1.533	1.523	1.525				1.526	1.527
C9–C10	1.403	1.398	1.390	1.395			1.399	1.389
C10–C11	1.389	1.379	1.384	1.393			1.393	1.392
C11–C12	1.417	1.406	1.400	1.413			1.414	1.389
C12–C13	1.413	1.399	1.403	1.413			1.415	1.409
C13–C14	1.395	1.385	1.381	1.394			1.393	1.381
C14–C9	1.398	1.382	1.386	1.395			1.401	1.397
C7–C6	1.394	1.387	1.387		1.394		1.394	1.388
C6–C5	1.399	1.387	1.388		1.399		1.399	1.390
C5–C4	1.405	1.395	1.395		1.405		1.405	1.396
C4–C3	1.395	1.379	1.381		1.396		1.395	1.383
C3–C2	1.396	1.387	1.388		1.395		1.395	1.392
C2–C1	1.482	1.467	1.467		1.482	1.459(5)	1.480	1.470
C1–O1	1.369	1.356	1.359		1.379	1.352(4)	1.367	1.365
C2–C7	1.391	1.382	1.378		1.392		1.390	1.383
C15–C16							1.399	1.399
C16–C17							1.393	1.377
C17–C18							1.414	1.410
C18–C19							1.415	1.406
C19–C20							1.393	1.389
C20–C15							1.401	1.387
Bond angle [deg]								
C15–C8–C9	114.6	112.6	112.8				113.4	115.2
C9–C8–O1	108.4	107.6	108.9				108.2	108.0
C15–C8–O1	106.3	106.3	106.6				106.7	107.7
O1–C8–C7	102.4	102.4	102.7		104.9	104.2(3)	102.2	101.9
C15–C8–C7	111.2	112.2	112.1				114.7	113.0
C9–C8–C7	113.0	114.8	113.0				110.7	110.1
Torsion angle [deg]								
DMA / Pd	88.5	123.3	114.1				106.0	94.6
							107.5	108.6
DMA/DMA							75.0	66.7

In the X-ray analysis, all bond lengths of MGLA and MGL were determined with an accuracy of 0.002 Å, the accuracy of the bond angles measurements was 0.1°. An asymmetric unit of MGLA consists of two independent molecules, denoted as MGLA1 and MGLA2. Bond lengths and angles for Pd are presented with standard deviations in parentheses.¹⁸³ DFT calculations (ground state optimisation) were performed with a B3LYP/6–31G(d) basis set for MGLA, MGLA and DMA. Numbering scheme – see Fig. 4.1.

MGLA was repeatedly crystallized from *n*-propanol with decolorizing charcoal, the needles obtained melted at 143.5–145°C. The determined crystal structure belongs to the monoclinic symmetry space group, $P2_1/c$, with the following lattice parameters: $a=12.4288(5)$ Å, $b=7.6315(3)$ Å, and $c=28.6714(13)$ Å. The structure contains two independent MGLA molecules with almost identical symmetry – molecule 1 and molecule 2, hereinafter referred to as MGLA1 and MGLA2 (Fig. 4.2, Tab. 4.1).

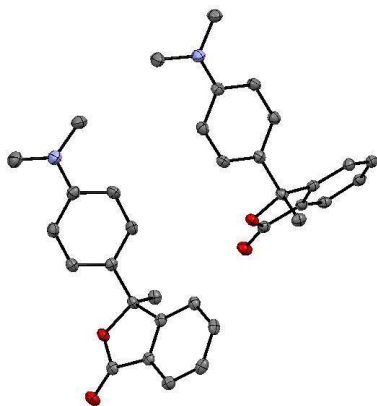


Fig. 4.2 A perspective view of the crystal structure (50% probability ellipsoids) of MGLA, excluding hydrogen atoms. An asymmetric unit consists of two independent molecules, denoted as MGLA1 and MGLA2.

The most apparent differences in the structure of both molecules (Tab. 4.1) are the torsion angles of the dimethylaniline moiety with respect to flat phthalide, 123.3° (MGLA1) and 114.1° (MGLA2). Also, the length of the C8–O1 bond differs in both molecules by 0.016 Å (longer in MGLA1). Bonds within the Pd moiety are of approximately the same length for both molecules, the same holds for the DMA substructure excluding the C9–C10 bond (longer by 0.008 Å for MGLA1).

MGL was crystallized from *n*-propanol, and the crystals obtained (needles) melted at 152° C. The determined crystal structure belongs to the same monoclinic symmetry space group $P2_1/c$ as does MGLA, with the following lattice parameters: $a=7.8513(3)$ Å, $b=21.8699(7)$ Å, and $c=12.7589(6)$ Å. It is important to note here that MGL has two polymorphic variants differing significantly in melting points (152° and 192°C). The solutions prepared with both polymorphic variants have the same NMR, absorption and emission characteristics. Crystal structures of both forms have been determined,¹⁸⁴ their detailed description is, however, beyond the scope of this thesis.

The electron-accepting moiety, common for MGLA and MGL, has very similar structure in both molecules, with the biggest difference in C–C

bond lengths being 0.004 Å. The length of the lactonic C8–O1 bond in MGL corresponds to the mean value of MGLA1 and MGLA2 (1.477 Å). According to the X-ray data reported for insulated Pd¹⁸³ the length of the C8–O1 bond in Pd is 1.455 Å. Comparison of the lactonic C–O bonds in MGLA, MGL and Pd allows to conclude that substitution of Pd at position 3 leads to significant elongation of this bond.¹⁸⁵ For the DMA moiety, the differences in bond lengths between MGL and MGLA are somewhat larger than those in Pd, up to 0.01 Å (for the C11–C12 bond). All bonds formed by the central carbon atom C8 (with other C atoms) are in the range of saturated bond lengths pointing to the lack of electronic delocalization from the aromatic rings.

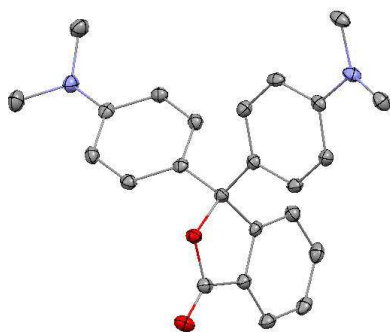


Fig. 4.3 A perspective view of the crystal structure (50% probability ellipsoids) of MGL, excluding hydrogen atoms.

For both, MGLA and MGL, the DFT calculations of the ground state geometry were performed on the B3LYP/6–31G(d) level. In general, the calculations reproduce relationships between the bond lengths, however, the bond lengths are overestimated (Tab. 4.1). When comparing calculations with the X-ray data one has to keep in mind that the DFT calculations are performed on isolated molecules in vacuum, whereas a molecule in crystal is always subject to various interactions (in this case: intermolecular CH/ π and C–H \cdots O interactions).

4.2 Absorption transitions in aprotic solvents

The absorption spectra of MGLA, MGL together with the spectra of reference compounds, leuco malachite green (MGH) and Pd, recorded in ACN at room temperature are presented in Fig. 4.4.

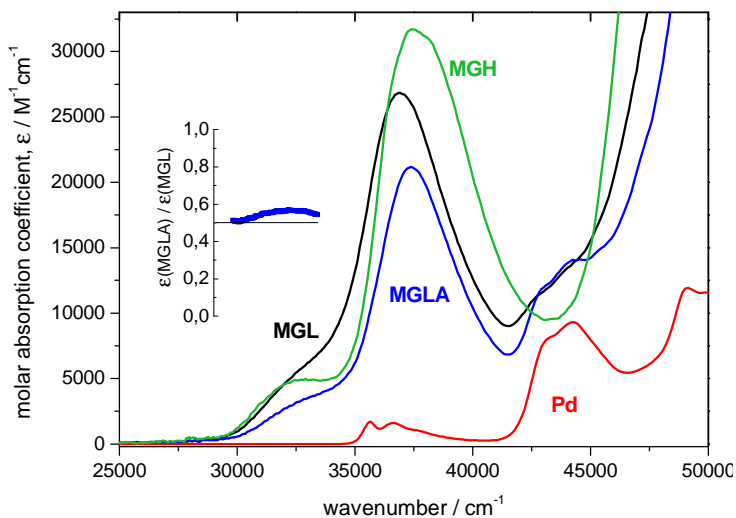
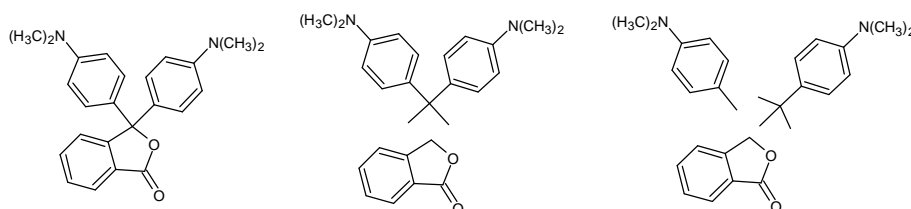


Fig. 4.4 Absorption spectra of MGL (black), MGLA (blue), MGH (green) and Pd (red) in ACN; inset: the ratio of molar absorption coefficients of MGLA and MGL in the spectral region 29800–33300 cm^{-1} .

The spectrum of MGH between 30000 and 40000 cm^{-1} resembles closely that of DMA with regard to the shape and the positions of maxima (Section 2.3).¹⁸⁶ The first absorption band, with a maximum at 32500 cm^{-1} , is ascribed to the L_b transition localized on DMA, the second band (37500 cm^{-1}) is a result of the L_a transition¹⁸⁶. According to Platt's¹⁸⁷ notation for assignment of the electronic levels of substituted benzenes, the transition to the L_a state is polarized parallel to the symmetry axis of a molecule (going through carbon atoms number 1 and 4), the L_b state has less polar character and the transition is polarized perpendicular to L_a . Molar absorption coefficients for both transitions of MGH are in the first approximation about twice as high as those for DMA¹⁸⁸ and comparable with the absorption coefficients for bis(dimethylaniline)methane¹⁸⁹ (Tab. 4.2). Thus, there is no substantial electronic interaction in the ground state between the two DMA units and the benzene ring across the tetrahedral carbon atom.

The spectra of MGLA and MGL generally include the transitions appearing in MGH and Pd, in agreement with earlier work on leuco-derivatives of TAM.^{52,66} The absorption spectrum of LTAM results essentially from a superposition of transitions of structural subunits and the lowest excited singlet state is localized on one of the DMA units. Nevertheless, compared with MGH, both MGL and MGLA display

enhanced absorption in the region where Pd does not absorb (32000 cm^{-1} – 34800 cm^{-1}). Since this effect is present in both molecules it must be related to a direct (probably weak) interaction between Pd and DMA moieties giving rise to a new absorption transition that extends over the two subunits and is therefore a CT transition in nature. The onset of the CT band in ACN lies below 32000 cm^{-1} where the spectra of MGL and MGH start to deviate from each other (Fig. 4.4). The position of the CT band can be estimated from the ratio of the molar absorption coefficients of MGLA and MGL as a function of wavenumber (Fig. 4.4). In the case there is no interaction between Pd and DMA, the ratio should be equal to 0.5 in the low energy region due to spectral additivity, reflecting the fact that the probability of photon absorption within the first absorption band per one MGLA molecule is twice as low as in MGL. The inset in Fig. 4.4 shows regular deviation of $\varepsilon(\text{MGLA})/\varepsilon(\text{MGL})$ from 0.5 in the region from 30400 to 33300 cm^{-1} , indicating that the CT state in MGLA is approximately energetically degenerate with or slightly above the S_1 state localized on the DMA moiety.



Compound	L_b transition		L_a transition	
	max. [cm^{-1}]	ε [$\text{M}^{-1}\text{cm}^{-1}$]	max. [cm^{-1}]	ε [$\text{M}^{-1}\text{cm}^{-1}$]
DMA	33600	2300	39800	14900
bisDMA	33100	4800	38600	35600
MGH	32500	5000	37500	31700
MGL	~32300	5200	36900	26700
MGLA	~32400	3100	37150	21000

Table 4.2 Comparison of positions and absorption coefficients of the first two absorption bands in DMA¹⁸⁸, bisDMA: (bis(dimethylaniline)methane),¹⁸⁹ MGH, MGL and MGLA.

The contribution of the CT state to the overall absorption spectrum and its oscillator strength is difficult to estimate due to significant overlap with other absorption bands. The DTF calculations are also unreliable in determining CT transition energies. Conclusions on the CT transition energies in a composite D–A molecule can also be hardly drawn from the

decomposition of the absorption spectrum into its components corresponding to transitions localized on the subunits.¹⁹⁰ The absence of any noticeable effect of solvent polarity on the absorption spectrum of MGLA (in MGL the solvent effect was very moderate) together with the lack of spectral additivity of absorption implies that the contribution from the CT state is rather insignificant compared to the local transitions but still not negligible.

The presence of a CT band in MGLA and MGL indicates that the excited state with charge separation can be populated directly from the ground state via absorption of a photon with the energy close to that of the $S_0 \rightarrow S_1$ (1L_b) transition localized on DMA. The intensity of the 1L_a transition in MGL (localized on DMA) is lower than that corresponding to the algebraic sum of two DMA ($\epsilon = 14900 \text{ M}^{-1}\text{cm}^{-1}$ at the maximum of the 1L_a in cyclohexane) and Pd transitions (Tab. 4.2), which means that the CT transition borrows the intensity from the 1L_a transition of the donor. The 1L_b state of the DMA moiety is not involved in the CT transition because of the presence of nodes of the orbitals involved in the transition at substitution positions.¹⁸⁹

The absorption spectra of MGLA solutions in aprotic and in protic solvents did not show any traces of absorption in the visible, both before and after fluorescence measurements, indicating that there were no coloured (i.e., ionic) forms resulting from, e.g., ground state dissociation of the lactonic bond, and that the solutions were generally photostable.

4.3 Fluorescence at room temperature

In this Chapter the deactivation of the excited state of MGLA as a function of solvent polarity and proticity is reported and compared with those of MGL, MGH and MGCN.

Room temperature fluorescence spectra of MGLA and MGL compared with MGH and tBuDMA in solvents of different polarity are shown in Fig 4.5, the fluorescence data for MGLA is presented in Tab. 4.3.

The emission spectra of MGLA were independent of excitation wavelength in all solvents used and the fluorescence excitation spectra reproduced well the absorption spectrum. Prolonged irradiation of MGLA solution in ACN with 310 nm (32260 cm^{-1}) light of a xenon lamp did not result in any changes in absorption or fluorescence spectrum proving that the molecules were photostable under the conditions of experiment.

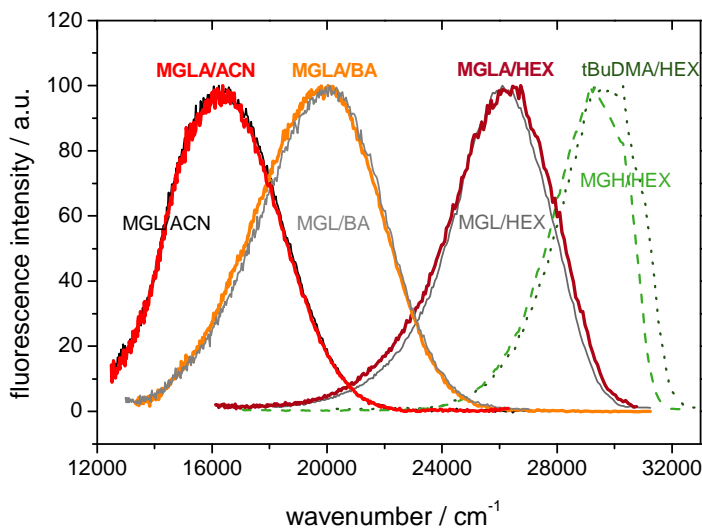


Fig. 4.5 Normalized fluorescence spectra of MGLA (thick lines) and MGL (thin lines) in HEX, BA and ACN compared with those of *t*-butyldimethylaniline (tBuDMA, dotted line) and leucomalachite green (MGH, dashed line) in HEX. The spectra were recorded at 295 K (excitation wavelength 310 nm – 32250 cm⁻¹).

MGLA displays a single, broad and structureless fluorescence band that is characterized by a huge Stokes shift (for HEX 8400 cm⁻¹) and strong solvatochromic effect. In all solvents the emission spectra agree almost perfectly with those of MGL. It is noteworthy that the solvatochromic shift for both molecules studied here (10400 cm⁻¹ for MGLA between HEX and DMSO) is higher than that for *fluoroprobe* molecule (10200 cm⁻¹)¹⁹¹ reported by Reichardt¹⁹² as the one having the largest frequency shift in response to change in solvent polarity.

In MGH the fluorescence is emitted from the S₁ state of DMA, as it is the case for MGCN reflecting negligible ground state and excited state interactions between individual chromophores.⁴⁶ The emission spectra of MGLA and MGL cannot be ascribed to come from the DMA moiety due to a huge difference in the maximum positions and a large half-width of the bands: in nonpolar HEX the emission of MGLA is strongly red-shifted compared to that of tBuDMA or DMA (maxima in HEX at 29300 cm⁻¹ and 30200 cm⁻¹, respectively)¹⁹³ and of MGH or MGCN (maxima in HEX at ~29300 cm⁻¹ for both compounds). This observation, together with the strong solvatochromic effect, imply that the origin of emission is another lower lying excited state with considerable dipole moment. This means that the primary excited state (localized on DMA subunit) is effectively quenched

by transition to the emitting polar state. Similarly as for MGL, the fluorescence comes from a CT state with a structure of an intramolecular radical ion pair, with positive charge on DMA and negative on Pd. Almost identical spectra of MGLA and MGL strongly suggest, that the emitting states in both molecules have similar electronic structures and properties. This in turn implies, that the presence of the second DMA moiety in MGL has no substantial impact, and that in the ET process only one electron donating subunit is involved.

As opposed to MGL, the fluorescence spectrum of MGLA in ACN recorded at 296 K showed a weak and relatively narrow band in the region 24000 – 29000 cm^{-1} with a peak intensity at 27500 cm^{-1} 50 times lower than in the maximum at 16500 cm^{-1} . The band resulted most probably from impurity traces in ACN and was not observed for MGLA in other solvents.

The upper limit for the rate of intramolecular quenching of the primary excited S_1 state of DMA subunit in MGLA (k_q) can be estimated using a method similar to that applied previously for MGL.⁷⁶ Since the quenching process is identified with charge separation, the estimation yields the time constant for intramolecular ET, k_{ET} . The upper limit for the integrated room temperature fluorescence intensity in the spectral region where possible fluorescence from the primarily excited DMA chromophore in ACN would occur, can be estimated as 6.9×10^{-3} times lower than that of the fluorescence band extending from 24000 cm^{-1} to below 12500 cm^{-1} (Fig. 4.5). The factor is somewhat higher than that for MGL in ACN (2.0×10^{-3}) but due to a lower Φ_{fl} for MGLA in ACN (≤ 0.001 (Table 4.3) vs. 0.0018 for MGL) the quantum yield of a possible fluorescence from the DMA chromophore in MGLA, Φ_q , is lower than 6.9×10^{-6} . Comparing the value with $\Phi_{DMA} = 0.11$ as reported for DMA in ACN,¹⁹⁴ one obtains a reduction in fluorescence quantum yield by a factor greater than 1.6×10^4 . This implies a very effective, ultrafast intramolecular electronic relaxation process, consisting in conversion of the primarily excited state localized on DMA to the emitting state, as for MGL. Assuming the first-order kinetics for the process and neglecting vibrational relaxation upon excitation, k_q can be roughly estimated by comparing Φ_{DMA} in ACN with the upper limit of Φ_q estimated above: $k_q = (\Phi_{DMA}/\Phi_q)(1/\tau_{DMA})$, where $\tau_{DMA} = 3.8$ ns is the fluorescence lifetime of DMA in ACN. The rate constant of the electronic relaxation process in MGLA estimated with this formula, $k_q \geq 4.2 \times 10^{12} \text{ s}^{-1}$, indicates that the primary electronic relaxation in MGLA is completed on a sub-250 fs time scale. The time domain closely resembles both that estimated for MGL with similar steady state approach ($7.8 \times 10^{12} \text{ s}^{-1}$) and

determined directly with fs transient absorption spectroscopy ($6.7 \times 10^{12} \text{ s}^{-1}$, upon excitation to the S_2 state).¹³ It also indicates that the rate constant of the primary photophysical process in MGLA is faster than both vibrational and solvent longitudinal dielectric relaxation times. Very fast rate of the transition to the emitting state proves quantitative (100%) conversion of the primary excited state into the CT state, as any competitive deactivation would have to be faster.

Tab. 4.3 Fluorescence of MGLA as a function of solvent polarity

solvent	$\tilde{\nu}_{fl}$ [cm ⁻¹]	FWHM [cm ⁻¹]	Φ_{fl}	τ_{fl} [ns]	k_r [x10 ⁻⁶ s ⁻¹]	k_{nr} [x10 ⁻⁷ s ⁻¹]	M_{fl} [D]
HEX	26400	4300	0.042	2.5	16.8	38.3	1.06
BE	22700	5760	0.088	15.9	5.5	5.7	0.74
iPE	22400	5070	–	–	–	–	–
EE	21850	5300	0.142	24.4	5.8	3.5	0.85
BA	20050	5150	0.082	18.8	4.4	4.9	0.80
EA	19400	5100	0.036	11.1	3.2	8.9	0.84
THF	19550	4900	0.057	13.8	4.1	6.8	0.80
DCM	19100	4800	0.056	14.9	3.8	6.3	0.77
DCE	18900	4900	0.043	12.5	3.4	7.7	0.73
BTN	17500	4850	0.005	2.4	2.1	41.5	0.68
ACN	16500	4650	≤0.001	~0.5	2	200	~0.79

$\tilde{\nu}_{fl}$ maximum of fluorescence band, FWHM–full width at half maximum, Φ_{fl} and τ_{fl} – fluorescence quantum yield and decay time, respectively; k_r –radiative rate constant, k_{nr} –nonradiative rate constant, M_{fl} –fluorescence transition dipole moment.

Radiative ($k_r = \Phi_{fl}\tau_{fl}^{-1}$) and total nonradiative ($k_{nr} = (1-\Phi_{fl})\tau_{fl}^{-1}$) decay constants and fluorescence transition dipole moments (M_{fl}) as a function of solvent polarity are given in Table 4.3. M_{fl} values were obtained with the formula:¹⁹⁵

$$M_{fl} = \sqrt{\frac{3hk_r}{64\pi^4 n^3 \tilde{\nu}_{fl}^3}} \quad \text{Eq. 4.1}$$

where $\tilde{\nu}_{fl}$ is the spectral position of fluorescence maximum and n is the refractive index of the solvent. Calculated rate constants and transition dipole moments are not solvent–dependent and follow the trend observed for MGL, but are slightly lower. This implies that the radiative transition probability is not affected by the environment and that the radiative

recombination is less probable in MGLA. The nonradiative rate constant, however, shows a strong solvent dependence, k_{nr} increases with growing polarity of the medium, indicating enhanced solvent polarity driven radiationless deactivation of the emitting state both in MGLA and MGL. The transition dipole moments, M_{fl} , for MGLA are lower than those found for MGL (0.8 D, 1.0 D, respectively) and much lower than the absorption transition dipole moments, M_{abs} , which were estimated using the approximate expression (Eq. 4.2):

$$M_{abs} = 0.09582 \sqrt{\frac{\epsilon_{max} \Delta v_{1/2}}{\tilde{\nu}_{abs}}} \quad \text{Eq. 4.2}$$

where ϵ_{max} [$M^{-1}cm^{-1}$] is the absorption coefficient at the band maximum, ν_{max} , and $\Delta v_{1/2}$ is the half – width of the band in cm^{-1} . Assuming $\epsilon_{max} = 3000 M^{-1}cm^{-1}$, $\nu_{max} = 32400 cm^{-1}$ and $\Delta v_{1/2} = 3500 cm^{-1}$ for MGLA in acetonitrile, one obtains $M_{abs} = 1.7 D$. Since the absorption spectrum displays almost no solvent dependence, the values of M_{abs} must have similar values for other solvents. Large difference between M_{fl} and M_{abs} values indicates that the emitting state is not that directly populated in absorption and must be a product of intramolecular electronic relaxation.

4.4 Excited state dipole moment

The polar character of the emitting state of MGLA was verified by estimation of its dipole moment with the solvatochromic shift method. Numerous variations of the method are based on the Onsager reaction field model,¹⁹⁶ which considers a solute molecule as a point dipole situated in a centre of a spherical cavity formed by solvent molecules surrounding the solute molecule and interacting with its dipole. As the lifetimes of the fluorescent state are much longer than the solvent orientational relaxation times, the dipole moment of the emitting state could be estimated from the solvent effect on spectral position of fluorescence maxima using Lippert–Mataga¹⁹⁷ approach modified for fluorescence maxima.¹⁹⁸ The shifts of fluorescence maxima were chosen here because the estimation of the excited state dipole moment from the solvent effect on the Stokes shift was not possible, as the absorption band to the emitting CT state of MGLA can be hardly determined. Assuming a point dipole moment situated in a centre of a spherical cavity and neglecting the mean solute polarizability in the states involved in the transition, the excited state dipole moment, $\bar{\mu}_e$, can be

calculated from the following expression:

$$hc\tilde{\nu}_{fl} \cong hc\tilde{\nu}_{fl}^{vac} - \frac{2\bar{\mu}_e(\bar{\mu}_e - \bar{\mu}_g)}{a_0^3} \left[\frac{\epsilon - 1}{2\epsilon + 1} - \frac{1}{2} \frac{n^2 - 1}{2n^2 + 1} \right] \quad \text{Eq. 4.3}$$

where $\bar{\mu}_g$ is the dipole moment of the solute in the ground state, and $\tilde{\nu}_{fl}$ and $\tilde{\nu}_{fl}^{vac}$ are the spectral positions of the solvent-equilibrated fluorescence maxima and the value extrapolated to the gas phase, respectively; a_0 is the radius of the Onsager cavity.

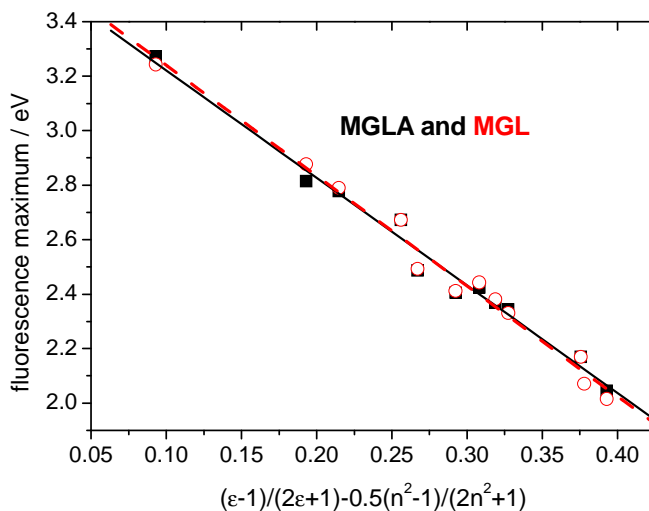


Fig. 4.6 Fluorescence maxima of MGLA (squares) and MGL (open circles) as a function of solvent polarity. Plot parameters: slope $(-2\bar{\mu}_e(\bar{\mu}_e - \bar{\mu}_g)/a_0^3) = -3.95$ eV, -4.00 eV, intercept $(hc\tilde{\nu}_{fl}^{vac}) = 3.62$ eV, 3.61 eV for MGLA and MGL, respectively; correlation coefficient $R = 0.99$ for both plots. Solid line represents linear fit for the MGLA data, dashed line – for those of MGL.

The plot of MGLA fluorescence maxima as a function of solvent polarity $f(\epsilon, n) = (\epsilon - 1)/(2\epsilon + 1) - 0.5(n^2 - 1)/(2n^2 + 1)$ is practically indistinguishable from that of MGL (Fig. 4.6). The slopes and intercepts for both plots are very close to each other: -3.95 eV and -4.00 eV (slopes), and 3.62 eV and 3.61 (intercepts), for MGLA and MGL, respectively. The overlap of solvatochromic plots for the two molecules implies that the energies of interaction of their CT states with the surrounding solvent are identical and that MGLA and MGL experience the same excited state energy stabilization with increasing solvent polarity. Differing by presence of one DMA moiety,

MGLA and MGL are considerably different in shape, in view of a striking similarity of the photophysical characteristics, however, their indistinguishable interactions with solvent shells can be rationalized with a conjunctive conclusion that their dipole moments in CT states and their radii of the effective⁷⁶ Onsager cavities, a_0 , are about the same.

Appropriate estimation of the a_0 value has critical impact on the final uncertainty of μ_e as a_0 enters the equations in the third power. The radius taken previously for MGL ($a_0 = 5.8 \text{ \AA}$) was estimated from the molecular dimensions of the compound calculated by molecular mechanics and was assumed as the distance between one of the amino nitrogens and the central carbon atom. Though MGLA is less spacious, the distance between the centre of the molecule and the furthest electrons is about the same as in MGL, and a sphere circumscribed around MGLA is very similar to that circumscribed around MGL. Assuming that $|\bar{\mu}_e| \gg |\bar{\mu}_g|$ ¹⁹⁹ and that the effective spherical radius of MGLA is equal to that of MGL, Eq. 4.3 yields $\mu_e = 24.8 \text{ D}$, which compares well with 25.0 D found for MGL.⁷⁶ Such large values reflect the electron transfer over a distance of 5 \AA and imply full charge separation between the DMA moiety and the lactone ring in the phthalide moiety. Moreover, the conclusion implies that the CT state in MGL essentially involves intramolecular ion pair with positive charge localised on one of the DMA groups, while the other DMA group does not contribute significantly both to the CS process and the electronic structure of the emitting CT state of MGL.

4.5 Absorption and fluorescence in alcohols

MGLA solutions in alcohols show generally similar absorption spectra to those in aprotic solvents of corresponding polarity and no additional bands indicating the presence of other molecular forms of MGLA or ground state complexes with the solvent have been observed. The first and the second absorption bands are slightly (by $50 - 100 \text{ cm}^{-1}$) blue-shifted in methanol compared with ACN. The fluorescence of MGLA in alcohols is extremely weak (estimated Φ_{fl} in MeOH $\ll 10^{-4}$, in PrOH: $\Phi_{fl} = 3.1 \times 10^{-4}$, in BuOH: $\Phi_{fl} = 5.7 \times 10^{-4}$) and strongly depends on the polarity and the length of the alcohol aliphatic chain. Similarly as in aprotic solvents, fluorescence spectra of MGLA in alcohols consist of one broad band with maximum position corresponding roughly to that in aprotic solvent of equal polarity, which proves that the CT state is rapidly populated also in protic solvents.

Fluorescence decay times were immeasurably short on the ns time scale (e.g. < 0.2 ns), indicating enhanced nonradiative process as compared with aprotic solvents. It is important to note that the photophysics and photochemistry of MGCN in alcohols were found to be similar to those in ACN (fluorescence from insulated DMA chromophore with $\Phi_{fl} = 0.005$ and polarity induced photodissociation of the CN group).¹⁹⁴ Transient absorption study of a structurally related LTAM, crystal violet lactone (CVL), revealed excited state C–O bond dissociation with formation of crystal violet dye cation in 1-propanol,⁸² which indicates active participation of the protic solvent in the excited state relaxation of MGLA (probably via hydrogen bonding induced lactone ring opening²⁰⁰) and significant geometrical rearrangement needed for transformation from tetrahedral to planar conformation of the molecule.

4.6 Nature of the triplet states populated at room temperature

The CT nature of the emitting singlet state of MGL was proved by femto-¹³ and nanosecond⁷⁶ transient absorption measurements, which revealed the cation radical signature of DMA (band at 470 nm). The anion radical spectrum of Pd was not observed in the transient absorption experiments, due to either overlap with a much stronger band of DMA⁺ or occurrence in different spectral region than that probed. The shape and structure of the TA spectra of MGL recorded on the ns scale after complete decay of the emitting singlet state are virtually identical with those recorded at time zero, strongly suggesting the presence of DMA⁺ in both the singlet and the triplet states. Hence, the charge separation in MGL is still maintained in the triplet state.

For MGLA, the $S_n \leftarrow S_1$ transitions were not monitored in the TA measurements carried out with a microsecond transient absorption technique,²⁰¹ but based on the similarity of the photophysical properties to MGL it can be safely assumed, that also in MGLA the cation radical band of DMA could be found (at “early” delays).

In μ s and sub- μ s experiments, transient absorption spectra of MGL and MGLA were recorded at different delays, ranging from 60 ns to a few microseconds (presented spectra were recorded at 60 ns delay if not stated otherwise). The samples were excited with 266 nm laser pulses (Nd-YAG laser, FWHM=7 ns). In the course of measurements, a decomposition of the MGL and MGLA samples was observed (no matter what solvent or laser intensity were used) and monitored by the change of steady-state absorption

spectra recorded during transient absorption measurements (growth of a red tail, slight changes in shape with appearance of isosbestic points; Fig. 4.7), fluorescence spectra (a new additional emission band appeared at 410 nm in ACN). The effect of sample decomposition on the TA spectra was, however, very weak, e.g., no new bands could be detected, only a slight decrease in the intensity of the primary TA band was observed.

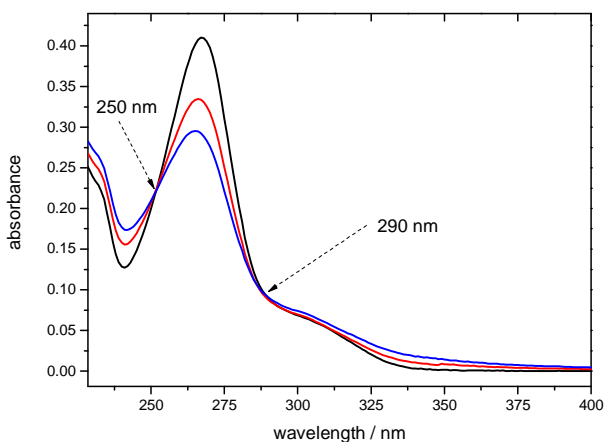


Fig. 4.7 Absorption spectra of MGLA in ACN recorded before TA measurements (black), after approximately 100 laser shots (red) and after 150 laser shots (blue).

The products of the photodegradation were not identified. From the literature it is known that lactones undergo decarboxylation when excited into higher triplet states.^{202,203,204} However, in this case, this type of degradation of the sample can be excluded since no coloured products of the photoreaction were observed. The observed decomposition of the samples though, may result from multiphoton processes initiated by long excitation pulses (about 7 ns) and be due to short lifetimes of the singlet excited states ($\tau_{fl} < 1$ ns). During single laser pulse the molecule can relax to the triplet state and subsequently can be excited in the triplet state by absorption of a photon from the same excitation pulse. This explanation is also supported by the fact that during femtosecond and nanosecond experiments (excitation pulse ~ 0.6 ns), where the excitation pulses were considerably shorter, no decomposition of the samples was observed.

In spite of the decomposition discussed above, it was possible to obtain reliable and reproducible triplet – triplet absorption spectra, suitable for qualitative analysis. The data for analysis and presentation was carefully selected, and only those T–T absorption spectra were taken into account,

where no steady-state absorption changes were observed (if any changes in the steady-state absorption spectrum were observed, a new sample was prepared).

The TA spectra of MGL and MGLA are presented in Fig. 4.8. Transient absorption spectra of both compounds in polar solvents (ACN, BTN) consist of only one characteristic band with a maximum around 470 – 480 nm, and a halfwidth of approximately 60 – 70 nm (3300 cm^{-1}). In MGLA, in low polar ethyl acetate, however, the 470 nm band does not decay to a noise level and on the blue side of the spectrum there is a noticeable increase in the signal. For MGL no TA signal in EA in the probed spectral region could be detected.

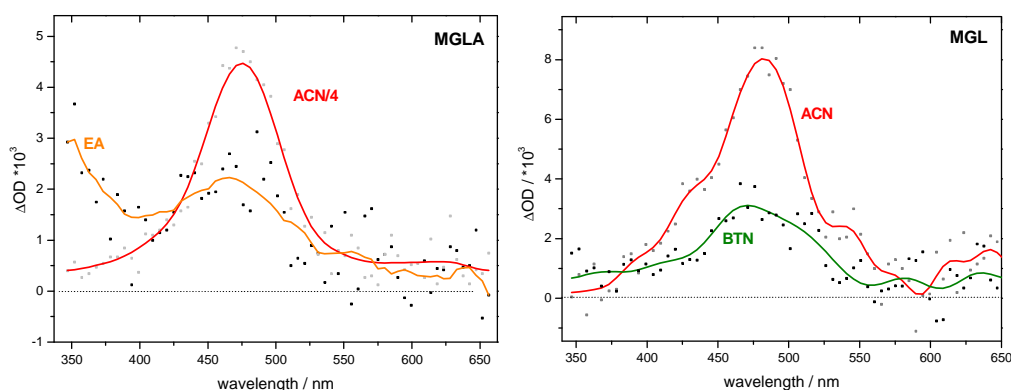


Fig. 4.8 Submicrosecond transient absorption spectra of MGLA (left) and MGL (right) recorded in different solvents with delay 60 ns.

The spectra recorded for both MGL and MGLA in polar solvents are in good agreement with the femtosecond transient absorption spectra and nanosecond transient absorption spectra recorded earlier, which also consist of single characteristic band with a maximum at about 476 nm, ascribed to the cation radical of dimethylaniline. Moreover, comparison of the recorded spectra with the literature triplet-triplet transient absorption spectrum of DMA,²⁰⁵ showing two peaks: more intense at 350 nm and a weaker one at 460 nm, rules out a contribution from the triplet state localized on DMA. On the other hand, for MGLA in EA, the transient absorption spectrum is very similar to the literature transient absorption spectrum of DMA, displaying two bands. In this case, it is very probable that the lowest triplet state for MGLA is the triplet state localized on DMA moiety. However, since the signal in EA is very weak, it is difficult to assign its origin unambiguously.

For a number of samples, transient absorption spectra were taken at microsecond delays (from 0.5 to 10 μ s). The shape and position of the 470 nm band in the microsecond spectra agree well with the nanosecond spectra (delay 60 ns), proving that only one triplet state with ion–pair structure is populated. The spectra are identical for degassed and non–degassed samples.

Due to a low quality of the decays recorded it can be only concluded that the decays of the measured triplet states are not monoexponential with lifetimes on the order of microseconds.

It is to be noted that the TA signals of MGL and MGLA in polar solvents are quite weak (i.e., Δ OD=0.008, 0.016 in ACN, at the maximum, respectively), and in solvents of low polarity just above the noise level thus impeding the interpretation. One of the possible explanations of that fact is that the triplet state is scarcely populated in these compounds, and that the direct radiationless recombination is the dominating deactivation process.

4.7 Fluorescence thermochromism and luminescence in glasses

4.7.1 Fluorescence thermochromism of MGL and MGLA

Fluorescence spectra of both MGL and MGLA are strongly temperature–dependent. The maxima of fluorescence spectra of MGL and MGLA in selected glass–forming solvents (MTHF, BTN, nPrOH) as a function of temperature are plotted in Fig. 4.9. For both molecules the dependencies of the positions of fluorescence maxima on temperature display similar trends in solvents used in the study (BTN, MTHF, nPrOH), showing strong thermochromism. The thermochromic shifts of MGL and MGLA extend over almost entire visible region, from deep blue (at low temperatures) to orange – red (in the supercooled liquid region). The same effect was observed for oxazine–4,²⁰⁶ and for molecules emitting CT fluorescence from the fluoroprobe family.²⁰⁷ Upon cooling, MGL and MGLA show the same behaviour (Fig. 4.9), and therefore, only MGLA will be described here in detail. All the conclusions drawn for MGLA hold also for its parent molecule (MGL).

At 293 K, MGLA in MTHF displays a greenish blue fluorescence with a maximum at 495 nm (19800 cm^{-1}), and the quantum yield of 0.051 (for MGL 0.055). Upon cooling from room temperature to 140 K the fluorescence band experiences a red shift (by 2100 cm^{-1}) and its intensity

decreases about two times. On further decrease of temperature, the red shift first levels off, and below 130 K changes to a dramatic blue shift (Fig. 4.9). This hypsochromic shift is accompanied by a huge gain in intensity. Such behaviour can be explained as follows. The solvent molecules reorient themselves around the emerging polar excited state. This mainly rotational relaxation stabilizes the CT state, but simultaneously destabilizes the Franck–Condon ground state reached upon fluorescence. Hence, the fluorescence from the probe molecule experiences a red shift, as long as the solvent reorientation is fast compared to the nanosecond lifetime of the excited state. The higher the dielectric constant of the medium, the greater the extent of stabilization. In MTHF, upon lowering the temperature the dielectric constant increases from 5.3^{210,208} at room temperature to 13 at 133 K, and hence the fluorescence is shifted towards longer wavelengths. Upon cooling into the supercooled liquid region (i.e., below the MTHF melting point, $T_m=135$ K) the dielectric relaxation time of MTHF increases rapidly from a few nanoseconds at 130 K to over 40 ns below 110 K²⁰⁷ and to tens of seconds when reaching the glass transition temperature ($T_g\sim 91$ K, $\tau = 31$ s), and the fluorescence does not any longer originate from a fully relaxed CT state, since the orientation polarization of the solvent is not fast enough compared to the nanosecond fluorescence lifetime.

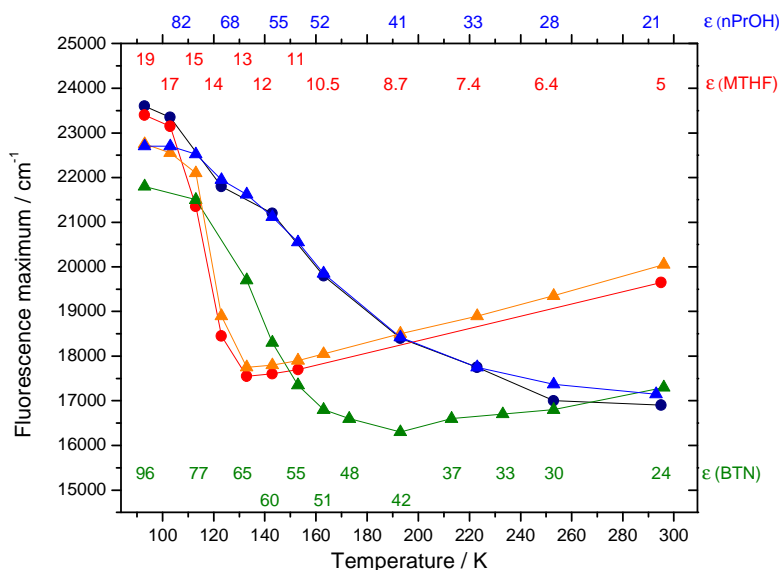


Fig. 4.9 Temperature–dependent positions of fluorescence maxima for MGL (triangles) and MGLA (circles) in MTHF (red and orange), nPrOH (blue and navy) and BTN (green). Dielectric constants for various temperatures are presented in the same colour coding: BTN,²⁰⁹ MTHF,²¹⁰ nPrOH²¹¹.

The changes in fluorescence intensity can be mainly attributed to the changes in the polarity of the surrounding medium upon cooling. The quantum yield of fluorescence of both MGL and MGLA decreases with increasing dielectric constant of the solvent, according to the energy gap law. In the supercooled liquid region, however, starting below 130 K, the intensity is recovered, most probably due to inhibition of radiationless processes by the rigid surrounding.

The thermochromic shift of the fluorescence band can be described with the Lippert–Mataga approach modified for fluorescence maxima in the temperature region where the lifetime of the emitting state is much longer than the solvent orientational relaxation times. The variation of the refractive index, n , and the dielectric constant, ϵ , in line with decreasing temperature results not only from increasing solvent density and viscosity, but also from increased orientation of the solvent molecules mostly due to inhibition of thermal motions.²¹²

To make use of the Lippert–Mataga plot for thermochromic shifts of MGLA and MGL fluorescence spectra, the appropriate values of n ²¹³ and ϵ ²¹⁰ at appropriate temperatures were taken from the literature, the effective radius of the Onsager cavity was set to $a_0 = 5.8 \text{ \AA}$ (as in the solvatochromic method for different solvents in Section 4.4 for both MGL and MGLA), and it was assumed that $|\bar{\mu}_e| \gg |\bar{\mu}_g|$. Fig. 4.10 shows the comparison of Lippert–Mataga plots obtained via thermochromic and solvatochromic shift method for MGLA and MGL.

	solvatochromic method			thermochromic method		
	slope [eV]	intercept [eV]	μ_e [D]	slope [eV]	intercept [eV]	μ_e [D]
MGLA	-3.95	3.62	24.8	-3.98	3.49	24.9
MGL	-4.00	3.61	25.0	-4.43	3.67	26.3

Tab. 4.4 Fitting parameters obtained from the solvatochromic and thermochromic method. Slope: $(-2\bar{\mu}_e(\bar{\mu}_e - \bar{\mu}_g)/a_0^3)$; Intercept: $(hc\bar{\nu}_{flu}^{vac})$; for all fits $R^2 > 0.99$.

The parameters of the fits from the solvatochromic and thermochromic methods are in good agreement. The calculated values of the excited state dipole moments are also comparable, as are the slopes, and the extracted fluorescence maxima in vacuum differ from each other by 0.13 eV and 0.06 eV for MGLA and MGL, respectively. Except for this minor

difference, the discussion above confirms the correspondence of the solvatochromic and thermochromic method in determining the excited state dipole moment.

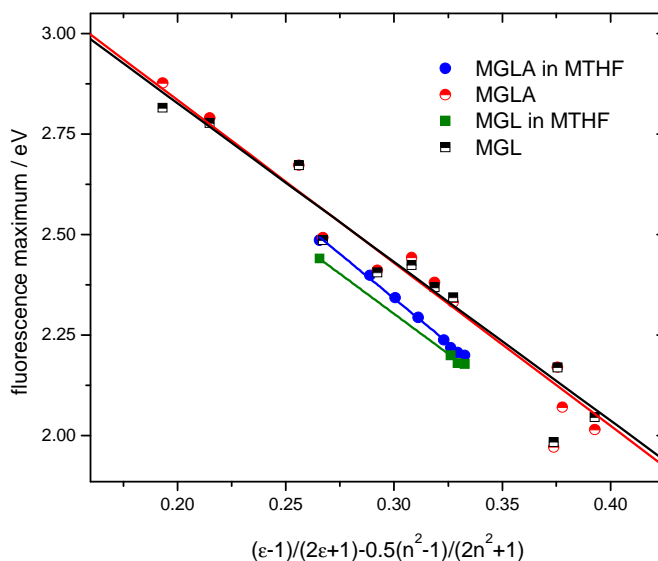


Fig 4.10 Thermochromic (for MTHF) and solvatochromic plots of fluorescence maxima for MGLA and MGLA. For solvatochromic data for MGLA see Tab. 4.3, for MGL ref. 76. Parameters obtained from the fits are summarized in Tab. 4.4.

Fig 4.10 presents also thermochromic data for MGL in BTN published earlier.⁷⁶ Generally, MGL in BTN behaves in the same way as in MTHF: upon cooling down to about 170 K a red shift is observed, and further decrease of temperature results in a huge blue shift of more than 5000 cm^{-1} accompanied by a dramatic increase of fluorescence intensity when entering the region of supercooled liquid (i.e., below 161 K). The thermochromism of MGL in BTN can be explained along the same lines as for MTHF, namely, that the red shift is due to a better stabilization (lowering of energy) of the emitting state in the solvation process (caused by the increase of the dielectric constant), and the blue shift results from emission from a not fully relaxed excited state. The relaxation in the temperature range corresponding to the supercooled liquid is not completed within the lifetime of the excited state, as the dielectric relaxation times increase with lowering temperature.

For MGLA and MGL in nPrOH, the dependence of the fluorescence maximum position on the temperature is different than that for MTHF or

BTN,⁷⁶ i.e., no red shift is observed. Lowering the temperature results in a continuous blue shift of the emission maximum accompanied by a strong increase of the fluorescence quantum yield. The reason for such behaviour is the short lifetime of both MGL and MGLA in nPrOH (estimated to be below 100 ps). Cooling nPrOH results in an increase of the dielectric constant, but more importantly, in an elongation of the characteristic solvation time (26 ps and $\epsilon=20.3$ at 295K;⁸⁵ 31.8 ms and $\epsilon=75$ at 113K,²¹⁴ respectively). The lifetime of the emitting state becomes shorter than the relaxation time of the solvent already at 253 K (Fig. 4.9), and consequently the emission does not originate from the fully relaxed CT state.

4.7.2 Charge transfer and local triplet states – luminescence in glasses

Phosphorescence and fluorescence of MGL in BTN at low temperatures was tentatively ascribed by Karpiuk⁷⁶ to come from states having CT character. In this section luminescence spectra of MGL in other solvents are presented and interpreted. Moreover, the investigations on temperature dependent fluorescence and luminescence in glasses were extended to include MGLA.

Total luminescence and phosphorescence emitted by samples at low temperatures were the two spectral observables available with the setup used to record the spectra. A good separation of fluorescence spectrum from the total luminescence was very difficult using the mechanical chopper system, since the energies of the singlet and triplet state of the investigated molecules were almost degenerate.

The luminescence spectra of MGLA and MGL were recorded in rigid glasses of BTN, MTHF and nPrOH at 93 and 77 K. The long-lived phosphorescence was mechanically separated from the total luminescence. The phosphorescence and total luminescence maxima of MGLA and MGL in different matrices are summarized in Tab. 4.5. The total luminescence spectra recorded at 93 and 77 K do coincide, the phosphorescence spectra, however, display a temperature effect, a decrease of temperature results in a shift of the phosphorescence maximum towards higher energies (by approximately 200 cm^{-1} for MGLA). Irrespectively of the medium, MGLA phosphorescence is always blue shifted with respect to the total luminescence (at 77 K: 400 cm^{-1} (BTN) and 250 cm^{-1} (MTHF)). Also for MGL, the phosphorescence spectra recorded in nPrOH and BTN at 77 K and in MTHF at 93 K are shifted towards higher wavelengths by 600, 400 and 400 cm^{-1} , respectively (Tab. 4.5).

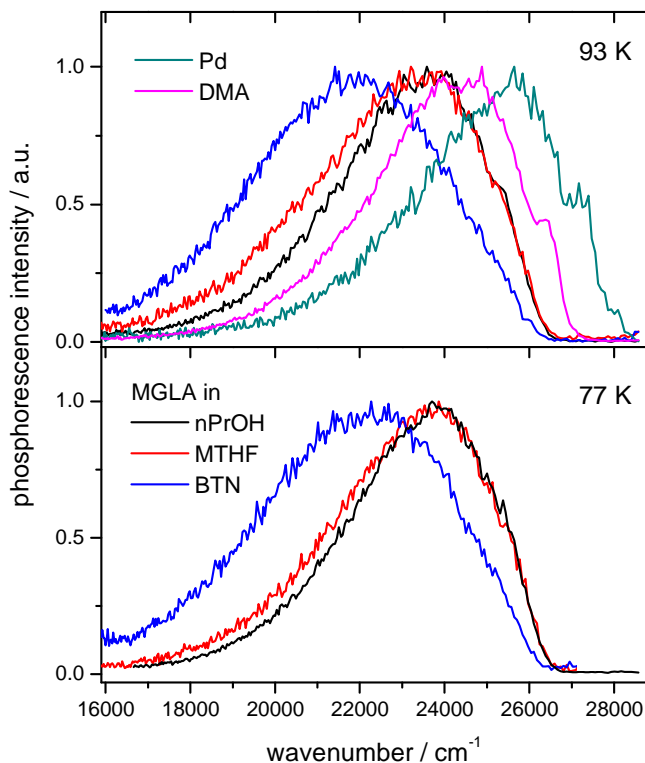


Fig. 4.11 Phosphorescence spectra of MGLA recorded at 93 and 77 K in MTHF, BTN and nPrOH, presented in comparison with the phosphorescence spectra of Pd (green) and DMA (magenta).

	T		BTN	MTHF	nPrOH
MGLA	77 K	total	21800	23400	23600*
		pho	22200	23660	23800
	93 K	total	21850	23400	23600
		pho	22000	23420	23620
MGL	77 K	total	21900	—	22650
		pho	22300	—	23380
	93 K	total	21800*	22220	22800
		pho	21250	22600	22760

Tab. 4.5 Comparison of phosphorescence (pho) and total luminescence (total) maxima of MGLA and MGL recorded in MTHF, BTN and nPrOH at 93 and 77 K. * denotes fluorescence maximum.

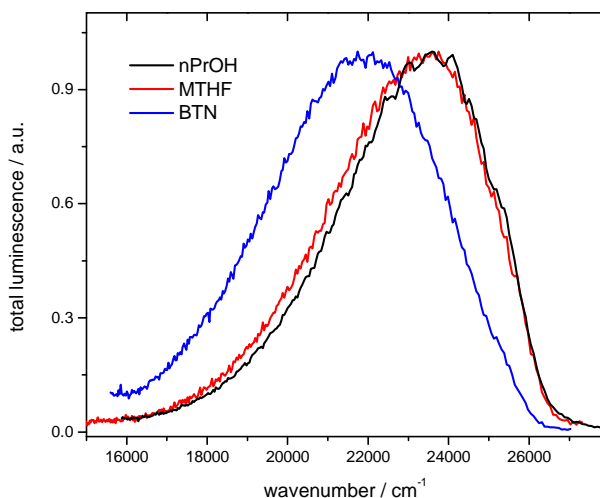


Fig. 4.12 Total luminescence spectra of MGLA recorded at 93 K in MTHF, BTN and nPrOH.

The phosphorescence spectra of MGLA in nPrOH and MTHF are very similar regarding both maximum position and shape, though the spectrum in MTHF is broadened on the red edge by 650 cm^{-1} . Both spectra resemble the phosphorescence spectrum of DMA (maximum at 24500 cm^{-1} in BTN) reproducing also an additional small peak noticeable in the latter at 26400 cm^{-1} . Based on this analysis it can be concluded that the emitting MGLA triplet state in nPrOH and MTHF is localized on the DMA subunit (Pd phosphorescence is emitted at higher energies, with a maximum at 25600 cm^{-1} in BTN). In case of MGLA in MTHF, however, a small contribution from the ^3CT triplet state cannot be excluded. The phosphorescence spectra in BTN differ significantly by shape and position of the maximum from the ones recorded in MTHF and nPrOH. The maximum is red-shifted (by 1460 cm^{-1} as compared to MTHF at 77 K), the band is broad and structureless ($\text{FWHM} = 5000\text{ cm}^{-1}$). This long-lived luminescence cannot come from the local triplet states as they are higher in energy, therefore its origin is most probably the ^3CT triplet state, with energy almost degenerate with that of the singlet CT state.

Phosphorescence spectra of MGL recorded at 93 K in nPrOH and MTHF are similar having the same shape and width. As for MGLA, the phosphorescence spectrum recorded in MTHF is slightly (160 cm^{-1}) shifted towards longer wavelengths. The phosphorescence spectrum in BTN reproduces the shape of the spectrum in MTHF, the maximum is, however,

red shifted by 1350 cm^{-1} . The measurements performed at 77 K reproduce the spectra recorded at 93 K, the phosphorescence maxima are blue shifted by 1050 and 620 cm^{-1} in nPrOH and BTN, respectively (Tab. 4.5). Based on the available data it is not possible to unambiguously assign the source of phosphorescence of MGL in MTHF and nPrOH, further studies are needed.

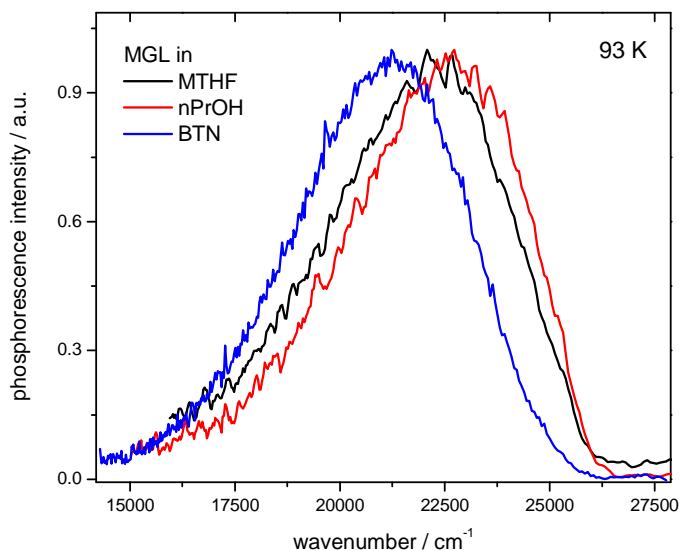


Fig. 4.13 Phosphorescence spectra of MGL recorded in MTHF, BTN and nPrOH at 93 K.

4.8 Discussion

MGLA is an analogue of MGL with a dyad D–A structure, i.e., it is composed of an electron accepting moiety – Pd, and an electron donating moiety – DMA. Reduced number of DMA units (by one) in MGLA does not have significant impact on the photophysics of the resulting D–A system which closely resembles MGL.

The structures of MGLA and MGL in the ground states are similar, and the corresponding bond angles and lengths are virtually identical in both molecules. All the C–C bonds of the central carbon in MGLA and MGL are comparable in length and have saturated character indicating that the delocalization of electrons from aromatic rings does not extend to the central carbon atom. Nevertheless, the results described in this thesis indicate that the widespread perception of non-interacting electronic subunits separated

by a sp^3 carbon atom must be revised. The ground state interaction between Pd and DMA gives rise to a weak, but noticeable CT absorption band, energetically overlapping the S_0 – S_1 transition localized on the DMA group. The S_1 state of MGLA reached in absorption is localized on the DMA moiety, and the CT state is degenerate with or slightly above the S_1 state. The CT absorption in MGLA and MGL results from a through-space interaction involving spacial overlap of molecular orbitals of DMA and the lactonic ring, however, since these subunits are approximately orthogonal, the contribution from the CT absorption is rather insignificant.

The absence of any fluorescence (even traces) from the locally excited DMA chromophore in MGLA (and in MGL or PP as well)⁷⁶ in non polar solvents results from extremely fast ET process and high yield of conversion of the locally excited state to the CT state. Very high rate of the primary ET process in MGLA proves that it occurs from a vibronically non-equilibrated level, and is faster than vibrational relaxation and orientational (diffusive) solvation. This indicates that only the effects of ultrafast inertial solvation dynamics may play a role as external factors affecting the CS kinetics. Consequently, solvent orientational relaxation does not pose a barrier for the primary ET, and the driving force for the process in MGLA is provided by a high-frequency vibrational mode coupled to the ET, in line with conclusions drawn for MGL.

The energetics of the excited state processes is schematically depicted in Fig. 4.15. High ET rate for MGLA can be predicted from the free energy change in the primary ET process, ΔG_{ET}^0 , estimated from the Weller equation (here in simplified notation as compared to Section 2, Eq. 2.2):²¹

$$\Delta G_{ET}^0 = -E_{00} + E(D^+/D^0) - E(A^0/A^-) - E_{ip} \quad \text{Eq. 4.4}$$

where E_{00} is the energy difference between the S_0 and S_1 states, $E(D^+/D^0)$ is the oxidation potential of the electron donor, $E(A^0/A^-)$ is the reduction potential of the electron acceptor, and E_{ip} is the ion pair stabilisation energy, estimated from equation $E_{ip} = e^2/\epsilon_s d_{ip}$, where e is the electron charge, ϵ_s is the dielectric constant of the solvent, and d_{ip} is the distance between the donor (DMA) and the acceptor (Pd) moieties. In view of a close structural analogy, the above quantities were assumed to be the same as those for MGL: $d_{ip} = 4.3 \text{ \AA}$, $E(D^+/D^0) = 0.79 \text{ eV}$ for DMA, $E(A^0/A^-) = -2.22 \text{ eV}$ for Pd, and $E_{00} = 4.1 \text{ eV}$, yielding $\Delta G_{ET}^0 = -1.19 \text{ eV}$ for ACN. The Sumi–Marcus two-dimensional ET model²¹⁵ relates such ΔG_{ET}^0 value to a very fast ET reaction rate ($k_{ET} \sim 7 \times 10^{12} \text{ s}^{-1}$)²¹⁶ and the highly exothermic ET process is expected to occur in a low-energy barrier or barrierless regime (ΔG_{ET}^0

close or equal to reorganization energy). Very short times of cation radical formation upon photoexcitation of MGL to S_2 and PP to the S_1 state support these estimates of k_{ET} for MGLA and in view of the analogies with MGL allows to suppose that the structural simplification of LTAM molecules to their analogues with one donor subunit does not affect the ultrafast electronic communication channel in the molecule.

The CT state deactivates via radiative and radiationless back ET. Low fluorescence transition dipole moments of the CT state point to a low probability and forbidden character of the radiative transition from the CT state, hence a substantial part of excited MGLA molecules decays via an efficient nonradiative deactivation channel. Strong dependence of k_{nr} on solvent polarity (Fig. 4.14), with k_r remaining relatively constant (Tab. 4.3), reflects increasing availability of nonradiative deactivation pathways in highly polar and in non polar solvents. Conformational changes, such as high amplitude motions including possible twisting of amino groups or entire DMA units can be ruled out as no substantial viscosity effect on the non-radiative decay has been found (Tab. 4.3).

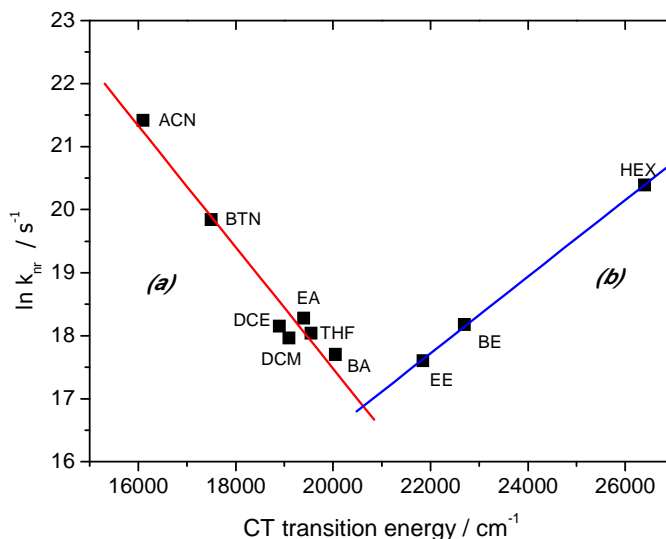


Fig. 4.14 Logarithmic plot of nonradiative rate constants ($\ln k_{nr}$) as a function of the CT transition energy (represented by fluorescence maximum) at room temperature in aprotic solvents. The straight lines represent linear fits for (a) solvents with $\nu_{fl} \leq 20500 \text{ cm}^{-1}$ (BA and more polar solvents) and (b) for solvents with $\nu_{fl} \geq 20050 \text{ cm}^{-1}$ (EE and less polar solvents), respectively. Correlation coefficients: $R^2 = 0.98$ and 0.99 for (a) and (b) straight lines, respectively.

The dependence of k_{nr} on solvent polarity points to different nonradiative deactivation ways of the CT state in MGLA in solvents with different dielectric constants. Possible deactivation paths are intersystem crossing, photodissociation of the C–O bond and direct radiationless charge recombination between DMA^+ and Pd^- . In polar solvents, the deactivation cannot occur via transition to a local triplet state, as triplet states of both DMA and Pd, are higher in energy. Moreover, transient absorption measurements and phosphorescence spectra indicate that the CT character is still maintained in the triplet state, hence the ^3CT is the lowest triplet state in polar solvents. Weak TA signals suggest low efficiency of the ISC process. Additionally, a polarity-driven ISC to the ^3CT state cannot be responsible for enhanced radiationless deactivation in highly polar solvents as the ^3CT state in MGLA is nearly degenerate with singlet CT and the kinetics of the $^1\text{CT} \rightarrow ^3\text{CT}$ ISC transition (spin inversion) is controlled mainly by spin-orbit coupling within the ion pair, which does not depend on solvent polarity or energy of the singlet CT state. On the other hand, ISC to the triplet state seems the most probable mechanism of radiationless deactivation operative in non polar solvents. The slope of the right-side straight line in Fig. 4.14 is indicative for the activation energy of the ISC transition to the local T_1 state. Also TA spectra suggest that already in low polar EA the local triplet state of DMA is populated rather than the ^3CT state. Another channel of enhanced nonradiative process in polar solvents may be the dissociation of the C–O bond in the CT state, similar to C–CN bond photodissociation in the S_1 state in MGCN⁴⁶ or adiabatic C–O bond dissociation in rhodamine lactones.^{121,122,123} The photodissociation in rhodamine lactones in aprotic solvents is independent of solvent polarity and proceeds from a vibrationally non-relaxed excited singlet state, whereas the photodissociation in MGCN proceeds from a vibrationally relaxed S_1 state and shows a threshold dependence on solvent polarity.²¹⁷ These two arguments allow to rule out the dissociation of the C–O bond as the mechanism of polarity driven nonradiative deactivation in MGLA in polar aprotic environment. The photodissociation may be, however, operative in protic solvents, in particular in view on the hydrogen bonding induced lactone ring opening observed for phthalide²⁰⁰ and the rapid deactivation of MGLA in alcohols.

Direct radiationless charge recombination between DMA^+ and Pd^- remains the most probable mechanism of the enhanced nonradiative deactivation of the CT state in MGLA. The intrinsic reason for the effect is the dependence of k_{nr} on the CT energy (strongly affected by solvent polarity). The decreasing energy gap between the excited CT state and the ground state with growing solvent polarity induces increasing efficiency of

the direct CR process. Similar effects were observed in excited intramolecular CT state deactivation in donor–acceptor carbazole derivatives²³² and for aryl derivatives of aromatic amines.^{218,219} The polarity driven enhancement of k_{nr} is based on the energy gap law^{76,220} relating the rate of the nonradiative decay of the lowest excited state in a molecule to the energy separation from the ground state. Since the Franck–Condon factor increases exponentially with decreasing energy difference between the excited and the ground states, a lower electronic transition energy leads to an increasing rate of radiationless decay²²¹ and should result in a linear correlation of $\ln k_{nr}$ with the transition energy if the Franck–Condon factor is important for determining the nonradiative decay.

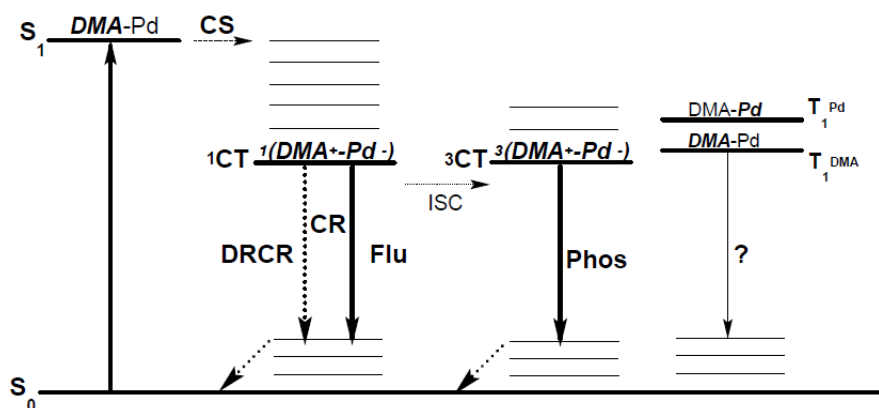


Fig. 4.15 Diagram of energy levels for MGLA together with excited singlet and triplet states of MGLA structural components. Abbreviations: CS, charge separation; CR, charge recombination; DRCR, direct radiationless charge recombination; ISC, intersystem crossing; DMA, dimethylaniline; Pd, phthalide; Flu, fluorescence; Phos, phosphorescence.

Both MGLA and MGL display pronounced thermochromism. Strong dependence of the excited state deactivation on temperature in liquid solutions comes mostly from the temperature dependence of the polarity of the medium. In rigid solution, especially below glass transition, due to restricted solute conformational changes and more importantly, orientational movements of solvent molecules, the nonradiative process becomes heavily dependent on dielectric relaxation of the supercooled environment. In supercooled and in glassy solvents, where the dielectric relaxation time exceeds the fluorescence lifetime, the solute molecule is no longer able to be energetically stabilised via interactions with the surrounding solvent molecules. Thus, fluorescence is emitted from a non-equilibrated level.

Rigidochromic MGL and MGLA are good probes for studying reorientation polarization in rigid and semirigid supercooled media.

The nature of triplet states populated at low temperatures in MGLA and in MGL depends on the surrounding medium. In BTN the origin of phosphorescence is the ^3CT state in both molecules. In MGLA in MTHF and nPrOH at low temperatures the local triplet state of DMA is most probably the source of phosphorescence. This assignment was done based on the analysis of the shape and position of the respective spectra. In the case of MGL in MTHF and nPrOH, the available data do not allow to assign the long lived emission to a specific triplet state, in this case either the ^3CT or the triplet state localized on the DMA subunit. Further studies are needed to assign – beyond doubt – the origin of MGL phosphorescence in MTHF and nPrOH. At this point it is important to note that because of near-degeneracy of the lowest singlet and triplet CT states, MGLA and MGL are unique candidates for studies of CT singlet–triplet coupling and interaction, as well as for exploring the (so far poorly investigated) area of CT phosphorescence.

So, the primary charge separation and the back electron transfer in a dyad analogue of MGL occur in close analogy to MGL. The photophysics at room temperature and the deactivation of the CT state are in both molecules virtually identical. These similarities prove that the simplification of the D–D–A triad structure to D–A dyad structure preserves all structural and electronic properties relevant for the ET process. Hence, it can be deduced that only one electron donating group in MGL is actively involved in the charge separation and recombination.

Chapter 5

Relaxation to the CT state as a general deactivation route for D–A–D and D–A structures

MGL, PP and MGLA are known to undergo ultrafast excited state ET. Derivatives and analogues of these molecules (Fig. 5.1) were investigated in order to answer the question if the relaxation to the CT state is a general property of LTAM structures based on a sp^3 carbon atom. Absorption and fluorescence studies confirm that on the ground state level, D and A subunits show only weak interactions, however in the excited state a strong electronic coupling is present. As a result, ET takes place after excitation to the S_1 state localized on the D moiety. The presence of the CT fluorescence in all molecules studied in this work allows to conclude, that the charge separation reaction is a general property of LTAM molecules.

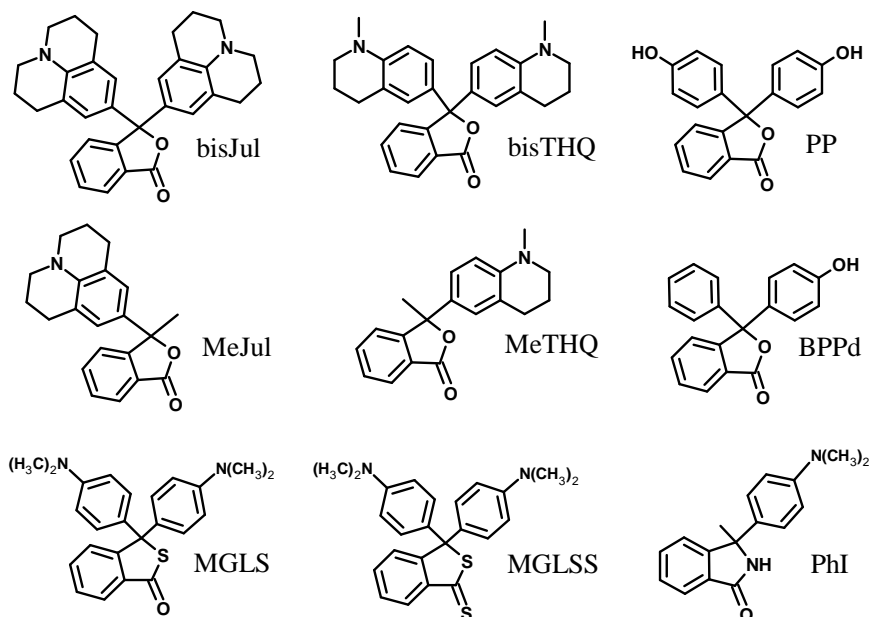


Fig. 5.1 Structures of LTAM molecules investigated in this Chapter.

5.1 Absorption in aprotic solvents

Fig. 5.2 present electronic absorption spectra of all MGL derivatives/analogues in ACN. The spectra of all compounds have similar shape, typical for aromatic and extended amines,²²² similarly as the spectrum of MGL, except for MGLSS and PhI, where electronic transitions localized on the A subunit become more visible. The absorption spectra consist essentially of two bands, with the lower energy one seen as a shoulder. As it is the case for MGL and MGLA, where the absorption spectrum of the dyad is somewhat shifted towards lower energies, also julolidine and THQ derivatives follow this trend (Tab. 5.1).

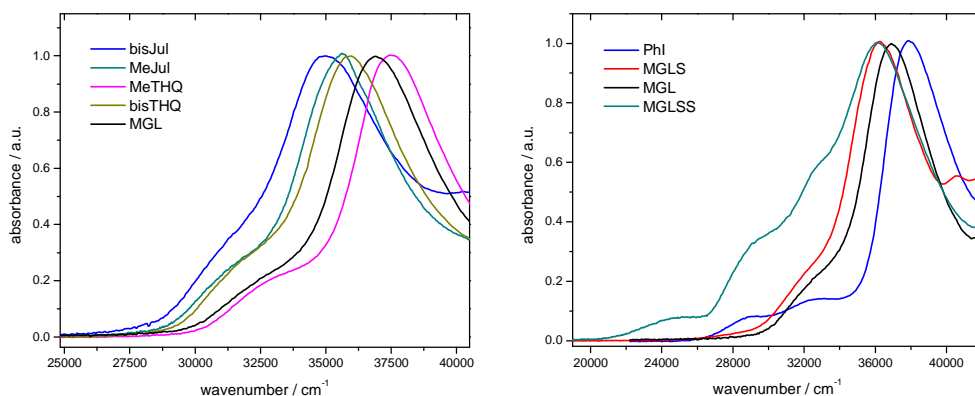


Fig. 5.2 Left: absorption spectra of bisJul, MeJul, bisTHQ, MeTHQ and MGL in ACN at room temperature. Right: absorption spectra of PhI, MGLS, MGLSS and MGL in ACN at room temperature.

When absorption spectra in pairs of structural analogues (D–D–A and D–A type) are compared, a red shift of the spectrum of the D–bisubstituted molecules can be observed (Tab. 5.1, the maxima of the first band are given approximately due to a strong overlap with the second absorption band). This is especially pronounced in the case of bisTHQ. The reason for such a behaviour is unclear and needs further study. A possible explanation could be a weak through space interaction between the two π -electron systems lowering the energy of the system.

The absorption spectrum of MGLS is very similar to the spectrum of MGL, it is, however, red shifted by approx. 900 cm^{-1} and displays an additional band that is seen as a “tail” on the red edge of the spectrum. A

shift of the spectrum towards lower frequencies upon introducing sulphur into the lactone ring is typical and was observed for a number of compounds, i.e., sulphur derivatives of CVL and LRB.^{223,224,225} When the carbonyl oxygen atom is replaced with sulphur, the absorption bands of the new compound shift further towards the red (for LRB derivatives by another 300 cm^{-1}). Additionally, a new weak band arises (for bisulphuric derivative of LRB at 24100 cm^{-1} and with absorption coefficient of 1600 $\text{M}^{-1}\text{cm}^{-1}$)²²⁵ which can be ascribed to come from absorption transitions localized on dithiophthalide. Moreover, a clear increase of the absorption coefficient of the band at 30850 cm^{-1} is noticeable for the dithio-derivative. This observation strongly suggests that the second transition of dithiophthalide overlaps with the absorption band of LRB (31650 cm^{-1})²²⁶ and the shape of the absorption spectrum of MGLSS strongly supports the conclusion. For MGLSS, two additional bands appear (with respect to MGL), at 24900 and 29500 cm^{-1} , which can be assigned to transitions localized on dithiophthalide.

compound	max. I [cm^{-1}]	Δ_{I} [cm^{-1}]	max. II [cm^{-1}]	Δ_{II} [cm^{-1}]
MGLA	~32300	100	37150	250
MGL	~32400		36900	
MeJul	~31800	1000	35600	600
bisJul	~30800		35000	
Jul	32200		37400	
MeTHQ	~33100	1350	37500	1600
bisTHQ	~31750		35900	
THQ	33100		40300	

Tab. 5.1 Absorption data for all compounds in ACN; max. I and max. II are absorption maxima, Δ_{I} and Δ_{II} are the differences between respective absorption maxima in each pair of structural analogues.

The absorption spectrum of Phi differs from that of MGL by the presence of an additional band at 29000 cm^{-1} . The origin of this band lies most probably in the presence of phthalimidine in the molecule and not in impurity traces. The other two bands coming from transitions localized on DMA are shifted towards shorter wavelengths with respect to MGL (32900 and 37900 cm^{-1}). No noticeable solvatochromic effect on the absorption spectrum was observed.

The absorption spectra of BPPd and PP are presented separately since

they appear in a different energy region. PP is composed of phthalide and two orthogonally arranged phenol moieties (D–D–A type structure). The photophysics of PP was studied earlier in our laboratory with steady-state⁸⁰ and in collaboration with Prof. E. Riedle's group from LMU from Munich with time-resolved spectroscopies.¹³ The author of this thesis synthesized a PP analogue of the D–A type, 3-phenyl-3-(4-hydroxyphenyl)-phthalide (BPPd) during her master thesis.

The absorption spectra of BPPd and PP together with their structural subunits as a function of molar absorption coefficient are presented in Fig. 5.3. For both, BPPd and PP, no absorption in the visible region could be observed, proving the absence of coloured ionic forms. The absorption spectrum of BPPd consists basically of two bands, one with vibronic structure at 36250 cm^{-1} , and another with the maximum at 44100 cm^{-1} . On going from HEX to ACN no significant solvatochromic effect on the absorption spectrum was observed (100 cm^{-1}).

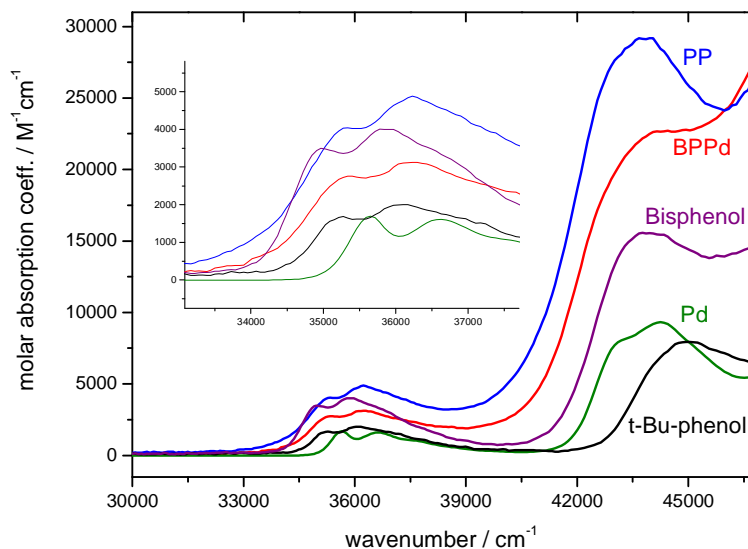


Fig. 5.3 Absorption spectra of PP, BPPd and their subunits, Pd, bisphenol and 4-*t*-butylphenol.

As seen from comparison in Fig. 5.3, the first absorption band comprises of at least two electronic transitions localized on Pd and phenol moieties. Comparison of the molar absorption coefficients of BPPd and PP with respective subunits allows for concluding that for both molecules the absorption spectra are superpositions of transitions localized on D and A

units. This fact leads to the conclusion that ground-state interactions between structural components are negligibly small, and that direct optical charge transfer transitions are absent. The ratio of the molar absorption coefficients of BPPd and PP in the low energy region ranges from 0.4 to 0.7, proving spectral additivity of subunits. Deviations from 0.5 can result either from additional absorption transitions localized on the phenyl ring of BPPd or, as it is the case for MGLA, from the presence of a CT absorption band.

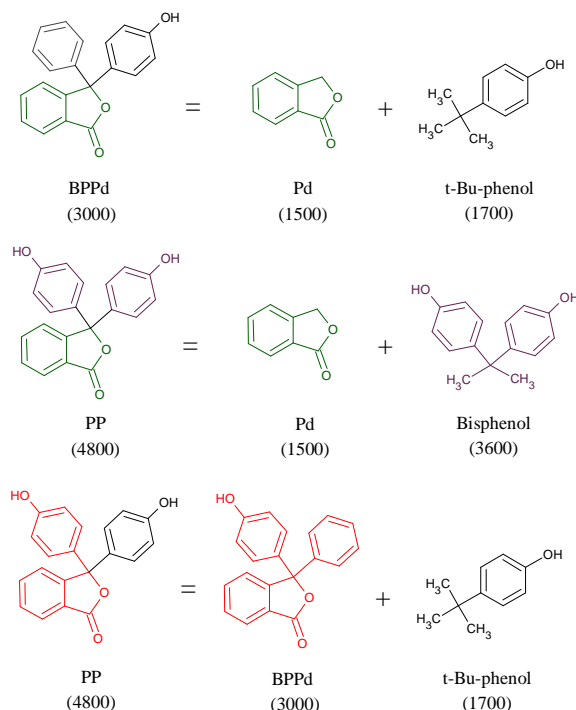


Fig. 5.4 A schematic presentation of chromophore additivity in BPPd and PP in the low energy region. Numbers in parentheses are absorption coefficients $\epsilon(\nu)$ [$M^{-1}cm^{-1}$] at 36000 cm^{-1} .

5.2 Fluorescence at room temperature

Fig. 5.5 presents fluorescence spectra of MeTHQ and bisTHQ compared with those of MGL in solvents of different polarity. MeTHQ displays a single, broad and structureless fluorescence band that is characterized by a huge Stokes shift (for CHEX around 7000 cm^{-1}) and a large solvatochromic effect (9800 cm^{-1} between ACN and CHEX). As in

MGLA, the fluorescence spectrum of both MeTHQ and bisTHQ in ACN recorded at room temperature shows a very weak and relatively broad band in the region $23000 - 30000 \text{ cm}^{-1}$ with an intensity about 100 times lower than in the maximum at 15800 cm^{-1} . This band results most probably from impurity traces in ACN and was not observed for MeTHQ and bisTHQ in EA or CHEX. It is important to note, that the fluorescence quantum yield in ACN for both compounds is very low and the recorded spectra are of poor quality. The additional band in ACN may also be an artifact due to a very low fluorescence signal.

The emission spectra of julolidine (MeJul, bisJul) and phthalimidine (PhI) derivatives are not presented here due to problems with purification of these materials.

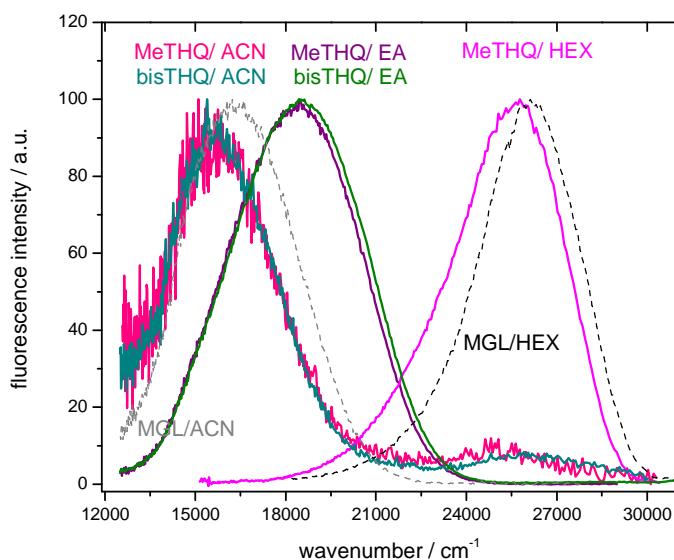


Fig. 5.5 Comparison of fluorescence spectra of bisTHQ, MeTHQ and MGL in ACN, EA and HEX.

The recorded emission spectra of MeTHQ overlap almost perfectly with those of bisTHQ. The emissions of MeTHQ and bisTHQ cannot be ascribed to come from the THQ moiety due to a huge difference in maxima and large half-widths of the bands: in nonpolar CHEX the emission of MeTHQ is strongly red-shifted compared to that of insulated tetrahydroquinoline (maxima in CHEX at 25800 cm^{-1} and 30300 cm^{-1} , respectively).²²² Moreover, the emission of MeTHQ is similar to that of MGL, in terms of shape and spectral width of the band, the fluorescence of

MeTHQ is, however, shifted towards lower energies. This observation, together with the strong solvatochromic effect imply that the origin of the emission is another lower lying excited state with a large dipole moment. Similarly as for MGL and MGLA, the fluorescence comes from a CT state with a structure of an intramolecular radical ion pair, with the positive charge on THQ and negative on Pd.

Based on the available data and similarity to MGLA, a rough estimate of the excited state dipole moment of MeTHQ was made using the solvatochromic shift method based on the reaction field model developed by Onsager (Section 4.4). Under the assumption that $|\bar{\mu}_e| \gg |\bar{\mu}_g|$ and with the effective spherical radius of MeTHQ equal to 6.2 Å (the value estimated from molecular dimensions of the molecule calculated by molecular mechanics), the equation (Eq. 4.3) yields μ_e approximately 28 D. The value is of the same order of magnitude as the excited state dipole moment of MGLA (24.8 D) and indicates full electron transfer from the THQ moiety to phthalide.

Almost identical spectra of MeTHQ and bisTHQ imply that the emitting state in both molecules has similar electronic structure. This in turn supports the conclusions drawn for the analogue pair MGL–MGLA that the presence of a second D moiety in an LTAM molecule has no substantial impact and that only one electron donating subunit is involved in the ET process.

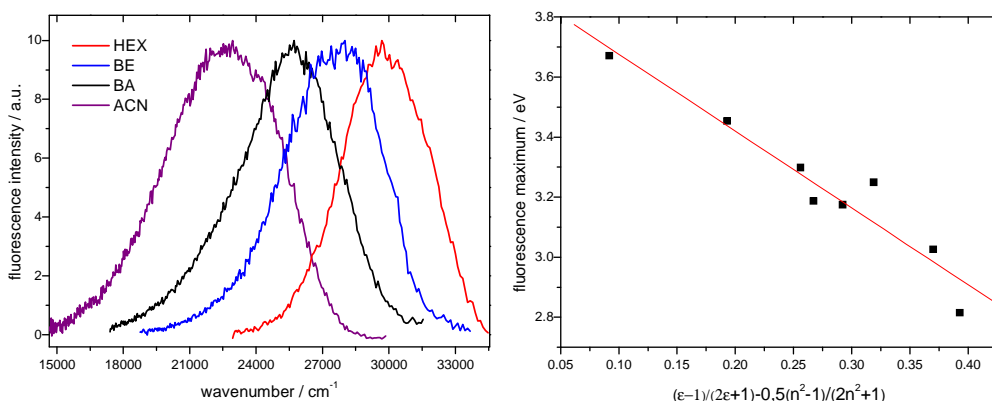


Fig. 5.6 Left: Fluorescence spectra of BPPd recorded at room temperature in ACN, BA, BE and HEX. Right: Plot of BPPd fluorescence maxima as a function of solvent polarity. Plot parameters: slope -2.56 eV, intercept 3.93 eV; correlation coefficient $R=0.97$.

The fluorescence spectrum of BPPd in all solvents consists of one broad band with FWHM from 4150 cm^{-1} in HEX to 6200 cm^{-1} in ACN (Fig. 5.6, left). It is characterized by a strong solvatochromic effect (7000 cm^{-1} on going from HEX to ACN) and a large Stokes shift (6650 cm^{-1} in HEX, 13650 cm^{-1} in ACN). The fluorescence displayed by BPPd cannot be ascribed to come from a local chromophore, since phthalide does not emit at room temperature and phenol as well as toluene fluoresce at higher energies (phenol: 34300 cm^{-1} in CHEX, toluene: 35700 cm^{-1}).²²⁷ Based on these facts it can be concluded that the fluorescence of BPPd comes from a highly polar state with CT character, as it is the case for PP and MGL.¹³ Similarly as for other molecules described in this Chapter, it can be interpreted as a radiative recombination process of the radical ion pair formed as a result of ultrafast electron transfer.

The solvatochromic shift method was employed to determine the excited state dipole moment of BPPd. Assuming the effective radius of the Onsager cavity equal to 6 \AA , the excited state dipole moment of BPPd amounts to 21 D, as it is the case for PP (Fig. 5.6, right).

Fluorescence spectra of sulphur derivatives of MGL – MGLS and MGLSS are presented in Fig. 5.7 and 5.8. Both molecules display single fluorescence bands with half-widths of about 4000 cm^{-1} that are characterized by moderate Stokes shifts (for MGLSS in ACN: 8100 cm^{-1} , for MGLS the Stokes shift could not be determined due to the shape of the absorption spectrum) and rather insignificant solvatochromic effect (for MGLSS between ACN and CHEX: 2000 cm^{-1} , for MGLS between ACN and EA: 1600 cm^{-1}). Moreover, the fluorescence of MGLS is weak, and in ACN a small band at about 30600 cm^{-1} can be observed. It can be ascribed to either ACN or impurity traces, since the position of the absorption spectrum excludes its origin in the MGLS molecule.

The studies completed within this thesis did not allow for unambiguous identification of the origin of fluorescence in sulphur derivatives. Small solvatochromic effect and moderate Stokes shifts preliminary exclude any highly polar CT state as the source of emission. A state localized on thio- or dithiophthalide, respectively, is a good candidate for the source of the observed fluorescence, no data on fluorescence of thiophthalide is, however, available in the literature. 3,3-dimethylthiophthalide was synthesised by Dr. Jacek Nowacki, but the obtained product was not measured yet due to problems with obtaining pure crystals.

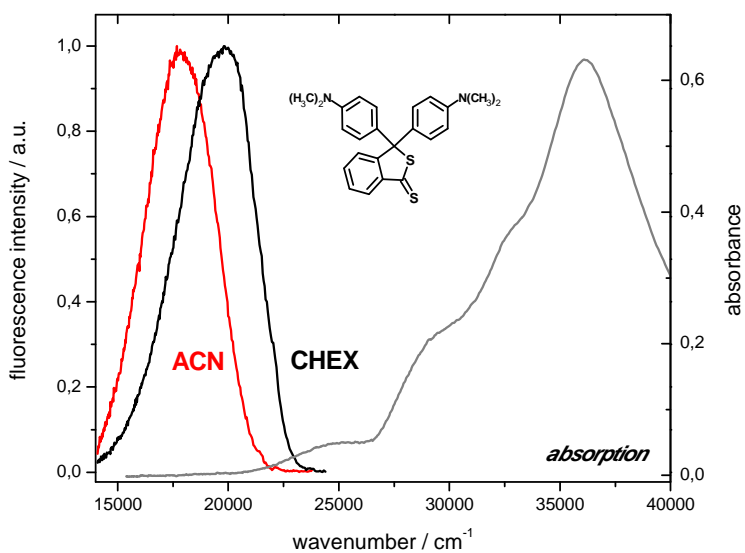


Fig.5.7 Fluorescence (ACN, CHEX) and absorption (ACN) spectra of MGLSS at room temperature.

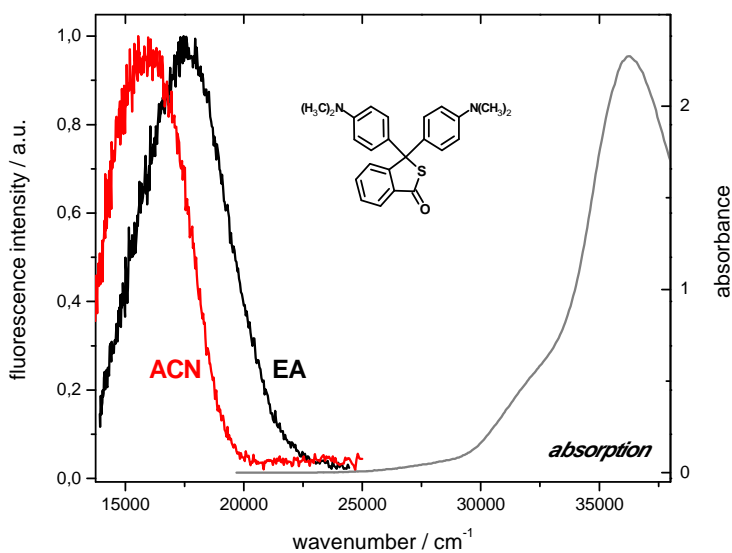


Fig.5.8 Fluorescence (ACN, EA) and absorption (ACN) spectra of MGLS at room temperature. The spectrum in CHEX could not be measured due to MGLS insolubility in CHEX.

5.3 Summary

Even though the experimental data presented in this Chapter allows for somewhat limited insights into the photophysics of MGL derivatives/analogues and needs further studies, some important conclusions concerning characteristic features that are shared by all LTAM molecules with a D–D–A or D–A structures can be drawn.

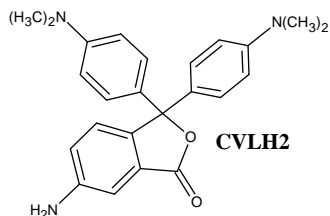
The electronic absorption spectra of both D–D–A and D–A type LTAM in the low energy region can be approximately treated as a superposition of absorption transitions localized on their structural subunits. This form of the absorption spectrum proves that D–A systems build around tetrahedral carbon atom are characterized by an insignificant electronic coupling between the structural moieties in the ground state. The lowest excited state that is populated in absorption is the S_1 state of the electron donating moiety (in case of BPPd it can be also phthalide). Based on the emission spectra, that are characterized by a huge Stokes shift, strong solvatochromic effect and large half widths, the fluorescent state can be identified with a highly polar CT state of a radical ion pair structure. Lack of fluorescence from states localized on chromophores – structural subunits of a LTAM molecule – proves that the deactivation process seen as electronic relaxation of the local excited state is ultrafast and efficient, resulting in populating a state with charge transferred from the donor moiety to phthalide. The energy of the charge separated state depends on the oxidation potential of the D and reduction potential of the A chromophores. A lower oxidation potential of the D ($E^\circ(\text{phenol})^{228} > E^\circ(\text{DMA})^{229} > E^\circ(\text{THQ})^{230} > E^\circ(\text{Jul})^{230}$) while keeping the same A moiety (phthalide), translates to a lower energy of the CT state, and thus to shifting the fluorescence spectrum to the red. Low fluorescence quantum yields in polar solvents suggest, that the CT state deactivates via direct radiationless recombination (non-radiative back ET).

The analysis of the data collected for pairs of structural analogues (bisTHQ–MeTHQ, BPPd–PP) confirms the conclusions drawn earlier for MGL and MGLA. The primary charge separation and the back ET occur in close analogy in all the pairs of molecules studied, the nature of the emitting CT state and the deactivation paths are virtually the same. These similarities prove that the simplification of the D–D–A structure to a D–A dyad structure preserves all their structural and electronic properties, indicating that only one D group in LTAM is actively participating in the excited state ET process.

Chapter 6

Dual fluorescence from two polar excited states in an amino analogue of Crystal Violet Lactone (CVLH2)

CVLH2 is a structural analogue of CVL, where the 6-DMAPd subunit is replaced by 6-aminophthalide (6-APd). Taken as independent molecules, both 6-APd and 6-DMAPd are highly efficient blue emitters with high fluorescence quantum yields (in ACN 0.73 and 0.82, respectively).¹²⁴ Due to higher ionization potential of the -NH_2 group, the lowest excited state of 6-APd is higher in energy than in 6-DMAPd, and this in turn translates into a higher energy of the local state in CVLH2. The photophysical consequences of such a structural change are subject of this Chapter.



6.1 Ground state structure

The calculated ground state structure of CVLH2 (DFT, B3LYP/6-31G(d)) is presented in Fig. 6.1. The structure, bond lengths and angles are almost identical (differences of 0.001 Å) for both CVLH2 and CVL (Tab. 6.1). Only the bonds in which the C4 atom is involved, i.e. the carbon atom of phthalide to which the amino group is attached, are for CVLH2 shorter by approximately 0.008 Å. The calculated spatial arrangements of the aniline subunits and aminophthalide are the same for both molecules. However, the dihedral angle (C19-C20)- (C8-O1) is larger for CVL by 2.3°.

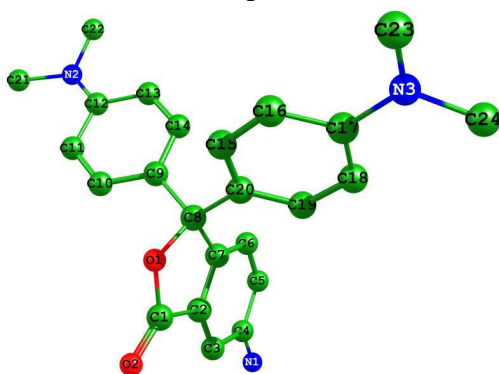


Fig. 6.1 Calculated structure of CVLH2 together with atomic numbering scheme.

Bonds [Å]	CVLH2	CVL
C8–C20	1.527	1.528
C8–C9	1.531	1.531
C8–C7	1.524	1.523
C8–O1	1.476	1.476
C2–C7	1.388	1.387
C2–C3	1.390	1.389
C3–C4	1.403	1.412
C4–C5	1.414	1.422
C5–C6	1.394	1.394
C6–C7	1.394	1.392
C4–N1	1.396	1.388
Angle [deg]		
O1–C8–C7	102.3	102.3
Dihedral angles [deg]		
(C19–C20)–(C8–O1)	61.0	63.3
(C9–C10)–(C8–O1)	160.4	160.0

Tab. 6.1 Comparison of bond lengths and angles for CVLH2 and CVL calculated with DFT (B3LYP/6–31+G(d)) method.

6.2 Absorption in aprotic solvents

The electronic absorption spectra of CVLH2 in solvents of different polarity are presented in Fig. 6.2. Due to a very poor solubility of the compound in CHEX and other non polar hydrocarbons, the spectra recorded in BE are shown. The spectra did not show any absorption in the visible region, both before and after fluorescence measurements, indicating lack of coloured ionic forms.

The absorption spectrum of CVLH2 consists essentially of three bands in the region from 26000 to 40000 cm^{-1} , with the maxima at 28800, 32100, and 36780 cm^{-1} in ACN. The lowest band with the weakest intensity shows a large solvatochromic effect (1780 cm^{-1} red shift of the maximum from CHEX to DMSO). The absorption spectrum recorded in alcohols (MeOH and nPrOH) resembles very closely in shape and band positions the absorption spectrum in ACN proving the absence of specific interactions with the solvent at the ground state level.

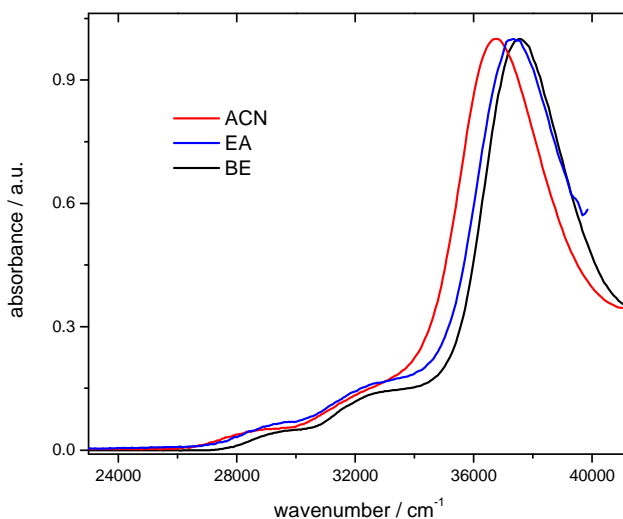


Fig. 6.2 Absorption spectra of CVLH2 in ACN, EA and BE, normalized to the strongest absorption band at around 37000 cm^{-1} . Concentration of the solutions was approximately $2 \times 10^{-5}\text{ mol/dm}^3$.

The absorption spectrum of CVLH2 – when compared with the spectra of compounds mimicking its structural moieties, 6-APd and *t*-butyl-dimethylaniline (*t*-BuDMA) – can be considered in the first approximation as a superposition of transitions localized on the subunits (Fig. 6.3). The lowest energy band with the maximum at 28800 cm^{-1} closely resembles the first absorption band of 6-APd, being shifted in CVLH2 by 1600 cm^{-1} towards longer wavelengths. Additionally, the absorption coefficient of CVLH2 and 6-APd within this absorption band is almost equal (2700 and $2930\text{ M}^{-1}\text{cm}^{-1}$, respectively), suggesting that the band (and corresponding electronic transition) is only weakly perturbed by other transitions localized on DMA units. This assignment is in agreement with the findings reported for CVL. Moreover, the solvatochromic effect observed for the first absorption band of CVLH2 points to optical charge transfer nature of the lowest transition. The nature of the first electronic transition in 6-APd was studied earlier,¹²⁴ where – based on TDDFT calculations and experimental data – it could be concluded that the $S_1 \rightarrow S_0$ transition in aminophthalide involves significant displacement of the charge density from the orbital localized on the amino nitrogen to the orbital localized on the phenyl ring. The second and the third (observed as a shoulder) bands are almost identical for CVLH2 and CVL, and point to a localization of the corresponding transitions on the DMA subunits (Fig. 6.3).

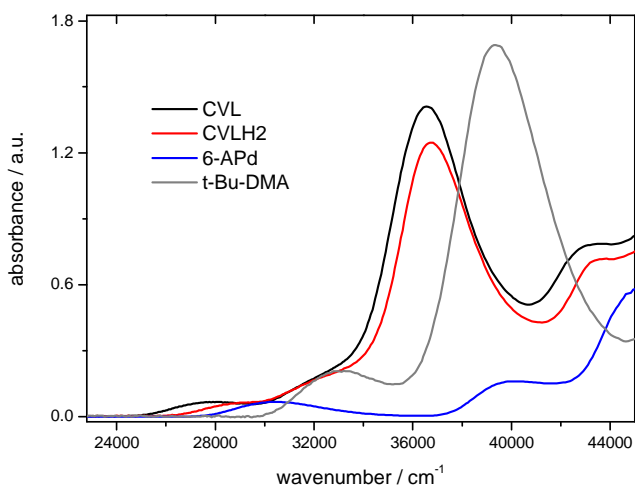


Fig. 6.3 Comparison of the absorption spectrum of CVLH2 with the spectra of compounds modelling its structural parts: 6-APd and t-BuDMA. Additionally the absorption spectrum of CVL is presented. All the spectra were recorded in ACN.

According to the theory of dielectric polarization, a red shift of the absorption band with increasing solvent polarity is expected for molecules which have higher dipole moments in the (Franck–Condon) excited state than in the ground state. The solvent polarity effect on the spectral position of the absorption band maximum can be analysed with Eq. 6.1,^{231,232} assuming that the solute molecule can be approximated by a point dipole situated in the centre of spherical cavity and that the mean solute polarizability in the states involved in the transition can be neglected:

$$hc\tilde{\nu}_{abs} \cong hc\tilde{\nu}_{abs}^{vac} - \frac{2\bar{\mu}_g(\bar{\mu}_e - \bar{\mu}_g)}{a_0^3} \left[\frac{\varepsilon - 1}{2\varepsilon + 1} - \frac{1}{2} \frac{n^2 - 1}{2n^2 + 1} \right] \quad \text{Eq. 6.1}$$

where $hc\tilde{\nu}_{abs}$ and $hc\tilde{\nu}_{abs}^{vac}$ are energies related to spectral positions of the absorption maxima in solution and extrapolated to the vacuum, respectively; $\bar{\mu}_g$ and $\bar{\mu}_e$ are the dipole moments in the ground and in the excited state, respectively; a_0 is the effective radius of the Onsager cavity; ε is the dielectric constant and n is the refractive index of a solvent. Virtually equal slopes of the absorption solvatochromic plots of CVLH2 and 6-APd (Fig. 6.4, Tab. 6.2) demonstrate similar solvent effects on the first absorption band in the two molecules, and consequently similar nature of the lowest electronic transition and – indirectly – its localisation on the 6-APd moiety of CVLH2.

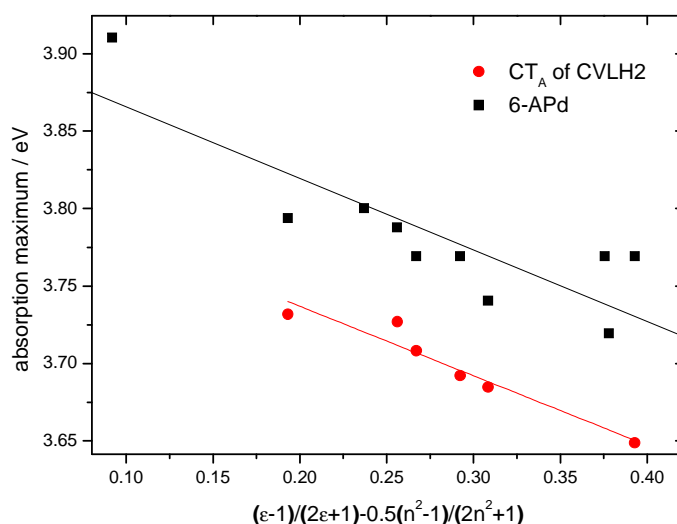


Fig. 6.4 Solvatochromic shift of the first absorption maximum of CVLH2 and 6-APd as a function of solvent polarity. The correlation coefficient for the linear fit of the CVLH2 data is $R=0.99$.

	CVLH2	6-APd
$\bar{\mu}_g (\bar{\mu}_e - \bar{\mu}_g) / a_0^3$ *	0.22	0.22
$hc\tilde{\nu}_{abs}^{vac}$	3.83	3.91

Table. 6.2 Slopes and intercepts of absorption solvatochromic plots for CVLH2 and 6-APds in eV. * is the halved slope of the fitting straight line, see Eq. 6.1.

6.3 Fluorescence at room temperature

The fluorescence spectrum of CVLH2 at room temperature shows a very strong dependence on solvent polarity (Fig. 6.5). In non polar solvents, such as CHEX, BE or iPE the fluorescence spectrum consists of one band (A band), with the maximum shifting to the red on increasing polarity of the medium. When the polarity exceeds a certain threshold value (above $\epsilon=3.0$ / iPE and below $\epsilon=4.3$ / EE), a second fluorescence band (B band) appears. In solvents of polarity between EE ($\epsilon=4.3$) and THF ($\epsilon=7.6$) dual emission can be observed, with increasing dielectric constant of the medium, however, the share of the A band decreases substantially. In polar BTN and ACN only the

B band can be observed. The appearance of the long-wave B band is accompanied by a decrease in fluorescence quantum yields. Moreover, both bands display a strong solvatochromic effect. The relative intensity of the fluorescence bands in a given solvent is independent of the excitation wavelength.

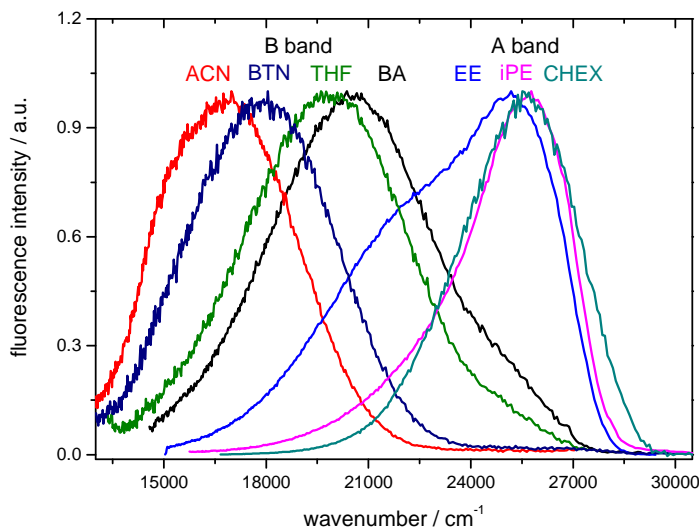


Fig. 6.5 Fluorescence spectra of CVLH2 as a function of solvent polarity.

Fluorescence decay times measured at the blue and the red slope of the A and the B band, respectively, are equal and no rising components were detected on the ns time scale of measurement. Fluorescence excitation spectra were measured using samples with absorbance lower than 0.1 in the entire spectral range studied. Excitation spectra recorded in various solvents with fluorescence monitored in both A and B band are identical and reproduce well the absorption spectrum of CVLH2, hence, both bands are emitted from the compound under study but from different electronic states. The polar character of both emitting states can be deduced based on considerable Stokes shifts, strong solvatochromic effect (B band: 5700 cm^{-1} between EE and ACN) and large bandwidths. Therefore, in analogy to CVL, the two emitting states will be denoted as CT_A and CT_B to indicate significant charge displacement in their electronic structures as compared with the ground state of CVLH2.

Comparison of the solvatochromic effect, the Stokes shifts, the maxima and bandwidths of the A band with 6-APd leads to the conclusion,

that in CVLH2 the local state of the electron acceptor moiety is the CT_A state. Moreover, comparison with CVL supports this conclusion. However, it is important to note that the fluorescence maxima in 6-APd are higher in energy (by 570 and 600 cm⁻¹ in BE and THF, respectively) than in CVLH2 and in CVL (1170 and 550 cm⁻¹ in BE and THF, respectively)

Comparison of the CVLH2 long wavelength fluorescence with the B band of CVL and the fluorescence of MGL shows great similarities between these emissions in terms of the halfwidths, the maxima positions and the solvatochromic shifts (for CVLH2: 5700 cm⁻¹, MGL: 5300 cm⁻¹, between EE and ACN). These spectral similarities imply that the emissive states in all three compounds have very similar electronic structures. This allows also for concluding that the B fluorescence of CVLH2 comes from a state with electron transferred from the DMA moiety to the lactone ring of the phthalide moiety. The fluorescence of CVLH2 is displayed with slightly lower energies (by approximately 500 cm⁻¹) than the respective band in MGL.

Tab. 6.3 Fluorescence of CVLH2 as a function of solvent polarity

Solvent	$\tilde{\nu}_{fl}^{CT}$ (A)	$\tilde{\nu}_{fl}^{CT}$ (B)	Φ_{fl} (A)	τ_{fl} (A)	τ_{fl} (B)	Φ_{fl} (B)
	[cm ⁻¹]	[cm ⁻¹]		[ns]	[ns]	
CHEX	25750					
BE	25700		0.44	7.0		
iPE	25800					
EE	25800	22550	0.031	13.3*		0.069
BA	25350	20650	0.015	15.8	15.3	0.125
EA	25200	19900	0.003	13.6	14.4	0.087
THF	25200	19850	0.003	6.1	6.2	0.057
BTN		18000			4.3	0.017
ACN		16850			1.2	0.002
DMSO		16850				

$\tilde{\nu}_{fl}^{CT}$ maximum of the fluorescence band, Φ_{fl} and τ_{fl} – fluorescence quantum yield and decay time, respectively; * main component of a strongly nonexponential fluorescence decay.

For CVLH2 the total quantum yield decreases with increasing solvent polarity, with the most dramatic change between BE and EE, just when the CT_B band appears: the quantum yield drops from 0.44 to 0.1 (Tab. 6.3). The value 0.44 agrees very well with the yield for insulated 6-APd in BE ($\Phi_{fl}=0.44$) definitely proving that, in terms of fluorescence emission,

CVLH2 in non polar solvents behaves like 6-APd molecule. Also the fluorescence decay times measured for both compounds in BE are nearly the same (7.8 and 7.0 ns for 6-APd and CVLH2, respectively).

Quantum yields of CT_A and CT_B fluorescences in solvents where dual emission is observed were obtained by decomposition of the experimentally recorded dual fluorescence spectrum of CVLH2 into the fluorescence bands (also experimentally recorded) of insulated MGL and 6-APd (Fig. 6.6). The separation of the bands was done under the assumption that the shapes of A and B bands are the same as the fluorescence bands of MGL and 6-APd in a given solvent, and that these bands are shifted on the energy scale as compared to these model compounds. Using such an approach, excellent agreement was obtained between the experimental CVLH2 spectrum and the sum of MGL and 6-APd spectra, as appropriately shifted and weighted (Fig. 6.6).

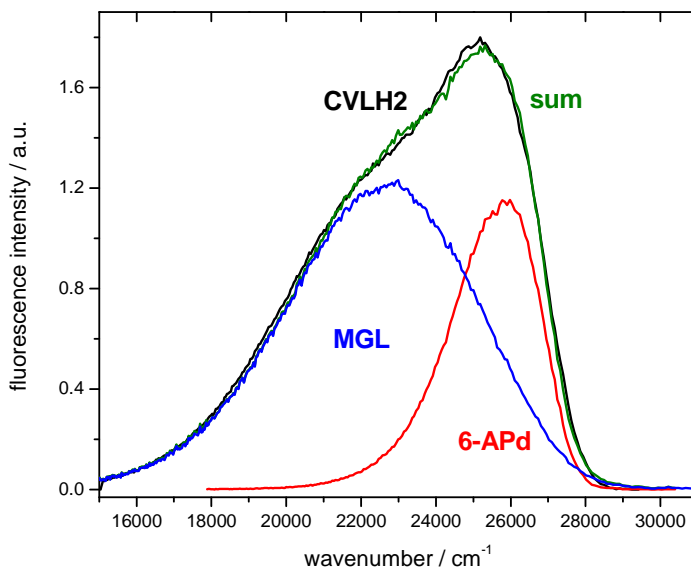


Fig. 6.6 Fluorescence spectrum of CVLH2 in EE recorded experimentally and represented as a superposition of appropriately weighted 6-APd and MGL fluorescence bands recorded in the same solvent and shifted by 700 cm^{-1} to the red and 1000 cm^{-1} to the blue, respectively.

For the CT_A state, $\Phi_{fl}(A)$ decreases with growing solvent polarity, what suggests efficient intramolecular quenching mechanism involving the CT_B state. In general, the quantum yield of CT_B fluorescence decreases with growing solvent polarity. From BA on, Φ_{fl} of the CT_B emission are of the

same order of magnitude as the yields for insulated MGL (BA: 0.125 and 0.123; THF: 0.057 and 0.072; ACN: 0.017 and 0.019; for CVLH2 and MGL, respectively). These results strongly indicate that in more polar solvents the population of the primary excited state in CVLH2 is quantitatively transferred to the CT_B state.

The fluorescence lifetimes measured for CVLH2 are also solvent polarity dependent. In solvents where single emission band is observed, the recorded decays correspond largely to the decays of the model molecules: for BE to 6-APd (7 and 7.8 ns for CVLH2 and 6-APd, respectively), for BTN and ACN to MGL (BTN: 4.3 and 3.0 ns; ACN: 1.2 and below 0.4 ns for CVLH2 and MGL, respectively).

CVLH2 is more sensible to solvent polarity than CVL. This effect is caused by the smaller energy gap between the CT_A and CT_B states in CVLH2. Lowering the dielectric constant by 0.6 (from 4.2 to 3.64) allows the observation of fluorescence from almost pure CT_B state to fluorescence from both CT_A and CT_B states with similar intensities (Fig. 6.7).

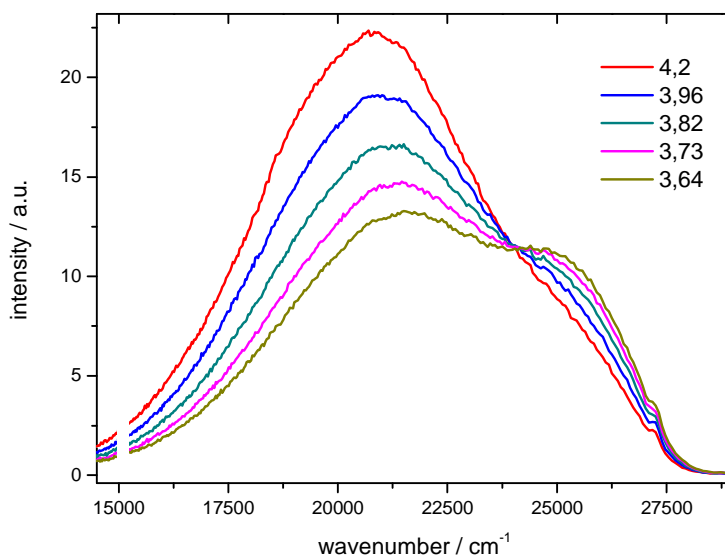


Fig. 6.7 CVLH2 in a binary solvent mixture (BE and EA). The dielectric constant values ϵ for mixed solvents were calculated as the weighted average of the mixture components, assuming ideal solvent mixture and additive function of solvent concentrations: $\epsilon_{mix} = a_1\epsilon_1 + a_2\epsilon_2$, where a_i is a volume fraction of i -th solvent, and ϵ_i is its dielectric constant in the pure state (excess ϵ was neglected).²³³

6.4 Excited state dipole moment

The solvatochromic shift method was employed to confirm the polar character of the emitting states and to determine the excited state dipole moments (Section 4.4). An appropriate selection of the Onsager cavity radius is critical, since it enters the equation in the third power. Moreover, for a molecule composed of nearly non interacting moieties displaying dual fluorescence, additional assumptions concerning the cavity radius for both emitting states are to be made, since the state displaying A fluorescence is localized on the 6-APd moiety and the state emitting B fluorescence is distributed over the entire molecule. Different distributions of charge density in CT_A and CT_B state polarize the surrounding solvent molecules in different ways. Therefore, as it was the case for CVL, different spherical Onsager cavities for both emitting states are assumed, since only those solvent molecules that surround the part of the molecule that is directly involved in the radiative transition form the cavity. Assuming a point dipole moment situated in the centre of a spherical cavity and neglecting the mean solute polarizability in the states involved in the transition, the excited state dipole moment, $\bar{\mu}_e$, can be calculated from the following expression (Section 4.4, Eq. 4.3):

$$hc\bar{\nu}_{fl} \cong hc\bar{\nu}_{fl}^{vac} - \frac{2\bar{\mu}_e(\bar{\mu}_e - \bar{\mu}_g)}{a_0^3} \left[\frac{\epsilon - 1}{2\epsilon + 1} - \frac{1}{2} \frac{n^2 - 1}{2n^2 + 1} \right] \quad \text{Eq. 4.3}$$

where $\bar{\mu}_g$ is the dipole moment of the solute in the ground state, and $\bar{\nu}_{fl}$ and $\bar{\nu}_{fl}^{vac}$ are the spectral positions of the solvent-equilibrated fluorescence maxima and the value extrapolated to the gas phase, respectively; a_0 is the radius of the Onsager cavity.

Fig. 6.8 shows the plot of fluorescence maxima as a function of solvent polarity $f(\epsilon, n) = (\epsilon - 1)/(2\epsilon + 1) - 0.5(n^2 - 1)/(2n^2 + 1)$ for both states of CVLH2 compared with 6-APd and MGL modelling the CT_A and CT_B states, respectively. When comparing the fit parameters for CVLH2 one has to keep in mind that the position of fluorescence maxima in solvents of higher polarity than in iPE is difficult to estimate (even using the decomposed spectra) due to low intensity and huge overlap with the stronger CT_B fluorescence. Hence, the parameters of the solvatochromic plots for the A band of CVLH2 and for 6-APd differ from each other. However, for the B

band and MGL the parameters are similar indicating that the energies of interaction with the surrounding solvent molecules are similar for both emitting states and hence point to their similar dipole moments of corresponding excited states (Tab. 6.4).

	CVLH2 (A)	6-APd	CVLH2 (B)	MGL	CVL (B)
$\vec{\mu}_e(\vec{\mu}_e - \vec{\mu}_g)/a_0^3$ [eV]	-0.28	-0.73	-2.19	-2.0	-2.04
$hc\tilde{\nu}_{fl}^{vac}$ [eV]	3.31	3.64	3.82	3.61	3.74
$\vec{\mu}_e$ [D]	8.0	8.3	26.2	25.0	25.2
a_0 [Å]	3.0	3.0	5.8	5.8	5.8

Tab. 6.4 Slopes of the fluorescence solvatochromic plots for CVLH2 A and B bands, 6-APd, MGL (acc. to Eq. 4.3), and the dipole moments calculated for the respective excited states.

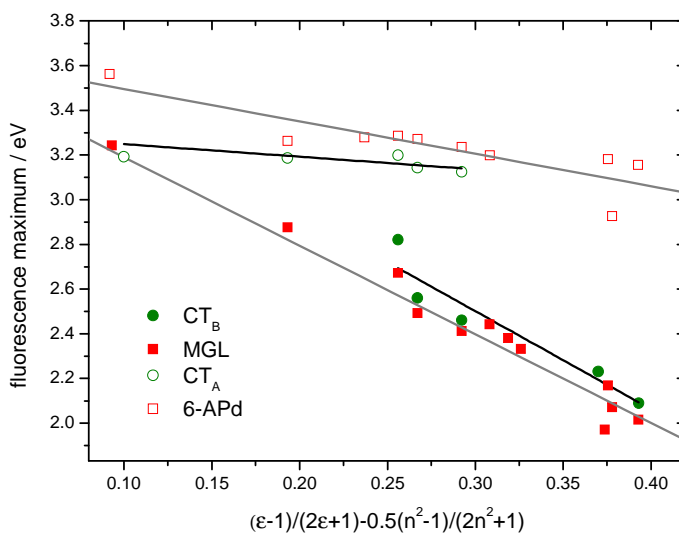


Fig. 6.8 Solvatochromic shifts of fluorescence maxima for both A and B bands of CVLH2 as a function of solvent polarity, compared with those for MGL and 6-APd.

Determination of the excited state dipole moment value of the CT_A state from Eq. 4.3 requires knowledge of the Onsager cavity radius, a_0 , the ground state dipole moment, $\vec{\mu}_g$, and the angle between $\vec{\mu}_g$ and $\vec{\mu}_e$. The Onsager cavity radius was set equal to that used in estimation of $\vec{\mu}_e$ for 6-APd, i.e., $a_0 = 3 \text{ \AA}$, the ground state dipole moment of CVLH2 was

calculated with the DFT method (B3LYP/6-31+G(d)) to 5.8 D. The difference $\Delta\mu_{eg} = |\vec{\mu}_e - \vec{\mu}_g|$ was calculated from the plot of the Stokes shift vs. solvent polarity function according to the Lippert–Mataga equation (Eq. 6.2), since the CT_A state is directly populated in absorption ($\Delta\mu_{eg} = 3.25$ D):

$$hc(\tilde{\nu}_{abs} - \tilde{\nu}_{fl}) \cong hc(\tilde{\nu}_{abs}^{vac} - \tilde{\nu}_{fl}^{vac}) + \frac{2(\vec{\mu}_e - \vec{\mu}_g)^2}{a_0^3} \left[\frac{\epsilon - 1}{2\epsilon + 1} - \frac{n^2 - 1}{2n^2 + 1} \right] \quad \text{Eq. 6.2}$$

Good linear correlation between $hc(\tilde{\nu}_{abs} - \tilde{\nu}_{fl})$ and the solvent polarity function allowed for direct determination of the value $(\vec{\mu}_e - \vec{\mu}_g)^2 / a_0^3$, and hence for calculation of $\Delta\mu_{eg} = 3.25$ D. From the slope of the solvatochromic plot for absorption spectra ($-\vec{\mu}_g \Delta\vec{\mu}_{eg} / a_0^3 = 0.22$ eV), the angle between $\vec{\mu}_g$ and $\Delta\vec{\mu}_{eg}$ vectors was calculated since:

$$\vec{\mu}_g (\vec{\mu}_g - \vec{\mu}_e) / a_0^3 = -\vec{\mu}_g \Delta\vec{\mu}_{eg} / a_0^3 = \mu_g \Delta\mu_{eg} \cos \beta / a_0^3 \quad \text{Eq. 6.3}$$

$$\cos \beta = \cos(180 - C) = -\cos C = \frac{[\vec{\mu}_g (\vec{\mu}_e - \vec{\mu}_g) / a_0^3] a^3}{\mu_g \Delta\mu_{eg}} \quad \text{Eq. 6.4}$$

$$C = 120.7^\circ$$

Having two sides of the triangle, $\vec{\mu}_g$ and $\Delta\vec{\mu}_{eg}$, and the angle C , it is possible to determine the third side, $\vec{\mu}_e$. It has been found that for CVLH2 $\vec{\mu}_e = 8.0$ D and the angle between the dipole moments of the ground and the excited state is $A = 20.6^\circ$. The values obtained for 6-APd using the same formalism are similar ($\vec{\mu}_e = 8.3$ D; $\alpha = 26^\circ$).¹²⁴ These results strongly support the conclusion on a very similar electronic structure of the S₁ excited state in 6-APd and the CT_A state in CVLH2.

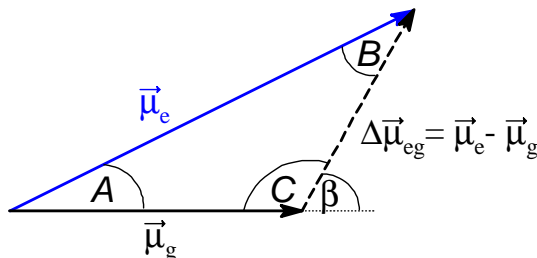


Fig. 6.9 Triangle of $\vec{\mu}_g$, $\vec{\mu}_e$ and $\Delta\vec{\mu}_{eg}$ vectors.

In determination of the dipole moment of the CT_B state, the ground-state dipole moment of CVLH2 was neglected, since the solvent effect on the B fluorescence band is very strong pointing to a considerable CT character. Hence, the assumption made for CT_B state of CVL that $|\bar{\mu}_e| \gg |\bar{\mu}_g|$ holds also for CVLH2. The CT_B state is not localised on a particular chromophore but extends over the entire molecule for both CVL and CVLH2, and therefore the Onsager cavity radius was set to 5.8 Å, in analogy to MGL (and CVL). The excited state dipole moment calculated for the CT_B state of CVLH2 is equal to 26.2 D (Tab. 6.4). This value compares very well with 25.2 and 25 D obtained for CVL and MGL, respectively, using the same cavity radius. Excellent agreement between the slopes of solvatochromic plots for CVLH2 and MGL (and CVL) proves, that in all three molecules the CT_B state has similar electronic configuration, and thus, that the specific substitution of phthalide at position 6 does not affect much the CT_B state.

6.5 Nature of the triplet states populated at room temperature

The nature of the emitting states in CVL was confirmed by means of fs and ns-transient absorption (TA) measurements.^{82,83} In low polar solvents, where only the emission from 6-DMAPd is observed, the shape and position of the transient absorption spectrum of CVL is very similar to that measured for 6-DMAPd. In polar solvents however, only a band characteristic for the radical cation of DMA is detected on the ns time scale (with the maximum around 472 nm), the same as in the case of MGL, proving the CT character of the CT_B state. The transient absorption spectra recorded for CVL in BE at a long delay (40 ns, allowing to consider the singlet population to be negligible) also coincide with the spectrum for 6-DMAPd indicating that in low polar solvents CVL undergoes intersystem crossing to the local triplet state of 6-DMAPd moiety. In polar solvents, the spectrum recorded after a complete decay of the singlet states resembles closely the S₁→S_n spectrum (preserving the 472 nm band), which suggests that in this case, the charge separation is still maintained in the triplet state.

Transient absorption spectra of CVLH2 were measured with two setups, one nitrogen laser-based allowing for delays up to 100 ns at temporal resolution of about 1 ns, and the other one based on a Nd-YAG laser (7 ns pulse) with delays up to microseconds.

Transient absorption spectrum of CVLH2 in polar solvent (ACN) recorded at 0 ns delay (i.e., during the excitation pulse) is almost identical with the spectrum recorded for CVL under the same conditions and consists of one band with the maximum at approximately 460 nm (Fig. 6.9). From this it follows, that the electronic configuration of the singlet state of both CVL and CVLH2 in ACN is very similar and consists of a radical ion pair.

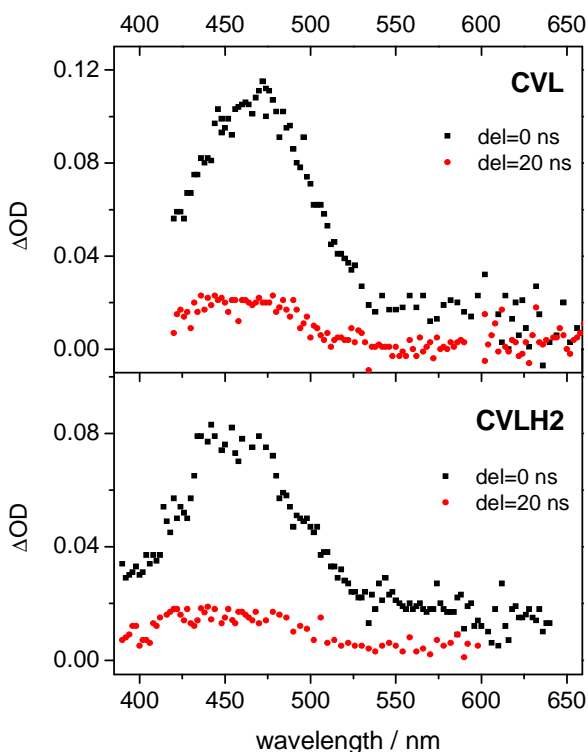


Fig. 6.9 Comparison of CVL and CVLH2 spectra recorded in ACN with different delays: when the probe and pump pulse coincided (black) and after a 20 ns delay time (red).

The TA spectra recorded after complete decay of the singlet state of both molecules in ACN look again very much alike and reproduce the $S_1 \rightarrow S_n$ spectra. The TA band in CVLH2 is by 10 nm (480 cm^{-1}) shifted towards shorter wavelengths (maximum at 450 nm) while preserving the band shape recorded for CVL (Fig. 6.9). Based on the observation of the signature of the radical cation of DMA it can be concluded, that both in CVL and in CVLH2 the charge separation is maintained in the triplet state (in polar solvents). TA spectra of CVLH2 in low polar solvents were impossible

to obtain in good quality due to insufficient solubility of the compound.

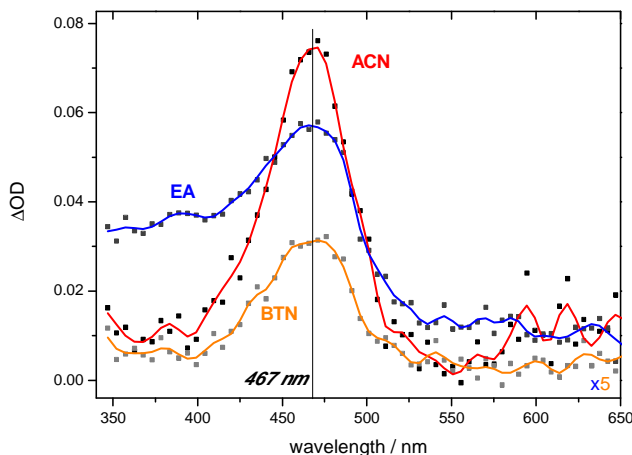


Fig. 6.10 Transient absorption spectra of CVL in ACN, BTN (multiplied by factor of 5) and EA (multiplied by factor of 5). Ground state absorbance at 355 nm (excitation wavelength) was around 0.1.

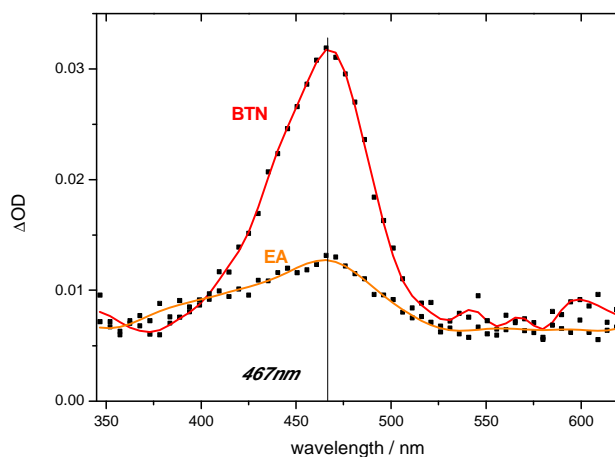


Fig. 6.11 Transient absorption spectra of CVLH2 in BTN and EA. Ground state absorbance at 355 nm (excitation wavelength) was approximately 0.1.

Triplet–triplet transient absorption spectra of CVL and CVLH2 (Fig. 6.10 and Fig. 6.11) were recorded at different delays, ranging from 60 ns to a few microseconds, the samples were excited with a 355 nm Nd–YAG laser pulse (FWHM=7 ns). The concentrations of the samples used in measurements were about 4×10^{-5} M. The excitation laser energy for

solutions in ACN and BTN was about 0.4 mJ, for EA solutions the laser energy was increased about ten times in order to obtain a measurable signal.

During these TA measurements a decomposition of both molecules was observed, and the process was independent of the solvent and the laser energy used. The decomposition process was recognised by slight changes in the steady-state absorption spectra (Fig. 6.12). For all compounds the peak near 270 nm (transition localized on the DMA subunit) decreased and a new band emerged manifesting its presence as a red shoulder. An isosbestic point was observed at about 300 nm for both CVL and CVLA. However, the effect of sample decomposition on the TA spectra was very weak, e.g., no new bands could be detected, only a slight decrease in the intensity of the primary TA band was observed. The products of photodegradation were not identified. The decomposition of the samples may be due to multiphoton processes initiated by long excitation pulses (about 7 ns). During a single laser pulse the molecule can pass to the triplet state and subsequently can be excited in the triplet state by absorption of a photon (i.e., $T_1 \rightarrow T_n$ absorption) from the same pulse (Fig. 6.13). It is known that in various lactones the higher triplet state reached on this pathway can undergo a fast photochemical change.^{202,203,204} Despite the decomposition of the samples it was possible to obtain reliable triplet-triplet absorption spectra. For presentation and conclusions only the spectra recorded in the initial phase of the measurement series were taken into account.

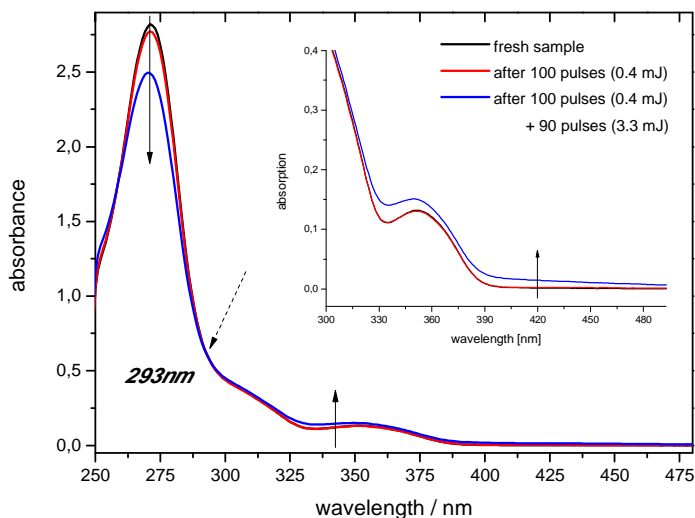


Fig. 6.12 Absorption spectra of CVL in EA recorded before (black), during (red) and after (blue) transient absorption measurements. The isosbestic point is marked with an arrow at 292 nm.

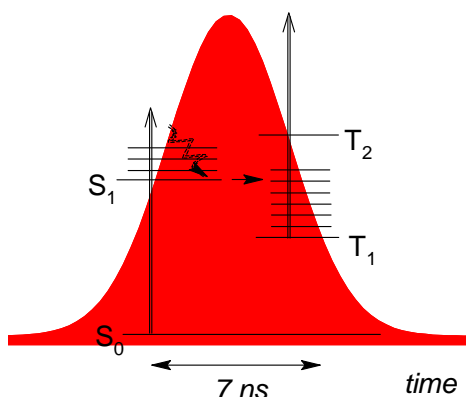


Fig. 6.13 Illustration of photo-physical processes that can take place during single long pulse. Pulse halfwidth is 7 ns, and singlet state decay time is 1.5 ns.

Transient absorption spectra of both CVL and CVLH2 in highly polar solvents (ACN and BTN) recorded at 60 ns delay look very much alike, displaying only single band with the maximum at 467 nm and a halfwidth of approximately 2700 cm^{-1} , and are ascribed to the radical cation of DMA. These spectra are in good agreement with the “early” ns spectra (recorded at 0 ns delay) of both compounds implying that in polar solvents the populated triplet state has also considerable CT character. Moreover, a comparison of the measured spectra with the $T_1 \rightarrow T_n$ transient absorption spectrum of dimethylaniline from literature,²⁰⁵ which shows two peaks: more intense at 350 nm and a weaker one at 460 nm, rules out a contribution from the triplet state localized on dimethylaniline.

In medium polarity solvents like EA the spectra of CVL and CVLH2 recorded with 60 ns delay are also similar and show the presence of the 467 nm band, on the blue side, however, between 350 and 430 nm an additional band is visible. The interpretation of the data is hindered by the fact that the absorbance signal of both compounds in EA was very low.

The spectra recorded under the same conditions but with different delays (up to microseconds) in a given solvent display the same shape and position of the TA band and agree well with the nanosecond spectra, only the intensity decreases. This observation points to the fact that only one triplet state (with radical ion-pair structure) is populated.

6.6 Luminescence in glasses

Luminescence spectra of CVLH2 in BTN glass recorded at 77 K are presented in Fig. 6.14. The luminescence spectrum of CVLH2 consists of

one phosphorescence band with the maximum at around 20000 cm^{-1} and one fluorescence band (maximum at approximately 23000 cm^{-1}) forming a shoulder at the short-wave side of the luminescence spectrum. The long-lived emission resembles closely the phosphorescence spectrum of 6-APd with regard to both the location and the shape. The fluorescence spectrum, however, cannot be ascribed to come from the electron-accepting subunit since its maximum is red-shifted by 3000 cm^{-1} . On the other hand, a similarity between the fluorescence spectrum of CVLH2 and the fluorescence spectrum of MGL in BTN (77 K , maximum at 22000 cm^{-1}) implies that the singlet CT_B state is most probably the origin of the short-lived emission.

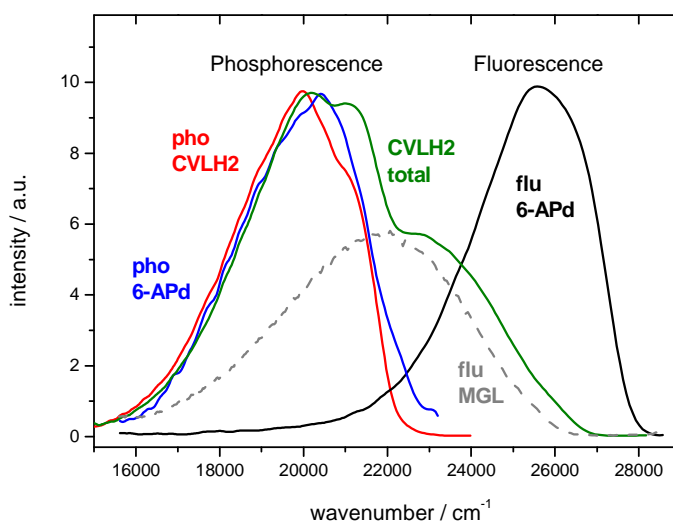


Fig. 6.14 Fluorescence, phosphorescence and total luminescence spectra of CVLA compared with 6-APd and MGL recorded at 77 K .

6.7 Discussion

CVLH2 and CVL belong to triarylmethane lactones of the D-D-(DA) type, i.e., two identical donor moieties are connected to the aminophthalide subunit that has both electron-donating (amino group) as well as electron-accepting (lactone ring) properties. The structural modification of CVLH2 consists in substituting the phthalide moiety at position 6 with a free amino group, whereas in CVL a dimethylamino group is present. This subtle change in the structure induces considerable changes

in the photophysics of the congener molecule, since the change of the ionization potential of the DA subunits has strong impact on the excited states energetics.

The calculated ground state structures of CVL and CVLH2 are almost identical, the only differences concern the bond lengths between atoms that are connected to the C4 carbon atom. Structural subunits of CVLH2 as well as of CVL are electronically decoupled in the ground state, which results in the absorption spectrum being a superposition of absorption transitions localised on the moieties. On the excited state level, however, both molecules display a strong electronic coupling which enables the ET process. The excited state reached in absorption is the local CT_A state of the DA part and is populated as a result of an optical charge displacement process from the amino group to the lactone ring. The strong similarity of the solvatochromic plots (slopes and intercepts) of absorption (of the A band) vs. solvent polarity function of CVLH2 and 6-APd, and nearly equal excited state dipole moments prove that the character and electronic structure of these excited states is very similar. The difference in the slopes of solvatochromic plots of fluorescence maxima of the CT_A band and 6-APd has most probably to do with the difficulty to determine fluorescence maxima in solvents more polar than iPE due to its overlap with the much stronger CT_B band. The second excited state (CT_B), which becomes accessible in more polar solvents, has a strong CT character. Also in this case, the solvatochromic plots for absorption and fluorescence maxima are similar to those for the model molecule – MGL (phthalide moiety has only hydrogen atoms in position 6), likewise, as are the values of the dipole moments of the highly polar excited states in CVLH2, MGL and CVL. Based on these facts it can be concluded, that in all three molecules the CT_B state has similar electronic configuration, and thus, that the specific substitution of phthalide at position 6 does not significantly affect the energy and electronic structure of the CT_B state.

In both CVL and CVLH2, the two excited states, the CT_A (less) and the CT_B (much more) have a CT character and their energies strongly depend on solvent polarity. The solvent polarity dynamically determines the relative energetics of both CT states and controls the availability of the ET process and various deactivation pathways. The ultrafast photoinduced ET process converting reversibly CT_A to CT_B occurs when the two states become temporarily isoenergetic which happens when the medium surrounding the molecule provides required energy stabilization for the CT_B state down to the CT_A level, i.e., in solvents above certain threshold dielectric constant. In CVL, the threshold ϵ value for appearance of the red fluorescence band

emitted from the CT_B state is between 7.6 (THF) and 8.9 (DCM). CVLH2 is even more susceptible to solvent polarity, the B band appears in solvents with ϵ between 3.8 (iPE) and 4.3 (EE), but when ϵ exceeds 7.6 (THF) the primary emission (A band) is not present anymore. The initial energy gap between the non-solvated CT_A and CT_B states, ΔE , is of essential importance for the threshold of the medium dielectric constant required for appearance of the CT_B fluorescence (Fig. 6.16). While the lower threshold ϵ is due to smaller ΔE , the narrow polarity range of dual fluorescence results from a smaller stabilization of the CT_A state in CVLH2 due to its lower dipole moment than in CVL. In highly polar solvents, the solvationally and vibrationally relaxed CT_B level in CVLH2 lies significantly below CT_A , so that the back ET, $CT_A \leftarrow CT_B$, is energetically and kinetically not possible and the equilibrium is completely shifted towards the CT_B state (Fig. 6.15).

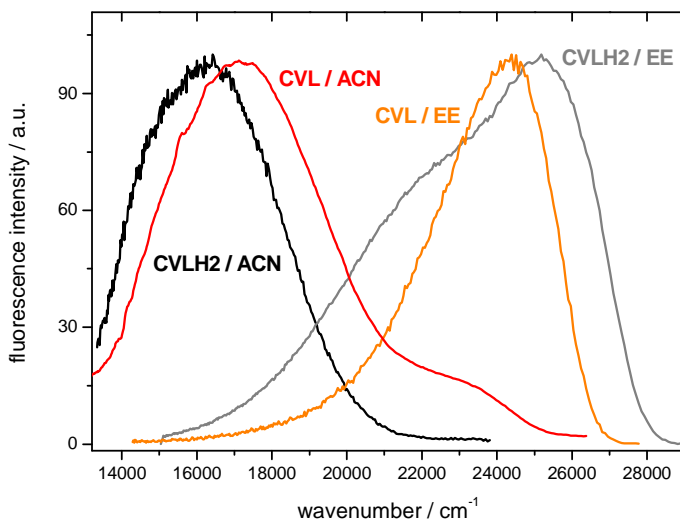


Fig. 6.15 Comparison of fluorescence spectra of CVLH2 and CVL in the same solvents (EE and ACN).

In our case, ΔE was changed by changing the energy of the CT_A state (S_1 state of DA), i.e., by introducing a new DA molecule with a higher ionization potential. Due to the higher ionization potential of the $-NH_2$ group, the lowest excited state of 6-APd is higher in energy than in 6-DMAPd (absorption maximum in HEX at 31550 cm^{-1} vs. 29450 cm^{-1}) and the emission maximum of 6-APd is blue shifted by $2100\text{--}2600\text{ cm}^{-1}$. Lower excited state dipole moment of 6-APd (8.5 D) than 6-DMAPd (11.2 D) translates into a smaller solvatochromic shift of the fluorescence band.

Because the two parts of CVLH2 molecule involved in creation of the CT_B state (one DMA group and the lactone ring) are the same as in CVL, the CT_B state of CVLH2 is expected to have the same energy in a given solvent as that in CVL, both before and after stabilization by solvation. Combined with higher energy of the CT_A , this leads to a considerably lower ΔE between non-solvated CT_A and CT_B states in CVLH2 (Fig. 6.16).

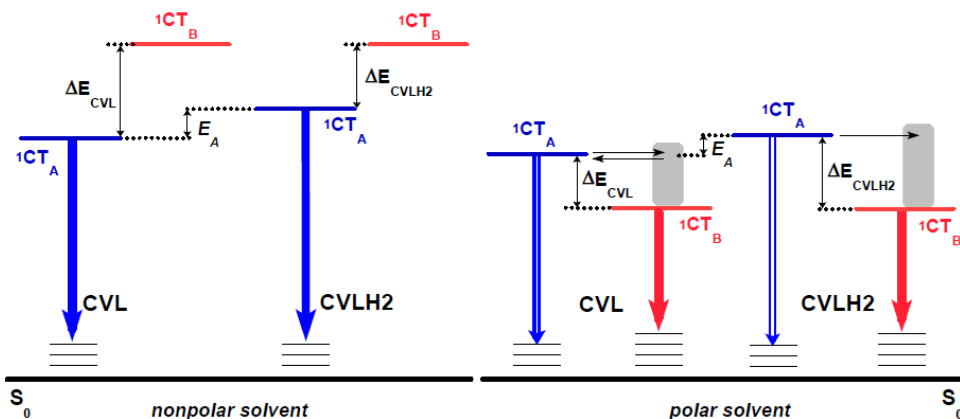


Fig. 6.16 Energy levels of the two lowest excited states of CVL and CVLH2 in low and highly polar solvents. ΔE indicates the energy gap between the non-solvated CT_A and CT_B states, E_A denotes the energy difference between the CT_A states in CVL and CVLH2, showing its change along with solvation dynamics.

The triplet state populated at room temperature in polar solvents in both CVLH2 and CVL have the same electronic structure as the singlet state. The observation of the radical cation band of DMA proves that in polar solvents the charge separation in the triplet state is still maintained. The interpretation of the TA spectra in low polar solvents is difficult due to a very weak signal. Such a small signal is most probably due to a small fraction of molecules that undergo intersystem crossing to the triplet state, i.e., in CVL in EA the quantum yield of fluorescence is 0.32,⁸² and most of the radiationless deactivation occurs via radiationless charge recombination. For both CVLH2 and CVL further research is needed to elucidate the electronic structure of the triplet state populated in low polar solvents.

The differences between CVLH2 and CVL become also noticeable at low temperatures. The phosphorescence of CVLH2 as well as of CVL comes from the local DA chromophore (6-APd and 6-DMAPd, respectively). The fluorescence observed at 77 K, however, has different origin in both molecules, in CVL it has been ascribed to come from the 6-DMAPd subunit. In CVLH2 the spectrum is strongly red shifted (maximum at 23000 cm^{-1})

and broader, moreover, it displays strong similarity to the spectrum of MGL (maximum at 22000 cm^{-1}) recorded under the same conditions. This strongly suggests that BTN at 77 K is still capable of stabilizing the CT_B state below the CT_A state so that the former is the only fluorescing state of CVLH2 under these conditions.

In summary, the introduction of a structural modification in the DA moiety of triarylmethane lactones of the D–D–(DA) class has a clear impact on the photophysics on the excited state level. Based on the results presented in this Chapter, the changes in the excited state energetics induced by introduction of electron accepting subunits with different ionization potential can be rationalized. They allow for extending conclusions drawn for CVL on other CVL analogues and for predicting how structural modifications in the DA subunit will affect the photophysics of the molecules.

Chapter 7

Ultrafast radiationless deactivation in spiro-bridged Crystal Violet Lactone structure (CVLB)

7.1 Spectroscopic characteristic of structural subunits of CVLB

The next two sections (7.1.1 and 7.1.2) present and discuss the spectroscopy of structural components (chromophores) of CVLB. The knowledge about the photophysics of structural components (chromophores) turned out to be essential for understanding of the excited state processes in CVL (see Section 2.4.4), because of the involvement of the locally excited (LE) state of the electron-accepting moiety (6-DMAPd). Since, structurally, CVLB can be divided into two chromophores with comparable S_1 state energies, DMAF, and 6-DMAPd, one may expect that the two LE states are actively involved in the CVLB photophysics. A detailed study of the photophysics of structural subunits is also necessary in view of possible spiroconjugation effects in CVLB. Moreover, the interpretation of the fluorescence spectra in different solvents and the temperature dependent emission spectra relies on the knowledge about the photophysics of CVLB subunits, DMAF and 6-DMAPd.

7.1.1 6-dimethylaminophthalide (6-DMAPd)

Amino derivatives of phthalide are a newly introduced class of highly luminescent fluorophores.^{124,125} High fluorescence quantum yields and long lifetimes together with sensitivity to polarity and proticity of the surrounding medium make them good candidates for applications as fluorescent probes and sensors, for example for transition metal cations.²³⁴ Photophysics of aminophthalides was studied in detail in another PhD thesis completed at the Institute of Physical Chemistry of the PAS by Y. Svartsov.¹²⁴ Due to limited accessibility of the work and for the sake of completeness a brief summary on photophysics of 6-DMAPd, a structural subunit of CVLB and CVL is given below. Except for X-ray structure and calculations presented in the present work, the data is taken from the Svartsov's work. Only the

information of 6-DMAPd is included here that is absolutely necessary to understand the processes occurring in CVLB.

7.1.1.1 Ground state structure

The crystal structure of 6-DMAPd belongs to the monoclinic symmetry space group, $P2_1/c$, with the following lattice parameters: $a=6.3837$ (2) Å, $b=19.3486$ (8) Å, and $c=7.0326$ (3) Å. A unit cell contains four 6-DMAPd molecules with planes of all phthalide systems virtually parallel to each other (Fig. 7.1).

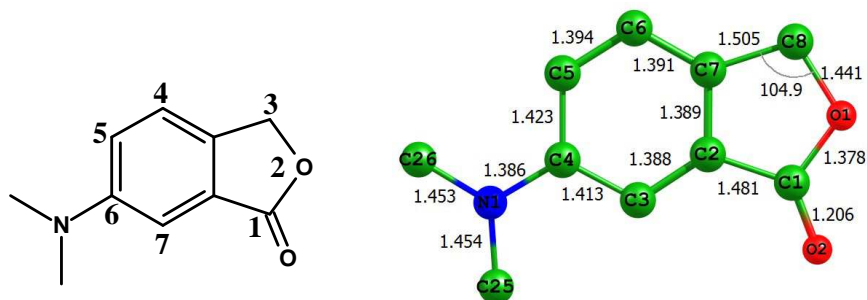


Fig. 7.1 Molecular formula of 6-DMAPd, with substitution positions numbered. b. DFT optimized ground state geometry of 6-DMAPd (6-31+G(d, p)) with indicated angle between C7-C8-O1 and bond lengths, with atom labelling scheme corresponding to that used for CVLB (Fig. 7.11).

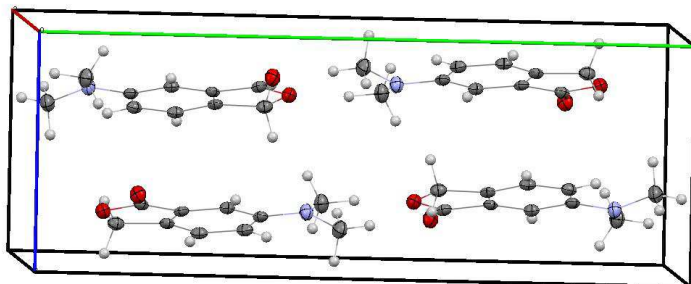


Fig. 7.2 A perspective view of the crystal structure (50% probability ellipsoids).

It is known that unsubstituted Pd as well as its nitro derivative (6-nitrophthalide) are both planar.²³⁵ In 6-DMAPd, the carbon atoms of Pd lie all in one plane (deviations from planarity are maximally 1.3°). Hence, the introduction of the alkyloamino substituent at the position 6 has no impact on the planarity of the Pd core. The nitrogen atom (N1) is moved out of the

benzene plane by 4°. Substitution of Pd with dimethylamino group at C4 has a minor effect on the length of C–C bonds and on the bond angles, the differences are within error limits of the measurements.

Bond	6-DMAPd		Pd
	X-ray [Å]	DFT [Å]	X-ray [Å]
C8–O1	1.454 (2)	1.441	1.455 (4)
C8–C7	1.497 (2)	1.505	1.491 (4)
C7–C6	1.384 (2)	1.391	
C6–C5	1.379 (2)	1.394	
C5–C4	1.423 (2)	1.423	
C4–C3	1.405 (2)	1.413	
C3–C2	1.387 (2)	1.388	
C2–C1	1.463 (2)	1.481	1.459 (5)
C1–O1	1.368 (2)	1.378	1.352 (4)
C1–O2	1.209 (2)	1.208	
C2–C7	1.383 (2)	1.389	
C4–N1	1.381 (2)	1.387	
N1–C26	1.447 (2)	1.455	
N1–C25	1.450 (2)	1.456	
O1–C8–C7	104.47 (0.13)	104.9	104.2 (3)

Tab. 7.1 Comparison of structural parameters for 6-DMAPd obtained from X-ray measurements at 100 K and DFT calculations (B3LYP/6-31+G(d,p)). The data for Pd is taken from the literature.²³⁶

DFT calculations reproduce well the relations between bonds, the bond lengths are, however, overestimated, usually by less than 0.01 Å (exceptions: C1–O1, C6–C5 and C1–C2). In the case of the C8–O1 bond, the calculations predict a bond shorter by 0.013 Å than the measured one.

7.1.1.2 Electronic structure

The absorption spectrum of 6-DMAPd (Fig. 7.3) consists of three absorption bands with increasing molar absorption coefficient, with maxima at 28500, 37500 and 44050 cm⁻¹ (in ACN). The first band shows significant solvatochromic effect on going from HEX to polar ACN (red shift by 1100 cm⁻¹). Based on MCD spectra and mirror symmetry of the absorption and emission spectra, it has been concluded that this band includes only one, S₀ → S₁ (HOMO→LUMO) electronic transition.¹²⁵

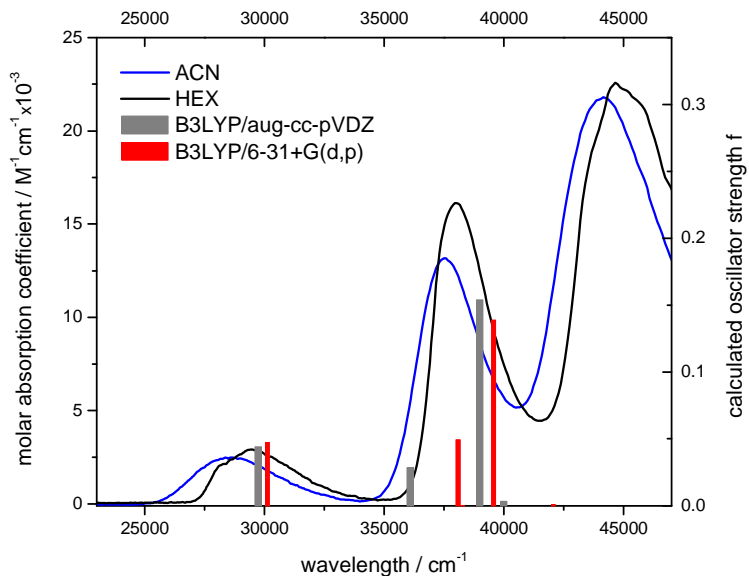


Fig. 7.3 Absorption spectra of 6-DMAPd in ACN and HEX shown as the molar absorption coefficient as a function of wavenumber. Bars represent the oscillator strengths of the first five transitions calculated with TD-DFT B3LYP/6-31+G(d,p) – in red, and TD-DFT B3LYP/aug-cc-pVDZ in grey.¹²⁴

The present calculations on 6-DMAPd are in agreement with those performed by Svartsov,¹²⁴ in spite of using different basis set in this work (B3LYP/6-31+G(d,p) vs B3LYP/aug-cc-pVDZ by Svartsov). The first electronic transition at 30130 cm^{-1} is essentially a HOMO→LUMO transition involving charge displacement from the amino nitrogen lone pair to the Pd moiety. The relatively low value of the calculated oscillator strength (0.0475) is reflected in low experimentally determined absorption transition dipole moments (1.47 D – 1.61 D in organic aprotic solvents¹²⁴), and points to a small overlap of molecular orbitals involved in the CT transition. The dipole moment of the vertically excited S_1 state equals 10.9 D, the experimentally determined value of the relaxed S_1 state is 11.2 D.¹²⁴ The ground state dipole moment obtained from calculations (6.6 D) is also in a very good agreement with the experimentally obtained value 6.2 D.¹²⁴

We performed calculations with two different basis sets, B3LYP/6-31G(d) and B3LYP/6-31+G(d,p). The orbital shapes obtained with the two basis sets are very similar, and the only difference is that in energy. Also, the order of orbitals in the B3LYP/6-31G(d)-based calculations was different than that obtained with B3LYP/6-31+G(d,p) and in Svartsov's calculations

(inter alia, HOMO–1 and HOMO–2 obtained with B3LYP/aug-cc-pVDZ are HOMO–2 and HOMO–1, respectively, B3LYP/6–31G(d)). In Fig. 7.4 the orbitals are presented in the order according to Svartsov’s calculations (and our calculations with the basis B3LYP/6–31G(d,p)).

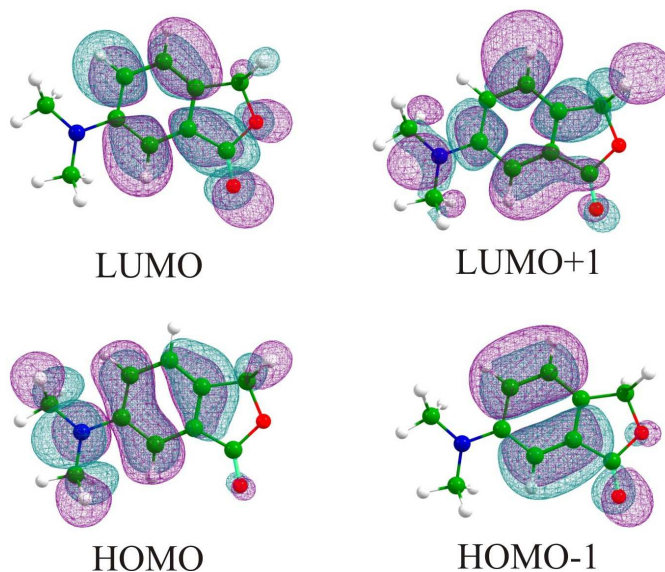


Fig. 7.4 Molecular orbitals of 6–DMAPd involved in the lower electronic transitions calculated with TDDFT method at B3LYP/6–31+G(d,p) level.

The analysis of molecular orbitals, together with absorption measurements and estimation of the excited state dipole moment (both in the Franck–Condon and the emitting states) imply that the the $S_1 \leftarrow S_0$ transition results in displacing charge from the amino group to the lactone ring of 6–DMAPd. This means, that the absorption transition populates optically an excited state with significant CT character.

7.1.1.3 Emission as a function of solvent polarity and temperature

The fluorescence spectrum of 6–DMAPd in aprotic solvents consists of one relatively broad band with full width at half maximum of about 3000 cm^{-1} . The fluorescence band shows a bathochromic shift (3600 cm^{-1}) when going from HEX to strongly polar ACN (Fig. 7.5, left). The quantum yields of fluorescence, Φ_{fl} , increase in line with medium polarity and reach the value of 0.73 in ACN. The fluorescence lifetimes reflect the same trend,

from several nanoseconds to tens of nanoseconds in polar media. The radiative and nonradiative rate constants decrease with increasing solvent polarity as do fluorescence lifetimes due to stabilization of the charge displacement in polar solvents. It suggests that the stabilization of the S_1 state by the medium polarity results in an increase in the singlet–triplet energy gap and hence makes the intersystem crossing less efficient.

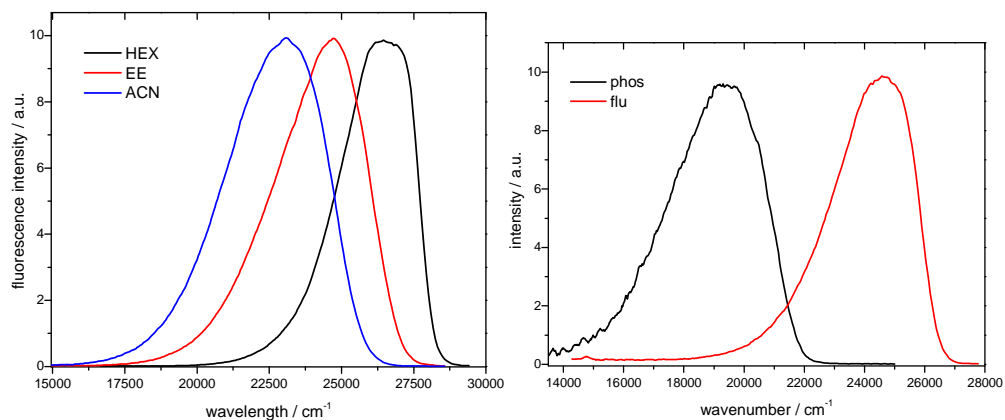
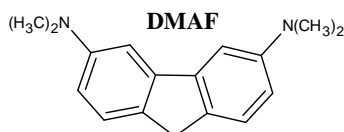


Fig. 7.5 Left: Emission spectra of 6-DMAPd in aprotic solvents at 295 K, as a function of solvent polarity. Right: flu – fluorescence (red) and phos – phosphorescence (black) spectra of 6-DMAPd recorded in butyronitrile at 77 K.

The low temperature spectra of 6-DMAPd in BTN are presented in Fig. 7.5 (right). The luminescence spectrum of 6-DMAPd consists of one fluorescence band with a maximum at 24650 cm^{-1} and a phosphorescence band of lower intensity at 19450 cm^{-1} . The fluorescence maximum in glass appears at lower energies than in hexane at 295 K, the red shift is equal to 1980 cm^{-1} .

7.1.2 3,6-bis(dimethylamino)fluorene (DMAF)

3,6-bis(dimethylamino)fluorene (DMAF) moiety is a structural subunit of CVLB acting in this molecule as an electron donor. From a purely structural point of view, this part of CVLB can be seen either as a new single chromophore with π -electronic system extending between the dimethylamino groups over the fluorene core, or as two dimethylaniline units of CVL rigidly



bridged via a C–C bond. In 1954 Barker and Barker¹⁶⁷ first synthesized DMAF and its triarylmethane analogues with the aim to solve the problem of fluorene structure, based on absorption spectra of the newly synthesized compounds. They discovered, that cationic fluorene-based analogues of triarylmethane dyes share a valuable feature, namely they have absorption bands in the near IR (absorption maxima for bridged MG analogue 480 nm, 505 nm, 850 nm, 955 nm; for bridged CV analogue: 470 nm, 647 nm, 850 nm).²³⁷ Since then, various extended fluorene derivatives were synthesised and studied in the context of their absorption in the near IR region.^{238,239,240}

7.1.2.1 Ground state structure

The crystal structure of DMAF was determined using X-ray diffraction. The results were compared with those from DFT calculations of the ground state geometry. The structural data is summarized in Fig. 7.4 and Tab. 7.2.

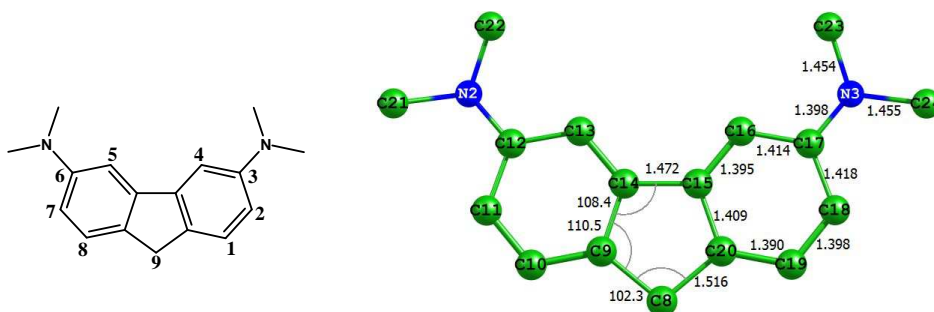


Fig. 7.6 Left: Structural formula of 3,6-bis(dimethylamino)fluorene with numbers marking substitution positions. Right: DFT (B3LYP/6-31G+(d,p)) optimized ground state geometry of DMAF with bond angles and lengths, and a scheme of atomic numbers corresponding to the respective scheme of CVLB (Section 7.2, Fig. 7.10). Due to C_{2v} symmetry, bond lengths and angles are shown for a half of the molecule only.

The crystal structure of DMAF belongs to the monoclinic symmetry space group, $P2_1/c$, with the following lattice parameters: $a = 6.35590$ (10) Å, $b = 23.2255$ (3) Å, and $c = 9.45330$ (10) Å and cell angles $\alpha = 90.00^\circ$, $\beta = 101.581$ (2)°, $\gamma = 90.00^\circ$. A unit cell contains four DMAF molecules (Fig. 7.7).

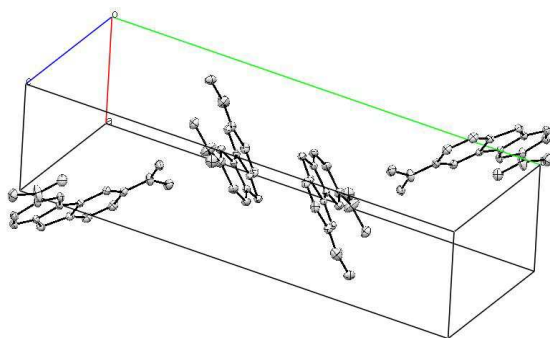


Fig. 7.7 A perspective view of the crystal packing of DMAF (50% probability ellipsoids).

DMAF has approximately C_{2v} symmetry, the bond lengths of both aromatic rings are equal within error limits (Tab. 7.2). The molecule is not planar, the two planes of the aromatic rings form an angle of 1.9° . In a crystallographic study on unsubstituted fluorene (at 159 K) Gerkin *et al.*²⁴¹ found that it was “slightly unplanar”, i.e., having a “V” shape (with a dihedral angle 1.3°). The bond lengths and angles of DMAF and unsubstituted fluorene reported in that work are comparable (within error limits), except for the case, where the involved carbon atoms form additional bonds with nitrogen, i.e., C17 and C12. Introduction of a dimethylamino group in the positions 3 (C17) and 6 (C12) of fluorene leads to elongation of the bonds formed by these atoms (C18–C17 and C17–C16 longer in DMAF than in fluorene by 0.033 \AA and 0.020 \AA , respectively).

In both, unsubstituted fluorene and in DMAF, all the bond lengths in the aromatic rings are from 1.384 to 1.413 \AA , thus in the typical range for carbon–carbon bonds in benzene derivatives. The bonds C8–C9 or C8–C20 are, however, significantly longer (1.504 \AA for fluorene and 1.516 \AA for DMAF) strongly suggesting saturated character of the bonds involving the C8 carbon atom. The length of the bond that links directly the two dimethylaminobenzene rings (C14–C15) in DMAF is 1.469 \AA , whereas in unsubstituted fluorene it is shorter by 0.003 \AA . In comparison, the length of the bond connecting two benzene rings in biphenyl is 1.507 \AA ²⁴², unlike fluorene, however, this molecule is not planar (torsional angle in crystal is equal to 35°).²⁴³

The calculated bond lengths and angles agree well with those determined in X-ray studies (Tab. 7.2), though the experiment gives

somewhat smaller values for the bond lengths (by 0.004 Å on average).

Bond length [Å]	DMAF	DMAF	Fluorene
	DFT	X-ray	X-ray
C8–C9	1.516	1.508	1.504 (2)
C8–C20	1.516	1.507	1.504 (2)
C15–C20	1.409	1.406	1.397 (2)
C20–C19	1.390	1.387	1.386 (2)
C19–C18	1.398	1.390	1.385 (2)
C18–C17	1.418	1.418	1.385 (2)
C17–C16	1.414	1.410	1.390 (2)
C16–C15	1.395	1.390	1.387 (2)
C14–C15	1.472	1.469	1.472 (3)
C9–C10	1.390	1.388	
C10–C11	1.398	1.392	
C11–C12	1.418	1.417	
C12–C13	1.414	1.410	
C13–C14	1.395	1.391	
C14–C9	1.409	1.406	
Bond angle [deg]			
C9– C8 –C20	102.3	102.28 (7)	102.7 (2)

Tab. 7.2 Structural parameters of DMAF. Structural parameters for DMAF obtained from X-ray measurements at 100 K and DFT calculations (B3LYP/6–31G+(d,p)). Fluorene parameters are taken from the literature.²⁴¹ In the X-ray analysis, all bond lengths of DMAF were determined with an accuracy of 0.001 Å.

The calculations predict that the aminofluorene moiety in DMAF is planar, with four methyl substituents being moved out of plane by 13°. The bond lengths in the two benzene rings fall in a range typical for carbon–carbon bonds in aromatic molecules (around 1.40 Å), i.e., 1.390–1.414 Å. The bonds C14–C15, C8–C9, C8–C20 are considerably longer indicating their saturated character and suggesting that there is no substantial delocalization of π -electrons from the aromatic rings. These observations are also in agreement with calculations performed by Platts and Howard²⁴⁴ on the structure of 4,5-dimethylamino substituted fluorene (4,5-DMAF). In the latter molecule, the interring C14–C15 bond is considerably longer (1.502 Å) than in DMAF (1.472 Å), which results presumably from steric strains between the two neighbouring dimethylamino substituents. Due to spatial proximity of the basic amino centers, 4,5-DMAF displays exceptionally high basicity constants and is an effective proton sponge.²⁴⁵

7.1.2.2 Electronic structure

The absorption spectrum of DMAF in different solvents, together with calculated transitions shown as bars representing oscillator strengths is presented in Fig. 7.8.

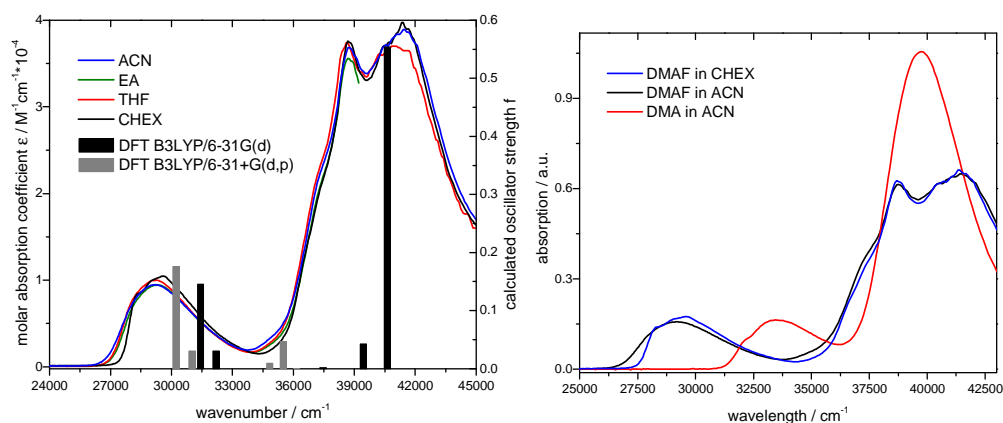


Fig. 7.8 Left: Electronic absorption spectrum of DMAF in ACN, EA, THF and CHEX plotted as the molar absorption coefficient as a function of wavenumber. The bars represent oscillator strengths of the first five transitions calculated with TDDFT B3LYP/6-31G(d) – in black, and TDDFT B3LYP/6-31+G(d,p) – in grey. Right: Electronic absorption spectrum of DMAF (in CHEX and ACN) compared with that of DMA in ACN.

The electronic absorption spectrum of DMAF consists essentially of one well separated band in the low energy region with a maximum at 29250 cm^{-1} in ACN, and a set of three overlapping bands with maxima around 37500 , 38750 and 41450 cm^{-1} . When changing the solvent to nonpolar cyclohexane, the first absorption band exhibits a minor blue shift of 350 cm^{-1} and a vibronic structure becomes visible. The values of the molar absorption coefficient at the band maximum are almost equal in all solvents, approximating $10000\text{ M}^{-1}\text{cm}^{-1}$. The DFT calculations predict two transitions within the first absorption band, assigned to HOMO→LUMO and HOMO-1→LUMO, however, only the first transition has a fully allowed character ($f = 0.1456$), the second having a five times lower oscillator strength. The molecular orbitals of DMAF are presented in Fig. 7.9.

The TDDFT calculations on DMAF were performed with two basis sets, B3LYP/6-31G(d) and B3LYP/6-31+G(d,p). Compared with B3LYP/6-31G(d), the transition energies calculated with the extended basis set are lower by 1300 , 1150 and by 2700 cm^{-1} for the first, second and third

transition, respectively. The vector of the ground state dipole moment of DMAF lies in the intersection of two planes, the fluorene plane and the symmetry plane (perpendicular to the fluorene plane and cutting the DMAF molecule into two identical halves); its calculated value equals to 2.2 D. The excited state dipole moment for the S_1 (Franck–Condon) state is twice as high (4.2 D) as that in the ground state, preserving its direction. The value of the calculated dipole moment of the S_2 state is only slightly higher than that of S_1 (4.7 D). Both $S_0 \rightarrow S_1$ and $S_0 \rightarrow S_2$ transitions have (π, π^*) character, with electron density being shifted from the alkylamino substituents to the fluorene core.

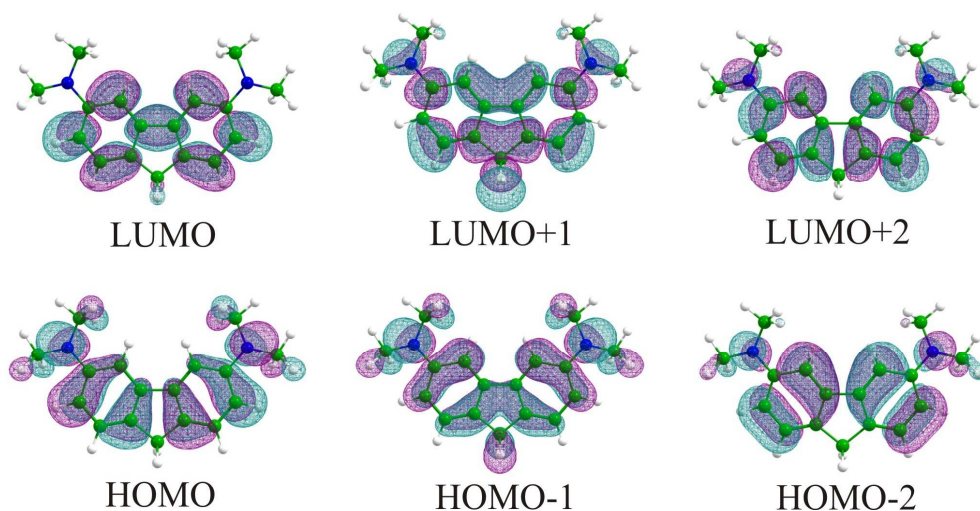


Fig. 7.9 Molecular orbitals of DMAF involved in the lower electronic transitions calculated with TD–DFT method at B3LYP/6–31+G(d,p) level.

	energy		f	μ	assignment		assignment	
	[eV]	[cm ⁻¹]		[D]		[%]		[%]
S_1	3.75	30233	0.1756	4.2	H → L	86		
S_2	3.85	31022	0.0300	4.7	H-1 → L	90		
S_3	4.32	34836	0.0091	4.2	H → L+1	80	H-1 → L+3	10
S_4	4.40	35507	0.0470	5.0	H-1 → L+1	48	H → L+3	36
S_5	4.48	36159	0.0002	3.3	H → L+2	71	H-2 → L	10

Tab. 7.3 Transition energies, oscillator strengths (f), dipole moments of the vertically excited states (μ), and orbitals (abbreviations: H– HOMO, L–LUMO) involved in the transition together with their shares in the transition as calculated with TDDFT B3LYP/6–31+G(d, p) method for DMAF. Only transition with the share larger than 10% are listed.

The absorption spectrum of DMAF can be also compared with the absorption of its parent molecule, fluorene. Generally, the absorption spectrum of fluorene both in polar and nonpolar solvents consists of three structured bands: the first band in the region between 33000–35000 cm^{-1} , the second band starting at 35000 cm^{-1} and ranging over 8000 cm^{-1} with the absorption coefficient of 10900 $\text{M}^{-1}\text{cm}^{-1}$,²⁴⁶ and the third, strongest band with the maximum at approximately 47000 cm^{-1} .²⁴⁷ Substitution of fluorene at position 9 results in bathochromic shift of the absorption spectrum and in broadening of the bands, but the three-band structure is preserved, similarly as for 9-phenyl-9-fluorenol.²⁴⁷ However, when fluorene is substituted along its long axis, for example at position 2, then the absorption spectrum is more perturbed, and only two bands can be distinguished instead of the three-bands structure. The first two long-wave bands melt into a single broad, structureless and red-shifted band, (for 2-dimethylamino-9-fluorenol, the maximum is at 25700 cm^{-1} , FWHM \sim 4000 cm^{-1}).²⁴⁷ This spectrum resembles closely the absorption of DMAF, where the first band, however, is narrower and shifted to shorter wavelengths by 4000 cm^{-1} .

The absorption spectrum of 3,6-dimethylaminofluorene hydrochloride in ethanol was published by Barker and Barker.¹⁶⁷ The first absorption band splits into two bands with maxima around 350 and 320 nm (28600 and 31250 cm^{-1}) with absorption coefficients of about 7000 $\text{M}^{-1}\text{cm}^{-1}$ and is not so well separated from the next band as in DMAF. Additionally, a red tail is visible. On the “blue” side of the hydrochloride spectrum two maxima can be observed, at 255 and 245 nm (39200, 40800 cm^{-1} , respectively) that correspond to 38750 and 41600 cm^{-1} bands in DMAF. The differences in the absorption spectra measured by Barker and Barker and by us might result from impurities (especially the red tail) or from hydrochloride effect on the electronic structure of 3,6-dimethylaminofluorene.

7.1.2.3 Emission as a function of solvent polarity and temperature

The emission spectra of DMAF consist of one structureless band with a full width at half maximum of approximately 3000 cm^{-1} in all solvents, except for CHEX, where the fluorescence band is narrower and shows a vibronic structure (Tab. 7.4). The solvatochromic shift of fluorescence spectra between CHEX and ACN is not significant (2550 cm^{-1}), presumably due to a relatively small dipole moment of the excited state as suggested by the calculations (Tab. 7.3). Accordingly, the value of the Stokes shift is also

small, about 4100 cm^{-1} for ACN (1900 cm^{-1} for CHEX). The fluorescence spectrum of DMAF in MeOH overlaps with that in ACN pointing to the absence of specific interactions between the molecule and protic solvent in the excited state.

Fluorene displays narrow and structured fluorescence band with two maxima at 33000 and 32000 cm^{-1} (FWHM = 2600 cm^{-1}) characterised by a minor Stokes shift (230 cm^{-1} in MCHEx).²⁴⁷ Amino derivatives of fluorene, such as 2-dimethylamino-9-fluorenone, display broadened fluorescence that is shifted towards longer wavelengths (25700 cm^{-1}). Such a substitution pattern results in lowering the energy of the emitting state in respect to the non-substituted fluorene.

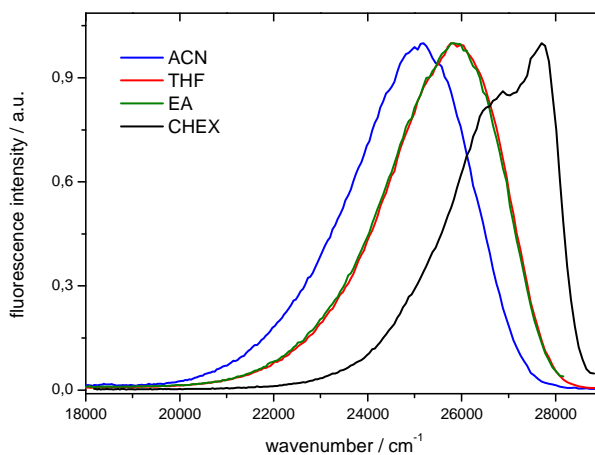


Fig. 7.10 Emission spectra of DMAF in aprotic solvents at room temperature.

The quantum yields of fluorescence of DMAF are around 0.4 in polar and medium polar solvents, whereas in nonpolar cyclohexane Φ_{fl} increases to around 0.6. The fluorescence lifetimes decay times seem to be solvent-independent and around 5 ns, however, in ACN τ_{fl} is about 20% longer than in other solvents. Fluorene is known to display fluorescence with the quantum yield of 0.8 and lifetime of 10 ns.²⁴⁶ Substitution of fluorene at position 2 with dimethylamino group leads to shortening of the fluorescence decay time (to 2.9 ns in HEX and 4.8 ns in DMSO).²⁴⁸

Tab. 7.4 Fluorescence data for DMAF in selected aprotic solvents

	$\bar{\nu}_{\text{abs}}$ [cm ⁻¹]	$\bar{\nu}_{\text{fl}}$ [cm ⁻¹]	FWHM [cm ⁻¹]	Φ_{fl}	τ_{fl} [ns]	k_{r} [10 ⁻⁷ s ⁻¹]	k_{nr} [10 ⁻⁷ s ⁻¹]	M_{abs} [D]	M_{flu} [D]	k_0 [10 ⁻⁷ s ⁻¹]	τ_0 [ns]
CHEX	29600	27700	2450	0.62	4.7	13.2	8.1	3.6	2.6	18.3	5.5
EA	29300	25850	2950	0.41	5.2	7.9	11.3	3.3	2.4	13.9	7.2
THF	29300	25900	2950	0.44	4.9	8.9	11.5	3.4	2.4	15.4	6.5
ACN	29250	25150	3000	0.43	6.4	6.7	8.9	3.5	2.4	13.2	7.6

Abbreviations: $\bar{\nu}_{\text{fl}}$ –maximum of the fluorescence band, FWHM– full width at half maximum, Φ_{fl} and τ_{fl} – fluorescence quantum yield and decay time, respectively; k_{r} – radiative rate constant ($k_{\text{r}}=\Phi_{\text{fl}}/\tau_{\text{fl}}$), k_{nr} – nonradiative rate constant ($k_{\text{nr}}=(1-\Phi_{\text{fl}})/\tau_{\text{fl}}$), k_0 – radiative rate constant calculated with the Strickler–Berg formula, τ_0 –natural lifetime calculated from k_0 .

The experimentally determined radiative rate constants of DMAF increase with growing solvent polarity, from $6.7 \times 10^7 \text{ s}^{-1}$ in ACN to $13.2 \times 10^7 \text{ s}^{-1}$ in CHEX, and this trend is also reflected in the k_0 values calculated using the Strickler–Berg²⁴⁹ formula:

$$k_0 = 8 \times 2303 c \pi \bar{\nu}^{-2} n^2 N_A^{-1} \int \epsilon d\bar{\nu} \quad \text{Eq. 7.1}$$

where c is the speed of light in vacuum, n – refractive index of the medium, N_A – Avogadro's number, $\bar{\nu}$ – frequency of the absorption transition and ϵ – molar absorption coefficient.

Derivation of the Strickler–Berg equation assumes, i. a., that only a single electronic transition is responsible for the integrated absorption band. In the case of DMAF the calculations indicate the presence of two transitions within the first absorption band, although of significantly different oscillator strengths (for $S_0 \rightarrow S_2$ it is lower by a factor of 5, pointing to a low probability of this transition; Tab. 7.3). Higher values of k_0 than of k_{r} by more than 50% (and for CHEX even by 70%) are presumably due to a non-zero contribution from the second transition to the integrated absorption band and not to significant changes in the nature of the electronic transition during the excited state relaxation. Accordingly, the natural lifetimes of the excited state (i.e., those calculated from the Strickler–Berg formula), τ_0 , are presumably underestimated being around only 20% longer than the measured fluorescence lifetimes τ_{fl} .

The absorption transition dipole moments were calculated using the equation 4.2 (Section 4.4). Their values are solvent independent and are around 3.5 D pointing to an allowed character of the first transition. The

same holds for fluorescence transition dipole moments, their values, however, are by about 25% lower than in the case of absorption transition dipole moments (around 2.4 D). The M_{abs} values were calculated based on the integrated first absorption band and most likely are overestimated due to the contribution from the $S_0 \rightarrow S_2$ transition to the first absorption band.

The low temperature spectra of DMAF in butyronitrile are presented in Fig. 7.11. Both, fluorescence and phosphorescence spectra are structured. The fluorescence band has a maximum at 26500 cm^{-1} and the band's shape closely resembles that recorded at room temperature in CHEX, preserving the same vibrational structure. The long-lived emission spectrum displays vibrational structure with four distinguished bands with maxima at 22100 , 21350 , 20650 and 19300 cm^{-1} and an additional band is seen as a "shoulder" at approximately 17800 cm^{-1} . The triplet (T_1) state energy has been estimated to 22100 cm^{-1} (2.74 eV) based on the highest energy maximum observed in the phosphorescence spectrum.

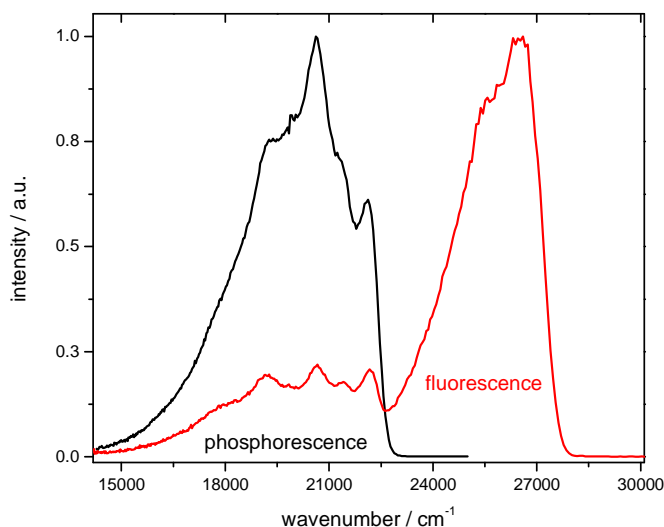
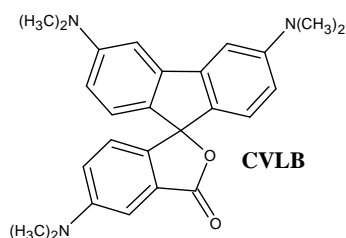


Fig. 7.11 Total luminescence (red) and phosphorescence (black) of DMAF in butyronitrile at 77 K.

7.2 Ground state structure of CVLB

CVLB is a structural analogue of crystal violet lactone (CVL), differing only by presence of an additional carbon–carbon bond (C14–C15) bridging two dimethylaniline units. Linking the two DMA groups into a fluorene moiety does not only rigidize the structure, but more importantly,



results in formation of a new chromophore – 3,6–bis(dimethylamino)fluorene (DMAF) within the CVLB molecule. Thereby, the tetrahedral central carbon atom in CVL transforms into a *par excellence* spiro carbon (C8), forcing perpendicular orientation of the structural components (“halves”) of the CVLB molecule: DMAF and 6–DMAPd. The change from a

triarylmethane–like structure into a spiro arrangement has great impact on the electronic structure and consequently on the photophysical properties of CVLB, primarily by allowing for intramolecular interactions between structural subunits that are not possible in CVL due to inappropriate conformation around the C8 atom.

This Chapter presents the structure of CVLB in solid state and in the gas phase, as studied by both experimental (crystallography, X–ray analysis) and theoretical methods (DFT). The structure of CVLB is compared with those of its subunits and confronted with structurally related molecules, CVL and rhodamine B lactone (LRB). Finally, the structure of MGLB, a structural analogue of malachite green lactone (MGL), which differs from CVLB by the absence of dimethylamino group at C6, is presented and discussed in relation to the CVL – MGL pair.

The crystal structure of CVLB belongs to the monoclinic symmetry space group, $P2_1/c$, with the following lattice parameters: $a=11.711(1)$ Å, $b=19.445(1)$ Å and $c=19.382(1)$ Å. The structure contains two independent CVLB molecules – molecule 1 and molecule 2 – with almost identical symmetry (Fig. 7.12, right, Tab. 7.5), similarly as in structurally related LRB.^{250,251} Bond lengths and bond angles in molecule 1 and molecule 2 are equal within error limits, except for the bonds between C9–C14, C1–C2 and C1–O2 due to significantly different surroundings. Spatial arrangements of substructures in molecule 1 and molecule 2 are also very similar, however, in molecule 2 the methyl group with C26 carbon is moved off the 6–DMAPd plane (the angle between the N1–C26 bond and 6–DMAPd plane is 15°).

Tab. 7.5 Structural data on CVLB, DMAF, 6-DMAPd and MGLB.

Bond length [Å]	DFT	CVLB		DMAF	6-DMAPd	MGLB	
		X-ray		X-ray	X-ray	DFT	X-ray
		Mol. 1	Mol. 2				
C8–O1	1.475	1.483	1.488		1.454	1.473	1.481
C8–C7	1.516	1.510	1.507		1.497	1.518	1.506
C8–C9	1.522	1.517	1.520	1.508		1.521	1.510
C8–C20	1.522	1.516	1.514	1.507		1.521	1.510
C15–C20	1.405	1.403	1.400	1.406		1.405	1.400
C20–C19	1.387	1.384(3)	1.384	1.387		1.388	1.376
C19–C18	1.397	1.386(3)	1.385(3)	1.390		1.397	1.387
C18–C17	1.418	1.416	1.413	1.418		1.419	1.406
C17–C16	1.418	1.415(3)	1.408	1.410		1.418	1.406
C16–C15	1.391	1.382	1.381	1.390		1.391	1.381
C14–C15	1.477	1.481	1.478	1.469		1.477	1.472
C9–C10	1.387	1.382(3)	1.379(3)	1.388		1.388	1.380
C10–C11	1.397	1.391	1.392	1.392		1.397	1.384
C11–C12	1.418	1.409(3)	1.412(3)	1.417		1.419	1.408
C12–C13	1.418	1.407(3)	1.411(3)	1.410		1.418	1.411
C13–C14	1.391	1.388	1.383	1.391		1.391	1.380
C14–C9	1.405	1.394	1.403	1.406		1.405	1.395
C7–C6	1.393	1.391	1.391		1.384	1.394	1.387
C6–C5	1.394	1.383	1.382		1.379	1.398	1.381
C5–C4	1.425	1.420	1.416		1.423	1.406	1.390
C4–C3	1.413	1.398	1.399		1.405	1.395	1.382
C3–C2	1.391	1.392	1.389		1.387	1.396	1.393
C2–C1	1.482	1.478	1.468		1.463	1.482	1.468
C1–O1	1.369	1.366	1.361		1.368	1.369	1.349
C1–O2	1.211	1.203	1.210		1.209	1.210	1.207
C2–C7	1.387	1.376	1.377		1.383	1.390	1.375
Bond angle [deg]							
C9–C8–C20	101.8	102.1(1)	102.1(1)	102.3(1)		101.9	102.4(1)
C9–C8–O1	110.4	110.2(1)	110.0(1)			110.7	110.1(1)
C20–C8–O1	110.4	111.3(1)	108.0(1)			110.7	110.5(1)
O1–C8–C7	102.6	102.3(1)	101.8(1)		104.5(1)	102.8	102.2(1)
C20–C8–C7	115.9	116.2(1)	117.4(1)			115.5	116.1(1)
C9–C8–C7	115.9	115.0(1)	116.5(1)			115.5	115.7(1)
Torsion angle [deg]							
DMAF and 6-DMAPd	90	89.9	88.5		planar	planar	89.2

In the X-ray analysis, all bond lengths of CVLB were determined with an accuracy of 0.002 Å (other values of standard deviations are given in parentheses). For MGLB the standard deviation for determination of interatomic distances is 0.002 Å, and for bond angles 0.15°. All bond lengths in DMAF and 6-DMAPd were determined with an accuracy of 0.001 Å and 0.002 Å, respectively. DFT calculations (ground state optimization) were performed with a B3LYP/6-31+G(d,p) basis set.

DFT calculations predict that both CVLB subunits, 6-DMAPd and DMAF, are planar: one plane contains the fluorene nuclei C8–C20 and the nitrogen atoms N2 and N3 from the dimethylamino substituents, while the other one includes the phthalide nuclei C1–C8, O1, O2 as well as the nitrogen atom N1 from the dimethylamino substituent. Both planes form 90° angle, which is typical for spiro-molecules. The structures of insulated DMAF and 6-DMAPd chromophores determined using quantum mechanical calculations are also planar, bond lengths agree very well with the respective bond lengths in CVLB, the maximum deviation being 0.005 Å. The only exceptions are bonds formed by the C8 central carbon atom: C8–O1 (6-DMAPd: 1.441 Å, CVLB: 1.475 Å) and C8–C7 (6-DMAPd: 1.505 Å, CVLB: 1.516 Å). The elongation of these bonds in CVLB is due to the effect of substitution at C8 in 6-DMAPd, especially the C8–O1 bond is sensitive to such structure modifications.^{185,252} Perpendicular arrangement of DMAF and 6-DMAPd around the tetrahedral carbon atom forces the molecules to be rigid and results in restriction of conformational movements.

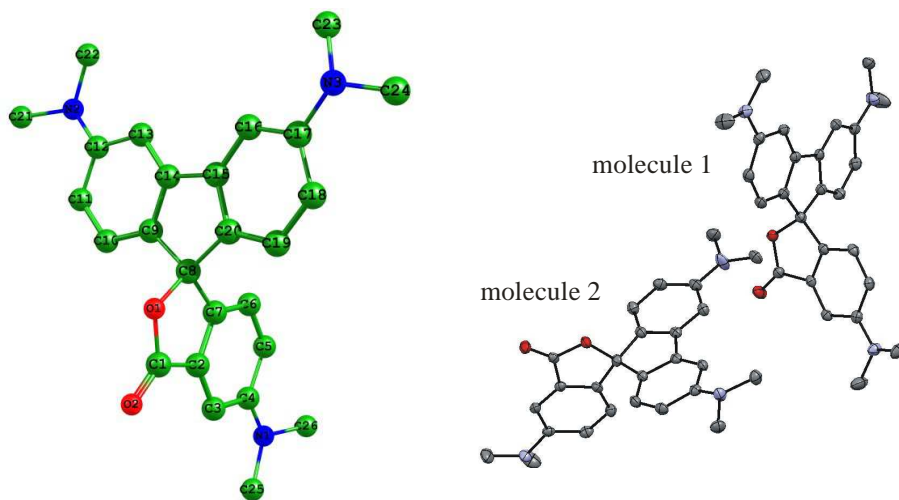


Fig. 7.12 Left: Atomic numbering scheme for of CVLB, also valid for for structurally related molecules with similar carbon framework and subunits. Right: A perspective view of the crystal structure (50% probability ellipsoids), excluding hydrogen atoms. An asymmetric unit consists of two independent CVLB molecules.

The structure of CVLB as obtained from the X-ray analysis shows small deviations from planarity for the DMAF subunit (smaller than 2°) and none for 6-DMAPd (the lactone and the benzene ring are coplanar). When compared with crystal structures of insulated subunits, the biggest

differences in bond lengths are found for all bonds formed by the central C8 carbon atom, for CVLB they are longer by approximately 0.01 Å. These differences are due to the presence of substituents in CVLB at C8 as opposed to the subunits where the C8 carbon has two hydrogen substituents.

The geometry of CVLB, especially around the spiro carbon atom (C8) can be compared not only with its subunits but also with the experimentally determined geometries of structurally related molecules, CVL²⁵³ and LRB.^{250,251} The results are summarized in Tab. 7.6.

Bonds	CVL ²⁵³	LRB ²⁵⁰	LRB ²⁵¹	CVLB	
	[Å]				
C8–O1	1.491 (4)	1.515 (5)	1.495 (1)	1.483 (2)	[Mol. 1]
		1.518 (5)	1.497 (1)	1.488 (2)	[Mol. 2]
C8–C7	1.514 (5)			1.510 (2)	[Mol. 1]
				1.507 (2)	[Mol. 2]
C8–C9	1.518 (5)			1.517 (2)	[Mol. 1]
				1.520 (2)	[Mol. 2]
C8–C20	1.518 (5)			1.516 (2)	[Mol. 1]
				1.514 (2)	[Mol. 2]
C1–O1	1.355 (4)		1.348 (1)	1.366 (2)	[Mol. 1]
				1.361 (2)	[Mol. 2]
Angles	[deg]				
C7–C8–O1	101.8 (3)	100.6 (3)		102.3 (1)	[Mol. 1]
		101.2 (3)		101.8 (1)	[Mol. 2]

Tab. 7.6 Selected geometric parameters for CVLB compared with structurally related molecules: CVL and lactone of rhodamine B (LRB). Standard deviations for bond lengths and angles are given in parentheses.

All the three C–C bonds formed by the central spiro atom (C8) are of comparable length both in CVL and CVLB, indicating that the delocalization of electrons from aromatic rings of DMA and DMAF does not extend to the central carbon atom. The distance between C8–O1 varies with different substitutions at C8, and is the shortest in CVLB, where DMAF is attached (1.483 Å). In CVL with DMA groups replacing DMAF the bond is elongated to 1.491 Å. The C–O bond is the longest one when aminoxanthene moiety is attached to phthalide (although there are inconsistencies between different X-ray data^{250,251}). The difference in C–O bond lengths for these three molecules reflects the extreme sensibility of this bond to the substitution at the position 3 (C8) of phthalide.¹⁸⁵ It is known that in phthalide-based spirocyclic compounds the C–O bond length varies from 1.45 Å in

iso(spirobenzofuran-xanthenones)²⁵⁴ to 1.527 Å which is typical for γ -lactones.^{255,256}

The angle C7–C8–O1 seems to be almost unaffected by different chromophores attached to the central carbon atom (around 102°). Moreover, in CVL and in CVLB the lactone and the benzene rings (C2–C7) are coplanar, however in structurally related LRB the two planes form an angle of 0.77°.²⁵⁰

Formally – the structures of CVLB and MGLB are very similar, chemically, the only difference between those two molecules is the absence (in MGLB) of the dimethylamino group at position 6 of phthalide (C24). The presence of the dimethylamino group in the phthalide moiety is crucial for the crystallographic structure and packing. In MGLB only four molecules are inside a unit cell, in CVLB, since there are two independent molecules in an asymmetric unit, the number of molecules in the unit cell is eight. The melting points of both molecules are very high (251–253°C for CVLB, literature values: 237–242°C;²⁵⁷ 244–246°C;²⁵⁸ 240–245°C¹⁵⁸), and for MGLB two temperatures were observed: 289°C and 312 – 313°C. This fact together with the densely packed unit cell indicates strong interactions between molecules in the solid state.

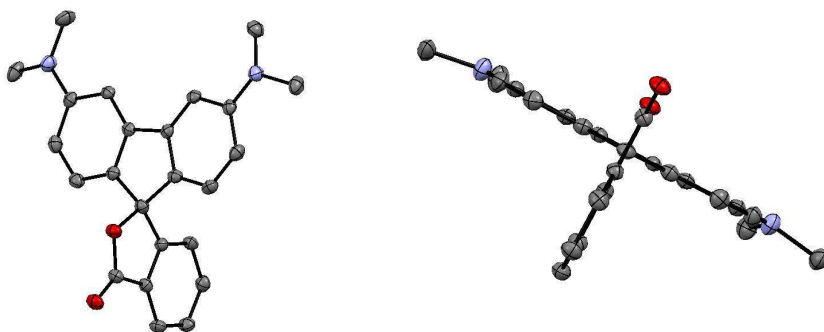


Fig. 7.13 Left: A perspective view of the crystal structure of MGLB (50% probability ellipsoids), excluding hydrogen atoms. Right: Projection of MGLB illustrating perpendicular arrangement of DMAF and 6-DMAPd moieties.

The absence of the dimethylamino group in the phthalide moiety in MGLB leads to modifications of the bond lengths where the C4 carbon is involved, i.e., C4–C5 and C4–C3 (Tab. 7.5). These bonds are remarkably shorter in MGLB (by 0.028 Å and 0.017 Å on average, respectively) than in CVLB. Interestingly, the DMAF moiety in MGLB is almost planar, with very small deviations from planarity (about 0.5°), whereas in CVLB the

deviations are four times bigger. The bond lengths in this subunit in both molecules are of comparable value (the largest difference for the C14–C15 bond, 0.009 Å). The two chromophores in MGLB, DMAF and Pd, are perpendicular to each other.

7.3 Electronic absorption in aprotic solvents

Room temperature absorption spectra of CVLB in three solvents of different polarity (ACN, EA, and MCHEx) together with the calculated gas phase transition energies (TD–DFT B3LYP/6–31+G(d,p)) are depicted in Fig. 7.14.

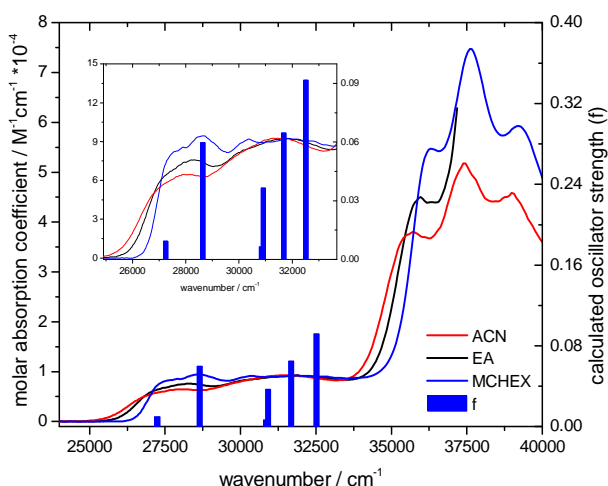


Fig. 7.14 Absorption spectra of CVLB recorded in solvents of different polarity (ACN, EA, MCHEx) shown as molar absorption coefficient (except for the spectrum in MCHEx, which is normalized to the two other spectra at 31900 cm^{-1} ; the molar absorption coefficient could not be determined in MCHEx due to poor solubility of CVLB); bars represent the calculated oscillator strengths for the first six transitions in CVLB computed with TDDFT B3LYP/6–31+G(d,p).

The spectrum of CVLB does not show traces of absorption in the 450–800 nm region (i.e., from 22200 to 12500 cm^{-1} , respectively), before and after irradiation, indicating lack of coloured ionic species. The spectrum consists of two low energy bands of comparable intensity with unclear positions of band maxima around 27500 cm^{-1} and 31600 cm^{-1} (in ACN). Higher energy transitions are significantly stronger and form a characteristic

set of three bands with maxima around 35600, 37400 and 39100 cm^{-1} (in ACN). The molar absorption coefficient, ϵ , for the maxima of the first two bands is 7000 $\text{M}^{-1}\text{cm}^{-1}$ and 9000 $\text{M}^{-1}\text{cm}^{-1}$, respectively, in ACN), however, in the set of the three bands of higher energies the ϵ values reach 37000, 52000, and 46000 $\text{M}^{-1}\text{cm}^{-1}$.

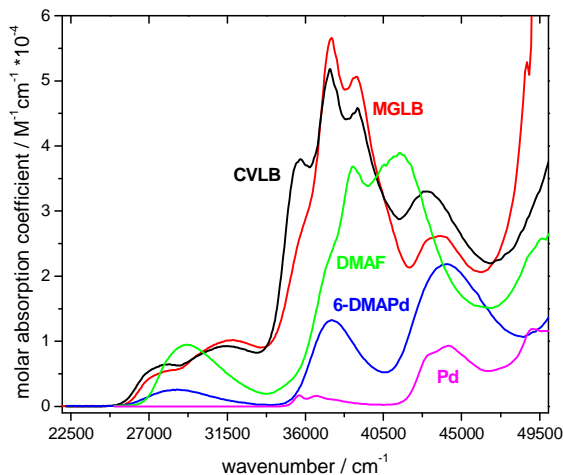


Fig. 7.15 Comparison of the molar absorption coefficient determined in ACN at room temperature for CVLB and its subunits, DMAF and 6-DMAPd, and for MGLB and Pd.

The absorption spectrum of CVL in low energy region is a superposition of transitions localized on structural subunits, 6-DMAPd and DMA,⁸² the spectrum of CVLB cannot be, however, considered as such one (Fig. 7.15). Similar maximum positions of the first absorption bands in CVLB subunits: DMAF (29150 cm^{-1} , $\epsilon_{\text{max}}=9350 \text{ M}^{-1}\text{cm}^{-1}$) and 6-DMAPd (28550 cm^{-1} , $\epsilon_{\text{max}}=2550 \text{ M}^{-1}\text{cm}^{-1}$) in ACN indicate that the S_1 states in these molecules are nearly degenerate. On the other hand, the energies of the S_1 states of DMAF and Pd ('halves' of MGLB) differ considerably, with absorption maxima of the lowest absorption band at 29600 cm^{-1} ($\epsilon_{\text{max}}=10800 \text{ M}^{-1}\text{cm}^{-1}$, CHEX), and 35950 cm^{-1} ($\epsilon_{\text{max}}=1700 \text{ M}^{-1}\text{cm}^{-1}$, HEX), respectively. The lowest absorption band of 6-DMAPd includes a single $S_0 \rightarrow S_1$ transition which is not affected by any mixing with other electronic singlet states ($\Delta E(S_2 - S_1) = 6300 \text{ cm}^{-1}$)¹²⁴ and corresponds essentially to a HOMO-LUMO transition involving a displacement of charge density from the nitrogen lone pair to the benzene ring.¹²⁴ For DMAF, the TDDFT computations indicate that the lowest absorption band includes two electronic transitions ($S_0 \rightarrow S_1$ and $S_0 \rightarrow S_2$) separated from each other by a

low energy gap (about 800 cm^{-1}). Moreover, the presence of the second low energy absorption band (maximum in ACN at about 31500 cm^{-1}) suggests considerable ground–state interactions of the two perpendicular halves, since none of the insulated substructures absorbs in that spectral region. A more detailed analysis of absorption spectra in non polar polar solvents (Fig. 7.16) shows, however, that the first absorption band of CVLB resembles closely that of DMAF, but is red–shifted by $800 - 930\text{ cm}^{-1}$. The analysis of molecular orbitals (see next section) strongly suggests that the second band in CVLB is mainly due to cumulated (red and blue) shifts of other transitions from both DMAF and 6–DMAPd moieties. In addition, striking similarity of the CVLB and MGLB electronic absorption spectra in the low–energy region proves that the presence of the dimethylamino group in the 6–DMAPd moiety (which has a huge effect on the photophysics of phthalides) translates in a minor effect on the electronic transitions in CVLB as compared with MGLB.

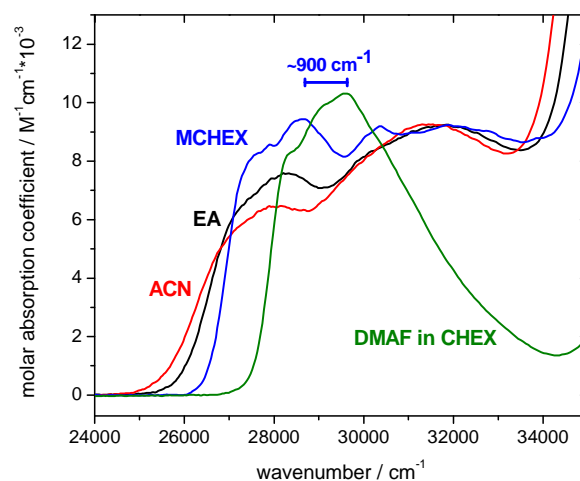


Fig. 7.16 Absorption spectra of CVLB in MCHEx (blue), EA (black) and ACN (red) in the low energy region. The spectra for CVLB in EA and ACN represent the molar absorption coefficient as a function of wavenumber, the spectrum in MCHEx was normalized to the two other spectra at 31900 cm^{-1} (the maximum of the second absorption band in EA).

Given significant differences in electronic structures of 6–DMAPd and Pd, a low molar absorption coefficient of 6–DMAPd below 35000 cm^{-1} , and a much higher one of DMAF, one can conclude that the low–energy absorption transitions in CVLB and MGLB are essentially those localized on the DMAF chromophore modified due to interaction with the orbital(s) of

the phthalide moiety, in particular those extending over the lactone ring. This is confirmed not only by the analysis of molecular orbitals as shown below, but also by an unusual solvent dependence of the low energy part of the CVLB absorption spectrum: a bathochromic shift of the lowest absorption band maximum is accompanied by a noticeable decrease of ϵ_{\max} in this band, with unchanged ϵ in the second band (Fig. 7.16). Moreover, a two band structure observed in acetonitrile between 25000 and 34000 cm^{-1} transforms into a four maximum structure in cyclohexane, suggesting that the spectral region includes more than two separate electronic transitions in CVLB. This unusual solvatochromism was also observed for MGLB and can be explained by assuming that the low energy bands in both molecules are composed of a number of electronic transitions that respond differently to varying solvent polarity: ones red-shift more, while the other are apparently less sensitive. In such a case, the net result of increasing solvent polarity would be to broaden the absorption band and to decrease its peak intensity, i.e., exactly what is observed for CVLB. Magnetic circular dichroism spectra recorded for both molecules in different solvents reproduced the absorption spectrum in the region of the first two bands, with a negative sign, and were inconclusive as to allow for any statements concerning the number of transitions in the observed wavelength region.

Calculations of molecular orbitals and transition energies of CVLB, DMAF and 6-DMAFd were performed with the TDDFT method using the basis set B3LYP/6-31+G(d,p). For CVLB, the transition energies compared with absorption spectra are shown in Fig.7.14, additionally, the energies of the vertical electronic transitions with oscillator strengths for the first six transitions are presented in Tab. 7.7.

	energy		f	μ [D]	assignment	share [%]
	[eV]	[cm^{-1}]				
S ₁	3.38	27245	0.0093	18.0	HOMO → LUMO	99.2
S ₂	3.55	28645	0.0597	7.1	HOMO → LUMO+1	96.4
S ₃	3.82	30839	0.0064	19.1	HOMO-1 → LUMO	87.2
S ₄	3.83	30916	0.0366	9.6	HOMO-2 → LUMO	85.1
S ₅	3.93	31680	0.0646	8.2	HOMO-1 → LUMO+1	94.5
S ₆	4.03	32518	0.0916		HOMO → LUMO+2	83.9

Tab. 7.7 Transition energies, oscillator strengths (f), dipole moments of the vertically excited states (μ), and orbitals involved in the transition together with their shares, calculated with TD-DFT B3LYP/6-31+G(d,p) method for CVLB.

Calculated vertical transitions for the optimised ground state geometry of CVLB are in reasonable agreement with the experimentally recorded absorption transitions. The first two absorption bands comprise at least 6 electronic transitions. Calculations predict that the first (S_1) and the third (S_3) transition of CVLB have considerable CT character and have very small oscillator strengths. Since the DFT is known to underestimate the energy of states with large charge displacement, the position of these transitions must be taken with care. Hence, in further analysis these transitions will be neglected.

7.4 Molecular orbitals

The non-additivity of absorption transitions together with saturated character of the bonds formed by the spiro carbon atom (C8) indicate that the π -electronic systems of DMAF and 6-DMAPd (Pd) moieties do not interact through bonds, and the inter-moiety ground state interaction results from stereoelectronic effects. Perpendicular arrangement of almost planar DMAF and planar 6-DMAPd subunits in CVLB allows for spiroconjugation.

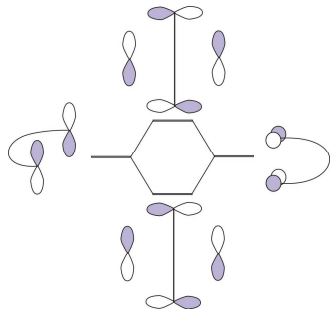


Fig. 7.17 Relative phases of the terminal orbitals at atoms around the spiro carbon atom. Molecular orbitals of the perpendicular halves of a spiro molecule are antisymmetric with respect to the two bisecting planes.

In spirocyclic molecules spiroconjugation leads to creation of new molecular orbitals enabling delocalization of electronic density over the entire molecule.^{259,260} Spiroconjugation between two π -electronic subsystems can take place, provided that their molecular orbitals have the same symmetry, i.e., are antisymmetric with respect to the two bisecting planes, leading to a nonzero overlap (Fig. 7.17). The interaction between a pair of orbitals of suitable symmetry gives rise to two new orbitals spanning over the entire molecule, one of a lower energy that corresponds to the binding combination, and one of a higher energy representing the antibonding combination of the two initial orbitals. Though nearly degenerate orbitals allow for maximizing the spiroconjugation,^{261,262, 263} a

number of systems with quite a large energy gap between the HOMO and LUMO orbitals, including spiroconjugated CT dyes reported by Maślak *et al.*,²⁶⁴ provide examples of effective spiroconjugation. In our case, the symmetry analysis performed for orbitals from HOMO-4 to LUMO+4 for both subunits shows that antisymmetric orbitals with the potential to spiroconjugate are HOMO, HOMO-2 and HOMO-4 of DMAF and HOMO, HOMO-4 of 6-DMAPd (in CVLB), and HOMO-3 of Pd (in MGLB).

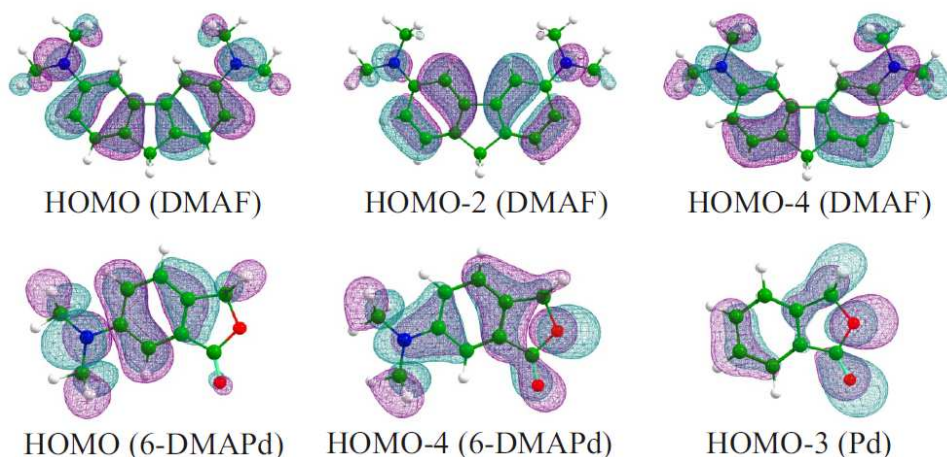


Fig. 7.18 Orbitals of DMAF, 6-DMAPd, and Pd that are antisymmetric with respect to the two bisecting planes of CVLB (MGLB).

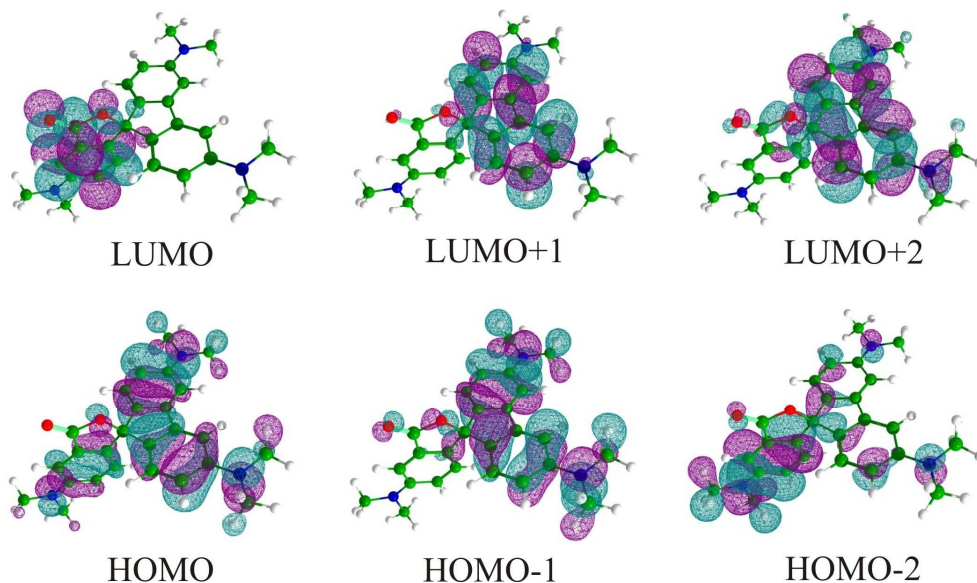


Fig. 7.19 Molecular orbitals of CVLB.

Except for HOMO and HOMO–2, graphical representations of the analysed Kohn–Sham molecular orbitals in CVLB indicate that they are localised on the subunits and their electron density distributions are very similar to the corresponding orbitals in isolated DMAF or 6–DMAPd molecules (Fig. 7.19). For instance, the LUMO of CVLB is essentially that localised on 6–DMAPd moiety (corresponding to the LUMO of 6–DMAPd), whereas the LUMO+2, LUMO+1 and HOMO–1 are virtually the unperturbed LUMO+1, LUMO and HOMO–1 of the DMAF moiety, respectively (Fig. 7.19). The energy gap between the LUMO and LUMO+1 orbitals in CVLB is rather small (1380 cm^{-1}), suggesting that they may inverse their positions in energy, and each of them can be the lowest unoccupied molecular orbital of CVLB, depending on interactions with the solvent. Though substantial parts of HOMO and HOMO–2 orbitals of CVLB bear significant resemblance to the corresponding localized orbitals of CVLB subunits, i.e., HOMO of DMAF and HOMO of 6–DMAPd, respectively, they are essentially 3–dimensional orbitals extending over the whole CVLB molecule. Compared with the HOMO in DMAF, the HOMO in CVLB is destabilized by about 1500 cm^{-1} , whereas the HOMO–2 in CVLB is stabilized by some 500 cm^{-1} vs. the HOMO in 6–DMAPd, resulting in a HOMO (DMAF) – HOMO (6–DMAPd) splitting of about 2000 cm^{-1} (0.25 eV). The splitting, but also the electron density distributions, indicate spiroconjugative coupling between the HOMO orbitals of the halves to yield HOMO and HOMO–2 in CVLB. The splitting energy compares well with the computed spiroconjugation energies reported for other spirocyclic molecules with different halves²⁶⁵ and can be identified with spiroconjugation energy in CVLB.

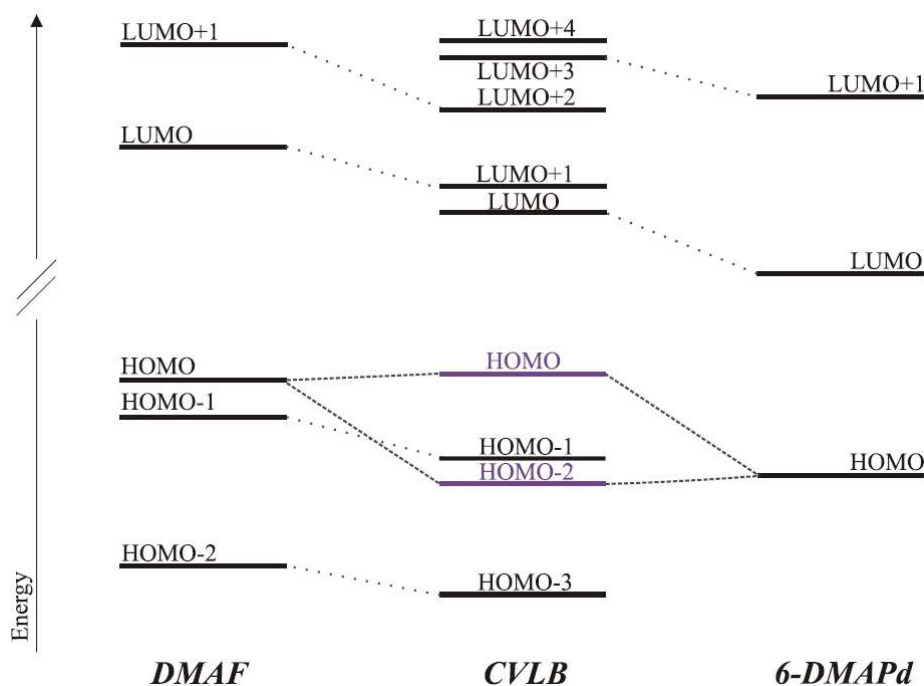


Fig. 7.20 Energy diagram for CVLB, DMAF and 6-DMAPd. Marked in violet are orbitals of CVLB (HOMO and HOMO-2) formed via spiroconjugation of HOMO orbitals of subunits (dashed lines). Dotted lines connect orbitals of CVLB with the respective orbitals of subunits.

The spiroconjugation effect and the destabilization of the HOMO orbital combined with much smaller changes of LUMO and LUMO+1 energies, are primarily responsible for the bathochromic shift of the first absorption band in CVLB as compared to DMAF (900 cm^{-1} , Fig. 7.12). Spiroconjugative stabilization of the HOMO-2 leads to the blue shift of S_4 transition and formation of the second absorption band (maximum at 31500 cm^{-1} in ACN) in CVLB. Moreover, the S_5 transition (HOMO-1 \rightarrow LUMO+1) in CVLB corresponding to the HOMO-1 \rightarrow LUMO in DMAF also experiences a blue shift due to stabilization of the HOMO-1 in CVLB (in respect to DMAF). Within the first 6 transitions of CVLB that were analysed, no transitions localised purely on 6-DMAPd are present.

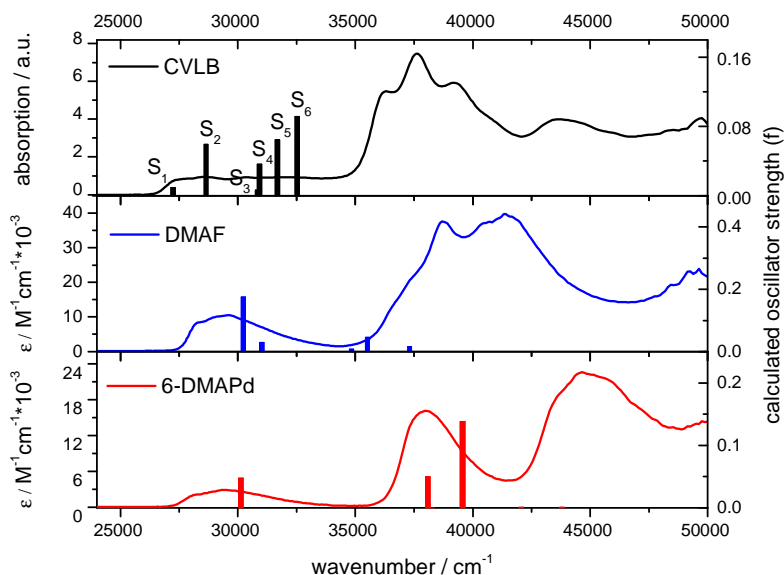


Fig. 7.21 Electronic absorption spectra recorded in CHEX compared with calculated transitions (oscillator strengths (bars) from TDDFT B3LYP/6-31+G(d,p). S_1 – S_6 denote electronic transitions according to Tab. 7.7.

7.5 Fluorescence at room temperature

The fluorescence spectra of CVLB in aprotic solvents at room temperature and their variation with solvent polarity (Fig. 7.22) and proticity seemingly resemble those of CVL. In low polar aprotic solvents, CVLB displays one band shifting moderately to the red on increasing solvent polarity. Above certain solvent polarity threshold (for $6.0 \leq \epsilon \leq 7.6$), dual fluorescence is displayed, and the second band, spectrally much broader than the first one, appears on the red side of the spectrum. In reference to earlier reports on CVL⁸² we designate the short-wave band as ‘A’ and the long-wave band as ‘B’. Large energy gap between the maximum positions and different solvatochromism of the two fluorescence bands prove that they are emitted from two different electronic states.

The fluorescence spectrum in non polar HEX consists of one structured band (A band) with a maximum at 26200 cm^{-1} and a halfwidth (FWHM) of 2700 cm^{-1} . In general, with increasing polarity of the solvent the fluorescence shifts towards longer wavelengths and the spectrum becomes broader and structureless (in BA, the fluorescence maximum is at

24250 cm^{-1} , $\text{FWHM}=4300\text{ cm}^{-1}$). In THF a second fluorescence band (B band) appears, noticeable as a shoulder on the red side of the A band. It is difficult to determine the position of the B band in solvents of medium polarity due to its low intensity. A procedure of spectral decomposition of the dual fluorescence into two Gauss functions, however, gave satisfactory results, but only for polar solvents, and allowed for identification of fluorescence maxima (Tab. 7.8). In polar solvents the B band is more intense and displays strong solvatochromism (2700 cm^{-1} on going from BTN to ACN). When compared with CVL, the B fluorescence in CVLB is blue-shifted by approximately 800 and 1100 cm^{-1} in ACN and BTN, respectively.

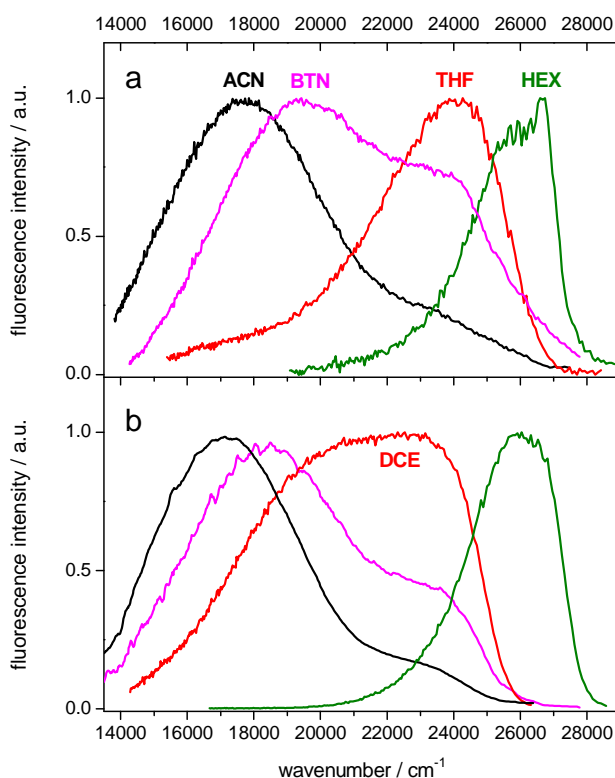


Fig. 7.22 Fluorescence spectra of CVLB (a) as a function of solvent polarity compared with those of CVL (b).

Unlike CVL, the quantum yield of both fluorescences of CVLB, even in low polar solvents, is extremely low, about 3 orders of magnitude lower than that in CVL, and increases with growing dielectric constant of the solvent (Tab. 7.8). Also the fluorescence lifetimes for low polar solvents are

in the low ps domain (see below), indicating very efficient non-radiative deactivation of the emitting state.

Tab. 7.8 Fluorescence data for CVLB in solvents of different polarities.

solvent	$\tilde{\nu}_{fl}(A)$ [cm ⁻¹]	$\tilde{\nu}_{fl}(B)$ [cm ⁻¹]	Φ_{fl} [x10 ⁴]	$\tau_{fl}(1)$ [ns]	contrib. [%]	$\tau_{fl}(2)$ [ns]	contrib. [%]
HEX	26200		1.4	<<0.5	95	6	5
BE	24800		7.2				
EE	24200		2.4	<0.5	80	1.5	20
BA	24250		6.1				
THF	23950	19000	5.1	<0.5	88	5	12
$\epsilon=9.02$	23750	18500					
BTN	23800	19000	9.4	0.5	95	7	5
ACN	23400	17700	10	1.5	93	9	5
MeOH	22850	17300	1.3				
nPrOH	23570	17700	7.6				

Abbreviations: $\tilde{\nu}_{flu}(A)$ and $\tilde{\nu}_{flu}(B)$ – maximum of fluorescence of A and B band, respectively, determined with spectral decomposition procedure of the fluorescence spectrum into two Gaussian functions; Φ_{fl} – fluorescence quantum yield; $\tau_{fl}(1)$ and $\tau_{fl}(2)$ – two components of a biexponential decay; contrib. – contribution of a decay component defined as $Q_i = A_i \tau_i / \sum A_i \tau_i$.

In the simple picture reached for CVL where the ‘A’ band could be ascribed to the LE state localized on the 6-DMAPd moiety is blurred here, and its interpretation and assignment is complicated by the fact that the CVLB structure includes two chromophores, DMAF and 6-DMAPd, with nearly degenerate S₁ excited states. Additional issue is the spiroconjugation perturbing the HOMO orbitals of the subunits and giving rise to a delocalized HOMO of CVLB. Although the perturbed HOMO orbitals in CVLB are significantly centered on the DMAF moiety, the HOMO delocalization allows for localized LUMO→HOMO transitions to occur without significant charge displacement, no matter wherever the LUMO is localized. The lower unoccupied molecular orbitals of CVLB, LUMO and LUMO+1, are localized on 6-DMAPd and DMAF units, respectively (TDDFT). Due to different calculated dipole moments in the S₁ states of 6-DMAPd and DMAF, 11.2 D¹²⁵ and 4.2 D, respectively, the S₁ states of these moieties (and corresponding fluorescence transitions) respond differently to changing solvent polarity. Due to their energetic proximity, even little change in polarity of the environment may result in their

inversion, and effectively – in terms of molecular orbitals – in changing the role of LUMO and LUMO+1 under low polarity conditions. As a result, the LUMO orbital of CVLB may be that localized on 6-DMAPd or DMAF moiety depending on solvent polarity and rigidity, which in fact is observed as switching of the emitting state in temperature dependent fluorescence spectra in low and medium polar solvents (see below). Therefore, for reasons discussed above, any general assignment of the ‘A’ band in CVLB fluorescence spectra is not possible, and the assignment must be solvent and temperature-specific. Hence, this localised excited state displaying the ‘A’ band will be further denoted as the LE or the A state.

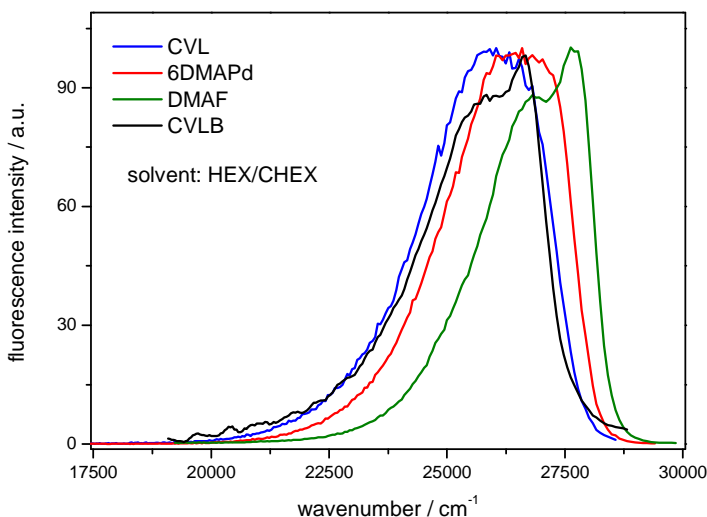


Fig. 7.23 Comparison of fluorescence spectra of CVLB recorded in HEX with fluorescence spectra of the subunits (DMAF and 6-DMAPd), and CVL.

The assignment of the B band is, paradoxically, more straightforward and can be supported by what is known about the photophysics of CVL and MGL, as well as by fluorescence spectroscopy of MGLB, which has only one fluorescent structural subunit (DMAF; Pd is non-fluorescent). Considerable red shift of the spectral position of the B band (2300 cm^{-1} between BTN and ACN) and increasing Stokes shift and the band halfwidth (for ACN: 5300 cm^{-1}) on increasing solvent polarity strongly suggest highly polar, charge transfer nature of the state emitting the B band, similarly as in CVL. This state will be denoted as the CT_B state, both because of the same character as in CVL and to maintain nomenclature consistent with that proposed for CVL.

The quantum yields and fluorescence lifetimes of CVLB increase with increasing solvent polarity by one order of magnitude (between CHEX and ACN). All fluorescence decays measured by the single photon counting technique (Tab. 7.8) were biexponential with the main component being shorter than 0.5 ns (so below the time resolution in these experiments, which was approximately 0.5 ns), only for ACN the lifetime was 1.5 ns. For three selected solvents the fluorescence lifetimes were measured (in collaboration with Dr. Piotr Fita) with a 100 fs resolution using fluorescence up-conversion technique (excitation wavelength 365 nm). Also in this case, all measured decays were biexponential with a fast picosecond and a slow nano- or sub-nanosecond component, it has to be noted, however, that the measured signals were very weak.

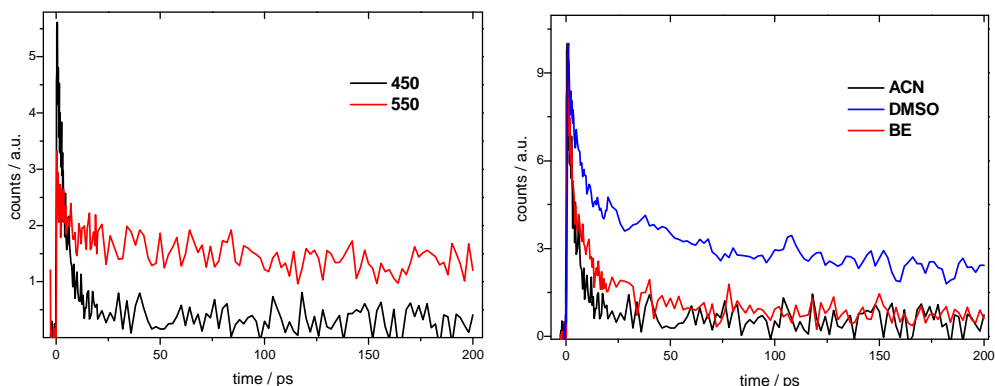


Fig. 7.24 Left: Decays of CVLB fluorescence measured at 450 (black) and 550 nm (red) in ACN. Right: Normalized decays of CVLB fluorescence recorded in ACN (black), DMSO (blue) and BE (red) at 450 nm. Different shares of the two decay times result from the fact, that the position of fluorescence is solvent dependent.

In low polar BE no dependence on the emission wavelength was observed, the fitted decay times are 3.4 and 109 ps. In polar ACN, the contribution of the slower component increased with longer emission wavelength (Fig. 7.24), and the parameters of the simultaneous fit for all wavelengths were 4.3 and 540 ps (for DMSO: 10.5 and 450 ps). The value of the longer component has to be treated with care since the time range of the measurements was too narrow to determine such long decay times. Thus, these results (i.e., 540 ps for ACN and 450 ps for DMSO) are not in conflict with the results obtained from the single photon counting measurements (e.g., 1.5 ns for ACN, confirmed by TA in the ns range, see Section 7.8, the faster component was beyond the resolution of the TA setup). These observations can be interpreted in terms of two fluorescing excited species,

the short-lived one transforming into the longer lived individual. Hence, these measurements speak for the two state interconversion model similar to that developed for CVL, where the A state (LE) undergoes fast conversion to the longer living B state (CT_B).

7.6 Excited state dipole moment

Fig. 7.25 presents the solvatochromic plot for the A band of CVLB compared with the A band of CVL and fluorescence maxima of 6-DMAPd and DMAF plotted against the solvent function. The parameters of the fits are summarized in Tab. 7.9. Closely positioned solvatochromic plots of CVL and 6-DMAPd indicate similar nature and similar dipole moments of the corresponding emitting states. For CVLB, comparison of solvatochromic plots with those of the subunits does not give a direct answer which of the two chromophores emits fluorescence. The difference of the position of fluorescence maxima of CVLB and 6-DMAPd is approximately 500 cm^{-1} in low and medium polar solvents (the same difference was observed in CVL and 6-DMAPd), but the slope for the subunit is higher by 0.05 eV. On the other hand, the slopes of solvatochromic plots of CVLB and DMAF are equal, however, the difference in energy of the fluorescence of both molecules is 0.23 eV (1850 cm^{-1}), which roughly corresponds to the destabilization energy of the HOMO orbital on CVLB (compared to the energy of HOMO orbital of DMAF). The solvatochromic plots (Fig. 7.25) are inconclusive with regard to a definite assignment of the emitting state. This lack of assignment of the emitting state makes the determination of the excited state dipole moment of the A state problematic, i.e., due to the problems connected with the choice of the Onsager cavity radius.

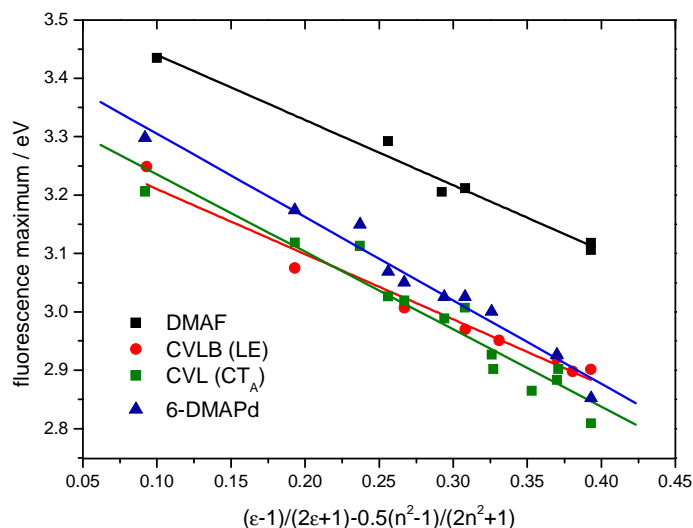


Fig. 7.25 Solvatochromic shifts of fluorescence maxima for the A band of CVLB (LE state) and CVL (CT_A), and for 6-DMAPd¹²⁵ and DMAF as a function of solvent polarity corresponding to modified Lippert–Mataga model (Eq. 4.3).

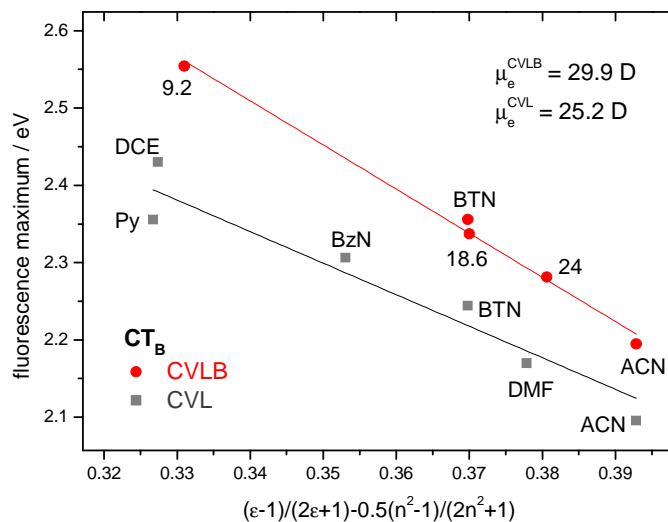


Fig. 7.26 Solvatochromic shifts of fluorescence maxima for the B band of CVLB (CT_B state) and CVL (CT_B)⁸² as a function of solvent polarity corresponding to modified Lippert–Mataga model (Eq. 4.3). The points denoted as 24, 18.6 and 9.2 are fluorescence maxima recorded in binary solvent mixtures (EA/ACN) of the respective dielectric constant. BzN stands for benzonitrile, Py for pyridine and DCE for dichloroethane.

	CVLB (LE)	CVL (CT _A)	6-DMAPd	DMAF	CVLB (CT _B)	CVL (CT _B)
$\bar{\mu}_e(\bar{\mu}_e - \bar{\mu}_g) / a_0^3$	-0.56	-0.66	-0.71	-0.56	-2.86	-2.04
$hc\nu_{fl}^{vac}$ [eV]	3.32	3.37	3.45	3.55	4.45	3.74
a_0 [Å]		3.6	3.6	4.0	5.8	6.0
$\bar{\mu}_e$ [D]	—	10.7	11.2	7.9	29.9	31.5

Tab. 7.9 Slopes and intercepts (in eV) of the fluorescence solvatochromic plots for CVLB (A and B bands), CVL (A and B bands⁸²), and their subunits (6-DMAPd¹²⁵ and DMAF), and the dipole moments calculated for the respective excited states. For the CT_B state of CVLB, two Onsager cavity radii were chosen. Excited state dipole moment of DMAF was estimated based on the assumption that the dipole moments in excited and ground state are parallel.

Polar nature of the emitting CT_B state of CVLB was verified using the solvatochromic shift method (Tab. 7.9). In view of the strong sensitivity to solvent polarity, $\bar{\mu}_g$ was neglected (due to its much lower value than $\bar{\mu}_e$) as was the case for the CT_B state in CVL. Excited state dipole moments were estimated using two Onsager cavity radii, 5.8 Å (as for CVL)⁸² and 6.0 Å (estimation from crystallographic structure). With these assumptions and using the Eq. 4.3, the excited state dipole moment of the CT_B state in CVLB was calculated and equals 29.9 D and 31.5 D, respectively. These values are higher by approximately 5 D than the CT_B dipole moment for CVL. Such a large value of dipole moment (31.5 D) corresponds to a CS distance of 6.2 Å and approximately agrees with the distance between the oxygen atom in lactone ring and the nitrogen atom of DMAF. Hence, the positive charge on the D moiety cannot be symmetrically distributed over the DMAF moiety but must be localised on one of the amino groups. This fact speaks for far going similarities in the structure of CT_B state in CVL and CVLB. Also the fs-TA measurements described in Section 7.8 confirm this statement by revealing similar transient absorption bands for both the CT_B state in both molecules.

7.7 Temperature dependent fluorescence switching

Fluorescence of CVLB in MCHEx at room temperature (and still at 253 K) is very weak and strongly resembles in shape the fluorescence of DMAF in HEX (26300 cm⁻¹). At 223 K the fluorescence band shifts towards longer wavelengths (maxima at 23950 and 25000 cm⁻¹) and is approximately

25 times stronger than at room temperature. Further decrease in temperature down to 153 K has no effect on the shape and position of the spectrum, but the intensity gradually increases. After passing the melting point of MCHEx (147 K), dramatic change in the fluorescence pattern is observed, the fluorescence becomes structureless and the maximum shifts to 23150 cm^{-1} . Further decrease in temperature to 93 K results only in a minor shift of the band by 250 cm^{-1} to the blue (Fig. 7.27).

The fluorescence of CVLB in MTHF as a function of temperature also displays two temperature regimes where different emissions can be observed, however, in this case, switching of the emissive state is reversed as compared with MCHEx, the spectrum changes from structureless to a double-peaked structure with fluorescence maxima shifted towards higher energies (Fig. 7.28).

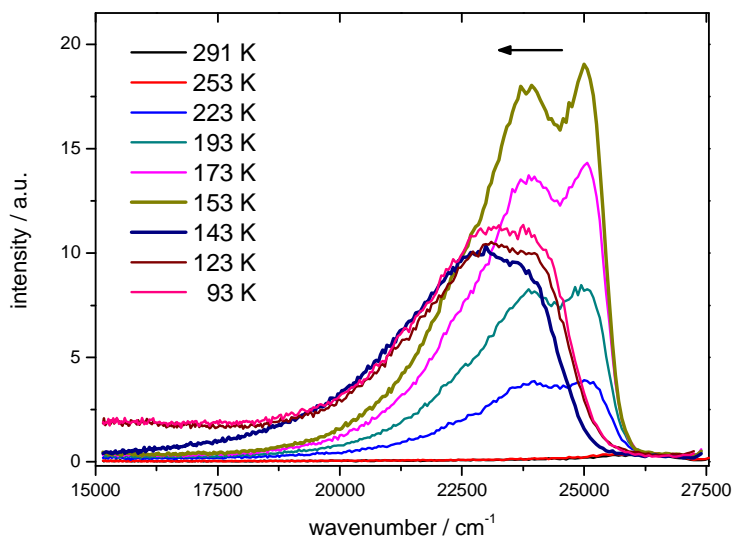


Fig. 7.27 Fluorescence of CVLB in MCHEx as a function of temperature.

In the temperature range between 295 and 203 K the fluorescence spectrum of CVLB in MTHF preserves its structureless character and maximum position (approximately at 23500 cm^{-1}) (Fig. 7.28). Starting at 203 K, where the dielectric constant of the solvent is equal to 8.2,²¹⁰ the CT_B fluorescence becomes noticeable as a red shoulder of the A band (approximately at 19000 cm^{-1}). The CT_B fluorescence is still present at 143 K ($\epsilon=12$), further decrease in temperature results, however, in its disappearance despite increasing dielectric constant. Hence, a different

parameter controls the presence of the B band when the temperature exceeds the melting point of MTHF (147 K). The fluorescence spectrum recorded at 123 K is an intermediate spectrum between 133 K and 113 K with structureless shape but already shifted towards higher energies (maximum at 23850 cm^{-1}). At 113 K, the fluorescence switching has already taken place and a double-peaked spectrum is observed (25000 and 24200 cm^{-1}), similar to that of CVLB in CHEX in the temperature range from 295–153 K. Further cooling to 93 K has no effect on fluorescence spectrum of CVLB.

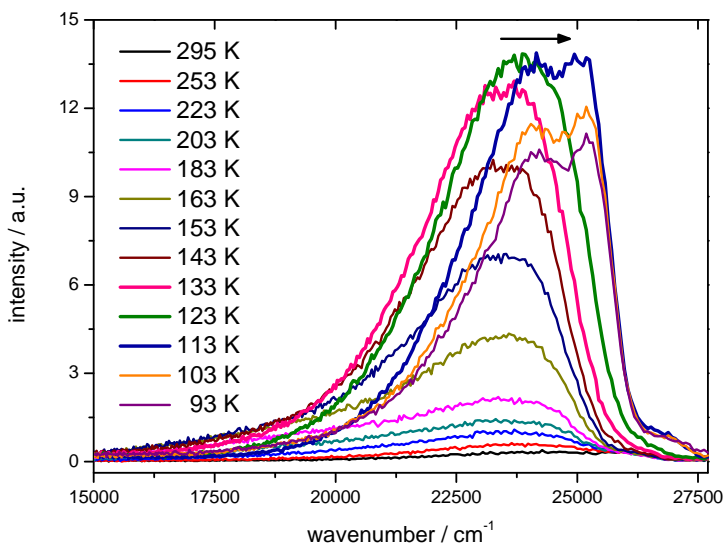


Fig. 7.28 Fluorescence of CVLB in MTHF as a function of temperature.

Additionally, temperature-dependent fluorescence spectra were recorded for CVLB, CVL and 6-DMAPd in EE (Fig. 7.29, Fig. 7.30). On cooling down CVL in EE from room temperature to 163 K, the A band shifts towards longer wavelengths by 650 cm^{-1} from 24450 cm^{-1} , and gradually the CT_B band becomes noticeable at approximately 20000 cm^{-1} . The thermochromic behaviour of 6-DMAPd is very similar to that of the A band of CVL, on cooling down to 163 K from room temperature, the spectral shift towards lower energies by 750 cm^{-1} (to 23950 cm^{-1}) is accompanied by an increase in intensity. For CVLB, a minor shift of the A band is observed when the sample is cooled down from room temperature by 10 degrees (from 24200 to 23900 cm^{-1}), further cooling down to 163 K results only in an increase in fluorescence intensity, no CT_B band appears, in contrast to CVL. Fig 7.30 presents a comparison of CVLB, CVL and 6-DMAPd in EE at two selected temperatures, 273 and 163 K. The spectra in EE of all three

compounds are similar in position and shape pointing to 6-DMAPd as origin of fluorescence for CVLB (in analogy to CVL).

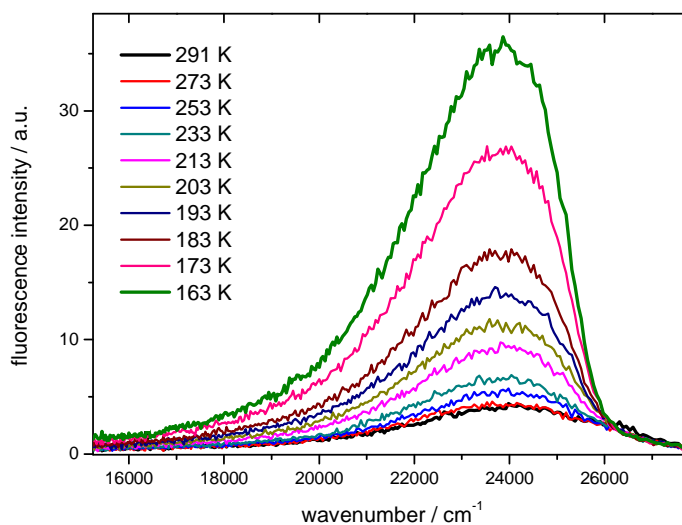


Fig. 7.29 Fluorescence of CVLB in EE as a function of temperature.

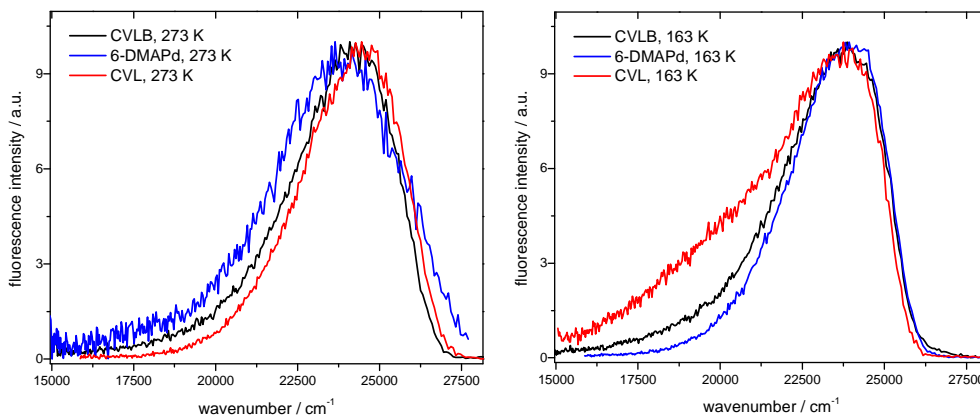


Fig. 7.30 Comparison of fluorescence spectra of CVLB, CVL and 6-DMAPd in EE recorded at 273 and 163 K.

The double peaked spectrum of CVLB present in CHEX in the temperature range above 153 K and in MTHF below 113 K, can be assigned to DMAF based on shape analysis. The broader and structureless band present at remaining temperatures (and in EE in the whole measured regime down to 163 K) can be ascribed to come from the 6-DMAPd subunit. The changes in the temperature dependent spectra can be interpreted in terms of

orbital energy inversion, i.e., the change of the LUMO of CVLB localized either on DMAF or on 6–DMAPd moiety.

7.8 Electron transfer and ring opening reaction – a transient absorption study

Femtosecond transient absorption of CVLB was recorded in three solvents of different polarities and dielectric relaxation times. Prior to these experiments, CVL in ACN was measured to order to verify the earlier results by Karpiuk *et al.*⁸³ Comparing the spectra recorded on two different transient absorption setups, the only discrepancy observed is that in the shape (relative intensity) of the 500 nm band for short delays. This disagreement can be explained either by the dependence of the relative intensities of the TA bands on the overlay of the pump and probe beams since, most probably, the spatial distribution of different wavelengths is not uniform in the probe beam, or by the fact, that the time resolution of our experiments was lower. However, the TA pattern and the kinetics for both experiments are very similar (Fig. 7.31 and ref. 83). Moreover, the results were analyzed using global analysis with 2 and 3 ($\tau_1=0.61$ ps; $\tau_2=9.5$ ps; $\tau_3=720$ ps) decay constants and reproduced the kinetics obtained by Karpiuk *et al.* The interpretation of the TA experiments is presented in Section 2.4.5. The primary short wavelength band is ascribed to 6–DMAPd, the secondary band comes from absorption of the cation radical of DMA (460 nm).

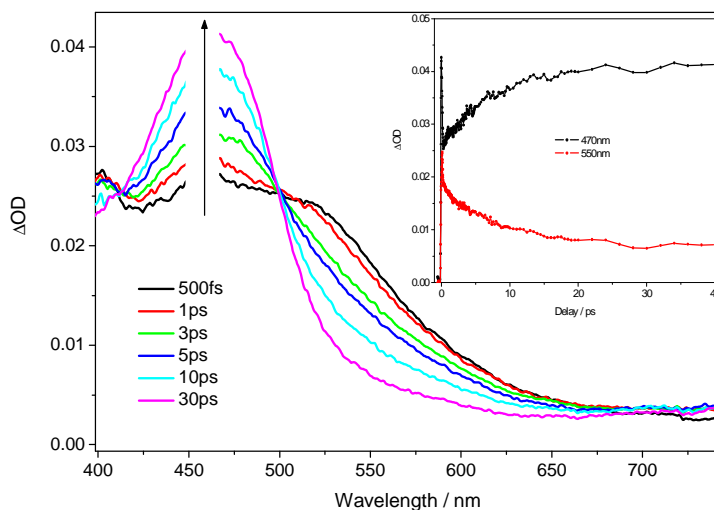


Fig. 7.31 Transient absorption spectra of CVL in ACN recorded at different delays. Insert: TA decay traces recorded at 470 and 550 nm.

The TA spectra of CVLB in ACN differ from those of CVL, especially by the presence of an absorption band at 650 nm (Fig. 7.32). The spectrum of CVLB recorded with 500 fs delay resembles the respective spectrum of CVL, with one broad band with the maximum between 420 and 500 nm (ascribed in CVL to the TA of 6-DMAPd). In CVLB this band decays, but simultaneously a new band with the maximum at 645 nm appears with the time constant of 4.8 ps (kinetic model, Tab. 7.10). Furthermore, an isosbestic point is noticeable at 620 nm for the first 30 ps, and afterwards both bands decay (645 nm band decays with $\tau_1=107$ ps).

Transient absorption recorded on the nanosecond scale is in agreement with fluorescence decay data (Tab. 7.8). The fluorescence decay time of CVLB in ACN determined in both bands with single photon counting technique is 1.5 ns, TA measurements in the 465 nm region gave the decay constant equal to 1.3 ns. Additionally the formation of the triplet state with the same time constant was observed at 415 nm (Fig. 7.34). The kinetics of the 645 nm band could not be resolved in the ns measurements (time resolution of approx. 1 ns), only a very fast decay is observed.

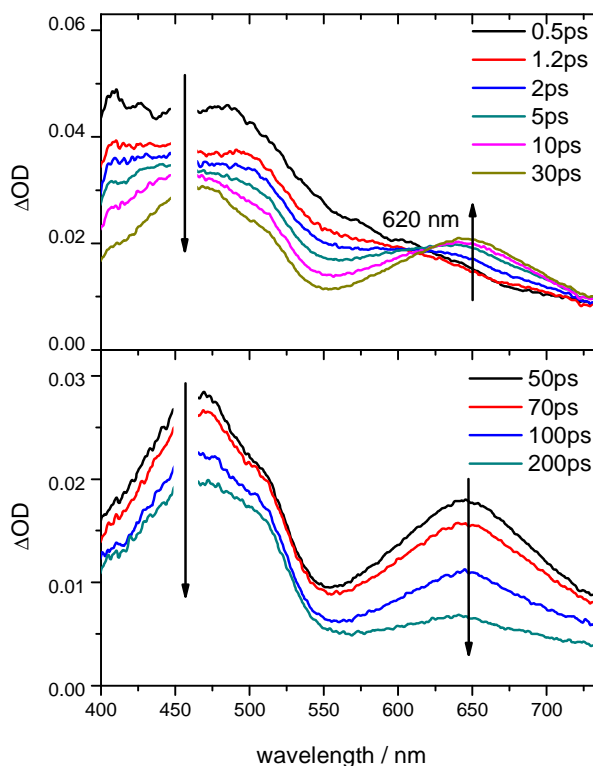


Fig. 7.32 TA spectra of CVLB in ACN recorded for the delays times ranging from 0.5 ps to 200 ps).

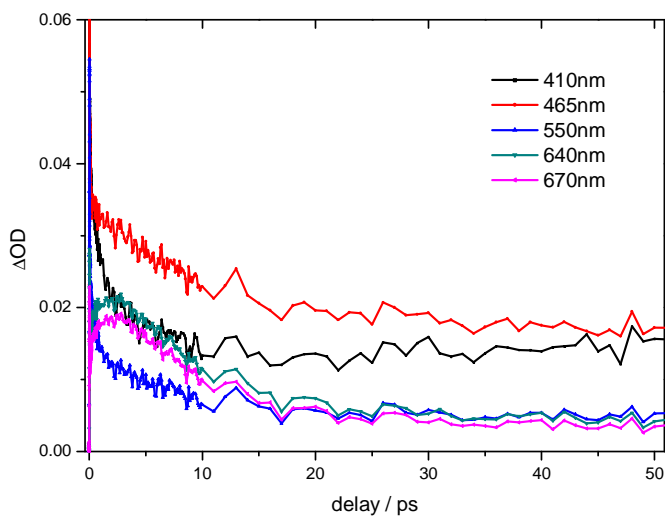


Fig. 7.33 Transient absorption decays recorded at various wavelengths for CVLB in ACN at room temperature. Excitation wavelength centered around 365 nm.

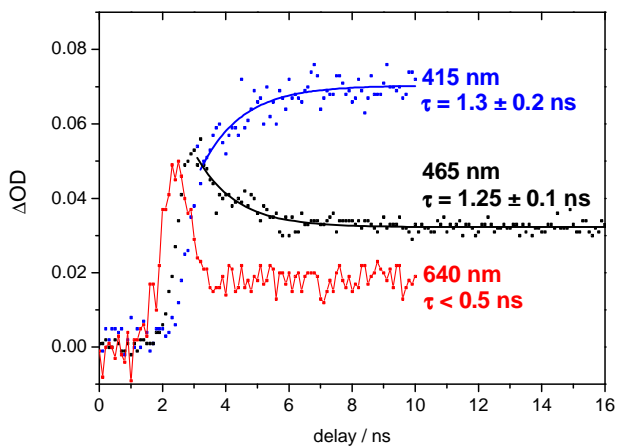


Fig. 7.34 Transient absorption kinetic curves of CVLB in ACN recorded at 415, 465 and 640 nm. Decays are not corrected for the zero delay time related to wavelength-dependent temporal profile of the probing dye laser.

TA spectra recorded for CVLB in DMSO show the same band patterns as those in ACN, however, all processes are slower (Fig. 7.35). Initially, the absorption in the short-wave range decreases with simultaneous grow of the TA signal in the region around 660 nm. An isosbestic point is also observed, however, it is “diffuse” (around 650 nm). After some 50 ps,

the TA signal starts to decay in both bands. The decay time of the $S_1 \rightarrow S_n$ absorption at around 460 nm is 1.75 ns. This value compares well with the fluorescence lifetime in a highly polar environment (ACN, 1.5 ns). Moreover, formation of a new band at approximately 410 nm can be observed at delays longer than 500 ps. This band can be ascribed to the TA from a triplet state which is populated under these conditions.

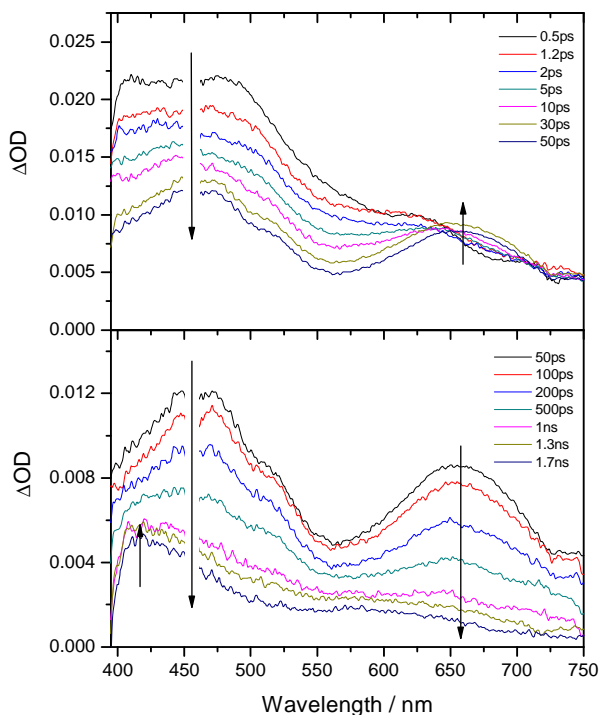


Fig. 7.35 TA spectra of CVLB in DMSO at room temperature recorded for delays ranging from 0.5 ps to 1.7 ns.

The TA spectra of CVLB in a low polar solvent (EE) are presented in Fig. 7.36. At first, it seems that the TA signal decays uniformly in the whole observed range. A closer look, however, reveals that at the beginning of the time evolution, a weak band between 630 and 650 nm is growing. Fast decay of the TA signal makes the observation of a “clear” isosbestic point impossible, nevertheless, when comparing spectra recorded at a delay of 0.5 and 5 ps one can conclude that the position of the isosbestic point is at approximately 615 nm. A closer inspection of the kinetics shows that the long wavelength band rises with the time constant of 1.8 ps (and the 450 nm band decays), which is 2–3 times faster than in ACN (4.8 ps) (kinetic model

Tab. 7.10). The TA signal in EE decays within 12–13 ps, again much faster than in the polar solvent (by two orders of magnitude) (Fig 7.37).

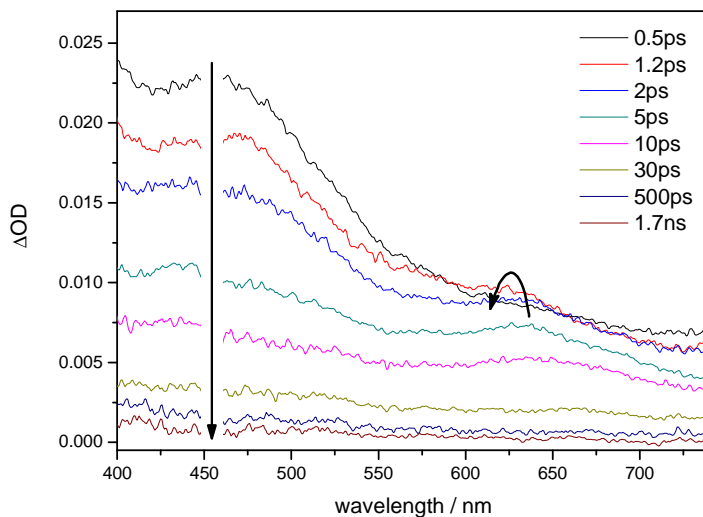


Fig. 7.36 TA spectra of CVLB in EE at room temperature recorded for delays ranging from 0.5 ps to 1.7 ns.

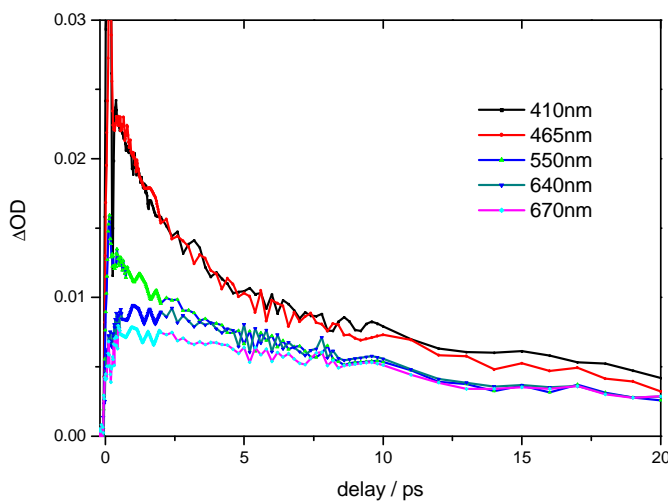


Fig. 7.37 Decays of CVLB recorded in EE at room temperature. Excitation wavelength centered around 365 nm.

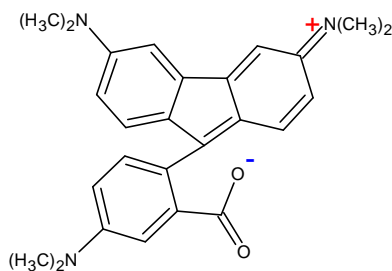
In summary, the TA spectra recorded at 0.5 ps delay are similar in all three solvents, displaying a broad short wavelength band in the region between 400–600 nm, indicating that the initially formed state has the same

structure in all three solvents (Fig. 7.38). Furthermore, when compared with CVL, where a similar structure is visible (however, somewhat broader) and the primary excited state is localized on 6-DMAPd, one can conclude that also in CVLB the lowest excited state populated in absorption is localized on the 6-DMAPd moiety, even in low polar EE. This conclusion is supported by the fact that in the temperature dependent fluorescence measurements in EE and in more polar MTHF, 6-DMAPd is the origin of fluorescence (at room temperature and in some temperature range below room temperature).

	time range [ps]	τ_1 [ps]	τ_2 [ps]	τ_3 [ps]
ACN	300	const	107	4.8
	100	0.6	187	7.1
DMSO	1700	const	334	5.3
	1700	1750	320	5.3
EE	470	const	13	1.8
	100	const	12	1.8

Tab. 7.10 Parameters obtained from global analysis of the TA data. Assumed number of decays 3, const – constant, when one time constant was assumed to be infinite.

The long-wave TA band is not present in CVL. The position of this band is solvent dependent, in low polar EE its maximum is at approximately 630 nm, in ACN at 645 nm and in DMSO at 660 nm, and has direct effect on the localization of the temporary isosbestic point. The isosbestic point can be observed for the first 30 ps in ACN (~40 ps in DMSO), and in EE it lasts for 2 ps. Its presence is a strong indication for a precursor-successor reaction taking place in the excited state between the species absorbing at 650 nm and at 460 nm. The species absorbing at 650 nm is most probably the



zwitterionic form of CVLB, where the C–O bond is cleaved. This hypothesis is supported by the fact, that the stationary absorption spectrum of CVLB in ACN with addition of diluted sulphuric acid (formation of the cation) displays a weak transition at 630 nm (with identical halfwidth as the TA spectrum, 90 nm). The structure of the open-ring form of CVLB is presented on the

left. From emission measurements it follows that in polar solvents dual fluorescence is observed from both the A and the CT_B states. In the TA

measurements, however, the CT_B state is not clearly visible, probably due to an overlap with a stronger TA band of 6-DMAPd.

The results from global analysis are presented in Tab. 7.10. A three state model was employed to obtain the time constants. The decay times were calculated for different time regimes.

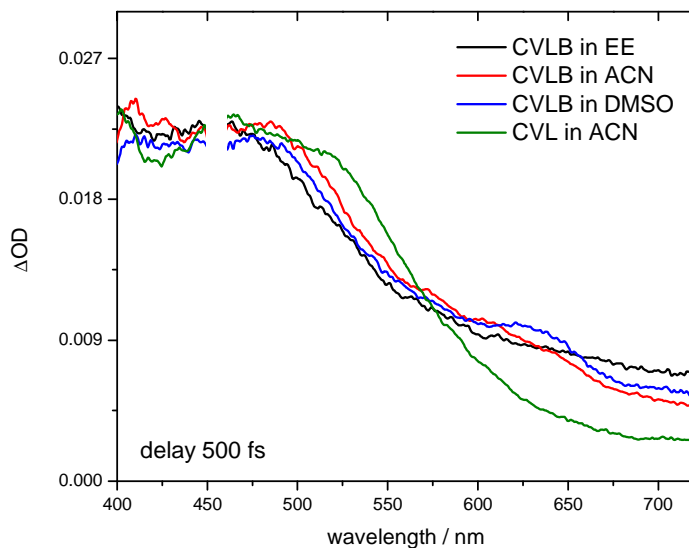


Fig. 7.38 Comparison of TA spectra of CVLB in EE, ACN and DMSO and CVL in ACN. All spectra recorded at 500 fs delay.

7.9 Luminescence in glasses

Luminescence spectra of CVLB compared with its subunits recorded at 77 K in BTN are shown in Fig. 7.39. The luminescence spectrum of CVLB consists of one fluorescence band with the maximum at 24200 cm^{-1} and a structureless phosphorescence band with the maximum at 19000 cm^{-1} . Both emissions cannot come from a triplet (phosphorescence) or a singlet (fluorescence) state localized on DMAF, as they are lower in energy (by more than 2000 cm^{-1}) and display no structure. However, the fluorescence spectrum of CVLB resembles closely in structure, halfwidth and position the one of 6-DMAPd (maximum at 24600 cm^{-1}) and CVL (24000 cm^{-1}). Also the phosphorescence spectrum of CVLB reproduces the long lived luminescence spectrum of 6-DMAPd, the red-shift for CVLB being 400 cm^{-1} . Hence, it can be concluded, that the local singlet and triplet state of 6-DMAPd are the emitting states in CVLB in polar environment at 77 K.

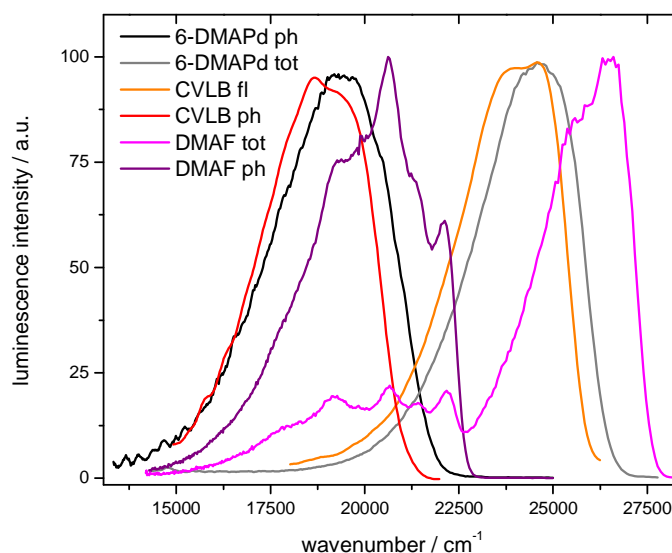


Fig. 7.39 Fluorescence (fl), phosphorescence (ph) and total luminescence (tot) spectra of CVLB, 6-DMAPd and DMAF recorded at 77 K in BTN.

7.10 Summary and discussion

CVLB is a structural analogue of CVL having a spiro architecture. The two molecules share the same acceptor subunit (6-DMAPd), the donor moiety in CVLB, however, consists of two DMA moieties bridged via a C–C bond forming a new rigid chromophore, DMAF. The ground state structure of CVLB determined by X-ray analysis is reproduced by DFT calculations. The two subunits are planar and form an angle of approximately 90°. Rigidized spiro-structure of CVLB gives rise to intramolecular interchromophoric interactions between DMAF and 6-DMAPd that do not occur between the DMA and 6-DMAPd moieties in parent CVL. The non-additivity of absorption transitions together with saturated character of the bonds formed by the spiro carbon atom (C8) indicate that the π -electronic systems of the subunits do not interact through bonds, and the inter-moiety ground state interaction results from stereoelectronic effects. This type of interaction, called spiroconjugation, takes place between orbitals that are antisymmetric with respect to the two bisecting planes of a spiro-molecule. As a consequence, two new molecular orbitals are created, spanning over the whole molecule. Based on the analysis of orbitals of CVLB it was concluded, that the HOMO of DMAF and HOMO of 6-DMAPd interact,

resulting in formation of HOMO and HOMO-2 of CVLB, in which the electron density is distributed over the entire molecule. The transition from these orbitals dominate in the first two absorption bands, which explains the appearance and non-additivity of the CVLB absorption spectrum (no superposition of absorption spectra of subunits in the low energy region).

The fluorescence pattern of CVLB is similar to that of CVL, depending on solvent polarity an interplay between dual and single fluorescence can be observed. The two fluorescence bands come from two different electronic states, which manifests, e.g., by their different solvatochromic behaviour. The 'B' band displaying pronounced solvatochromism can be attributed to a CT state, as is the case in CVL. The determined excited state dipole moment of this band is very high (29.9 D) pointing to a strong charge transfer character. Such a high value of dipole moment indicates that the charges are shifted by 6.2 Å. Hence, the positive charge on the D moiety cannot be symmetrically distributed over the DMAF moiety but must be localised on one of the amino groups. This fact speaks for far going similarities in the structure of CT_B state in CVL and CVLB.

The simple picture in CVL where the 'A' band could be ascribed to the LE state localized on 6-DMAPd moiety is blurred in CVLB, and its interpretation and assignment is complicated by the fact that CVLB structure includes two chromophores, DMAF and 6-DMAPd, with nearly degenerate S₁ excited states. Additional issue is the spiroconjugation perturbing the HOMO orbitals of the subunits and giving rise to a delocalized HOMO of CVLB. Analysis of the fluorescence bands shape suggests that in non polar CHEX, CVLB emits from the DMAF moiety (LUMO localized on DMAF). It seems that the polarity of BE is already sufficient to inverse the LUMO orbitals, and emission is tentatively ascribed to come from 6-DMAPd. The inversion of LUMO states in this direction is also justified by the excited state (S₁) dipole moments of DMAF and 6-DMAPd. The higher value of the excited dipole moment of 6-DMAPd results from a CT character of this state, and explains its "better" solvation in polar solvents. Moreover, these conclusions are supported by the observation of fluorescence switching with lowering temperature. Nevertheless, further research is needed for a definite identification of fluorescing states, especially time resolved fluorescence measurements would contribute to solving this problem.

CVLB exhibits unusual behaviour with decreasing temperature. Switching between two emitting states (localized on DMAF and 6-DMAPd) takes place, when the melting point of the solvent is reached. However, the direction of changes depends strongly on the type of solvent. In MTHF,

where initially the state localized on 6-DMAPd emits, DMAF becomes the lowest excited state, when the melting point is reached. This behaviour can be rationalized by taking into account that with decreasing temperature, the dielectric constant and the dielectric relaxation time of the solvent increase (see Section 4.7.1). Considerable growth of the dielectric relaxation time of MTHF around the melting point results in a situation, where the state localized on 6-DMAPd is not stabilised below the less polar state localized on DMAF. In MCHEx above the melting point, fluorescence from DMAF can be observed. The switching of the emitting state to 6-DMAPd while passing through the melting point cannot be rationalized the same way as for MTHF, since MCHEx has practically no dipole moment. This behaviour is still unclear, further research is needed.

Low quantum yields and lifetimes in the ps region of CVLB point to effective and fast deactivation channel of the emissive states. Rigid structure of CVLB excludes significant contributions from conformational changes in the excited state, hence, we propose that the depopulation of the excited state in all solvents takes place mainly via a lactone ring opening reaction, similarly as in structurally related rhodamine lactones. Breaking of the C–O bond results in formation of a zwitterionic species, with transient absorption localized in the region around 650 nm. The proposed model for excited state processes in CVLB is depicted in Fig. 7.40. After excitation, the hot molecule undergoes vibrational cooling within a few picoseconds. During this process, before final stabilization of the locally excited state, the ring opening reaction can take place. This reaction occurs diabatically with formation of the ground state zwitterionic species that decays within hundreds of ps (in polar solvents) with formation of the ground state lactonic form of CVLB. The CVLB molecule in its S_1 state (A/LE state) can also undergo ET provided that the charge separated state is stabilized enough by surrounding solvent molecules, in full analogy to CVL. It is important to note, that the presence of a CT state is not a prerequisite for the ring opening reaction, since the formation of the zwitterionic species was observed in low polar EE, where no charge separation takes place (deduced from the lack of CT_B fluorescence).

On a longer time scale (in polar solvents) a thermal equilibrium between the 'A' state and CT_B is established. On the ps time scale however, the two fluorescing states decay with different time constants. The triplet state populated at low temperatures has local character, as is the case for CVL. In both molecules at 77 K the fluorescence and phosphorescence comes from the 6-DMAPd moiety.

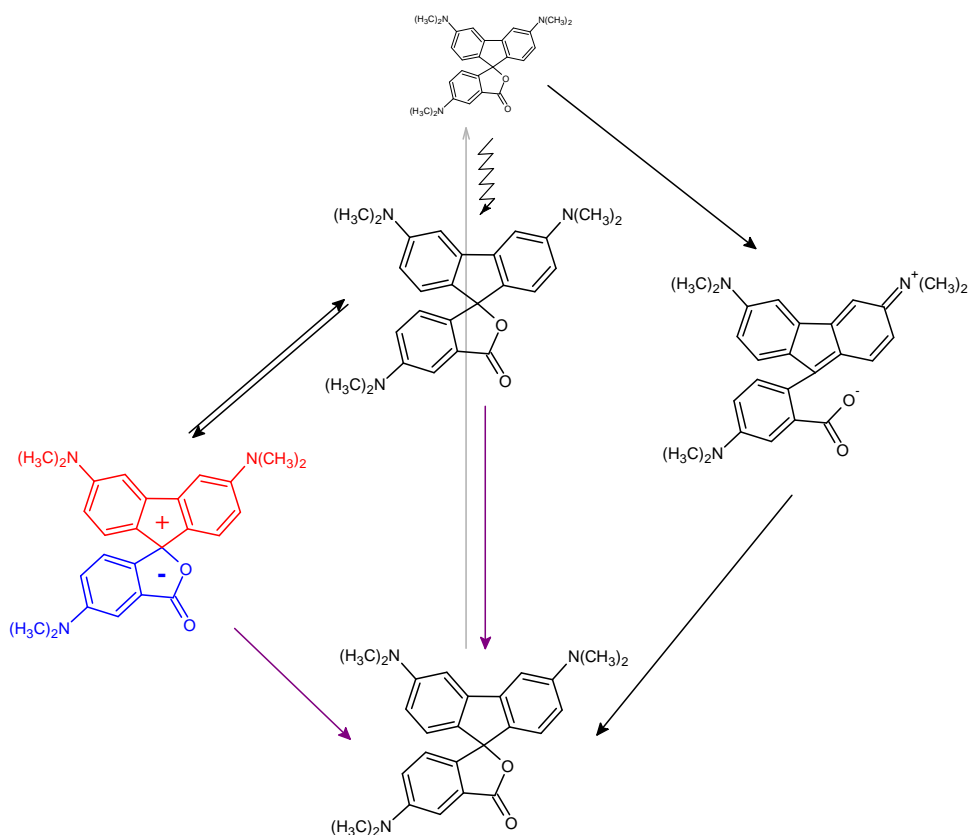


Fig. 7.40 Scheme depicting the excited state processes of CVLB.

Focussing on a seemingly minor structural detail, our study demonstrates that a fine modification in molecular geometry results in a major difference in electronic structure and photophysics due to formation of a spirocyclic structure and spiroconjugative interaction across the spiro linkage in CVLB. This realization led us to a deeper understanding of the roles played by the spiro carbon link and the spiro carbon–heteroatom bond in the excited state electronic communication in spiroheterocyclic D–A systems. This knowledge is a necessary prerequisite for designing optimum geometries for ultrafast electron transfer in spiomolecules, recently more and more often proposed systems for organic optoelectronic applications.²⁶⁶

Chapter 8

White fluorescence – main goal or byproduct?

In Section 2.7 strategies for generation of white light for photoluminescent and electroluminescent applications were reviewed. This Chapter focuses on an interesting option for monomolecular white light emitters, namely on making use of dual fluorescence from molecules where emission arises from both a locally excited state and a state populated in an adiabatic photophysical or photochemical process. In general, the latter state can be formed in an intramolecular electron or proton transfer process, but can also be a product of adiabatic photodissociation. It has been pointed out recently that dual fluorescence can be successfully used to broaden the emission of organic fluorophores, both polymers²⁶⁷ and small molecules,²⁶⁸ up to the spectral width corresponding to white light. Given potential benefits, the development of monomolecular white fluorophores has been surprisingly slow as yet, with only a few systems reported to date, employing energy,¹⁰⁶ proton^{149, 269} and electron²⁶⁸ transfer processes.

D–D–(DA) type triarylmethane lactones discussed in this thesis display dual fluorescence from two polar excited states with considerably different dipole moments. These systems combine in their structure a highly luminescent local blue fluorophore (herein referred to as the CT_A state) with a yellow–orange emitting highly polar intramolecular exciplex (CT_B state), in which a part/group of the local fluorophore acts as an independent electron acceptor. The polarity of the surrounding medium (represented here by the dielectric constant) does not only affect the equilibrium between the two emitting states and thus the position and ratio of the two fluorescences, but more importantly, it determines the occurrence of the CT_B band. Generally, the equilibrium and the energy of the emitted photons can be tuned by the structure of both fluorescing states.

A crucial parameter for the shape of the fluorescence spectrum, and hence the threshold for the dielectric constant of the medium required for the appearance of the CT_B band is the energy gap between the non–solvated CT_A and CT_B states, ΔE (Section 2.4.5, Fig. 2.11). Smaller ΔE translates to lower ϵ needed to stabilize the CT_B state to the energy equal to that of CT_A. Since the CT_A state is localized on the DA moiety, any change in its structure (e.g., different substituents at the position 6 of phthalide) has an effect on the

energy gap (CVLH2 vs. CVL). Another way to influence ΔE is to modify the electron-donating moiety and hence to change the energy of the CT_B state by introducing different D molecules (with different oxidation potentials), i.e., by bridging the two DMA units in CVL in rigid DMAF in CVLB. In this section, the structural modification of the DA moiety will be discussed first, followed by the effect of the rigidization of the CVL molecule on the ET.

8.1 DA structure effect on the equilibrium between the emitting states

The CVL and CVLH2 molecules are composed of three structural subunits: two DMA (D–D) groups attached to 6–DMAPd or 6–APd (DA), respectively. Due to higher ionization potential of the $-NH_2$ group, the lowest excited singlet state of 6–APd is, higher in energy than in 6–DMAPd (by 2000 cm^{-1} as estimated from the absorption maxima in HEX) and the emission maximum of 6–APd is blue shifted by $2100\text{--}2600\text{ cm}^{-1}$, depending on the solvent. The lowest electronically excited state of CVL and CVLH2 is the optically populated, polar state localized on the DA moiety (CT_A , dipole moment $\mu_e^{CVL} = 11.2\text{ D}$, $\mu_e^{CVLH2} = 8.0\text{ D}$) that displays efficient, single fluorescence in low polar solvents. In medium polar aprotic solvents both molecules emit dual fluorescence from two different polar excited states, CT_A (band A), and a highly polar CT state (CT_B , $\mu_e^{CVL} = 25.2\text{ D}$, $\mu_e^{CVLH2} = 26.2\text{ D}$, band B) populated upon electron transfer ET from the initially excited CT_A state. Since the structural elements involved in creation of the CT_B state are the same in CVL and in CVLH2, the CT_B state in both molecules has the same energy in a given solvent. The threshold ϵ value for appearance of the second fluorescence band emitted from the CT_B state in CVL at room temperature is between 7.6 (THF) and 8.9 (DCM). CVLH2 is more susceptible to solvent polarity than CVL, the B band appears in solvents with ϵ between 3.8 (iPE) and 4.3 (EE), but when ϵ exceeds 7.6 (THF) the primary emission is not present anymore. Lower ϵ threshold for CVLH2 is caused by smaller ΔE , the narrow window of polarity range where the dual fluorescence can be observed, results in turn from a lower stabilization of the CT_A state due to smaller excited state dipole moment of 6–APd than 6–DMAPd. Also, the back ET process, $CT_A \leftarrow CT_B$, is energetically not possible due to a larger ΔE in highly polar solvents, hence the equilibrium is entirely shifted in favour of the CT_B state.

Due to different dipole moments of CT_A and CT_B states, the two

fluorescence bands of CVL and CVLH2 show different solvatochromic behaviour and both are displayed with solvent polarity dependent quantum yields which is reflected in changing fluorescence spectrum and band intensity ratio. This high sensitivity to medium polarity can be purposely used to customize the shape, width and other parameters of the fluorescence spectrum, especially in medium polarity range, where the two bands are of comparable intensity (Fig. 8.1). Because of lack of neat aprotic media with suitable dielectric properties, EA/ACN mixtures were used to cover this polarity range. The dielectric constant of mixed solvent, ϵ , was calculated as weighted average of the mixture components, assuming ideal solvent mixture and additive function of component concentrations: $\epsilon_{mix} = a_1\epsilon_1 + a_2\epsilon_2$, where a_i is a volume fraction of the i -th solvent, and ϵ_i is its dielectric constant in the pure state (excess ϵ was neglected).²⁷⁰ It is to be noted that the spectra of CVL fluorescence in neat solvents (e.g., BTN or ACN) do not deviate from those observed for binary mixtures with corresponding calculated ϵ indicating only a small contribution from the excess ϵ into the total ϵ of binary EA/ACN mixtures.

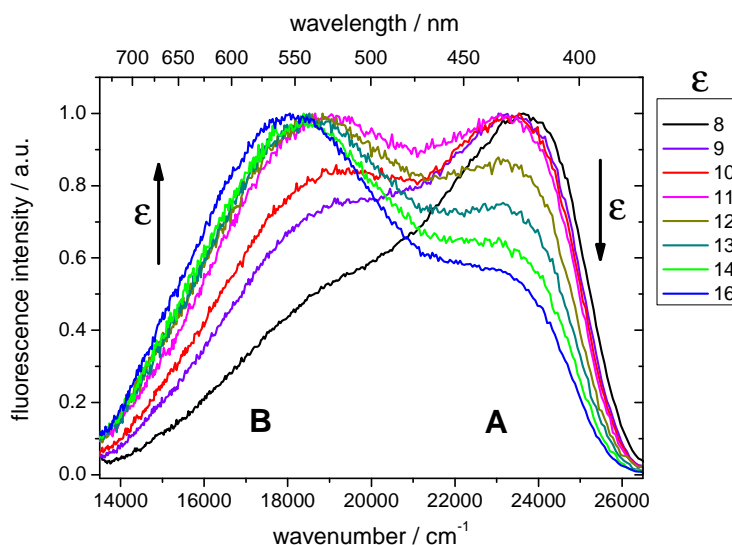


Fig.8.1 Fluorescence spectra of CVL in EA/ACN mixtures as a function of solvent polarity (dielectric constant of the binary solvent, ϵ , was varied from 8 to 16). The samples were excited at $\lambda = 335$ nm (29850 cm^{-1}).

Fig. 8.1 shows normalized fluorescence spectra of CVL in EA/ACN binary solvent in a polarity range corresponding to ϵ between 8 and 16. In this polarity range CVL displays dual fluorescence from the CT_A and CT_B

states. Each of the bands displays different solvatochromism caused by the difference in the dipole moments of the emitting states. With increasing dielectric constant of the medium the intensity ratio shifts in favour of the CT_B band. The FWHM reaches its maximal value of 9150 cm⁻¹ for $\epsilon = 12$ (Tab. 8.1). In the wavelength representation, the widest fluorescence spectrum observed extends from 404 to 626 nm (FWHM) and was recorded for $\epsilon = 16$. The difference in width between the two representations is due to a λ^2 factor that is used in conversion between the two representations.²⁷¹ The total fluorescence quantum yield of CVL decreases from 0.11 for $\epsilon = 8$ to 0.018 for $\epsilon = 16$, in line with decreasing fluorescence decay times (from 9.5 to 2.8 ns, Tab. 8.1). The decay times measured in a given binary solvent at blue and red slopes of the A and B bands, respectively, (excitation at 337 nm) are equal on the ns time scale used in measurements due to rapid equilibration of both emitting states on the time scale of solvation dynamics⁸³ (on the ns timescale only the longest component is visible). The spectra recorded in neat solvents and binary mixtures of the same dielectric constant are identical, however, the quantum yields and lifetimes of fluorescence in binary solvent mixtures are lower.

dielectric constant*	FWHM [cm ⁻¹]	Φ_{fl}	τ [ns]	1931 CIE coordinates (x,y)
8	6650	0.11	9.5	(0.21, 0.20)
10	8600	0.05	6.2	(0.24, 0.26)
12	9150	0.038	5.0	(0.26, 0.30)
14	8750	0.021	3.5	(0.28, 0.33)
16	8550	0.018	2.8	(0.30, 0.35)
20.7	7100	0.032	5.6	(0.30, 0.37)
37.5	5450	0.0045	1.5	(0.36, 0.36)

Tab. 8.1 Spectral widths (FWHM), total quantum yields and decay times of CVL fluorescence as a function of solvent polarity. * Measurements performed in EA/ACN mixtures except for butyronitrile (20.7) and acetonitrile (37.5).

The impressive colour tuning capabilities of CVL fluorescence in response to changing solvent polarity are best illustrated by plotting 1931 CIE colour coordinates in the chromaticity diagram (Fig. 8.2). The 1931 CIE colour coordinates have been calculated from emission spectra using colour matching functions (see Section 2.8). In the solvent polarity range corresponding to ϵ between 16 and 20, the fluorescence spectrum of CVL approaches pure white light (0.33, 0.33), though gravitating slightly towards the blue (0.30, 0.35) (Fig. 8.2, left).

The fluorescence displayed by solutions with ϵ between 12 and 20 appears nearly white to the eye and due to its spectral width can be regarded as pseudowhite light²⁷² with different hues of white. The main reason for the gravitation to the blue is the position of the A band, however, the B band does not input enough orange–red to counterbalance the A band. This indicates that both the positions of the two bands and the spectral interval between them must be addressed if an optimized CVL–like molecule is to display a pure white light spectrum.

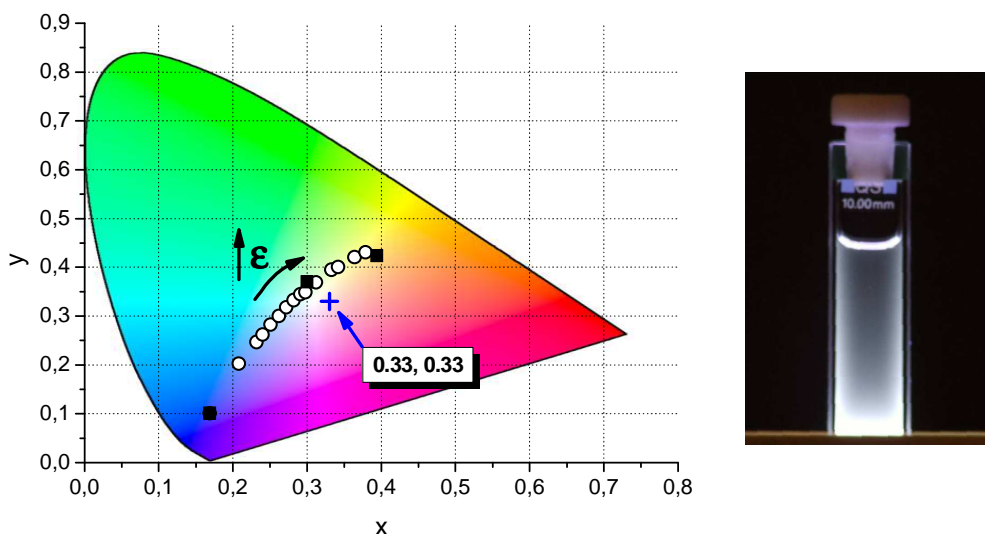


Fig. 8.2 Left: Tuneable chromaticity of CVL fluorescence shown in a 1931 CIE diagram as a function of solvent polarity: white circles – CVL in EA/ACN mixtures (ϵ ranges from 8 to 32), black solid squares – CVL in EA ($\epsilon = 6.0$), BTN ($\epsilon = 20.7$), and ACN ($\epsilon = 37.5$). The cross indicates pure white (0.33, 0.33) and the curved arrow indicates increasing ϵ values. Right: CVL in EA/ACN mixture with dielectric constant equal to 16.

The structure–photophysics relationship emerging from comparison of CVLH2 with CVL shows that decreasing ΔE with unchanged energy of the non–solvated CT_B state leads to a (undesired) blue shift of the fluorescence spectrum. Pure white light can be obtained by making use of a reverse trend: increased ΔE combined with lower energy of the non–solvated CT_B state. Both parameters can be controlled by adjusting the redox potentials of the amino group in aminophthalide, and of the D and A moieties involved in formation of the highly polar CT_B state.

8.2 Effect of spirocyclic structure on the parameters of white fluorescence

Unlike CVL, in CVLB the two DMA groups are linked via a single carbon–carbon bond forming a new chromophore, DMAF. The spacial arrangement of the two subunits of CVLB leads to spiroconjugation, which has a significant effect on electronic transitions in this molecule. In spite of different ground–state interactions in CVLB and CVL, the fluorescence pattern of CVLB as a function of solvent polarity is very similar to that of CVL. In low polar solvents, a single blue fluorescence band is observed (A band), tentatively ascribed to come from the 6–DMAPd in solvents polar than CHEX. The threshold ϵ value for appearance of the second fluorescence band emitted from the CT_B state at room temperature is between 6.0 (EA) and 7.6 (THF), similar as for CVL. In solvents with higher dielectric constant than EA, the solvational and vibrational relaxation of the primary excited state takes place in competition with the ET process populating the intramolecular exciplex (CT_B). The electronic structure of the CT_B state is similar to that of CVL, the difference being that the positive charge is located not on the DMA but on the DMAF moiety. The spectral position of the B band of CVLB depending on solvent polarity is similar to that of the non–bridged molecule since the excited state dipole moments are comparable ($\mu_e^{\text{CVL}} = 25.2$ D, $\mu_e^{\text{CVLB}} = 29.9$ D). In spite of spectral similarity and unlike CVL, the quantum yield of CVLB fluorescence in low polar solvents is by more than three orders of magnitude lower than that of CVL, due to a very efficient non–radiative process in CVLB that is absent in CVL. The dramatic drop in fluorescence quantum yield and extreme shortening of fluorescence decay time in response to rigidization of the structure was anything but expected, as restriction of internal movements in a molecule usually results in inhibited non–radiative decay.²⁷³ The enhanced non–radiative process in CVLB is due to its spiro structure and involves photodissociation of the C–O bond in the lactone ring, in analogy with rhodamine lactones.

The spectrally broadest fluorescence of CVLB is observed in BTN (FWHM = 8400 cm⁻¹). The CIE coordinates for CVLB in BTN are (0.24, 0.30), which means, that the emitted light is bluish–white. Also in this case, as for CVL, the blue component is dominating. Any modifications of this spirostructure, however, are rather not reasonable, due to the poor fluorescence quantum yields of CVLB.

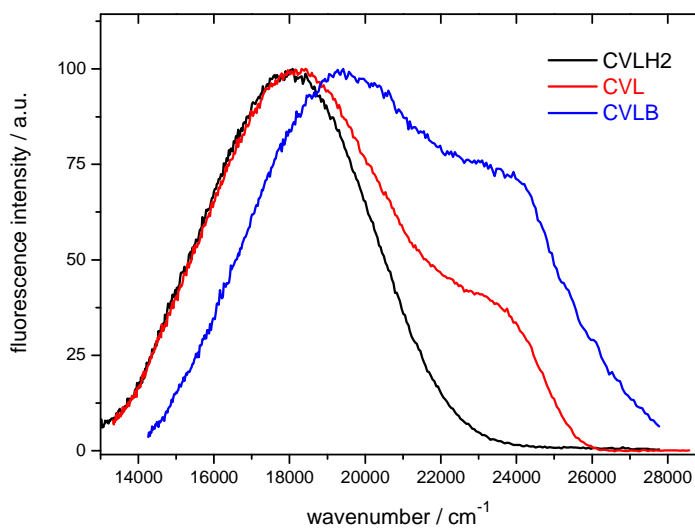


Fig. 8.3 Fluorescence spectra of CVL (red), CVLH2 (black) and CVLB (blue) recorded at room temperature in BTN.

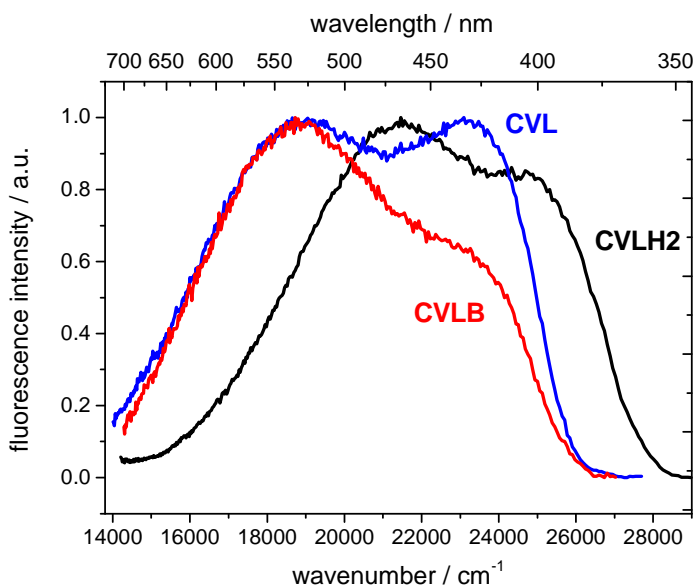


Fig. 8.4 Dual fluorescence spectra of CVLH2 in BE/EA mixture (black line, $\epsilon = 5.0$, FWHM = 8150 cm^{-1} , CIE = (0.20, 0.26)) and CVLB in EA/ACN mixture (red line, $\epsilon = 18.6$, FWHM = 8300 cm^{-1} , CIE = (0.27, 0.33)) compared with CVL in EA/ACN mixture (blue line, $\epsilon = 11$, FWHM = 9100 cm^{-1}).

8.3 Summary

Spectral characteristics of CVL, CVLH2 and CVLB demonstrate clearly that a broad dual fluorescence is a general property of triarylmethane lactones of D–D–(DA) type. These systems combine a local blue fluorophore with a yellow–orange emitting intramolecular exciplex, in which structural part of the local fluorophore acts as an independent electron acceptor (Fig. 8.4). Using two CVL analogues, it was shown that dual emission is a general property of D–A structures built on a sp^3 carbon atom. In non–bridged systems, the sp^3 link preserves individual photophysical properties of molecular subunits and at the same time serves as an effective channel for intramolecular electronic communication.

Polar nature of the two emitting states in the systems studied allows to tune their energy levels and set the final energy gap between them by changing solvent polarity. The energetics of CVL–like systems may be further customized by appropriate substitutions at electron–donating and accepting moieties. These properties make D–D–(DA) structures very promising candidates for single component white emitters. All the structures studied here display spectrally continuous white (dual) fluorescence (Fig. 8.4), though the spectral parameters like the fluorescence quantum yield and the shift to the red must be adjusted in order to obtain highly luminescent pure white fluorophores. Nevertheless, the presented molecules provide the proof of the concept and demonstrate the capability to display tuned hues of white. The work on optimisation of CVL–like structures to obtain pure white light and higher fluorescence quantum yields is currently in progress, however, it is beyond the scope of this thesis.

Chapter 9

Summary and outlook

The general objective of this thesis was to elucidate the structure–photophysics relationship in triarylmethane lactones. For this purpose, a series of LTAM molecules was designed, synthesized and characterized by spectroscopical methods. It should be noted that some of the molecules studied here were for the first time synthesised for the purpose of this thesis, including elaboration of a new, effective synthetic path leading to DMAF. A part of the results of the present thesis has already been published^{182,268} and presented on numerous conferences. A manuscript discussing the effects of D–A orientation and spiroconjugation on the LTAM photophysics is in final stage of preparation.

Based on the study of dyad–triad pairs it was found that not only the ET process occurs in close analogy in both molecules, also the deactivation paths of the CT state are virtually the same. Hence, it seems that at least for the systems studied, the simplification of D–D–A triad structure to D–A dyad preserves all the electronic properties relevant for the ET process and leads to the conclusion that in symmetric triads only one D group is actively involved in the charge separation process. The susceptibility of CT fluorescence to temperature of the surrounding medium results in pronounced rigidochromism of MGLA and MGL, making them good probes for studying dielectric relaxation in rigid and semi–rigid supercooled media. Moreover, the presence of triplet states with charge separation in these molecules was confirmed. The near–degeneracy of the ¹CT and ³CT makes MGL and MGLA good candidates for studies of CT singlet–triplet coupling and interactions, as well as for exploring the area of CT phosphorescence.

Photophysical studies on derivatives of MGL with different electron donors allowed for some general conclusions concerning LTAM molecules. In D–A systems built around a sp³ carbon atom with an orientation of subunits characteristic for LTAM, no significant electronic coupling between subunits in the ground state was found. Based on the absence of fluorescence from excited states localized on the subunits it was deduced that the deactivation process seen as electronic relaxation of the locally excited state is ultrafast and solvent independent, resulting in population of a state with charge transferred from the donor moiety to phthalide.

The work explored and attempted to rationalise the effect of structural modifications resulting in changing the reduction potential of the acceptor subunit in LTAM of D–D–(DA) type. The rate and yield of the ET process in these molecules is solvent dependent, since the solvation dynamics generally controls the energy and availability of the excited states. Special attention was paid to the effect of mutual orientation of the D and A subunits on the excited state processes in spiro-derivatives of LTAM. The presence of spiroconjugation between D and A was shown and its effect on the photophysics described. Almost equal energies of D and A subunits result in inversion of nearly degenerated excited states and fluorescence switching as a function of solvent and temperature. Moreover, the rigid spiro-structure affects not only the energetics, but most of all, it opens new deactivation pathways for the initially excited molecule. It was shown that a vibronically hot molecule can undergo a lactone ring-opening reaction with formation of a short-lived (on the ps time scale) zwitterionic species.

Last but not least, the question of exploiting dual fluorescence in white light generation in derivatives of CVL was addressed. Using two CVL analogues, it was shown that dual emission is a general property of D–D–(DA) structures built on a sp^3 carbon atom. In non-bridged systems, the sp^3 link preserves individual photophysical properties of molecular subunits and at the same time serves as an effective channel for intramolecular electronic communication. All the structures studied display spectrally continuous white (dual) fluorescence, providing the proof of the concept and demonstrating the capability to display tuned hues of white.

A minor modification of the structural subunits connected by the central sp^3 carbon atom, and at the same time a change in the energy of the lowest excited states, result in involvement of the primary ET process in a sequence of processes and thus enable manipulation of the charge separation reaction, even molecular engineering on the level of simple D–A systems. Ultrafast and barrierless ET processes in LTAM on the time scale of single vibrations with identified reaction coordinate allow for insights into different aspects of dynamics on a submolecular level and a better understanding of the basics of charge transfer reactions. In this context future research will concentrate on investigations of early stages of ET through a carbon linker, especially in the time domain of nuclear motions. Furthermore, theoretical work on the occurrence and role of resonant states of phthalide²⁷⁴ in the ET process is needed.

Moreover, the possibility of practical applications of LTAM molecules as probes of dielectric relaxation or solvation dynamics will be an

important issue in the future research. Optimization of the structure of CVL derivatives for displaying spectrally broad dual fluorescence resembling the sunlight spectrum and possible applications in photovoltaic devices are important and promising points in the plans for future.

Acknowledgements

Pragnę serdecznie podziękować mojemu promotorowi, dr hab. Jerzemu Karpiukowi za wybór tematu pracy oraz wprowadzenie w świat laktonów triarylometanowych. Dziękuję również za opiekę, wiele cennych uwag oraz poświęcony mi czas, jak również za twórcze dyskusje, nie zawsze na tematy naukowe.

Ponadto pragnę podziękować:

Dr Jackowi Nowackiemu z Wydziału Chemii Uniwersytetu Warszawskiego za syntezę każdej narysowanej przeze mnie cząsteczki,

Mgr Michałowi Kijakowi za wykonanie obliczeń kwantowomechanicznych, pomoc oraz liczne rozmowy,

Dr Piotrowi Ficie z Wydziału Fizyki Uniwersytetu Warszawskiego za wykonanie pomiarów pikosekundowych bez których nie udałoby się poznać tajemnic CVLB,

Prof. Bo Albinsson oraz dr Joannie Wiberg (Chalmers University of Technology, Geteborg) za umożliwienie pomiarów absorpcji przejściowej oraz opiekę podczas pobytów w Geteborgu,

Prof. Krzysztofowi Woźniakowi oraz mgr Fabioli Sanjuan–Szklarz z Wydziału Chemii Uniwersytetu Warszawskiego za wykonanie pomiarów rentgenostrukturalnych,

Pawłowi Spryszakowi za pomiary absorpcji przejściowej w zakresie ns,

Dr Gonzalo Angulo za dyskusje podczas których dzielił się ze mną wiedzą o procesach przeniesienia elektronu,

Jędrzejowi, Sylwestrowi, Saszy, Gabrysi oraz Natalii za pomoc oraz silne wsparcie duchowe w trakcie realizacji tej pracy,

Koleżankom i Kolegom z Zakładu Fotochemii i Spektroskopii za pomoc, współpracę oraz dobrą atmosferę podczas pracy.

Szczególnie podziękowania składam Rodzicom za stworzenie idealnych warunków do nauki oraz nieustanne duchowe wsparcie i motywację. Bratu dziękuję za sprowadzanie mnie na ziemię oraz ciągłą gotowość do pomocy. Babci i Dziadkowi dziękuję za niezachwianą wiarę we mnie.

Publications

- [1] J. Karpiuk, E. Karolak, J. Nowacki, *Pol. J. Chem.* **2008**, 82, 865
- [2] J. Karpiuk, E. Karolak, J. Nowacki, *Phys. Chem. Chem. Phys.* **2010**, 12, 8804

Conferences

- [1] E. Karolak, J. Karpiuk, *Singlet and triplet charge transfer states in donor-acceptor systems based on tetrahedral carbon*; Central European Conference on Photochemistry 2006, 04–09.03.2006, Bad Hofgastein, Austria; poster
- [2] E. Karolak, J. Karpiuk, *Wpływ rozpuszczalnika na rekombinację ładunków w laktonach barwników triarylometanowych o niesymetrycznym układzie donora elektronu*; X Mikrosymposium Kinetyczne metody badania reakcji w roztworach, 12.05.2006, Poznań; poster
- [3] E. Karolak, J. Nowacki, J. Karpiuk, *Dual fluorescence from two polar excited states in CVL-analogues. A key role of solvent polarity in excited state energetics*; ICP 2007 – XXIII International Conference on Photochemistry, 28.07–04.08.2007, Koln, Germany; poster
- [4] E. Karolak, J. Nowacki, J. Karpiuk, *Stany trypletowe w dezaktywacji wzbudzonych laktonów triarylometanowych*; Polish Photoscience Seminar, 11–13.06.2008, Lipnik; poster
- [5] E. Karolak, J. Nowacki, J. Karpiuk, *Low temperature studies on lactone forms of triarylmethane dyes*; XXII IUPAC Symposium on Photochemistry, 28.07–01.08.2008, Gothenburg, Sweden; poster
- [6] E. Karolak, J. Nowacki, J. Karpiuk, *Key role of the solvent effect in revealing structure–photophysics relationship in triarylmethane lactones*; Polish Photoscience Seminar, 16–18.06.2009, Lipnik; poster
- [7] E. Karolak, P. Fita, J. Nowacki, J. Karpiuk, *Enhanced nonradiative deactivation following rigidization of molecular structure. Photophysics of bridged crystal violet lactone*; Central European Conference on Photochemistry 2010, 07–11.02.2010, Bad Hofgastein, Austria; poster

- [8] E. Karolak-Solarska, M. Kijak, P. Fita, J. Nowacki, J. Karpiuk, *Role of spiroconjugation in excited state processes in bridged analogue of crystal violet lactone*; ICP 2011 – XXV International Conference on Photochemistry, 06–13.08.2011 Beijing, China; poster
- [9] E. Karolak-Solarska, M. Kijak, P. Fita, J. Nowacki, J. Karpiuk, *Electron transfer and photodissociation in a spirocyclic bichromophoric molecule*; Molecules and Light 2011, 19–23.09.2011, Zakopane; oral presentation
- [10] E. Karolak-Solarska, J. Karpiuk, *Photoinduced electron transfer in structurally decoupled D-A systems. Structure-photophysics relationship in triarylmethane lactones*; Reaction Kinetics in Condensed Media 2012, 11–16.09.2012, Łochów; poster

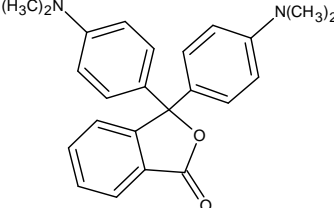
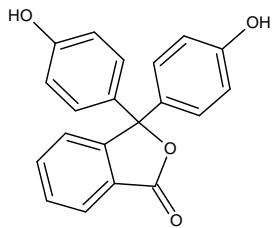
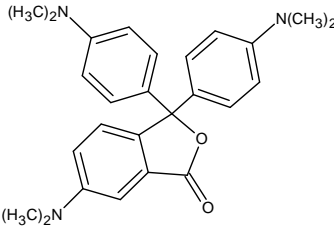
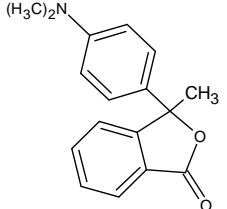
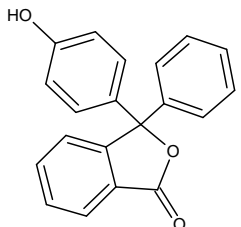
This work was supported by the Grants 3T09A06929 (J. Karpiuk), IP2010 017070 (E. Karolak-Solarska), NN204127540 (J. Karpiuk) from the Ministry of Science and Higher Education.

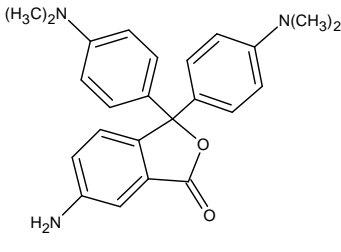
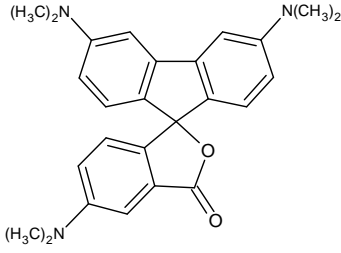
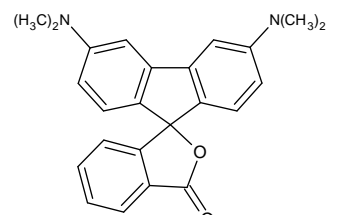
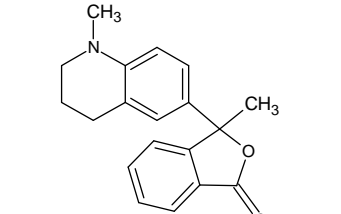
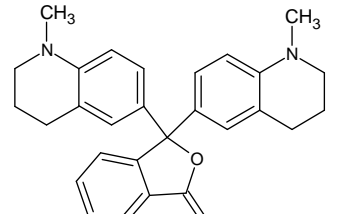
Appendix

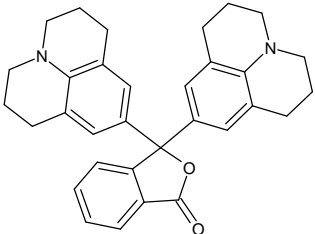
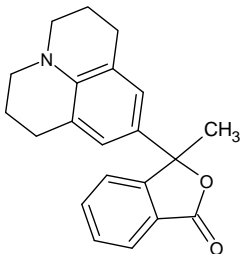
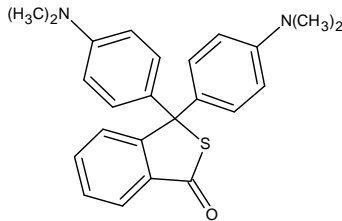
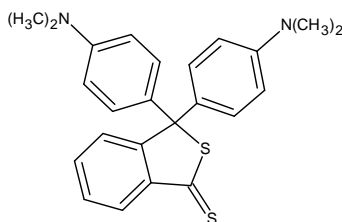
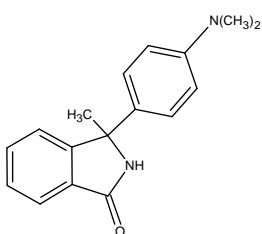
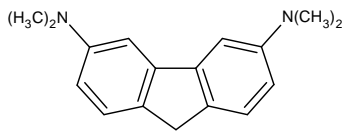
List of abbreviations

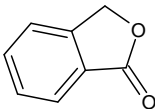
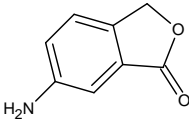
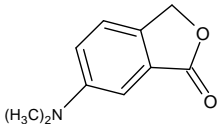
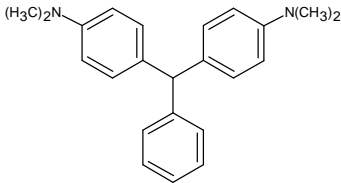
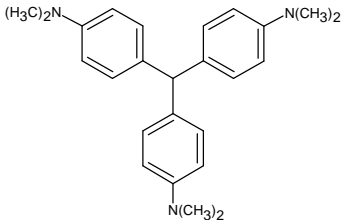
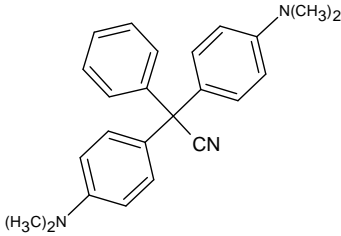
A	electron acceptor
CR	charge recombination
CS	charge separation
CT	charge transfer
CVL	crystal violet lactone
D	electron donor
DFT	density functional theory
DMA	dimethylaniline
ET	electron transfer
FWHM	full width at half maximum
LTAM	triarylmethane lactones
LRB	rhodamine B lactone
MGL	malachite green lactone
Pd	phthalide
PET	photoinduced electron transfer
PP	phenolphthaleine
TAM	triarylmethane
TDDFT	time-dependent density functional theory
THQ	1-methyl-1,2,3,4 tetrahydroquinoline

Important compounds mentioned in the text:

Structure	Name	Abbreviation
	Malachite Green Lactone	MGL
	Phenolphthaleine	PP
	Crystal Violet Lactone	CVL
	3-methyl-3-(4-dimethylamino phenyl)phthalide	MGLA
	3-phenyl-3-(4-hydroxyphenyl)phthalide	BPPd

	3,3-(4-dimethylaminophenyl)-6-aminophthalide	CVLH2
	Spiro-3-[3,6-bis(dimethylamino)fluorene]6-dimethylaminophthalide	CVLB
	Spiro-3-[3,6-bis(dimethylamino)fluorene]phthalide	MGLB
	3-Methyl-3-(1-methyl-1,2,3,4-tetrahydroquinolin-6-yl)phthalide	MeTHQ
	3,3-bis(1-methyl-1,2,3,4-tetrahydroquinolin-6-yl)phthalide	bisTHQ

	3,3-bis(julolidin-9-yl)phthalide	bisJul
	3-Methyl-3-(1-methyl-1,2,3,4-tetrahydroquinolin-6-yl)phthalide	MeJul
	3,3-bis(4-dimethylaminophenyl)thiophthalide	MGLS
	3,3-bis(4-dimethylaminophenyl)dithiophthalide	MGLSS
	3-methyl-3-(4-dimethylaminophenyl)phthalimide	PhI
	3,6-dimethylaminofluorene	DMAF

	Phthalide	Pd
	6-aminophthalide	6-APd
	6-dimethylaminophthalide	6-DMAPd
	Malachite Green	MG
	Crystal Violet	CV
	Malachite Green Leucocyanide	MGCN

Photograph on the front cover is available at:
http://ichf.edu.pl/press/2010/10/index101006_PL.html

References

- ¹ A.E. Johnson, K. Tominaga, G.C. Walker, W. Jarzęba, P.F. Barbara, *Pure & Appl. Chem.* **1993**, *65*, 1677
- ² M. Bixon, J. Jortner, *Chem. Phys.* **1993**, *176*, 467
- ³ D.M. Guldi, H. Imahori, K. Tamaki, Y. Kashiwagi, H. Yamada, Y. Sakata, S. Fukuzumi, *J. Phys. Chem. A* **2004**, *108*, 541
- ⁴ D.O. Hall, K.K. Rao (Eds.), *Photosynthesis*, Cambridge University Press, ed. 5, Cambridge, 1995. Polish edition, *Fotosynteza*, WNT, 1999
- ⁵ W. Zinth, J. Wachtveitl, *Chem. Phys. Chem* **2005**, *6*, 871
- ⁶ S.K. Deb, *Curr. Opin. Solid State Mater. Sci.* **1998**, *3*, 51
- ⁷ R. Huber, J.E. Moser, M. Grätzel, J. Wachtveitl, *J. Phys. Chem. B* **2002**, *106*, 6494
- ⁸ J. Schnadt, P.A. Brühwiler, L. Patthey, J.N. O'Shea, S. Södergren, M. Odelius, R. Ahuja, O. Karis, M. Bäessler, P. Persson, H. Siegbahn, S. Lunell, N. Martensson, *Nature* **2002**, *418*, 620
- ⁹ J. Jortner, M. Bixon, H. Heitele, M.E. Michel-Beyerle, *Chem. Phys. Lett.* **1992**, *197*, 131; M. Bixon, J. Jortner, *J. Phys. Chem.* **1993**, *97*, 13061
- ¹⁰ E. Baigar, P. Gilch, W. Zinth, M. Stöckl, P. Härter, T. Von Feilitzsch, M.E. Michel-Beyerle, *Chem. Phys. Lett.* **2002**, *352*, 176
- ¹¹ D.H. Son, P. Kambhampati, T.W. Kee, P. F. Barbara, *J. Phys. Chem. A* **2002**, *106*, 4591
- ¹² S. A. Kovalenko, J.L. Perez Lustres, N.P. Ernsting, W. Rettig, *J. Phys. Chem. A* **2003**, *107*, 10228
- ¹³ T. Bizjak, J. Karpiuk, S. Lochbrunner, E. Riedle, *J. Phys. Chem.* **2004**, *108*, 10763
- ¹⁴ K. Ohkubo, H. Kotani, J. Shao, Z. Ou, K.M. Kadish, G. Li, R.K. Pandey, M. Fujitsuka, O. Ito, H. Imahori, S. Fukuzumi, *Angew. Chem. Int. Ed.* **2004**, *43*, 853.
- ¹⁵ Y. Zheng, M.B. Zimmt, *J. Am. Chem. Soc.* **1991**, *113*, 5107; Y. Zheng, M.B. Zimmt, *J. Phys. Chem.* **1992**, *96*, 8395
- ¹⁶ A.M. Oliver, M. Paddon-Row, J. Kroon, J.W. Verhoeven, *Chem. Phys. Lett.* **1992**, *191*, 371

- 17 M.R. Wasielewski, *Chem. Rev.* **1992**, 92, 435
- 18 C. Luo, D.M. Guldi, H. Imahori, K. Tamaki, S. Sakata, *J. Am. Chem. Soc.* **2002**, 122, 6535
- 19 J.W. Verhoeven, *J. Photochem. Photobiol. C: Photochem. Rev.* **2006**, 7, 40
- 20 A.C. Benniston, A. Harriman, *Chem. Soc. Rev.* **2006**, 35, 169
- 21 D. Rehm, A. Weller, *Isr. J. Chem.* **1970**, 8, 259
- 22 A. Weller, *Z. Physik. Chem. N.F.* **1982**, 130, 129
- 23 R.A. Marcus, *Annu. Rev. Phys. Chem.* **1964**, 15, 155
- 24 R.A. Marcus, N. Sutin, *Biochem. Biophys. Acta* **1985**, 265
- 25 R.A. Marcus, *Angew. Chem. Int. Ed. Engl.* **1993**, 32, 1111
- 26 J.R. Miller, J.V. Beitz, R.K. Huddleston, *J. Am. Chem. Soc.* **1984**, 106, 5057
- 27 N. Mataga, S. Taniguchi, H. Chosrowjan, A. Osuka, K. Kurotobi, *Chem. Phys. Lett.* **2005**, 403, 163
- 28 I.R. Gould, J.E. Moser, B. Armitage, S. Farid, J.L. Goodman, M.S. Herman, *J. Am. Chem. Soc.* **1989**, 111, 1917; T. Asahi, N.J. Mataga, *J. Phys. Chem.* **1991**, 95, 1956; E. Vauthey, *J. Phys. Chem. A* **2001**, 105, 340
- 29 J. Jortner, *Chem. Phys.* **1976**, 64, 4860
- 30 J.R. Miller, J.V. Beitz, R.K. Huddleston, *J. Am. Chem. Soc.* **1984**, 106, 5057
- 31 S. Efrima, M. Bixon, *Chem. Phys. Lett.* **1974**, 25, 34
- 32 H.B. Gray, J.R. Winkler, *Proc. Natl. Acad. Sci. U.S.A.* **2005**, 102, 3534
- 33 L.D. Zusman, *Chem. Phys.* **1980**, 49, 295
- 34 H. Sumi, R.A. Marcus, *J. Chem. Phys.* **1986**, 84, 4272
- 35 E. Åkesson, A.E. Johnson, N.E. Levinger, G.C. Walker, T.P. Du Bruil, P.F. Barbara, *J. Chem. Phys.* **1992**, 96, 7859; G.C. Walker, E. Åkesson, A.E. Johnson, N.E. Levinger, P.F. Barbara, *J. Phys. Chem.* **1992**, 96, 3728
- 36 P.F. Barbara, G.C. Walker, T.P. Smith, *Science* **1992**, 256, 975
- 37 J. Jortner, M. Bixon, *J. Chem. Phys.* **1988**, 88, 167
- 38 M. Bixon, J. Jortner, *Adv. Chem. Phys.* **1999**, 106, 35

- 39 L.S. Pratt, *The Chemistry and Physics of Organic Pigments*; John Wiley: New York, 1947
- 40 D.F. Duxbury, *Chem. Rev.* **1993**, *93*, 381
- 41 V. Nair, S. Thomas, S.C. Mathew, K.G. Abhilash, *Tetrahedron* **2006**, *62*, 6731
- 42 D. Ben-Amotz, C.B. Harris, *J. Chem. Phys.* **1987**, *86*, 4856
- 43 S.Liu, Z. Zhang, Q.Liu, H. Luo, W. Zeng, *J. Pharm. Biomed. Anal.* **2002**, *30*, 685; J. Preat, D. Jacquemin, V. Wathélet, J.M Andre, E.A. Perpete, *Chem. Phys.* **2007**, *335*, 177
- 44 T. Matsubara, Y. Ichikawa, K. Aramaki, A. Katagiri, *Sol. Energ. Mater. Sol. Cell.* **2005**, *85*, 269
- 45 E. Fischer, O. Hoffmann, E. Prado, R. Bone, *J. Bacteriol.* **1944**, *48(4)*, 439
- 46 V.V. Jarikov, D.C. Neckers, *Adv. Photochem.* **2001**, *26*, 1
- 47 G.N. Lewis, M. Calvin, *Chem. Rev.* **1939**, *25*, 273; G.N. Lewis, T.T. Magel, D. Lipkin, *J. Am. Chem. Soc.* **1942**, *64*, 1774; V. Sundstrom, T. Gillbro, *J. Chem. Phys.* **1984**, *81*, 3463; F.T. Clark, H.G. Drickamer, *J. Chem. Phys.* **1984**, *81*, 1024; L.M. Lewis, G.L. Indig, *Dyes and Pigments* **2000**, *46*, 145
- 48 Y. Maruyama, O. Magnin, H. Satozono, M. Ishikawa, *J. Phys. Chem. A* **1999**, *103*, 5629
- 49 E.P. Ippen, C.V. Shank, A. Bergman, *Chem. Phys. Lett.* 1976, *38*, 61; F. Pellegrino, A. Dagen, R.R. Alfano, *Chem. Phys.* **1982**, *67*, 11
- 50 P. Fita, A. Punzi, E. Vauthey, *J. Phys. Chem. C* **2009**, *113*, 20705
- 51 H. A. Kramer, *Physica* **1940**, *7*, 284; G. Oster, Y. Nishijima, *J. Am. Chem. Soc.* **1956**, *78*, 1851; T. Förster, G. Hoffman, *Z. Phys. Chem. N.F* **1971**, *75*, 63; D. Magde, M. Windsor, *Chem. Phys. Lett.* **1974**, *24*, 144; D.A. Cremers, M. Windsor, *Chem. Phys. Lett.* **1980**, *71*, 27; K. Kemnitz, K. Yoshihara, *Chem. Lett.* **1990**, 1789
- 52 M.L. Herz, *J. Amer. Chem. Soc.* **1975**, *97(23)*, 6777
- 53 G.L. Fisher, J.C. LeBlanc, H.E. Johns, *Photochem. Photobiol.* **1967**, *6*, 757
- 54 M. Stavola, G. Mourou, W. Knox, *Opt. Commun.* **1980**, *34(3)*, 404
- 55 V. Sundstrom, T. Gillbro, H. Bergstrom, *Chem Phys.* **1982**, *73*, 439; M.S. Baptista, G.L. Indig, *J. Phys. Chem. B* **1998**, *102*, 4678

- 56 J.R. Babendure, S.R. Adams, R.Y. Tsien, *J. Am. Chem. Soc.* **2003**,
125, 14716
- 57 J.Y. Ye, T. Hattori, H. Inouye, H. Ueta, H. Nakatsuka, *Phys. Rev. B*,
1996, 53(13), 8351
- 58 D. Ben-Amotz, C.B. Harris, *J. Chem. Phys.* **1987**, 86, 5433; D. Ben-
Amotz, C.B. Harris, *J. Chem. Phys.* **1987**, 86, 6119
- 59 K.M. Abedin, J.Y. Ye, H. Inouye, T. Hattori, H. Sumi, H. Nakatsuka,
J. Chem. Phys. **1995**, **103**, 6414
- 60 J. Lifschitz, *Chem. Ber.* **1919**, 52, 1919
- 61 E.O. Holmes, *J. Phys. Chem.* **1966**, 70(4), 1037
- 62 V.V. Jarikov, D.C. Neckers, *J. Org. Chem.* **2001**, 66, 659
- 63 R.G. Brown, J. Cosa, *Chem. Phys. Lett.* **1977**, 45(3), 429
- 64 R.M. Miller, K. G. Spears, J. H. Gong, M. Wach, *J. Phys. Chem.* **1994**,
98, 1376
- 65 K.G. Spears, T. H. Gray, D. Huang, *J. Phys. Chem.* **1986**, 90, 179
- 66 L.E. Manring, K. S. Peters, *J. Phys. Chem.* **1984**, 88, 3516
- 67 M. Irie, *J. Am. Chem. Soc.* **1983**, 105, 2078
- 68 S. Abbruzzetti, M. Carcelli, P. Pelagatti, D. Rogolino, C. Viappiani,
Chem. Phys. Lett. **2001**, 344, 387
- 69 J. Karpiuk, *Wiedza i Życie* **2007**, 5, 52; to be downloaded from:
http://ichf.edu.pl/r_act/act_pl/karpiuk4.html
- 70 National Cash Register Corporation, *U.S. Patent 2505470*, 1950
- 71 N. Nakasuji, T. Kataoka, H. Inagaki, S. Nakashima, *U.S. Patent*
4028118, 1977
- 72 M. A. White, *J. Chem. Educ.* **1998**, 75, 1119; J. Luthern, A. Peredes, *J.*
Mater. Sci. Lett. **2000**, 19, 185; C.F. Zhu, A.B. Wu, *Termochimica*
Acta **2005**, 425, 7
- 73 Y. Ma, B. Zhu, K. Wu, *Solar Energy* **2001**, 70(5), 417
- 74 N.S. Allen, N. Hughes, P. Mahon, *J. Photochem.* **1987**, 37, 379
- 75 Y. Kaneko, D.C. Neckers, *J. Phys. Chem. A* **1998**, 102, 5356
- 76 J. Karpiuk, *Phys. Chem. Chem. Phys.* **2003**, 5, 1078
- 77 K. Suwińska, J. Karpiuk, unpublished results
- 78 M. Kuzuya, F. Miyake, T. Okuda, *Chem. Pharm. Bull.* **1983**, 31, 791
- 79 I.L. Belaits, R. N. Nurmukhametov, *Zh. Fiz. Khim.* **1970**, 44, 29

- 80 A. Rybka, Bachelor thesis, Cardinal Stefan Wyszyński University,
Institute of Physical Chemistry, Warsaw, 2001
- 81 S.J. Rosenthal, X. Xie, M. Du, G.R. Fleming, *J. Chem. Phys.* **1991**, *95*,
4715
- 82 J. Karpiuk, *J. Phys. Chem. A* **2004**, *108*, 11183
- 83 U. Schmidhammer, U. Megerle, S. Lochbrunner, E. Riedle, J. Karpiuk,
J. Phys. Chem. A **2008**, *112*, 8487
- 84 L. Onsager, *J. Am. Chem. Soc.* **1936**, *58*, 1486
- 85 M.L. Horng, J.A. Gardecki, A. Papazyan, M. Maroncelli, *J. Phys.*
Chem. **1995**, *99*, 17311
- 86 X. Li, M. Maroncelli, *J. Phys. Chem. A* **2011**, *115*, 3746
- 87 H. Jin, X. Li, M. Maroncelli, *J. Phys. Chem. B* **2007**, *111*(48), 13473
- 88 P.K. Chowdhury, M. Halder, L. Sanders, T. Calhoun, J.L. Anderson,
D.W. Armstrong, X. Song, J. Petrich, *J. Phys. Chem. B* **2004**, *108*,
10245
- 89 P. Mandal, M. Sarkar, A. Samanta, *J. Phys. Chem. A* **2004**, *108*, 9048
A. Paul, P.K. Mandal, A. Samanta, *J. Phys. Chem. B* **2005**, *109*, 9148
- 90 H.V.R. Annapureddy, C.J. Margulis, *J. Phys. Chem. B* **2009**, *113*,
12005
- 91 H. Jin, X. Lee, M. Maroncelli, *J. Phys. Chem. B* **2010**, *114*, 11370
- 92 K. Santhosh, A. Samanta, *J. Phys. Chem. B* **2010**, *114*, 9195
- 93 X. Li, M. Liang, A. Chakraborty, M. Kondo, M. Maroncelli, *J. Phys.*
Chem. B **2011**, *115*, 6592
- 94 A. Weller, *Z. Elektrochem.* **1956**, *60*, 1144
- 95 K. Weber, *Z. phys. Chem. (B)* **1931**, *15*, 18
- 96 Y. Inoue, P. Jiang, E. Tsukada, T. Wada, H. Shimizu, A. Tai, M.
Ishikawa, *J. Am. Chem. Soc.* **2002**, *124*, 6942
- 97 P. Valat, V. Wintgens, J. Kossanyi, L. Biczok, A. Demeter, T. Berces,
J. Am. Chem. Soc. **1992**, *114*, 946
- 98 M. Beer, H.C. Longuett–Higgins, *J. Chem. Phys.* **1955**, *23*, 1390; P.M.
Rentzepis, *Chem. Phys. Lett.* **1968**, *2*, 117
- 99 J.B. Birks, C.E. Easterly, L.G. Christophorou, *J. Chem. Phys.* **1971**,
66, 4231
- 100 P.O. Andersson, S.M. Bachilo, R.L. Chen, T. Gillbro, *J. Phys. Chem.*
1995, *99*, 16199

- 101 J. B. Birks, *Photophysics of Aromatic Molecules*; Wiley–Interscience: London, 1970
- 102 H. Masuhara, Y. Maeda, H. Nakajo, N. Mataga, K. Tomota, H. Tatemitsu, Y. Sakata, S. Misumi, *J. Am. Chem. Soc.* **1981**, *103*, 634
- 103 Y.P. Sun, C.E. Bunker, B. Ma, *J. Am. Chem. Soc.* **1994**, *116*, 9692
- 104 T. Wismontski–Knittel, P.K. Das, E. Fisher, *J. Phys. Chem.* **1984**, *88*, 1163
- 105 J. Dey, I.M. Warner, *J. Phys. Chem. A* **1997**, *101*, 4872
- 106 P. Coppo, M. Duati, V.N. Kozhevnikov, J.W. Hofstraat, L. De Cola, *Angew. Chem. Int. Ed. Engl.* 2005, **44**, 1806
- 107 E. Lippert, W. Lüder, F. Moll, W. Nägele, H. Boos, H. Prigge, I. Seibold–Blankenstein, *Angew. Chem.*, **1961**, *73*, 695
- 108 K. Rotkiewicz., K.–H. Grellmann, Z.R. Grabowski, *Chem. Phys. Lett.* **1973**, *19*, 315; Z.R. Grabowski, K. Rotkiewicz, W. Rettig, *Chem. Rev.* **2003**, *103*, 3899
- 109 K.A. Zachariasse, M. Grobys, Th. von der Haar, A. Hebecker, Yu.V. Il'ichev, O. Morawski, I. Rückert, W. Kühnle, *J. Photochem. Photobiol. A: Chem.* **1997**, *105*, 373
- 110 K.A. Zachariasse, *Chem. Phys. Lett.* **2000**, *320*, 8
- 111 K.A. Zachariasse, Th. von der Haar, U. Leinhos, W. Kühnle, *J. Inf. Rec. Mats.* **1994**, *21*, 501
- 112 F. Schneider, E. Lippert, *Ber. Bunsenges. Phys. Chem.* **1970**, *74*, 624
- 113 M. Jurczok, P. Plaza, M.M. Martin, Y.H. Meyer, W. Rettig, *Chem. Phys.* **2000**, *253*, 339
- 114 <http://goldbook.iupac.org/E02246.html>
- 115 H. Leonhardt, A. Weller, *Ber. Bunsenges. Phys. Chem.* **1963**, *67*, 791; H. Leonhardt, A. Weller, *Z. Phys. Chem. N. F.*, **1961**, *29*, 277
- 116 A. Weller, *Pure Appl. Chem.* **1968**, *16(1)*, 115; A. Weller, *The Exciplex*; Gordon, Editors: M. Ware, Academic Press: New York, 1975
- 117 F.D. Lewis, G.D. Reddy, S. Schneider, M. Gahrt, *J. Am. Chem. Soc.* **1991**, *113*, 349
- 118 F.D. Lewis, J.D.M. Bassad, E.L. Burch, B.E. Cohen, J.A. Engleman, G. D. Reddy, J.S. Schneider, W. Jaeger, P. Gedeck, M. Gahr, *J. Am. Chem. Soc.* **1995**, *117*, 660

- 119 A.M. Swinnen, M. Van der Auweraer, F.C. De Schryver, *J. Photochem.* **1985**, 28, 315
- 120 J.W. Verhoeven, *Pure Appl. Chem.* **1990**, 62, 1585
- 121 T.M. Grigoryeva, V.L. Ivanov, M.G. Kuzmin, *Dokl. Akad. Nauk* **1978**, 238, 603
- 122 J. Karpiuk, Z.R. Grabowski, F.C. De Schryver, *J. Phys. Chem.* **1994**, 98, 3247
- 123 U.K.A. Klein, F.W. Hafner, *Chem. Phys. Lett.* **1976**, 43, 141.
- 124 Y.N. Svartsov, *Photophysics of aminosubstituted phthalides*, PhD Thesis, Institute of Physical Chemistry, Polish Academy of Sciences, Warsaw, 2006
- 125 J. Karpiuk, Y.N. Svartsov, J. Nowacki, *Phys. Chem. Chem. Phys.* **2005**, 7, 4070
- 126 S. Nakamura, T. Mukai, N. Iwasa, *U.S. Patent* 5578839, 1996
- 127 T.L. Dawson, *Color. Technol.* **2010**, 126, 1
- 128 J. Kido, M. Kimura, K. Nagai, *Science* **1995**, 267, 1332; Y. Sun, N.C. Giebink, H. Kanno, B. Ma, M.E. Thompson, S.R. Forrest, *Nature* **2006**, 440, 908
- 129 A.A. Bol, A. Meijerink, *Phys. Chem. Chem. Phys.* **2001**, 3, 2105–2112; H.S. Chen, S. J.J. Wang, C.J. Lo, J.Y. Chi, *Appl. Phys. Lett.* **2005**, 86, 131905; M.J. Bowers II, J.R. McBride, S.J. Rosenthal, *J. Am. Chem. Soc.* **2005**, 127, 15378
- 130 H. Sun, J. Zhang, H. Zhang, Y. Xuan, C. Wang, M. Li, Y. Tian, Y. Ning, D. Ma, B. Yang, Z.Y. Wang, *Chem. Phys. Chem.* **2006**, 7, 2492; W. Ki, J. Li, *J. Am. Chem. Soc.* **2008**, 130, 8114; Y.L. Liu, Y.H. Wu, C.Y. Hsu, *Nanotechnology* **2009**, 20(23), 235704
- 131 X. Ma, X. Li, Y–E. Cha, L–P. Jin, *Cryst. Growth Des.* **2012**, 12, 5227
- 132 J. He, M. Zeller, A.D. Hunter, Z. Xu, *J. Am. Chem. Soc.* **2012**, 134, 1553
- 133 Y. Liu, M. Pan, Q–Y. Yang, L. Fu, K. Li, S–C. Wei, C–Y. Su, *Chem. Mater.* **2012**, 24, 1954
- 134 C.W. Ko, Y.T. Tao, *Appl. Phys. Lett.* **2001**, 79, 4234
- 135 K.O. Cheon, J. Shinar, *Appl. Phys. Lett.* **2002**, 81, 1738
- 136 D. Quin, Y. Tao, *Appl. Phys. Lett.* **2005**, 86, 113507

- 137 C. Ego, D. Marsitzky, S. Becker, J. Zhang, A.C. Grimsdale, K. Müllen, J.D. MacKenzie, C. Silva R.H. Friend, *J. Am. Chem. Soc.* **2003**, *125*, 437
- 138 J. Liu, Q. Zhou, Y. Cheng, Y. Geng, L. Wang, D. Ma, X. Jing, F. Wang, *Adv. Mater.* **2005**, *17*, 2974
- 139 G. He, D. Guo, C. He, X. Zhang, X. Zhao, C. Duan, *Angew. Chem., Int. Ed.* **2009**, *48*, 6132
- 140 J. Kalinowski, M. Cocchi, D. Virgili, V. Tattori, J.A.G. Williams, *Adv. Mater.* **2007**, *19*, 4000; W. Mróz, C. Botta, U. Giovanella, E. Rossi, A. Colombo, C. Dragonetti, D. Roberto, R. Ugo, A. Valore, J.A.G. Williams, *J. Mater. Chem.* **2011**, *21*, 8653
- 141 Y. Yang, M. Lowry, C.M. Schowalter, S.O. Fakayode, J.O. Escobedo, X. Xiangyang, H. Zhang, T.J. Jensen, F.R. Fronczek, I.M. Warner, R.M. Strongin, *J. Am. Chem. Soc.* **2006**, *128*, 14081
- 142 H. Okamoto, K. Satake, M. Kimura, *ARKIVOC* **2007**, *8*, 112
- 143 S.Y. Li, Q. Wang, Y. Qian, S. Q. Wang, Y. Li, G.Q. Yang, *J. Phys. Chem. A* **2007**, *111*, 11793; W.H. Sun, S.Y. Li, R. Hu, Y. Qian, S.Q. Wang, G.Q. Yang, *J. Phys. Chem. A* **2009**, *113*, 5888
- 144 J. Kalinowski, G. Giro, M. Cocchi, V. Fattori, P. Di Marco, *Appl. Phys. Lett.* **2000**, *76*, 2352
- 145 Y. Liu, M. Nishiura, Y. Wang, Z. Hou, *J. Am. Chem. Soc.* **2006**, *128*, 5592
- 146 Z. Zhao, B. Xu, Z. Yang, H. Wang, X. Wang, P. Lu, W. Tian, *J. Phys. Chem.* **2008**, *112*, 8511
- 147 A.H. Shelton, I.V. Sazanovich, J.A. Weinstein, M.D. Ward, *Chem. Commun.* **2012**, *48*, 2749
- 148 D. Sykes, I.S. Tidmarsh, A. Barbieri, I.V. Sazanovich, J.A. Weinstein, M.D. Ward, *Inorg. Chem.* **2011**, *50*, 11323
- 149 S. Park, J.E. Kwon, S.H. Kim, J. Seo, K. Chung, S.-Y. Park, D.-J. Jang, B.M. Medina, J. Gierschner and S.Y. Park, *J. Am. Chem. Soc.* **2009**, *131*, 14043; S.H. Kim, S. Park, J.E. Kwon, S.Y. Park, *Adv. Funct. Mater.* **2011**, *21(4)*, 644
- 150 G. He, D. Guo, C. He, X. Zhang, X. Zhao, C. Duan, *Angew. Chem. Int. Ed.* **2009**, *48*, 6132

- 151 H.J. Bolink, F. De Angelis, E. Baranoff, C. Klein, S. Fantacci, E. Coronado, M. Sessolo, K. Kalyanasundaram, M. Grätzel, Md.K. Nazeeruddin, *Chem. Comm.* **2009**, *31*, 4672
- 152 <http://www.cie.co.at>
- 153 R. Hunter, R.W. Harold, *The measurement of appearance*, J. Wiley & Sons, 2nd edn, 1987
- 154 R.W.G. Hunt, *Measuring Colour*, Fountain Press, 3rd edn, 1998
- 155 O. Fischer, *Justus Liebigs Ann. Chem.* **1881**, *206*, 83
- 156 W.L.F. Armarego; D.D. Perrin, *Purification of Laboratory Chemicals*, 4th ed.; Butterworth–Heinemann: Oxford, 1996
- 157 P. Sutter, C.D. Weiss, *Dyes and Pigments* **1990**, *12*, 287
- 158 S.M. Burkinshaw, J. Griffiths, A.D. Towns, *J. Mater. Chem.* **1998**, *8*, 2677
- 159 S.D. Ross, M. Schwarz *J. Am. Chem. Soc.* **1955**, *77*, 3020
- 160 M. Sekiya, Y. Terao *Chem. Pharm. Bull.* **1972**, *20*, 2128
- 161 H. Ahlbrecht, E.O. Dübner, J. Epsztajn, R.M.K. Marcinkowski, *Tetrahedron* **1984**, *40*, 1157
- 162 H. Takahashi, Y. Hashimoto, K. Nagasawa, *Heterocycles* **2001**, *55*, 2305
- 163 F. Ulmann, A. Maric, *Ber. Dtsch. Chem. Ges.* **1901**, *34*, 4307
- 164 A. Kliegl, *Ber. Dtsch. Chem. Ges.* **1906**, *39*, 1266
- 165 S.G.R. Guinot, J.D. Hepwarth, M. Weinwright, *J. Chem. Res. Miniprint* **1997**, *6*, 1252
- 166 A. Barker, C.C. Barker, *J. Chem. Soc.* **1954**, 870
- 167 A. Barker, C.C. Barker, *J. Chem. Soc.* **1954**, 1307
- 168 R.A. Velapoldi, National Beaureau of Standards 378, Proc. Conf. NBC, Gaithersburg, 1972; p. 231
- 169 D.F. Eaton, *Pure & Appl. Chem.* **1988**, *60*, 1107
- 170 K. Rechthaler, G. Köhler, *Chem. Phys. Lett.*, **1996**, *250*, 152
- 171 J. Jasny, *J. Lumin.*, **1978**, *17*, 143
- 172 J. Jasny, J. Sepioł, J. Karpiuk, J. Gilewski, *Rev. Sci. Instrum.* **1994**, *65*, 3646
- 173 APEXII–2008v1.0 Bruker Nonius 2007
- 174 SAINT V7.34A Bruker Nonius 2007

- 175 SADABS–2008/1 Bruker Nonius area detector scaling and absorption
correction, 2008
- 176 G.M. Sheldrick, *Acta Crystallogr. A* **1990**, *46*, 467.
- 177 G.M. Sheldrick, SHELXL93. *Program for the Refinement of Crystal
Structures*, Univ. of Göttingen, Germany.
- 178 *International Tables for Crystallography*, Ed. A. J. C. Wilson, Kluwer:
Dordrecht, **1992**, Vol. C
- 179 A.D. Becke, *J. Chem. Phys.* **1993**, *98*, 5648; A.D. Becke, *Phys. Rev. A*
1998, *38*, 3098
- 180 C. Lee, W. Yang, R.G. Parr, *Phys. Rev. B* **1988**, *37*, 785
- 181 R.E. Stratmann, G.E. Scuseria, M.J. Frisch, *J. Chem. Phys.* **1998**, *109*,
8218
- 182 J. Karpiuk, E. Karolak, J. Nowacki, *Pol. J. Chem.* **2008**, *82*, 865
- 183 Z. Majeed, W.R. McWhinnie, K. Paxton, T. Hamor, *J. Chem. Soc.
Dalton Trans.* **1998**, 3947.
- 184 F. Sanjuan–Szkларz, K. Woźniak, E. Karolak–Solarska, J. Karpiuk,
manuscript in preparation.
- 185 W.B. Schweizer, J.D. Dunitz, *Helvetica Chimica Acta* **1982**, *65*, 1547
- 186 M. Ballester, J. Riera, *Spectrochim. Acta* 1967, **23A**, 1533
- 187 J.R. Platt, *J. Chem. Phys.* **1949**, *17*, 484
- 188 W.D. Oosterbaan, M. Koeberg, J. Piris, R.W.A. Havenith, C.A. van
Walree, B.R. Wegewijs, L.W. Jenneskens, J.W. Verhoeven, *J. Phys.
Chem. A* **2001**, *105*, 5984
- 189 C.A. van Walree, M.R. Roest, W. Schuddeboom, L.W. Jenneskens,
J.W. Verhoeven, J.M. Warman, H. Kooijman, A.L. Spek, *J. Am.
Chem. Soc.* **1996**, *118*, 8395
- 190 J.W. Verhoeven, I.P. Dirks, T.J. De Boer, *Tetrahedron* **1969**, *25*, 4037
- 191 T. Scherer, W. Hielkema, B. Krijnen, R.M. Hermant, C. Eijckelhoff, F.
Kerkhof, A.K.F. Ng, R. Verleg, E.B. van der Tol, A.M. Brouwer, J.W.
Verhoeven, *Recl. Trav. Chim. Pays–Bas* **1993**, *112*, 535
- 192 C. Reichardt, *Chem. Rev.* **1994**, *94*, 2319
- 193 F.D. Lewis, J.M. Wagner–Brennan, A.M. Miller, *Can. J. Chem.* **1999**,
77, 595
- 194 F.G. Brown, J. Cosa, *Chem. Phys. Lett.* **1977**, *45*, 429
- 195 J.B. Birks, *Photophysics of Aromatic Molecules*, J. Wiley, New York,
1978

- 196 L. Onsager, *J. Am. Chem. Soc.* **1936**, 58, 1486
- 197 E. Lippert, *Z. Naturforschg.* **1955**, 10a, 541; N. Mataga, Y. Kaifu, M.
Koizumi, *Bull. Chem. Soc. Japan* **1955**, 28, 690
- 198 H. Beens, H. Knibbe, A. Weller, *J. Chem. Phys.* **1967**, 47, 1183
- 199 Ground state dipole moment of MGLA and MGL estimated with TD-
DFT calculations on the B3LYP/6-31G(d) level is the same and equal
to 6.5 D.
- 200 B.A. Kellog, R. Brown, R.S. McDonald, *J. Org. Chem.* **1994**, 59, 4652
- 201 All the following measurements and results were obtained in the
Department of Chemical and Biological Engineering / Physical
Chemistry and Organic Chemistry, Chalmers University of
Technology, Gothenburg, Sweden
- 202 R. Gavara, C. Laia, A.J. Parola, F. Pina, *Chem. Eur. J.* **2010**, 16, 7760
- 203 R.M. Wilson, K.A. Schnapp, M. Glos, C. Bohne, A.C. Dixon, *Chem.*
Commun. **1997**, 149
- 204 R.S. Givens, W.F. Oettle, *J. Am. Chem. Soc.* **1971**, 93, 3301
- 205 C.M. Previtali, *J. Photochem.* **1985**, 31, 233
- 206 E. Görlach, H. Gygax, P. Lubini, U.P. Wild, *Chem. Phys.* **1995**, 194,
185
- 207 M. Goes, M. de Groot, M. Koeberg, J.W. Verhoeven, N.R. Lokan,
M.J. Shephard, M.N. Paddon-Row, *J. Phys. Chem. A* **2002**, 106, 2129
- 208 A. Chowdhury, S.A. Locknar, L.L. Premvardhan, L.A. Peteanu, *J.*
Phys. Chem. A **1999**, 103, 9614
- 209 L. Janelli, A. Lopez, L. Silvestri, *J. Chem. Eng. Data* **1983**, 28, 166
- 210 C. Streck, R. Richert, *Ber. Bunsenges. Phys. Chem.* **1994**, 98, 619
- 211 D.W. Dawidson, R.H. Cole, *J. Chem. Phys.* **1951**, 19, 1484
- 212 G.U. Bublitz, S.G. Boxer, *J. Am. Chem. Soc.* **1998**, 120, 3988
- 213 J. Timmermans, *Physico-Chemical Constants of Pure Organic*
Compounds; Elsevier: Amsterdam, The Netherlands, 1986; Vol. 2
- 214 H. Wendt, R. Richert, *J. Phys. Chem. A* **1998**, 102, 5775
- 215 H. Sumi, R.A. Marcus, *J. Chem. Phys.* **1986**, 84, 4894
- 216 Y. Nagasawa, A.P. Yartsev, K. Tominaga, P.B. Bisht, A.E. Johnson,
K. Yoshihara, *J. Phys. Chem.* **1995**, 99, 653
- 217 Jr. E.O. Holmes, *J. Phys. Chem.* **1957**, 61, 434

- 218 J. Herbich, A. Kapturkiewicz, *Chem. Phys.* **1991**, *158*, 143
- 219 J. Herbich, A. Kapturkiewicz, *Chem. Phys.* **1993**, *170*, 221
- 220 R. Englman, J. Jortner, *Mol. Phys.* **1970**, *18*, 145
- 221 N.J. Turro, *Modern Molecular Photochemistry*, Benjamin/Cummings, New York, 1978
- 222 L.H. Schwartzman, *J. Org. Chem* **1950**, *15*, 517; T. Masamune, *J. Am. Chem. Soc.* **1957**, *79*, 4418
- 223 P.F. King, *U.S. Patent* 5220036, 1993
- 224 E.J. Dombrowski, J.R. Freedman, P.F. King, *U.S. Patent* 5196297, 1993
- 225 P.F. King, *U.S. Patent* 5028725, 1991
- 226 J. Karpiuk, *Photophysical and photochemical processes in lactones of some rhodamines*, PhD thesis, Institute of Physical Chemistry, Polish Academy of Sciences, Warsaw, 1996
- 227 I.B. Berlman *Handbook of Fluorescence Spectra of Aromatic Molecules*, Academic Press, New York and London, 1971
- 228 J.L.N. Xavier, E.Ortega, J.Z. Ferreira, A.M. Bernardes, V. Pérez-Herranz, *Int. J. Electrochem. Sci.* **2011**, *6*, 622
- 229 D. Bourget, P. Jacques, E. Vauthey, P. Suppan, E. Haselbach, *J. Chem. Soc., Faraday Trans.* **1994**, *90*, 2481
- 230 A. Kapturkiewicz, *Chem. Phys.* **1992**, *166*, 259
- 231 W. Liptay, *Excited states*; E.C. Lim, Ed.; Academic Press: New York, 1974; p 129
- 232 A. Kapturkiewicz, J. Herbich, J. Karpiuk, J. Nowacki, *J. Phys.Chem.* **1997**, *101*, 2332; A. Kapturkiewicz, J. Herbich, *J. Am. Chem. Soc.* **1998**, *120*, 1014
- 233 H. Masuhara, T. Hino, N. Mataga, *J. Phys. Chem.* **1975**, *79*, 994; A. Jouyban, S. Soltanpour, H.-K. Chan, *Int. J. Pharm.* **2004**, *269*, 353
- 234 H. Okamoto, A. Matsui, K. Satake, *Analyst*, **2011**, *136*, 3164
- 235 R.F. Bradley, C.H. Schwalbe, K.C. Ross, W. Fraser, S. Freeman, *Acta Crystallogr. Sect. C*, **1997**, *C53*, 1626
- 236 Z. Majeed, W.R. McWhinnie, K. Paxton, T. Hamor, *J. Chem. Soc. Dalton Trans.* **1998**, 3947
- 237 D.A. Brown, M.J.S. Dewar, *J. Chem. Soc.* **1954**, 2134

- 238 S. Nakatsuji, H. Nakazumi, H. Fukuma, T. Yahiro, K. Nakashima, M.
lyoda, S. Akiyama, *J. Chem. Soc., Chem. Comm.* **1990**, 489
- 239 S. Nakatsuji, H. Nakazumi, H. Fukuma, T. Yahiro, K. Nakashima, M.
lyoda, S. Akiyama, *J. Chem. Soc. Perkin Trans.* **1991**, 1881
- 240 S.G.R. Guinot, J.D. Hepworth, M. Wainwright, *Dyes and Pigments*
1999, *40*, 151
- 241 R. E. Gerkin, A. P. Lundstedt, W. J. Reppart, *Acta Cryst. C*, **1984**, *40*,
1892
- 242 G–P. Charbonneau, Y. Delugeard, *Acta Cryst. B* **1976**, *32*, 1420; X.
Miao, S. Chu, X.Xu, X. Jin, *Chinese Science Bulletin*, **1997**, *42*, 1803
- 243 V. J. Eaton, D. Steele, *J. Chem. Soc., Faraday Trans.2*, **1973**, *69*, 1601
- 244 J.A. Platts, S.T. Howard, *J. Org. Chem.* **1996**, *61*, 4480
- 245 H.A. Staab, T. Saupe, *Angew. Chem.* **1988**, *27*, 865
- 246 I.B. Berlman, *J. Phys. Chem.*, **1970**, *74*, 3085
- 247 T. Redzinski, J. R. Heldt, *J. Fluoresc.* **2003**, *13* (5), 393
- 248 F.G. Sanchez, M. Algarra, J. Lovillo, A. Aguilar, A.N. Diaz, *J. Incl.*
Phenom. Macrocycl. Chem. **2010**, *66*, 307
- 249 S.J. Strickler, R.A. Berg, *J. Chem. Phys.* **1962**, *37*, 814
- 250 X. Wang, M. Song, Y. Long, *J. Solid State Chem.* **2001**, *156*, 325
- 251 A. Kvick, G.B.M. Vaughan, X. Wang, Y. Sun, Y. Long, *Acta Cryst. C*
2000, *56*, 1232
- 252 W.B. Schweizer, J.D. Dunitz, *Helvetica Chimica Acta* **1982**, *65*, 1547
- 253 C.R. Theocharis, W. Jones, *J. Crystal. Spectrosc. Res.* **1984**, *14*, 121
- 254 M. Kubata, H. Yoshioka, K. Nakatsu, M. Matsumoto, Y. Sato,
Chemistry of Functional Dyes, ed. Z. Yoshida and T. Kitao, Mita
Press, Tokyo, 1989, p. 223
- 255 F.H. Allen, A.J. Kirby, *J. Am. Chem. Soc.* **1984**, *106*, 6197
- 256 A.J. Kirby, *Pure & Appl. Chem.* **1987**, *59* (12), 1605
- 257 Yamamoto Kagaku Gosei, *Eur. Pat.* 124 377, 1984
- 258 Yamamoto Kagaku Gosei, *Eur. Pat.* 278 614, 1988
- 259 V. I. Minkin, *Chem. Rev.* **2004**, *104*, 2751
- 260 P. Maslak, A. Chopra, C. R. Moylan, R. Wortmann, S. Lebus, A. L.
Rheingold, G. P. Yap, *J. Am. Chem. Soc.* **1996**, *118*, 1471

- 261 H.E. Simmons, T. Fukunaga, *J. Am. Chem. Soc.* **1967**, *89*, 5208; R. Hoffmann, A. Imamura, G.D. Zeiss, *J. Am. Chem. Soc.* **1967**, *89*, 5215
- 262 H. Dürr, R. Gleiter, *Ang. Chem.* **1978**, *90*, 591
- 263 H. Dürr, R. Gleiter, *Ang. Chem. Int. Ed. Engl.* **1978**, *90*, 559
- 264 P. Maslak, A. Chopra, *J. Am. Chem. Soc.* **1993**, *115*, 9331; P. Maslak, A. Chopra, C.R. Moylan, R. Wortmann, S. Lebus, A.L. Rheingold, G.P.A. Yap, *J. Am. Chem. Soc.* **1996**, *118*, 1471
- 265 V.I. Minkin, A.G. Starikov, *Doklady Akademii Nauk.* **2004**, *396*, 212; English translation: *Doklady Akademii*, **2004**, *396*, 99
- 266 T.P.I. Saragi, T. Spehr, A. Siebert, T. Fuhrmann-Lieker, J. Salbeck, *Chem. Rev.* **2007**, *107*, 1011
- 267 S.M. King, I.I. Perepichka, I.F. Perepichka, F.B. Dias, M.R. Bryce, A.P. Monkman, *Adv. Funct. Mater.* **2009**, *19*, 586
- 268 J. Karpiuk, E. Karolak, J. Nowacki, *Phys. Chem. Chem. Phys.* **2010**, *12*, 8804
- 269 K.C. Tang, M.J. Chang, T.Y. Lin, H.A. Pan, T.C. Fang, K.Y. Chen, W.Y. Hung, Y.H. Hsu, P.T. Chou, *J. Am. Chem. Soc.* **2011**, *133*, 17738
- 270 H. Masuhara, T. Hino, N. Mataga, *J. Phys. Chem.* **1975**, *79*, 994; A. Jouyban, S. Soltanpour, H.-K. Chan, *Int. J. Pharm.* **2004**, *269*, 353
- 271 G. Angulo, G. Grampp, A. Rosspeintner, *Spectrochim. Acta, Part A* **2006**, *65*, 727
- 272 W.H. Sun, S.Y. Li, R. Hu, Y. Qian, S.Q. Wang, G.Q. Yang, *J. Phys. Chem. A* **2009**, *113*, 5888
- 273 T. Förster, *Fluoreszenz Organischer Verbindungen*; Vandenhoeck & Ruprecht, Göttingen, 1951
- 274 B.G. Zykov, Y.V. Vasil'ev, V.S. Fal'ko, A.N. Lachinov, V.I. Khvostenko, N.G. Gileva, *JETP Lett.* **1996**, *64*, 439

B. 448/13



Biblioteka Instytutu Chemii Fizycznej PAN

F-B.448/13



90000000185663